# Improved Interflow and Infiltration Algorithms for Distributed Hydrological Models

by

Guoxiang Liu

A thesis
presented to the University of Waterloo
in fulfillment of the
thesis requirement for the degree of
Doctor of Philosophy
in
Civil Engineering

Waterloo, Ontario, Canada, 2010

I hereby declare that I am the sole author of this thesis. This is a true copy of the thesis, including any required final revisions, as accepted by my examiners.

I understand that my thesis may be made electronically available to the public.

**Abstract**

The shallow subsurface controls the partitioning of available energy between sensible and latent heat of the land surface, and the partitioning of available water among evaporation, infiltration, and runoff. It is a key component of both the hydrometeorological system and the terrestrial water cycle. A critical part of any hydrological or hydrometeorological forecast model is therefore the algorithms used to represent the shallow soil processes, which include infiltration, evaporation, runoff, and interflow. For climate models, coupled algorithms called "Land Surface Schemes" (LSSs) are developed to represent the lower boundary conditions that deal with the land-to-atmosphere energy and moisture fluxes. Similar algorithms are implemented in regional watershed models and day-to-day operational water resources forecasting models. It is the primary objective of this thesis to provide improved methods for simulating coupled land surface processes, which can be used as components of LSSs or within existing operational hydrology models. These new methods address a number of specific issues inadequately handled by current models, including the presence of shallow boundary conditions, heterogeneity in infiltration, and infiltration and interflow coupling processes.

The main objective of the proposed research is to provide consistent physically-based approach for simulating near surface soil moisture processes, so as to complete the parameterization of the interflow/infiltration algorithm in a Hydrology-Land-Surface scheme MESH. The work mainly focuses on the investigation and development of more physically-based infiltration and interflow algorithms. The hope is to determine appropriate relationships between internal state variables (specifically bulk soil moisture) and system boundary fluxes, while simultaneously reducing the number of nonphysical or unknown model parameters. Fewer parameters lead to reduced calibration requirements for distributed hydrological models and consequently accelerate the transfer of such models to engineering practice.

Multiple approaches were taken to provide improved relationships between infiltration and lateral drainage, fluxes and storage. These algorithms were tested by a specialized Richards' equation for sloping soils and Monte Carlo simulations. These tests demonstrated reasonable accuracy and improved representation for the hydrological processes.

**Acknowledgements**

It is my pleasure to take this opportunity to thank those who helped me through my graduate studies. First, I would like to thank my two supervisors: Dr. Eric D. Soulis and Dr. James R. Craig. You two have made available your support in a number of ways, not only for my work , but also for my life. I cannot be more grateful!

It is a pleasure to thank those who made this thesis possible, my committee members, for your invaluable advices and patience during my PhD studies. Most importantly, I want to thank each of you for a special experience during my studies: Dr. William L. Quinton, thank you for the best field work experience; Dr. Neil R. Thomson, thank you for the hardest but the best course; Dr. Bryan Tolson, thank you for the kindest help in the first course I took in Canada; Dr. Aaron Berg, thank you for traveling to Waterloo to be my external examiner.

This thesis would not be completed without help from colleagues and friends. All colleagues in the hydrology lab are thanked. Thanks to my friends: Andy, Beatrice, Mela, Sanders, Ting, and Tussane for joining me and supporting me in happy and hard times. Thank you Jinghua and Xiaohui, a kind couple I met at Waterloo, for you taking care of me during those bad times.

I owe my family too, too much, which cannot be described by words. I haven't taken the responsibility of being a family member, but you all always stand there for me and support me. I am grateful for parents giving me life and guiding me to become a good person. I am grateful to my older brother for sharing everything with me and guiding me when I am lost in life. I am grateful for getting invaluable guidance from my aunt and uncle. I am so proud of being a member of the Liu family.

Shenwei, my husband and lover, I cannot imagine where I would be without you. You tolerate my tempers and all my shortcomings. I am not always a good person to you, but you have always forgiven me. You are the man I dreamed of!

Lastly, thanks to all people I know for accompanying me through this long journey at the University of Waterloo. I appreciate everyone I met here and cherish my memories with each of you.

## Dedication

To my parents.

# Contents

# List of Tables

# List of Figures

# List of symbols

$[\Psi]$ Unknown variable $\psi$ vector

$[A]$ Coefficient vector

$[B]$ Constant vector

$\alpha$ Van-Genuchten empirical parameter, see equation (2.3), page 11

$\alpha_G$ Constant sorptive number [-]

$\alpha$ Initial condition index, page 28

$\bar{k}$ Mean of hydraulic conductivity $[LT^{-1}]$

$\bar{s}$ Bulk saturation [-]

$\bar{f}$ Mean infiltration rate $[LT^{-1}]$

$\Delta t$ Temporal discretization

$\Delta X$ Spatial discretization in $X$ direction

$\Delta Z$ Spatial discretization in $Z$ direction

$\epsilon(k_s, X)$ Deviation of the exact solution from the linear approximation

$\mathrm{erf}(x)$ Math command error function

$\mathrm{erfc}(x)$ Math command complementary error function

$\lambda$ Pore size index [-], see equation (2.3), page 11

$\Lambda$ Slope of the aquifer [-]

| | |
|---|---|
| $\lambda$ | Hydraulic conductivity decay factor, see equation (4.3), page 85 |
| $\mu_Y$ | Mean of log hydraulic conductivity |
| $\nabla$ | Gradient operator |
| $\psi$ | Pressure head $[L]$ |
| $\psi_f$ | Suction at the wetting front $[L]$ |
| $\psi_u$ | Up boundary pressure $[L]$ |
| $\psi_{ae}$ | Air entry pressure $[L]$ |
| $\sigma$ | Standard variance |
| $\sigma_Y$ | Standard deviation of log hydraulic conductivity |
| $\tan\beta$ | TOPMODEL topographic index |
| $\tau(t)$ | Time representation |
| $\Theta$ | Finite difference weighting factor $[-]$ |
| $\theta$ | Water content [-] |
| $\theta_i$ | Initial water content [-] |
| $\theta_r$ | Residual water content [-] |
| $\theta_s$ | Saturated water content [-] |
| $\theta_{fc}$ | Water content at field capacity [-] |
| $\varepsilon$ | Suction gradient index [-] |
| $A$ | Area $[L^2]$ |
| $A_C$ | Variable contribution area $[L^2]$ |
| $b$ | Clapp-Hornberger pore-size distribution index |
| $c_{i,j}^{n,m}$ | Specific water capacity of the soil |
| $D$ | Depth $[L]$ |

$D^*$ Semi-infinite depth $[L]$

$D_D$ Drainage density $[L^{-1}]$

$E$ Evaporation $[LT^{-1}]$

$E_F$ Relative error for the cumulative infiltration [-]

$E_f$ Relative error for the infiltration rate [-]

$F$ Cumulative infiltration $[L]$

$f$ Infiltration capacity $[LT^{-1}]$

$f_m$ Maximum infiltration capacity $[LT^{-1}]$

$f_{k\alpha}$ Joint probability distribution of saturated conductivity and initial condition

$h$ Hydraulic head $[L]$

$h_0$ Ponding depth $[L]$

$i$ Unit vector

$k$ Hydraulic conductivity $[LT^{-1}]$

$k_X$ Lateral hydraulic conductivity $[LT^{-1}]$

$k_Z$ Vertical hydraulic conductivity $[LT^{-1}]$

$k_{ref}$ Hydraulic conductivity at a reference depth $z_{ref}$ $[LT^{-1}]$

$k_{s0}$ Saturated hydraulic conductivity at the surface $[LT^{-1}]$

$L_S$ Average distance between the divide and the micro-drainage system stream channel $[L]$

$m$ Picard iteration level, see equation (3.1), page 35

$m$ Van-Genuchten empirical parameter, see equation (2.3), page 11

$n$ Time iterative level, see equation (3.2), page 36

$n$ Van-Genuchten empirical parameter, see equation (2.3), page 11

| | |
|---|---|
| $N_x$ | Number of blocks in $X$ direction |
| $N_Z$ | Number of blocks in $Z$ direction |
| $P$ | Precipitation $[LT^{-1}]$ |
| $q$ | Flow velocity $[LT^{-1}]$ |
| $R^2_{NS}$ | NASH-Sutcliffe coefficient |
| $S$ | Sorptivity $[LT^{-1/2}]$ |
| $s$ | Saturation [-] |
| $s_a(t)$ | Saturation at $X = 0$ |
| $S_s$ | Specific storage of soil $[L^{-1}]$ |
| $S_y$ | Specific yield [-] |
| $SD$ | Simulation duration $[T]$ |
| $t$ | Time $[T]$ |
| $t^*$ | Surrogate time $[T]$ |
| $T_0$ | Transmissivity $[L^2T^{-1}]$ |
| $t_b$ | The moment after which fully unsaturated conditions occur alone the entire seepage face $[T]$ |
| $t_c$ | The instant at which the seepage face ceases to be fully saturated $[T]$ |
| $t_p$ | Time to ponding $[T]$ |
| $W$ | Lambert function |
| $w$ | Rainfall rate $[LT^{-1}]$ |
| $X$ | Dimensionless time [-] |
| $X_s$ | Location of the interface between the saturated and unsaturated soil surface$[L]$ |
| $z$ | Elevation head $[L]$ |

$z_D^*$ Dimensionless distance to the bottom boundary [-]

$z_f$ Wetting front depth $[L]$

$z_i$ Water deficit $[L]$

$z_{ref}$ Reference depth $[L]$

# Chapter 1

# Introduction

The shallow subsurface controls the partitioning of available energy between sensible and latent heat of the land surface, and the partitioning of available water among evaporation, infiltration, and runoff [109]. It is a key component of both the hydrometeorological system and the terrestrial water cycle. A critical part of any hydrological or hydrometeorological forecast model is therefore the algorithms used to represent the shallow soil processes, which include infiltration, evaporation, runoff, and interflow. For climate models, coupled algorithms called "Land Surface Schemes"(LSSs) are developed to represent the lower boundary conditions to deal with the land-to-atmosphere energy and moisture fluxes. Similar algorithms are implemented in regional watershed models and day-to-day operational forecasting water resources models. It is the primary objective of this thesis to develop and test improved physically-based algorithms for simulating near surface soil moisture processes, which can be used as components of LSSs or within existing operational hydrology models. These new methods address a number of specific inadequacies in current models, including existence of shallow boundary conditions, heterogeneity in infiltration, and recharge coupling processes.

## 1.1 Motivation

Water is constantly cycled between the atmosphere, oceans, and land. Figure 1.1 represents a schematic of the entire water cycle. Precipitation moves water from the atmosphere to the Earth. Water infiltrates into the soil to generate subsurface runoff or flows over land as surface runoff into streams and oceans. Water evaporates from land, streams, and oceans. This water vapor rises into the atmosphere and again becomes the source of precipitation.

Because the soil plays a key part in the water circle, climatologists, hydrologists, and hydrogeologists have each developed their own means of simulating moisture redistribution in the shallow subsurface. Each discipline's models contain subroutines to simulate the boundary processes but often do not consider the interaction between them.

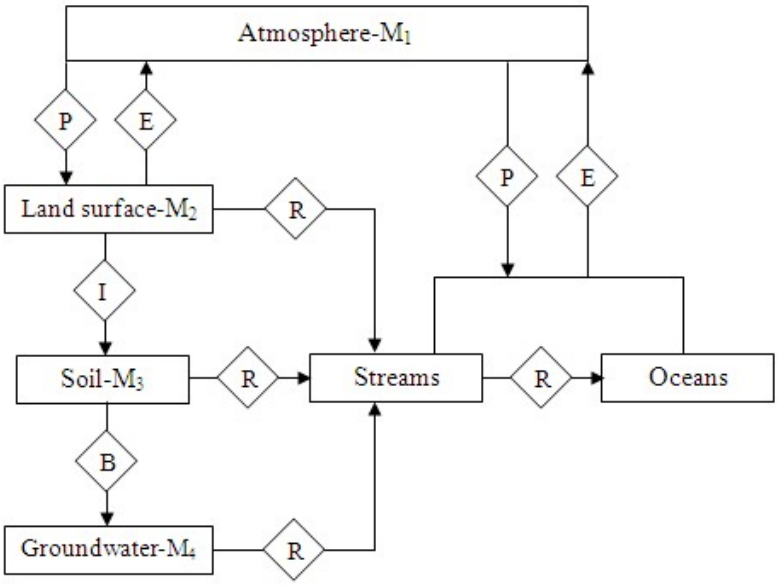


Figure 1.1: Schematic of simplified water cycle ($P$=Precipitation, $E$=Evaporation, $R$=Runoff, $I$=Infiltration, and $B$=Baseflow; $M_1$=Climate models, $M_2$=Land surface schemes, $M_3$=Hydrological models, and $M_4$=Groundwater models)

Recent efforts have been made to couple these models so that they can communicate with each other to improve model accuracy and/or reduce the simulation costs. The LSSs developed by climate models are focused on the vertical water and energy budgets, and typically have a well-developed evapotranspiration scheme whereas hydrological models focus on horizontal flow routing and contain more advanced baseflow, interflow, and infiltration schemes. By coupling a LSS with a hydrological model, the vertical water routines in the hydrological model can be replaced by that of the LSSs. The coupled system captures the best of each model and provides a comprehensive and systematic modeling scheme that avoids the delineation of the earth and atmosphere boundary.

Soil moisture is a crucial factor in any hydrological model. Infiltration, evapotranspiration, surface runoff, and drainage are functions of soil moisture. Evapotranspiration is

particularly sensitive to near surface soil moisture. A small change in soil moisture can result in a large change in the actual evapotranspiration, and further affect the large scale global water balance. Ideally, simulation of soil moisture must be simple, fast and robust [123]. To meet this goal, each discipline has taken a different approach. Numerous methods have been used to simulate soil moisture processes in large hydrological models. Early LSSs for atmospheric models use the Manabe bucket model [88], which is a simple and fast model that simulated all of the soil moisture processes simultaneously. However, the Manabe bucket model tends to over simplify the hydrologic processes: a single homogeneous soil layer is used to represent the soil structure and the water balance is represented as a simple exponential function of storage. The Manabe model can often match observed annual flows but fails to produce within-year details. More advanced modern LSSs adopt more complex soil reservoirs than that of the Bucket models, but they still use a smooth earth scheme with poor representation of lateral flow. At the other extreme, discretized numerical hydrological models based on Richards' equation (HYDRUS [118], WEPP [103], and SHE [1]) are able to represent physical process and are very powerful for solving the complex non-linear soil moisture simulation problem. However, such numerical models are computationally prohibitive and require detailed soil data that are usually unavailable.

Several compromises have evolved between the simple Bucket model and complicated numerical models, as shown in Figure 1.2. The Bucket model [88] contains only the vertical drainage process. In hillslope hydrology, saturated lateral subsurface flow has been included [71]. LSSs address the drainage between soil layers but most often use a flat surface and ignore lateral subsurface flow [141]. TOPMODEL ([10] [12]) predicts the spatial variability of the catchment response using a topographic index, which contains vertical flow in an unsaturated layer and lateral flow in a saturated layer. However, the infiltration and recharge are calculated independently and in a non-iterative manner.

As shown in Figure 1.2, interflow, defined as near surface lateral flow, is often neglected in the unsaturated zone. Drainage is calculated either by Darcy's law [141] or by empirical power functions [10], [71], which often match drainage characteristic curves but fail to provide a physical meaning of the parameters. A consistent relationship between internal state variables and the boundary flux has not been found. Regional soil heterogeneity is typically not accounted for and hillslope physics are often improperly handled. Also, in reality, infiltration, interflow, and recharge are simultaneous processes but haven't been properly coupled in many existing models, which typically treat processes independently.

This thesis aims to address many of these issues, in part, through further development of WATDRAIN. WATDRAIN is an independent subroutine to simulate the unsaturated zone lateral flow by relying on a solution to a simplified version of the Richards' equation. It can be incorporated into any hydrological model to represent the boundary flux and the

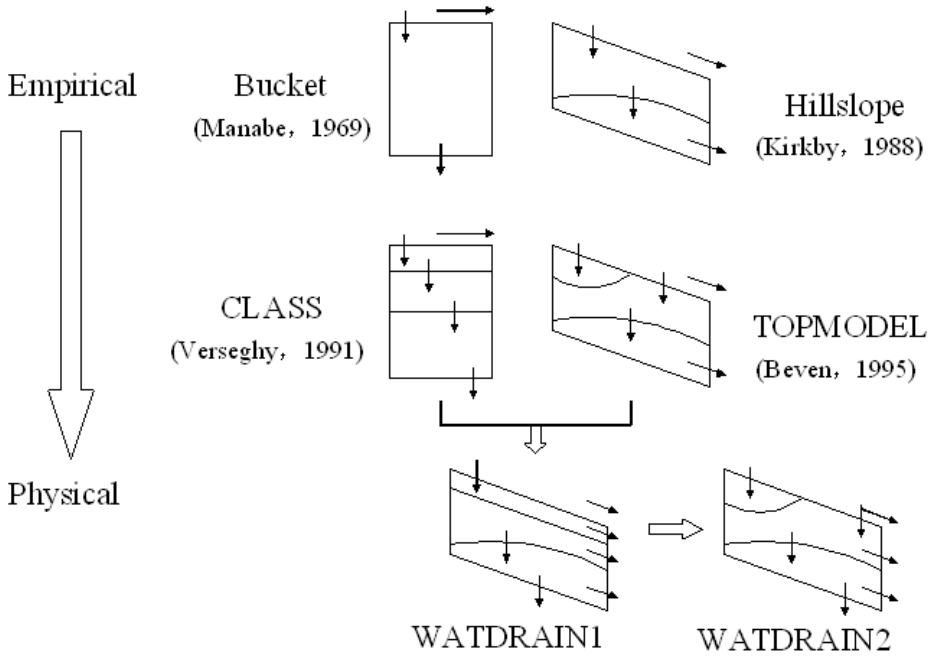


Figure 1.2: Evaluation of the soil mositure parameterization: From a purely empirical Bucket model to a physically-based, multi-layers land surface model and topographic based TOPMODEL; WATDRAINs in this study combines the vertical process of CLASS and lateral process of TOPMODEL, representing lateral process in unsaturated zone, to provide improved soil moisture simulation processes

distribution of the internal state variables. Currently, the WATDRAIN interflow algorithm has been incorporated into Modelisation Environmental Communitaire (MEC) [130] and the MEC Simulator for Hydrology (MESH, previously called WATCLASS, which is built from three existing models: a hydrological model WATFLOOD, a Canadian Land Surface Scheme (CLASS), and the subroutine WATDRAIN) modeling. The MESH model may be coupled to the Canadian Meteorological Center (CMC) operational numerical weather prediction system. The current implementation of soil processes in MESH is insufficient. For example, the infiltration process in CLASS is represented by a Green-Ampt sharp wetting front, which is a piston-like front of saturation parallel to the land surface that disappears after one time step. However, in reality, infiltration varies due to the non-uniform soil moisture distribution and the wetting front persists for many hours. There are similar shortcomings in the other vertical processes, namely parameterizations of between

layer transfers and recharge.

This research, based on preliminary results from the Mackenzie GEWEX study [129], continues the development of improved vertical infiltration, drainage, and lateral soil water simulation algorithms. This work firstly focuses on improving the simulation of vertical processes, mainly the infiltration calculation. The next step is incorporating an updated interflow algorithm into a stand-alone soil model. Third, methods are investigated for combining the vertical and lateral processes to provide an improved soil moisture model for Hydrology-Land-Surface Schemes (HLSSs). In the end, this research study intends to yield an improved algorithmic representation of the hydrologic soil processes. These collective improvements reduce the calibration requirements for distributed hydrologic models and consequently accelerate the transfer of such models to engineering practice.

## 1.2 Objectives

The essence of soil moisture modeling at the watershed or hillslope scale is to develop a relationship between boundary fluxes (e.g., infiltration or recharge) and the control volume storage. In this thesis, multiple approaches are taken to derive improved relationships between infiltration and lateral drainage, fluxes and storage so as to provide novel, robust, and efficient physically-based soil simulation processes. Though Beven [13] mentioned that it is very difficult to develop a functional representation of fluxes in terms of internal states, multiple useful parameterized flux relations are found in the current research.

To develop improved methods for more appropriately and accurately simulating near surface soil moisture processes, thereby improving the utility and robustness of the MESH land surface scheme. The work mainly focuses on the investigation and development of more physically-based infiltration and interflow algorithms. The hope is to determine appropriate non-empirical relationships between internal state variables (specifically bulk soil moisture) and the boundary fluxes, and thereby reduce the number of nonphysical or unknown model parameters. Fewer parameters lead to reduced calibration requirements for distributed hydrological models and consequently accelerate the transfer of such models to engineering practice.

To meet the primary objective of this thesis, a number of activities were undertaken:

- **Vertical infiltration algorithm amendments were investigated.** Infiltration can be significantly affected by the presence of shallow boundaries. Such shallow boundaries have not been considered in existing distributed infiltration models. The

limiting conditions under which the standard Green-Ampt infiltration model is appropriate and how lower boundary conditions affect the validity of the model are addressed. Modifications to the infiltration model under shallow boundary conditions are presented and tested via rigorous comparison with the numerical solution to the Richards' equation for a wide range of soil textures and model parameters.

- **An upscaled infiltration equation was developed.** Heterogeneity in soil moisture and soil properties is an important driver of net infiltration, one which has not been properly accounted for by most infiltration models. Here an upscaled infiltration equation for calculating regional-averaged infiltration rates into heterogeneous soils are developed. The upscaled solution is capable of addressing the variability in initial conditions, porosity, and the wetting front matric potential. It was compared to results of a Monte Carlo model with wide range of heterogeneity level and shows consistent results.

- **An analytical interflow algorithm was defined and tested.** Two versions of an analytical interflow algorithm were developed in this study. One is suitable for regions with wet soils and the other one is for regions that are dry for a long period. Both algorithms were compared against numerical solutions to the Richards' equation and are shown capable of replicating the correct physical behavior under the conditions they are intended.

- **A stand-alone soil model was implemented, tested, and refined.** The soil model was partitioned from a hydrology-land-surface model MESH for testing the improved analytical interflow algorithm. Unlike the original MESH, the interflow and infiltration were coupled in this model by a dynamic saturated surface area to provide a closer approximation of the physical processes observed.

- **A specialized finite difference code for unsaturated flow in sloping soils was developed.** It provides robust guidance for development of improved interflow and infiltration algorithms.

## 1.3 Outline of the Thesis

The remainder of the thesis consists of four chapters. Chapter 2 provides background on the pertinent subjects, including a literature review of subsurface hydrology, drainage/baseflow models, infiltration models, and hydrological similarity. Chapter 3 describes the development of the improved infiltration algorithms as well as a number of preliminary test results.

Chapter 4 discusses an improved interflow algorithm and its application in a Hydrological-Land-surface model for lateral and vertical flow coupling process. Also in Chapter 4, this interflow algorithm is coupled to an infiltration algorithm. The final chapter includes conclusions and provides recommendations for further research.

# Chapter 2

# Background

Chapter 2 provides a literature review of pertinent studies that have been done up to the present time in the areas of hydrological modeling of the shallow subsurface. Subsurface flow plays an important role in the global hydrological cycle. It has therefore received considerable attention in journals and publications. Drainage/baseflow models are reviewed beginning with a review of subsurface hydrology. Two types of popular infiltration models are reviewed: empirical models and physically-based Richards' equation models. One of the most widely used infiltration models, the Green-Ampt model, is described in detail to support later investigation of upscaling and applicability. At the end of chapter 2, the concept of hydrological similarity is briefly reviewed.

## 2.1 Subsurface Hydrology

Subsurface water movement can be described by a mass continuity equation with appropriate boundary conditions. The resulting equation, Richards' equation, is considered the most appropriate mathematical description of the subsurface physical process. To solve this partial differential equation, soil hydraulic characteristics functions and boundary conditions are needed. All these subjects will be discussed below.

### 2.1.1 Governing Equations

Darcy established the fundamental relationship for soil-water movement as [41]:

$$q = -k\nabla h \tag{2.1}$$

where $q$ is the flow velocity $[LT^{-1}]$, $k$ is the hydraulic conductivity $[LT^{-1}]$, $\nabla$ is the gradient operator, and $h$ is the total hydraulic head $[L]$, equal to the sum of the water pressure head $\psi$ $[L]$ and the elevation head $z$ $[L]$.

Richards extended Darcy's law to the unsaturated zone, assuming the soil-water pressure, $\psi$, and the hydraulic conductivity, $k$, are functions of soil water content, $\theta$. Combining Darcy's law with the mass continuity equation, a general form of Richards' equation is expressed as [111] :

$$S_s \frac{\theta}{\theta_s} \frac{\partial \psi}{\partial t} + \frac{\partial \theta}{\partial t} = \nabla k(\nabla \psi + \hat{i}) \tag{2.2}$$

where $S_s$ is the specific storage of soil $[L^{-1}]$, $\theta_s$ is the saturated water content [-], $t$ is time $[T]$, and $\hat{i}$ is a unit vector downward.

Equation 2.2 is the governing equation for subsurface water movement. It is a nonlinear partial differential equation and has been widely used in subsurface water modeling. Physical models of the full 3D Richards' equation are considered the most realistic means of shallow subsurface flow simulation.

Equation 2.2 is called the mixed form of Richards' equation [111]. There are two dependent variables: the water content, $\theta$, and the water pressure head, $\psi$. Relations to describe the interdependence among water content, soil pressure, and hydraulic conductivity are required to solve equation 2.2. One of the dependent variables, $\theta$, can be eliminated by adopting a specific moisture capacity, which is defined by taking a derivative of the soil water retention curve, $\frac{d\theta}{d\psi}$, to generate a pressure-head form of Richards' equation as:

$$S_s \frac{\theta}{\theta_s} \frac{\partial \psi}{\partial t} + \frac{d\theta}{d\psi} \frac{\partial \psi}{\partial t} = \nabla k(\nabla \psi + \hat{i}) \tag{2.3}$$

It is this version of Richards' equation is solved within this thesis.

### 2.1.2 Soil Hydraulic Characteristics

The term soil hydraulic characteristics is used to refer to the relations among the capillary pressure $\psi$, the water content $\theta$, and the hydraulic conductivity $k$. They provide the connection between the soil properties and states, and are therefore required to solve Richards' equation. There is no one straightforward functional or mathematical equation to describe the hydraulic characteristics. Normally, the simple and single-valued functions are used to find expressions that can be fit to the results of hydraulic measurements.

Gardner [53] introduced the earliest and most widely used exponential relationship for analytical solutions to flow problems. However, the applicability of Gardner functions is limited as empirical relative permeability data used to calibrate the model are not routinely available [55]. More physically-based mathematical expressions for soil hydraulic characteristics are those proposed by Brooks and Corey [24], which are more suited for flows in sandstone than soils and have been shown to be more appropriate for very uniform materials [121]. Van Genuchten [138] had proposed the most rigorous representation functions between hydrological variables and water content. Both Brooks-Corey and Van-Genuchten functions similarly have five parameters that define the shape of functions. They have been compared using identical values of parameters and results show that the Van-Genuchten functions have advantages for water content close to saturation and indicates a more realistic representation of soil wetting and drying characteristics [16]. A variant on the Brooks-Corey relationships has been addressed by Clapp and Hornberger [34] to smooth the characteristic curves at the air entry pressure.

Based on the analysis of a large collection of field data, assembled by the United States Department of Agriculture (USDA), the Van Genuchten functions are the most rigorous one among all existing soil hydraulic characteristics models[16]. The Gardner functions are useful for analytical solutions. The Brooks and Corey functions are intuitively attractive due to their simplicity. The Clapp and Hornberger functions are the same as the Brooks and Corey functions, except that the Brooks and Corey functions include the residual water content ($\theta_r$). In distributed surface water modeling, the Clapp and Hornberger functions are employed because of their simplicity, as is done in this study. Table 2.1 shows the hydraulic characteristics functions for each model.

Table 2.1: Summary of soil hydraulic characteristics

| Model | hydraulic functions | Legend |
|---|---|---|
| Gardner [53] | $\frac{\theta-\theta_r}{\theta_s-\theta_r} = \left[(1+0.5\alpha_G\psi)e^{-0.5\alpha_G\psi}\right]^{0.8}$ | $\theta_r$: residual water content [-] |
| | $\frac{k}{k_s} = e^{-\alpha_G\psi}$ | $\alpha_G$: a constant sorptive number [-] |
| Brooks-Corey [24] | $\frac{\theta-\theta_r}{\theta_s-\theta_r} = \left(\frac{\psi_{ae}}{\psi}\right)^{\lambda}$ | $\psi_{ae}$: air entry pressure $[L]$ |
| | $\frac{k}{k_s} = \left(\frac{\theta-\theta_r}{\theta_s-\theta_r}\right)^{3+2\lambda}$ | $\lambda$: pore size index [-] |
| Van-Genuchten [138] | $\frac{\theta-\theta_r}{\theta_s-\theta_r} = \left[\frac{1}{1+(\alpha\psi)^n}\right]^m$ | $\alpha$, $n$, and $m$: empirical parameters [-] |
| | $\frac{k}{k_s} = \frac{\left\{1-(\alpha\psi)^{n-1}[1+(\alpha\psi)^n]^{-m}\right\}^2}{[1+(\alpha\psi)^n]^{m/n}}$ | $m = 1-\frac{1}{n}$ |
| Clapp-Hornberger [34] | $\frac{\theta}{\theta_s} = \left(\frac{\psi_{ae}}{\psi}\right)^{1/b}$ | $b$: pore-size distribution index [-] |
| | $\frac{k}{k_s} = \left(\frac{\theta}{\psi}\right)^{c}$ | $c = 2b+3$ |

## 2.2 Overview of Drainage and Baseflow Models

Numerous methods have been used to simulate soil moisture processes in larger hydrological models and LSSs. Early LSSs for atmospheric models used the Manabe bucket model [88], which is a simple and fast model that was used to simulate all of the soil moisture processes simultaneously. More advanced LSSs adopt more complex soil reservoirs than that of the Bucket models, but still use a flat earth scheme with poor representation of lateral flow. At the other extreme, discretized numerical hydrological models based on Richards' equation (e.g., HYDRUS [118], WEPP [103], and SHE [1]) represent accurate physical process and are very powerful in solving a complex non-linear soil moisture simulation problem. However, numerical models are computationally prohibitive and require detailed soil data that are usually unavailable. The TOPography based hydrological model (TOPMODEL) [17] and Variable Infiltration Capacity model (VIC) [132] [79] have been developed as a compromise between computation efficiency and accurate representation of hillslope physics. TOPMODEL incorporates topographic information and the VIC model accounts for the spatial heterogeneity on the soil surface. They keep the basic physics of the soil and use relatively simple drainage and baseflow simulation scheme. However, the coupling of infiltration and drainage in these models is non-iterative and non physically-based.

### 2.2.1 Bucket and Power Approximations

The Manabe bucket model [88] is the first conceptual model to attempt to parameterize land surface processes in general circulation models. In this model, the soil is treated as a single water reservoir, with its storage, $\theta$, changing with the incoming water, defined as the difference between precipitation ($P$) and evaporation ($E$). Notice that no infiltration process is included in early bucket models. A maximum capacity, $\theta_s$, is defined as the maximum amount of water that can be stored in the bucket. Surface runoff is generated when the reservoir exceeds its maximum capacity ($\theta > \theta_s$) and subsurface runoff is generated when the storage exceeds the field capacity.

Figure 2.1 is a schematic representation for the single soil reservoir. The storage-subsurface runoff relation in bucket models has been represented by a simple linear model:

$$q = \begin{cases} \frac{(\theta - \theta_{fc})D}{\Delta t} & \text{for } \theta > \theta_{fc} \\ 0 & \text{for } \theta \leq \theta_{fc} \end{cases} \tag{2.4}$$

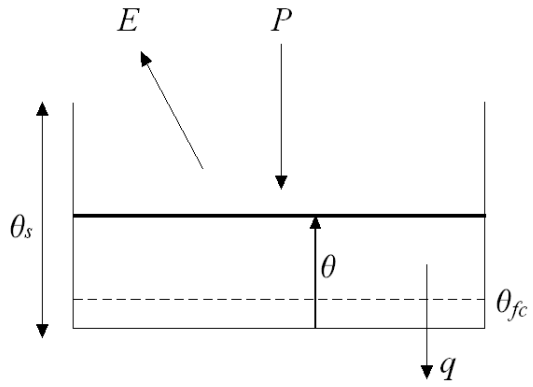


Figure 2.1: Schematic representation of the single soil reservoir: P-Precipitation; E-Evaporation; q-Subsurface Runoff

or more complex nonlinear power model:

$$q = \begin{cases} \left[\frac{(\theta-\theta_{fc})D}{a\Delta t}\right]^{\frac{1}{b}} & \text{for } \theta > \theta_{fc} \\ 0 & \text{for } \theta \leq \theta_{fc} \end{cases} \tag{2.5}$$

where $q$ represents the subsurface runoff, $\theta_{fc}$ is the soil water storage at field capacity, $D$ is the bucket depth, and $a$ and $b$ are empirical parameters.

The Manabe bucket provides a simple and fast runoff modeling process but it is best used as an annual rainfall-runoff model and fails to represent within-year details. Hydrological processes are simulated simultaneously and are not physically-based. Parameters used in the bucket model are poorly related to physics and have to be determined by calibration.

### 2.2.2 Hillslope/Boussinesq Models

Hillslope subsurface drainage is one of the key contributions to the peak of the stream hydrograph. It includes combined saturated and unsaturated water movement, which are best described by Richards' equation (equation 2.2). However, application of the Richards' equation is limited due to the fact that resulting solutions cannot be easily parameterized in practical terms for incorporation in catchment models [27], especially the high non-linearity in the unsaturated zone. Various approximations have been made for solving the Richards'

equation. Dupuit had made assumptions of a constant total head in the vertical direction to describe steady saturated flow of unconfined groundwater in horizontal aquifers, which led to:

$$\frac{\partial}{\partial X}\left(k_X h \frac{\partial h}{\partial X}\right) = S_y \frac{\partial h}{\partial t} \tag{2.6}$$

where $S_y$ is the specific yield, defined as "the quantity of water per unit area draining from the unsaturated soil for a unit drop in water-table height"[150]. For homogeneous hillslope, equation 2.6 becomes:

$$\frac{\partial}{\partial X}\left(h \frac{\partial h}{\partial X}\right) = \frac{S_y}{k_X} \frac{\partial h}{\partial t} \tag{2.7}$$

Equation 2.7 is called the second approximation of the Boussinesq equation [21]. A more general case of unconfined flow in a sloping aquifer is derived as [22]:

$$q = -k_X h \left(\frac{\partial h}{\partial X} \cos\alpha + \sin\alpha\right) \tag{2.8}$$

where $q$ is the flow rate in $X$ direction and $\alpha$ is the slope angle. Inserting equation 2.8 into the continuity equation results in:

$$-\cos(\alpha)\frac{\partial}{\partial X}\left(h \frac{\partial h}{\partial X}\right) - \sin(\alpha)\frac{\partial h}{\partial X} = \frac{S_y}{k_X} \frac{\partial h}{\partial t} \tag{2.9}$$

which is usually referred to as the first approximation of the Boussinesq equation and has been widely used in hillsope hydrology modeling. It is a nonlinear equation and general solutions have not been obtained. Despite the simplified form applications of such hillslope models are still limited due to data availability and intensive computation.

### 2.2.3 TOPMODEL

Another popular mixed infiltration/lateral flow model is TOPMODEL, which does a better job than other models by including physics. The three fundamental assumptions in TOPMODEL are [17]:

- There is a saturated zone in equilibrium with a steady recharge rate over an upslope contribution area.
- The water table is almost parallel to the ground surface such that the effective hydraulic gradient is equal to the local surface slope, $\tan\beta$.

- The transmissivity profile may be described by an exponential function of storage deficit, with a value of $T_0$.

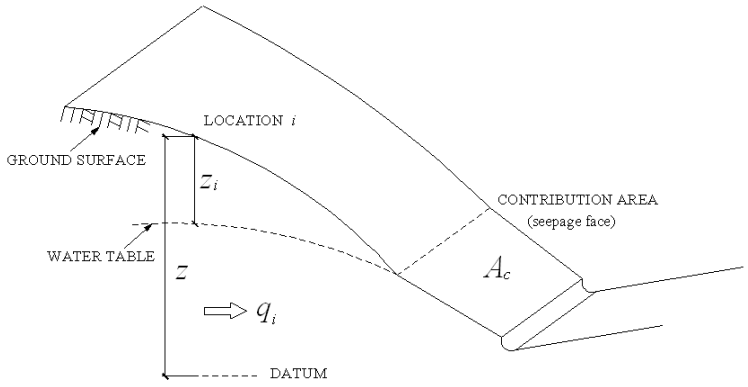


Figure 2.2: Schematic representation of a valley and the formation of runoff according to TOPMODEL: $A_C$-contributing area to the surface runoff; $q_i$-interflow corresponding to an area drained per unit contour length (Figure from [51])

Figure 2.2 shows the schematic representation of a valley and the formation of runoff according to TOPMODEL. Notice that the lateral flow only occurs under the water table and the surface runoff is generated on a variable contribution area $A_C$, which is related to a topographic index, $\ln(a/\tan\beta)$, of the basin and the water deficit $z_i$. Here $a$ is the area of the hillslope per unit contour length. The soil profile at location $i$ is represented by a set of stores, as shown in Figure 2.3. The upper one is the Root Zone (RZ) storage, where rainfall infiltrates until the field capacity is reached. Once the field capacity is exceeded, a second store starts filling until the water content reaches saturation. The gravity drainage store links the unsaturated (UZ) and the saturated zones (SZ).

TOPMODEL adopts a linear dynamic stores for the Unsaturated Zone (UZ) and a non-linear exponential representation for the Saturated Zone store (SZ); both are functions of the soil water storage deficit or water table depth, $z_i$. Beven [9] suggested an exponential form of unsaturated zone flux based on the basis of the Darcian flux for incorporating into the TOPMODEL soil moisture process. A decay factor in Beven's formulation has to be determined by observed data.

TOPMODEL performs better when the study site's characteristics meet the assumptions. However, TOPMODEL is not a fixed modeling scheme. Assumptions can be relaxed according to the nature of catchment, such as adopting a linear transmissivity function([2]

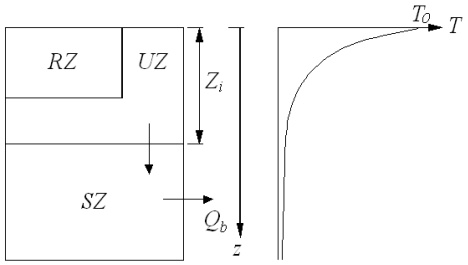


Figure 2.3: Soil structure in TOPMODEL

and [3]) or a power law transmissivity function ([46] and [69]). However, the steady state assumption is often unrealistic, especially during precipitation events [101]. Interflow in the unsaturated zone is not being taken into account and infiltration and drainage are non-iteratively treated.

### 2.2.4 VIC Model

VIC model was proposed by Stamm et al. [132] for representing a point land surface hydrological process as a single soil layer and then this was extended to multiple layers along other features by Liang et al. [79]. One of the most important merits of the VIC model is that it accounts for spatial variability of the infiltration capacity.

Figure 2.4 is a schematic representation of the three-layer structure of VIC. It shows that there is no lateral flow in the top two layers. Water movement between soil layers is represented by one-dimensional Richards' equation. The soil surface is characterized by a variable infiltration capacity as [80]:

$$f = f_m \left[1 - (1 - A)^{1/b_i}\right] \tag{2.10}$$

where

$$f_m = (1 + b_i)\theta_s z$$

where $f$ and $f_m$ are the infiltration capacity and maximum infiltration capacity respectively, $A$ is the fraction of the area for which the infiltration capacity is less than $i$, $b_i$ is an empirical infiltration shape parameter.

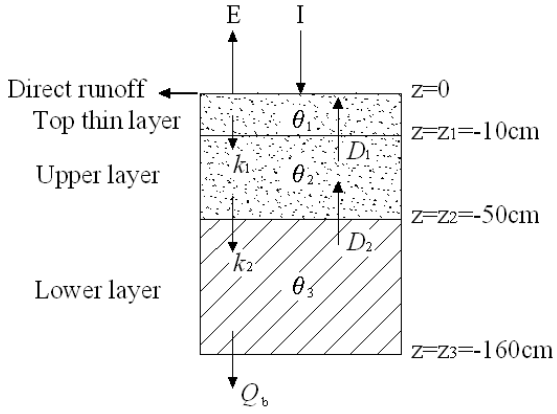


Figure 2.4: Schematic representation of the three-layer structure of VIC: $D_1$ and $D_2$ represent diffusions between soil layers, and $K_1$ and $K_2$ represent the drainage between soil layers, $Q_b$ represents the baseflow.

Subsurface runoff is generated only in the lower layer and is represented by either a linear or nonlinear recession dependent on a threshold of maximum water storage in this layer, which is site dependent and has to be obtained by calibration. The nonlinear drainage is required to represent situations under which the substantial subsurface storm flow occurs [80]. Although the spatial heterogeneity in infiltration is explicitly considered, how infiltration and drainage are coupled on the surface is not addressed by the VIC model.

### 2.2.5 Overview of LSS Models

LSSs are designed to simulate the fluxes of surface water and energy between the atmosphere and the land surface. Those exchanges are complex functions of physical, chemical and biological processes. Based on various simplifications, LSSs exhibit a wide range of complexity, from simple regression models to complex physically-based models. As previously stated, the simplest one is the Manabe BUCKET model [88]. Soil moisture in more sophisticated LSSs is often simulated by using the finite difference form of Richards' equation in vertical. Baseflow parameterization in the LSSs can be classified into three categories: empirical functions, free drainage, and proportional approach. The Manabe bucket model [88] does not take into account the subsurface flow. A revised bucket model [67] adopts linear or non-linear empirical functions for the subsurface runoff. The Biosphere

Atmosphere Transfer Scheme (BATS) [43], the Schematisation des EChanges Hydriques Interface Biosphere Atmosphere (SECHIBA) (Ducoudre et al., 1993), and the Variable Infiltration Capacity scheme (VIC) [79] employs empirical exponential decay functions. The CLASS [141] and the Meteorological Office Surface Exchange Scheme (MOSES) [48] permit free drainage. Drainage in the Interactions Soil-Biosphere-Atmosphere (ISBA) scheme [102] and the Simplified Simple Biosphere Model (SSiB) [149] is proportional to the water amount exceeding field capacity or to the wetness of the third soil layer.

Differences among soil model structures in these LSSs are mainly related to the number of soil layers included and the thickness of those layers. Tables 2.2, 2.3, 2.4, and 2.5 are a summary of widely recognized LSSs. The nonlinear soil water functions vary widely between models but most are primarily empirical and will therefore require calibration. LSSs have a high level of vertical resolution and structure, but a low level of horizontal resolution. A "flattened Earth"is used to represent the land surface in most of the LSSs. However, soil moisture dynamics, runoff production, and surface energy fluxed can be significantly affected by the topography. In addition, the spatial variability of soil properties is not taken into account.

Table 2.2: Soil water parameterization in LSSs

| Schemes | Soil model structure | Soil water parameterization | Remarks |
|---|---|---|---|
| Bucket model [88] | Single soil layer model | $\theta_k = \theta_{k-1} + \frac{(P-E)\Delta t}{D}$<br>$R = \frac{\theta_k - \theta_s}{\Delta t} D$ | $\theta_k$: water content at time $k$ [-]<br>$P$: precipitation $[LT^{-1}]$<br>$E$: evapotranspiration $[LT^{-1}]$<br>$R$: surface runoff $[LT^{-1}]$<br>$\Delta t$: time step $[T]$<br>$D$: bucket depth $[L]$<br>$\theta_s$: capacity of the bucket [-]<br>No subsurface flow is considered |
| Revised Bucket model [67] | One soil reservoir | Linear subsurface flow:<br>$Q = \frac{\theta - \theta_{fc}}{\Delta t}, \theta > \theta_{fc}$<br>$Q = 0, \theta \leq \theta_{fc}$<br>Non-linear:<br>$Q = \left(\frac{\theta - \theta_s}{a}\right)^{\frac{1}{b}}, \theta > \theta_s$<br>$Q = 0, \theta < \theta_s$ | $Q$: subsurface runoff $[LT^{-1}]$<br>$\theta_{fc}$: field capacity [-]<br>Subsurface flow is included |

Table 2.3: Soil water parameterization in LSSs (continue)

| Schemes | Soil model structure | Soil water parameterization | Remarks |
|---|---|---|---|
| ISBA [102] | Two-reservoir soil model: superficial and deep | $\frac{\partial\theta_1}{\partial t} = -C_1\frac{E_g - P}{\rho_w D_1}$ $-C_2\frac{\theta_1 - \theta_{fc}}{\tau}$ $\frac{\partial\theta_2}{\partial t} = -\frac{E_g + E_{tr} - P}{\rho_w D_2}$ $Q = C_3(\theta_2 - \theta_{fc})$ | $E_g$: the evaporation from the base ground $[LT^{-1}]$ $E_{tr}$: the transpiration rate $[LT^{-1}]$ $\rho_w$: density of water $[LT^{-1}]$ $C_i$: empirical coefficients [-] $D_i$: layer depth $[L]$ $\tau$: a time constant of one day $[T]$ |
| CLASS [141] | Three soil layers | water movement: Finite difference approximation of RE Drainage: Darcy's law | Suction gradient at the bottom is assumed to be zero |

Table 2.4: Soil water parameterization in LSSs (continue)

| Schemes | Soil model structure | Soil water parameterization | Remarks |
|---|---|---|---|
| BATS [43] | Three soil layers | $Q_1 = k_0\theta_1^{b+0.5}\theta_2^{b+0.5}$<br>$Q_2 = k_0\bar{\theta}^{b+0.5}\theta_1^{b+0.5}$<br>$Q_b = k_d\bar{\theta}^{b+0.5}$ | $Q_1$: drainage from the surface to root zone $[LT^{-1}]$<br>$Q_2$: drainage from root zone to total column $[LT^{-1}]$<br>$k_0$: saturated hydraulic conductivity $[LT^{-1}]$<br>$\theta_2$: saturation of the root zone [-]<br>$\theta_1$: saturation of the surface layer [-]<br>$\bar{\theta}$: saturation of the total soil column [-]<br>$b$: Clapp-Hornberger soil index [-]<br>$k_d$: an adjusted constant [-] |
| SECHIBA [97] | Two-reservoir soil model | $Q_i = Q_i^{min}\frac{\theta_i}{\theta_i^{max}}, \theta_i < \theta_i^{lim}$<br>$Q_i = Q_i^{min}\frac{\theta_i}{\theta_i^{max}} +$<br>$(Q_i^{max} - Q_i^{min})\left(\frac{\theta-\theta_i^{lim}}{\theta_i^{max}-\theta_i^{lim}}\right)^{d_i}$<br>$,\theta_i > \theta_i^{lim}$ | $Q_i$: drainage from the i-th reservior $[LT^{-1}]$<br>$\theta_i$: water content for i-th reservior [-]<br>$d_i$: a constant with a value of 1.5 [-] |
| MOSES [48] | Four soil layers | Finite difference approximation to the Richards equation.<br>Free drainage: $Q_b = k_N$ | $Q_b$: subsurface runoff $[LT^{-1}]$<br>$k_N$: hydraulic conductivity at the fourth layer $[LT^{-1}]$ |

Table 2.5: Soil water parameterization in LSSs (continue)

| Schemes | Soil model structure | Soil water parameterization | Remarks |
|---|---|---|---|
| VIC [79] | Two soil layers | $Q_b = \frac{aQ_b^{max}}{b\theta_s}\theta_2, \theta_2 < b\theta_s$<br>$Q_b = \frac{aQ_b^{max}}{b\theta_s}\theta_2 + \left(Q_b^{max} - \frac{aQ_b^{max}}{b}\right)$<br>$\left(\frac{\theta_2 - b\theta_s}{\theta_s - b\theta_s}\right)^2, \theta_2 > b\theta_s$ | $Q_b$: subsurface runoff $[LT^{-1}]$<br>$Q_b^{max}$: maximum subsurface runoff $[LT^{-1}]$<br>$\theta_s$: maximum soil water content in layer 2 [-]<br>$\theta_2$: soil moisture in layer 2 [-]<br>$a/b$: fraction of $Q_b^{max}/\theta_m$ [-] |
| SSIB [149] | Three soil layers | water movement:<br>finite difference form of RE<br>$Q_b = C\frac{\theta_3}{\theta_s}$ | $\theta_i$: water content in th ei-th layer [-]<br>$Q_b$: subsurface runoff $[LT^{-1}]$<br>$\theta_s$: saturated water content [-]<br>$C$: an empirical constant $[LT^{-1}]$ |

## 2.3 Infiltration Models

Infiltration is the process of water entering the soil from the ground surface (Figure 2.5). The rate of this process determines how much water will enter the unsaturated soil zone, and how much runoff will be generated [64]. Recharge from infiltration is the main source of water entry into the subsurface and is the ultimate source of base flow. Therefore, simulating the infiltration rate accurately is important in subsurface runoff parameterization. Due to the difficulty of direct measurement of infiltration, both empirical and the physically based models have been developed to evaluate the infiltration rate.

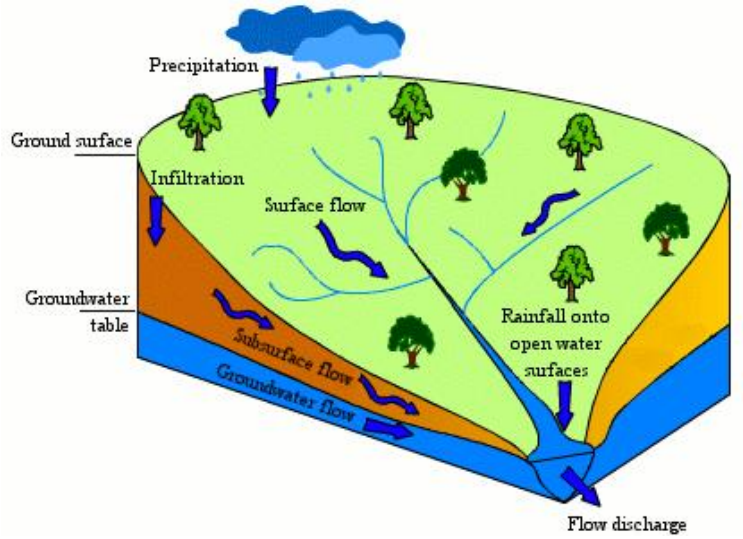


Figure 2.5: The infiltration process depending on soil type and flow [96]

These models ignore the effect of air flow. Air flow may be important in ponded infiltration, but can be ignored for most natural infiltration events [150].

### 2.3.1 Empirical Models

Empirical infiltration models usually take the form of simple equations, generated from a comparison with data. The parameters of the equations must be obtained by means of curve-fitting, and typically lack direct physical interpretation. However, their simplicities are appreciated by many users. The empirical models listed in table 2.6 are commonly used in simulating the infiltration process.

Table 2.6: Empirical infiltration models

| Developer | Infiltration capacity ($f$) | Cumulative infiltration ($F$) | Remarks |
|---|---|---|---|
| Kostiakov [73] | $f = \alpha t^{-\beta}$ | $F = \frac{\alpha}{1-\beta} t^{1-\beta}$ | $\alpha, \beta$: empirical coefficients [-]<br>$t$: time $[T]$<br>Since $\lim_{t\to\infty} i = 0$, Kostiakov proposed $t < \left(\frac{\alpha}{k_s}\right)^{1/\beta}$ |
| Horton [66] | $f = f_f + (f_0 - f_f)e^{-\gamma t}$ | $F = f_f t + \frac{(f_0 - f_f)(1-e^{-\gamma t})}{\gamma}$ | $f_0$: initial infiltration capacity $[LT^{-1}]$<br>$f_f$: final infiltration capacity $[LT^{-1}]$<br>$\gamma$: an empirical coefficient [-]<br>Rapid decrease of $f$ from very high value at small $t$ is not represented well [107] |
| Mezencev [91] | $f = f_f + \alpha t^{\beta}$ | $F = f_f t + \frac{\alpha}{1-\beta} t^{1-\beta}$ | Overcome the limitation of Kostiakov equation for large time |
| Holton [65] | $f = f_f + ab(\omega - I)^{1.4}$ | - | $a$: a factor variable range from 0.25 to 0.8 [-]<br>$b$: Holton equation flow factor [-]<br>$\omega$: initial moisture deficit [-]<br>Depend on soil water conditions, suitable for inclusion in catchment models |

### 2.3.2 Richards' Equation-Based Infiltration Models

Since flow in the unsaturated zone is often primarily vertical [32], infiltration can often be represented by using a one-dimensional form of Richards' equation in most hydrological models.

$$\frac{\partial \theta}{\partial t} = -\frac{\partial}{\partial z}\left(k\frac{\partial \psi}{\partial z}\right) - \frac{\partial k}{\partial z} \tag{2.11}$$

The concern of the infiltration theory is to solve the boundary value problems involving the nonlinear Richards' equation [121]. General analytical solutions to equation 2.11 have not been obtained: however, considerable simplifications can be made such that the Richards' equation can be solved analytically or numerically. The following inputs are required to obtain soil water flux for solving the Richards equation for infiltration:

- A surface boundary condition

  For $\psi|_{z=0,t} \geq \psi_p$:

  $$\psi|_{z=0,t} = \psi_p \tag{2.12}$$

  For $0 < \psi|_{z=0,t} < \psi_p$:

  $$\left.\frac{\partial \psi}{\partial t}\right|_{z=0,t} = w + k\left(\frac{\partial \psi}{\partial z} - 1\right)\Bigg|_{z=0,t} \tag{2.13}$$

  For $\psi|_{z=0,t} \leq 0$,

  $$w = k\left(\frac{\partial \psi}{\partial z} - 1\right)\Bigg|_{z=0,t} \tag{2.14}$$

  where $\psi_p$ is the ponding depth $[L]$ and $w$ is the rainfall rate $[LT^{-1}]$.

- An initial condition

  $$\theta|_{z,t=0} = \theta_i \tag{2.15}$$

- Soil hydraulic parameters

Many simple infiltration equations are solutions to the Richards equation under highly ideal conditions (e.g., sharp wetting front, constant diffusivity, linear soil characteristics, ponded surface, homogenous soil, and/or uniform initial moisture distribution, etc.). Table 2.2 lists several such infiltration equations [134].

In reality, these ideal conditions may not hold true. Therefore, these conditions in the models need to be relaxed, such that more physically-based infiltration models can be obtained.

Table 2.7: Richards' equation-based infiltration models ($T = \frac{k_s^2 t}{S^2}$, $S$ represents sorptivity)

| Developer | Cumulative infiltration $F$ |
|---|---|
| Philip [107] | $F = T^{1/2} + \lambda T$, $\lambda$ is a fitting parameter |
| Knight [72] | $F = T + \frac{\pi}{4} \ln \left[1 + erf \left(\frac{4T}{\pi}\right)^{1/2}\right]$ |
| Parlange [104] | $F = T + \frac{1}{2}\left[1 - e^{-2T^{1/2}}\right]$ |
| Brutsaert [26] | $F = T + \left(\frac{T^{1/2}}{1+mT^{1/2}}\right)$, $m$=2/3 or 1 |
| Collis-George [36] | $F = T + \frac{1}{N}\left(\tan N^2 T\right)^{1/2}$, $N$ varies between 1 and 4 |
| Swartzendruber-Clague [134] | $F = T + \frac{1}{n}\left[1 - e^{-nT^{1/2}}\right]$, $n$ is a constant |

### 2.3.3 The Green-Ampt Model (GA)

Green and Ampt [60] presented the first physically-based equation for describing the infiltration of water into soil. The Green-Ampt model (GA) is based on fundamental physics and also gives results that match with empirical observations. Barry et al. [6] found an exact solution for the Richards equation by assuming a specific functional form for moisture content. The cumulative infiltration model derived from the solution was in the form of the GA infiltration model.

The GA model assumes a constant hydraulic conductivity, homogeneous soil, a constant wetting front tension, and a piston-type water content profile with a well-defined wetting front, as shown in Figure 2.6.

Applying Darcy's law, the infiltration rate, $f$ , can be written as

$$f = k_s \frac{\partial H}{\partial z}|_{z=0} = k_s \frac{(|\psi_f| + z_f) - h_0}{z_f} \tag{2.16}$$

where $\psi_f$ is the suction at the wetting front $[L]$, $z_f$ is the wetting front depth $[L]$, and $h_0$ is the ponding depth $[L]$.

Note that if $h_0 = -D$ (ponding depth effect), equation 2.16 becomes

$$f = k_s \frac{|\psi_f| + z_f + D}{z_f} \tag{2.17}$$

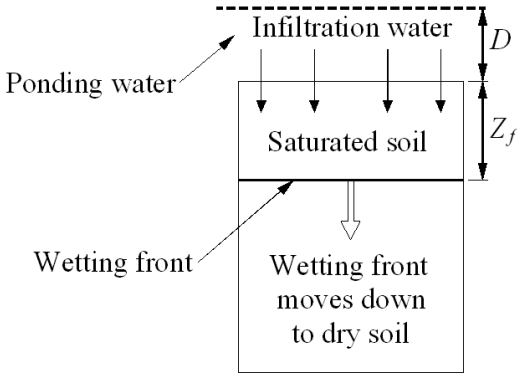


Figure 2.6: Assumptions in the Green-Ampt model

The depth of the wetting front can be related to the cumulative amount of infiltrated water as:

$$F = z_f(\theta_s - \theta_i) \tag{2.18}$$

where $\theta_i$ is the initial water content.

Substituting equation 2.18 into equation 2.17 leads to:

$$f = \begin{cases} w & \text{for } t \leq t_p \\ k_s \left(1 + \frac{(|\psi_f| + D)(\theta_s - \theta_i)}{F}\right) & \text{for } t \geq t_p \end{cases} \tag{2.19}$$

where $t_p$, time to ponding, is given by:

$$t_p = \frac{(|\psi_f| + D)(\theta_s - \theta_i)k_s}{w(w - k_s)} \tag{2.20}$$

Note that since the cumulative infiltration $F$ is a function of infiltration rate $f$, the solution is implicit.

### The implicit solution of the Green-Ampt equation

In the original Green-Ampt formulation, the ponded water of negligible depth covers the soil surface. Equation 2.19 becomes

$$f = \begin{cases} w & \text{for } t \leq t_p \\ k_s \left(1 + \frac{\alpha}{F}\right) & \text{for } t > t_p \end{cases} \tag{2.21}$$

where $\alpha = |\psi_f| (\theta_s - \theta_i)$.

Integrating equation 2.21 from $t = t_p$ to $t$, it transforms into an implicit relationship between $F$ and $t$ as:

$$t = \begin{cases} t_p + \frac{1}{k_s}\left[F - F_p + \alpha \ln\left(\frac{\alpha + F_p}{\alpha + F}\right)\right] & \text{for } t > t_p \\ \frac{F}{w} & \text{for } t < t_p \end{cases} \tag{2.22}$$

While usually expressed in implicit form, a numerical iteration procedure (usually Newton-Raphson) is required to determine the solution.

### The explicit solutions of the Green-Ampt equation

Diverse approximation techniques developed some explicit solutions [83], [113], [115], and [116]. Barry et al. [5, 6] have used Lambert $W$ function in order to develop a family of robust numerical approximates to the explicit Green-Ampt solution. The Lambert $W$ function is defined by solutions to

$$W(x)e^{W(x)} = x$$

Barry's approximation is highly accurate and simple to implement, and has a maximum relative error of $5e^{-5}\%$. This error is several orders of magnitude lower than any existing analytical approximation. Therefore, this function is recommended for use in standard Green-Ampt infiltration modeling schemes in this study.

### Extended applications of the Green-Ampt model (GA)

The GA model has been the subject of considerable developments in applied soil physics and hydrology owing to its simplicity and satisfactory performance for a great variety of hydrological problems [110]. In order to address situations beyond the scope of the original GA model, numerous modifications have been suggested in the literature. These modifications primarily focus on accounting for layered soil heterogeneity, unsteady rainfall, and/or ponding at the soil surface. Childs and Bybordi [31] were the first to study the impact of the soil profile heterogeneity. They divided the soil column into a succession of n layers with decreasing conductivity and developed a specified infiltration law according to the conductivity profile. Beven [8] extended the GA infiltration model to a class of non-uniform soils in which saturated hydraulic conductivity decreases as an exponential

function of depth, with a satisfactory comparison to the Childs and Bybordi solution for a layered sand profile ([8]). For implementation in more complex watershed models, these analytical models needed to be extended to the case of unsteady rainfall. Chu [33] was the first to extend the GA approach to compute infiltration into a homogeneous soil due to an unsteady rainfall event. Jia and Tamai [70] extended the GA model for infiltration into a multi-layered soil during an unsteady rain and verified the model against numerical solutions to the Richards' equation (RE), which was later extended by Liu et al. [84] to additionally account for non-uniform initial water content. Other researchers have investigated more specific situations in which the GA model is not wholly appropriate. Wang et al. [144] investigated a modified GA model taking account of surface deposition during muddy water infiltration. Chen and Young [28] explained the direct effect of the surface slope on infiltration and runoff generation by extending the GA equation onto sloping surfaces, and found that cumulative infiltration is increased with an increase of the slope angle. Gavin and Xue [54] proposed a modification to the traditional GA model by considering the slope, assuming a linearly distributed suction profile in the wetted zone. Although most of the GA modifications provide satisfactory results for amended conditions and extended the applicability of the GA model, no previous research has investigated the impact of individual assumptions upon the quality of the standard GA solution.

## 2.4 Hydrological Similarity

The spatial variability of geology, soil, land cover, and topography in a catchment all affect the relationship between rainfall and runoff. Detailed representation of these variabilities is impossible due to data availability and intensive computational demand. Hydrological similarity is used to identify points or units in a watershed to assess their similar hydrological response for a rainfall event. Such points or units have locally uniform hydrological response to meteorological input so that they can be represented as a group to increase the efficiency of hydrological models. Any catchment may be considered as an assembly of sub-elements. As the spatial scale of the element increases, the rainfall-runoff relationship becomes less sensitive to the spatial variations of the catchment characteristics. Further, a smaller scale is needed for capturing the heterogeneity of the catchment. Thus, a certain scale must be found such that the concept of homogeneity and the averaging of hydrological processes can be used. The spatiality is captured by using small subcatchment elements which can be called Hydrological Response Units (HRUs) [78] or Representative Elementary Areas (REAs) [148].

### 2.4.1 Hydrological Response Units (HRUs)

The main difficulty in dividing the catchment into HRUs is defining what constitutes a hydrologically homogeneous area [75]. The development of Geographical Information System (GIS) and remote sensing provides one method for addressing the problem. Maps of soil, geology, digital elevation, and vegetation can be stored in GIS. By overlaying the different layers of information, classification of catchment landscape for hydrological response can be performed. One HRU can be represented as one pixel in this concept and each HRU will be the subject of a unique water balance computation. By collecting many HRUs together, an entire catchment can be represented. However, the number of HRUs used is constrained by both data availability and computational limitations. Thus, the HRU approach is only appropriate for small catchments and grids since it is computationally expensive.

### 2.4.2 Grouped Response Units (GRUs)

To represent the inherent heterogeneity of a catchment without sacrificing computational simplicity, a more suitable approach for large catchments, the Grouped Response Units (GRUs) approach, has been developed [75]. A GRU is a collection of similar HRUs within a catchment, which is treated as a single representative computational unit. Using remotely

sensed land cover data, pixels are classified to a number of land cover classes and the ratio of each land cover in each computation grid are then determined to compute the GRUs [74]. A computational element consisting of multiple GRUs receives the same hydrological input data, but different land covers/GRUs will respond in their own characteristic manner. Hydrological responses from different groups of GRUs are then summed together and routed to the stream system.

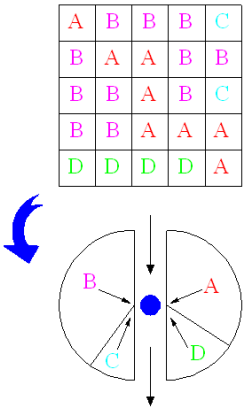


Figure 2.7: The Grouped response unit concept

Figure 2.7 shows the concept of GRUs. In Figure 2.7, there are twenty-five pixels in a grid, in which eight pixels are classified as belonging to land-cover class A, eleven pixels to class B, two pixels to class C, and four pixels for class D. For example, the total runoff for a grid is calculated as:

$$R = (R_A P_A + R_B P_B + R_C P_C + R_D P_D)A \tag{2.23}$$

where $R_i$ is the unit runoff generated from land-cover class $i$; $P_i$is the fraction of the land-cover class $i$; $A$ is the area for grid. $R_i$ can be applied to other grids if the similar land cover class is contained. The location of HRUs in a GRU is assumed not to affect the hydrological response. The GRU method was used in the original MESH hydrological land surface model.

### 2.4.3 TIlted Landscape Elements (TILE)

The TILE approach was developed to connect the micro-scale and the meso-scale physics by combining features of the LSSs, the topographic approach of TOPMODEL [11], and the group response unit approach from a hydrological model WATFLOOD [74]. This representation is used to drive many of the algorithms developed in this thesis. Any catchment can be treated as an assembly of TILEs, each with a connection to the drainage system. Figure 2.8 shows the schematic of the topography of a typical model grid element.

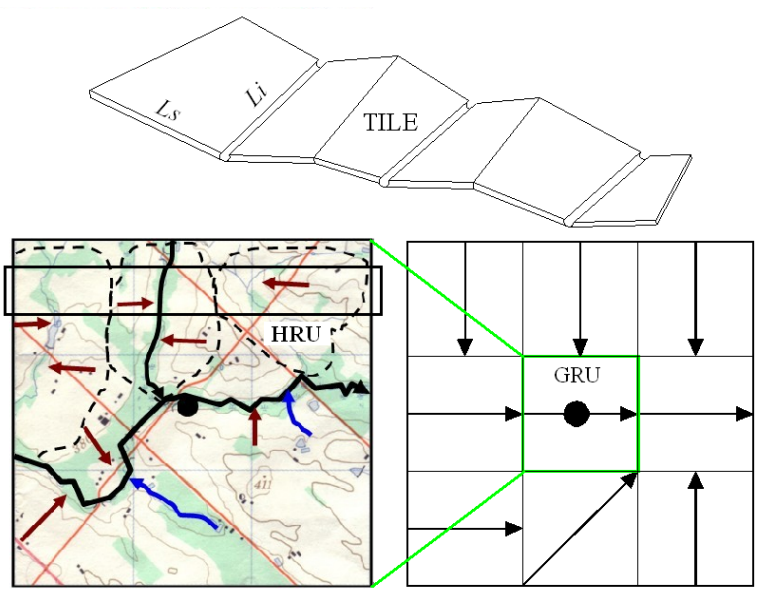


Figure 2.8: Schematic of the topography of a grid element in a watershed: $L_s$ is the average distance between the divide and the stream, $L_i$ is the length of the stream

A critical parameter for operation of the TILE framework is drainage density, defined as the total length of streams $L$ in a hydrological unit divided by the hydrological unit area $A$. Drainage density, $D_D$, is landform-dependent and typically ranges from 2/km to 100/km [45]. Other useful parameters include $L_S$, the average distance between the divide and the micro-drainage system stream channel and $\Lambda$, the typical valley slope which provides the topographic gradient for the flow from the soil blocks. Runoff parameterization in a TILE may include:

- Surface runoff: Manning's equation
- Drainage: Darcy's law
- Subsurface runoff: adjusted Richards' equation

One limitation for the TILE approach is that each block requires a stream element. Therefore, TILEs are required to be large enough to produce inter-element flow to the stream channel. This study incorporates the TILEs approach into the GRUs approach to provide a more rigorous hydrological similarity method.

# Chapter 3

# Improvements to the Infiltration Process

Recharge from infiltration is the main source of water into soils and is the ultimate source of interflow and baseflow. Simulating infiltration accurately is very important in subsurface runoff parameterizations. However, current algorithms do not sufficiently address issues such as shallow boundary conditions and spatial heterogeneity. Infiltration can be significantly affected by the presence of shallow boundaries, which have not been considered in existing infiltration models. The heterogeneity in soil moisture and soil properties is an important driver of net infiltration, one which also has not been properly accounted for by most infiltration models.

The infiltration process in this study is represented by the classical Green-Ampt model. The Green-Ampt model was developed for soils with infinite depth and does not account for the heterogeneity at the subbasin scale. In regional scale applications, these idealized conditions will often not be met. Revisions to the Green-Ampt infiltration model are suggested under such conditions. A specialized finite difference code to the Richards' equation for sloping soils and Monte Carlo simulations are used for testing these revisions. Results show that revisions are capable of addressing the effects they are intended to accommodate and can be incorporated into hydrology-land-surface schemes.

## 3.1 Numerical Solution of the Richards' Equation

Numerical solutions of the Richards' equation provide a basic understanding of water movement in porous media, and are here used as a benchmark for evaluating computationally efficient analytical solutions. A specialized finite difference scheme for sloping soils is described in this section, including the mathematical derivation and implementation of various boundary conditions. The solution has been verified by published results, where possible, and show to be capable of simulating a variety of soil systems.

### 3.1.1 Governing Equation and Finite Difference Scheme

Richards' equation governs the water flow in variable saturated soil and solutions to Richards' equation help provide a basic understanding of water movement in a soil layer. For a grid aligned with the arbitrary-oriented hillslope, equation 2.3 can be rewritten as:

$$\left(S_s\frac{\theta}{\theta_s}+\frac{d\theta}{d\psi}\right)\frac{\partial\psi}{\partial t}=\frac{\partial}{\partial X}k_X\left(\frac{\partial\psi}{\partial X}-\frac{\Lambda}{\sqrt{1+\Lambda^2}}\right)+\frac{\partial}{\partial z}k_Z\left(\frac{\partial\psi}{\partial z}+\frac{1}{\sqrt{1+\Lambda^2}}\right) \tag{3.1}$$

where $\Lambda$ indicates the land surface slope [-], $k_X$ is the lateral hydraulic conductivity $[LT^{-1}]$, $k_Z$ is the vertical hydraulic conductivity $[LT^{-1}]$, and $\Delta X$, $\Delta Z$, and $\Delta t$ are spatial and temporal discretizations. A general $\Theta$-weighted finite difference scheme is used to solve equation 3.1 and is derived below. The discretization involved for each finite difference approximation is show in Figure 3.1. The numerical discretization of equation 3.1 by the finite difference method leads to a nonlinear set of equations as:

$$[A]^m[\Psi]^{m+1}=[B]^m$$

where $[A]$, $[\Psi]$, and $[B]$ represent the coefficient vector, the unknown variable vector, and the constant vector, respectively. The superscript $m$ refers to the $m^{th}$ iteration level. This equation is solved by a standard Picard iterative method. The initial value of the dependent variables $[\Psi]$ at time $t+\Delta t$ and $m=1$ are computed by the known values of the dependent variables at time $t$. This value is successively substituted into the nonlinear equation until a pre-determined convergence, e.g., $[\Psi]^{m+1}$ is close enough to $[\Psi]^m$. A tolerance value of $1.0e-4$ is used in this study.

A general $\Theta$-weighted finite difference approximation of the left hand side ($LHS$) of

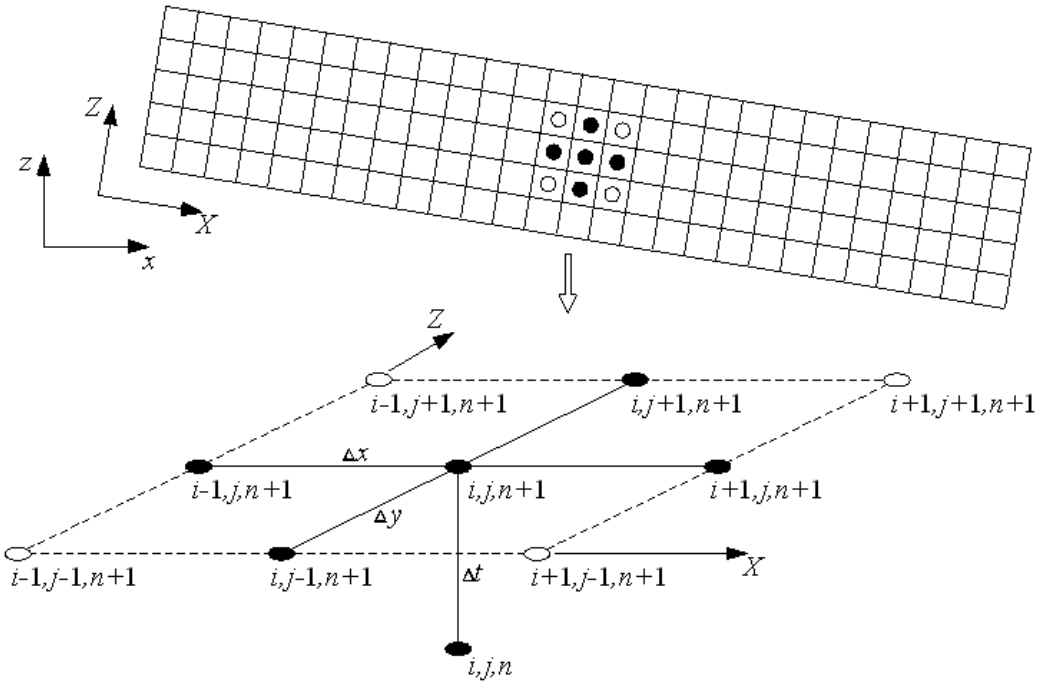


Figure 3.1: Number of grid blocks involved for each finite difference approximation: $i, j$-node location, $n$-$nth$ discrete time level, $\Delta X, \Delta Z, \Delta t$-spatial and temporal discretizations

equation 3.1 is:

$$\begin{aligned} LHS &= \left\{\Theta\left[S_s\frac{\theta_{i,j}^{n+1,m}}{\phi}+\left(\frac{d\theta}{d\psi}\right)_{i,j}^{n+1,m}\right]+(1-\Theta)\left[S_s\frac{\theta_{i,j}^{n}}{\phi}+\left(\frac{d\theta}{d\psi}\right)_{i,j}^{n}\right]\right\}\frac{\psi_{i,j}^{n+1,m+1}-\psi_{i,j}^{n}}{\Delta t} \\ &= \left[\Theta\left(S_s\frac{\theta_{i,j}^{n+1,m}}{\phi}+c_{i,j}^{n+1,m}\right)+(1-\Theta)\left(S_s\frac{\theta_{i,j}^{n}}{\phi}+c_{i,j}^{n}\right)\right]\frac{\psi_{i,j}^{n+1,m+1}-\psi_{i,j}^{n}}{\Delta t} \\ &= \left[\Theta\left(S_s\frac{\theta_{i,j}^{n+1,m}}{\phi}+c_{i,j}^{n+1,m}\right)+(1-\Theta)\left(S_s\frac{\theta_{i,j}^{n}}{\phi}+c_{i,j}^{n}\right)\right]\frac{\psi_{i,j}^{n+1,m+1}}{\Delta t}- \\ &\quad \left[\Theta\left(S_s\frac{\theta_{i,j}^{n+1,m}}{\phi}+c_{i,j}^{n+1,m}\right)+(1-\Theta)\left(S_s\frac{\theta_{i,j}^{n}}{\phi}+c_{i,j}^{n}\right)\right]\frac{\psi_{i,j}^{n}}{\Delta t} \end{aligned} \tag{3.2}$$

where $c_{i,j}^{n,m}$ is the specific water capacity of the soil, a function of the pressure head, $n$ represents the $n^th$ time level, and $\Theta$ is a weighting factor. According to the Clapp and

Hornberger soil hydraulic functions [34], one can get:

$$c = \frac{d\theta}{d\psi} = -\frac{\theta_s}{b\psi_{ae}} \left( \frac{\psi}{\psi_{ae}} \right)^{-\frac{1}{b}-1} \tag{3.3}$$

The $\Theta$-weighted finite difference approximation of the spatial terms of the right hand side of equation 3.1 is:

$$\begin{aligned} RHS \;=\; & \Theta \left[ \frac{k^{n+1,m}_{i+\frac{1}{2},j}}{\Delta X^2} \psi^{n+1,m+1}_{i+1,j} + \frac{k^{n+1,m}_{i-\frac{1}{2},j}}{\Delta X^2} \psi^{n+1,m+1}_{i-1,j} + \frac{k^{n+1,m}_{i,j-\frac{1}{2}}}{\Delta Z^2} \psi^{n+1,m+1}_{i,j-1} + \frac{k^{n+1,m}_{i,j+\frac{1}{2}}}{\Delta Z^2} \psi^{n+1,m+1}_{i,j+1} \right. \\ & - \left( \frac{k^{n+1,m}_{i+\frac{1}{2},j}}{\Delta X^2} + \frac{k^{n+1,m}_{i-\frac{1}{2},j}}{\Delta X^2} + \frac{k^{n+1,m}_{i,j-\frac{1}{2}}}{\Delta Z^2} + \frac{k^{n+1,m}_{i,j+\frac{1}{2}}}{\Delta Z^2} \right) \psi^{n+1,m+1}_{i,j} \\ & \left. - \frac{\Lambda}{\sqrt{1+\Lambda^2}} \frac{k^{n+1,m}_{i+\frac{1}{2},j} - k^{n+1,m}_{i-\frac{1}{2},j}}{\Delta X} + \frac{1}{\sqrt{1+\Lambda^2}} \frac{k^{n+1,m}_{i,j+\frac{1}{2}} - k^{n+1,m}_{i,j-\frac{1}{2}}}{\Delta Z} \right] \\ & + (1-\Theta) \left[ \frac{k^{n}_{i+\frac{1}{2},j}}{\Delta X^2} \psi^{n}_{i+1,j} + \frac{k^{n}_{i-\frac{1}{2},j}}{\Delta X^2} \psi^{n}_{i-1,j} + \frac{k^{n}_{i,j-\frac{1}{2}}}{\Delta Z^2} \psi^{n}_{i,j-1} + \frac{k^{n}_{i,j+\frac{1}{2}}}{\Delta Z^2} \psi^{n}_{i,j+1} \right. \\ & - \left( \frac{k^{n}_{i+\frac{1}{2},j}}{\Delta X^2} + \frac{k^{n}_{i-\frac{1}{2},j}}{\Delta X^2} + \frac{k^{n}_{i,j-\frac{1}{2}}}{\Delta Z^2} + \frac{k^{n}_{i,j+\frac{1}{2}}}{\Delta Z^2} \right) \psi^{n}_{i,j} \\ & \left. - \frac{\Lambda}{\sqrt{1+\Lambda^2}} \frac{k^{n}_{i+\frac{1}{2},j} - k^{n}_{i-\frac{1}{2},j}}{\Delta X} + \frac{1}{\sqrt{1+\Lambda^2}} \frac{k^{n}_{i,j+\frac{1}{2}} - k^{n}_{i,j-\frac{1}{2}}}{\Delta Z} \right] \end{aligned} \tag{3.4}$$

Define $RSH'$ as:

$$\begin{aligned} RSH' \;=\; & (1-\Theta) \left[ \frac{k^{n}_{i+\frac{1}{2},j}}{\Delta X^2} \psi^{n}_{i+1,j} + \frac{k^{n}_{i-\frac{1}{2},j}}{\Delta X^2} \psi^{n}_{i-1,j} + \frac{k^{n}_{i,j-\frac{1}{2}}}{\Delta Z^2} \psi^{n}_{i,j-1} + \frac{k^{n}_{i,j+\frac{1}{2}}}{\Delta Z^2} \psi^{n}_{i,j+1} \right. \\ & - \left( \frac{k^{n}_{i+\frac{1}{2},j}}{\Delta X^2} + \frac{k^{n}_{i-\frac{1}{2},j}}{\Delta X^2} + \frac{k^{n}_{i,j-\frac{1}{2}}}{\Delta Z^2} + \frac{k^{n}_{i,j+\frac{1}{2}}}{\Delta Z^2} \right) \psi^{n}_{i,j} \\ & \left. - \frac{\Lambda}{\sqrt{1+\Lambda^2}} \frac{k^{n}_{i+\frac{1}{2},j} - k^{n}_{i-\frac{1}{2},j}}{\Delta X} + \frac{1}{\sqrt{1+\Lambda^2}} \frac{k^{n}_{i,j+\frac{1}{2}} - k^{n}_{i,j-\frac{1}{2}}}{\Delta Z} \right] \end{aligned} \tag{3.5}$$

Therefore, 3.4 becomes

$$\begin{aligned} RHS &= \Theta\left[\frac{k^{n+1,m}_{i+\frac{1}{2},j}}{\Delta X^2}\psi^{n+1,m+1}_{i+1,j} + \frac{k^{n+1,m}_{i-\frac{1}{2},j}}{\Delta X^2}\psi^{n+1,m+1}_{i-1,j} + \frac{k^{n+1,m}_{i,j-\frac{1}{2}}}{\Delta Z^2}\psi^{n+1,m+1}_{i,j-1} + \frac{k^{n+1,m}_{i,j+\frac{1}{2}}}{\Delta Z^2}\psi^{n+1,m+1}_{i,j+1}\right. \\ &\quad - \left(\frac{k^{n+1,m}_{i+\frac{1}{2},j}}{\Delta x^2} + \frac{k^{n+1,m}_{i-\frac{1}{2},j}}{\Delta X^2} + \frac{k^{n+1,m}_{i,j-\frac{1}{2}}}{\Delta Z^2} + \frac{k^{n+1,m}_{i,j+\frac{1}{2}}}{\Delta Z^2}\right)\psi^{n+1,m+1}_{i,j} \\ &\quad \left. - \frac{\Lambda}{\sqrt{1+\Lambda^2}}\frac{k^{n+1,m}_{i+\frac{1}{2},j} - k^{n+1,m}_{i-\frac{1}{2},j}}{\Delta X} + \frac{1}{\sqrt{1+\Lambda^2}}\frac{k^{n+1,m}_{i,j+\frac{1}{2}} - k^{n+1,m}_{i,j-\frac{1}{2}}}{\Delta Z}\right] + RHS' \end{aligned} \tag{3.6}$$

where $k_{i\pm\frac{1}{2},j}$ and $k_{i,j\pm\frac{1}{2}}$ represent the mean hydraulic conductivity between two adjacent cells. They can be calculated by an arithmetic mean, a harmonic mean, or a geometric mean. Since this study focuses on investigating a homogeneous soil, the arithmetic mean is used due to its simplicity.

According to $LHS = RHS$, one can get

$$\begin{aligned} &\left[\Theta\left(S_s\frac{\theta^{n+1,m}_{i,j}}{\phi} + c^{n+1,m}_{i,j}\right) + (1-\Theta)\left(S_s\frac{\theta^{n}_{i,j}}{\phi} + c^{n}_{i,j}\right)\right]\frac{\psi^{n+1,m+1}_{i,j}}{\Delta t} \\ &- \left[\Theta\left(S_s\frac{\theta^{n+1,m}_{i,j}}{\phi} + c^{n+1,m}_{i,j}\right) + (1-\Theta)\left(S_s\frac{\theta^{n}_{i,j}}{\phi} + c^{n}_{i,j}\right)^n\right]\frac{\psi^{n}_{i,j}}{\Delta t} \\ = \;& \Theta\left[\frac{k^{n+1,m}_{i+\frac{1}{2},j}}{\Delta X^2}\psi^{n+1,m+1}_{i+1,j} + \frac{k^{n+1,m}_{i-\frac{1}{2},j}}{\Delta X^2}\psi^{n+1,m+1}_{i-1,j} + \frac{k^{n+1,m}_{i,j-\frac{1}{2}}}{\Delta Z^2}\psi^{n+1,m+1}_{i,j-1} + \frac{k^{n+1,m}_{i,j+\frac{1}{2}}}{\Delta Z^2}\psi^{n+1,m+1}_{i,j+1}\right. \\ &- \left(\frac{k^{n+1,m}_{i+\frac{1}{2},j}}{\Delta X^2} + \frac{k^{n+1,m}_{i-\frac{1}{2},j}}{\Delta X^2} + \frac{k^{n+1,m}_{i,j-\frac{1}{2}}}{\Delta Z^2} + \frac{k^{n+1,m}_{i,j+\frac{1}{2}}}{\Delta Z^2}\right)\psi^{n+1,m+1}_{i,j} \\ &\left. - \frac{\Lambda}{\sqrt{1+\Lambda^2}}\frac{k^{n+1,m}_{i+\frac{1}{2},j} - k^{n+1,m}_{i-\frac{1}{2},j}}{\Delta X} + \frac{1}{\sqrt{1+\Lambda^2}}\frac{k^{n+1,m}_{i,j+\frac{1}{2}} - k^{n+1,m}_{i,j-\frac{1}{2}}}{\Delta Z}\right] + RHS' \end{aligned} \tag{3.7}$$

Rearranging equation 3.7:

$$\begin{aligned}
& -\left[\Theta\left(S_s\frac{\theta_{i,j}^{n+1,m}}{\phi}+c_{i,j}^{n+1,m}\right)+(1-\Theta)\left(S_s\frac{\theta_{i,j}^{n}}{\phi}+c_{i,j}^{n}\right)\right]\frac{\psi_{i,j}^{n}}{\Delta t} \\
& -\Theta\left(-\frac{\Lambda}{\sqrt{1+\Lambda^2}}\frac{k_{i+\frac{1}{2},j}^{n+1,m}-k_{i-\frac{1}{2},j}^{n+1,m}}{\Delta X}+\frac{1}{\sqrt{1+\Lambda^2}}\frac{k_{i,j+\frac{1}{2}}^{n+1,m}-k_{i,j-\frac{1}{2}}^{n+1,m}}{\Delta Z}\right)-RHS' \\
= \;& \Theta\frac{k_{i+\frac{1}{2},j}^{n+1,m}}{\Delta X^2}\psi_{i+1,j}^{n+1,m+1}+\Theta\frac{k_{i-\frac{1}{2},j}^{n+1,m}}{\Delta X^2}\psi_{i-1,j}^{n+1,m+1}+\Theta\frac{k_{i,j-\frac{1}{2}}^{n+1,m}}{\Delta Z^2}\psi_{i,j-1}^{n+1,m+1}+\Theta\frac{k_{i,j+\frac{1}{2}}^{n+1,m}}{\Delta Z^2}\psi_{i,j+1}^{n+1,m+1} \\
& -\left[\Theta\left(\frac{k_{i+\frac{1}{2},j}^{n+1,m}}{\Delta X^2}+\frac{k_{i-\frac{1}{2},j}^{n+1,m}}{\Delta X^2}+\frac{k_{i,j-\frac{1}{2}}^{n+1,m}}{\Delta Z^2}+\frac{k_{i,j+\frac{1}{2}}^{n+1,m}}{\Delta Z^2}\right)\right. \\
& \left.+\frac{\Theta}{\Delta t}\left(S_s\frac{\theta_{i,j}^{n+1,m}}{\phi}+c_{i,j}^{n+1,m}\right)+\frac{(1-\Theta)}{\Delta t}\left(S_s\frac{\theta_{i,j}^{n}}{\phi}+c_{i,j}^{n}\right)\right]\psi_{i,j}^{n+1,m+1}
\end{aligned} \tag{3.8}$$

Discrimination finally yields the system of nonlinear equations:

$$\begin{aligned}
b_{i,j}^{n+1,m+1} = \;& a_{i+1,j}^{n+1,m+1}\psi_{i+1,j}^{n+1,m+1}+a_{i-1,j}^{n+1,m+1}\psi_{i-1,j}^{n+1,m+1}+a_{i,j}^{n+1,m+1}\psi_{i,j}^{n+1,m+1} \\
& +a_{i,j-1}^{n+1,m+1}\psi_{i,j-1}^{n+1,m+1}+a_{i,j+1}^{n+1,m+1}\psi_{i,j+1}^{n+1,m+1}, i=1..N_X, j=1..N_Z
\end{aligned} \tag{3.9}$$

where, $N_X$ and $N_Z$ are the number of blocks, and

$$\begin{aligned}
a_{i+1,j}^{n+1,m+1} &= \Theta\frac{k_{i+\frac{1}{2},j}^{n+1,m}}{\Delta X^2} \\
a_{i-1,j}^{n+1,m+1} &= \Theta\frac{k_{i-\frac{1}{2},j}^{n+1,m}}{\Delta X^2} \\
a_{i,j-1}^{n+1,m+1} &= \Theta\frac{k_{i,j-\frac{1}{2}}^{n+1,m}}{\Delta Z^2} \\
a_{i,j+1}^{n+1,m+1} &= \Theta\frac{k_{i,j+\frac{1}{2}}^{n+1,m}}{\Delta Z^2} \\
a_{i,j}^{n+1,m+1} &= -\left[\Theta\left(\frac{k_{i+\frac{1}{2},j}^{n+1,m}}{\Delta X^2}+\frac{k_{i-\frac{1}{2},j}^{n+1,m}}{\Delta X^2}+\frac{k_{i,j-\frac{1}{2}}^{n+1,m}}{\Delta Z^2}+\frac{k_{i,j+\frac{1}{2}}^{n+1,m}}{\Delta Z^2}\right)\right. \\
&\quad \left.+\frac{\Theta}{\Delta t}\left(S_S\frac{\theta_{i,j}^{n+1,m}}{\phi}+c_{i,j}^{n+1,m}\right)+\frac{(1-\Theta)}{\Delta t}\left(S_S\frac{\theta_{i,j}^{n}}{\phi}+c_{i,j}^{n}\right)\right]
\end{aligned}$$

and

$$
\begin{aligned}
b_{i,j}^{n+1,m+1} &= -\left\{\Theta\left[S_S\frac{\theta_{i,j}^{n+1,m}}{\phi}+c_{i,j}^{n+1,m}\right]+(1-\Theta)\left[S_S\frac{\theta_{i,j}^{n}}{\phi}+c_{i,j}^{n}\right]\right\}\frac{\psi_{i,j}^{n}}{\Delta t} \\
&\quad -\Theta\left(-\frac{\Lambda}{\sqrt{1+\Lambda^2}}\frac{k_{i+\frac{1}{2},j}^{n+1,m}-k_{i-\frac{1}{2},j}^{n+1,m}}{\Delta X}+\frac{1}{\sqrt{1+\Lambda^2}}\frac{k_{i,j+\frac{1}{2}}^{n+1,m}-k_{i,j-\frac{1}{2}}^{n+1,m}}{\Delta Z}\right)-RHS'
\end{aligned}
\tag{3.10}
$$

### 3.1.2 Initial and Boundary Conditions

Since the 2D Richards' equation discussed above is a transient second order partial differential equation, one initial condition and four boundary conditions are needed to determine a unique solution. The initial condition represents the initial state of the system as:

$$\theta = \theta_i(X, Z, t = 0.0)$$

or

$$\psi = \psi_i(X, Z, t = 0.0)$$

A general form for boundary conditions is [135]:

$$\alpha(X, Z, t)\psi(X, Z, t) + \beta(X, Z, t)\frac{\partial\psi}{\partial i}(X, Z, t) = \gamma(X, Z, t)$$

where $\alpha(X, Z, t)$, $\beta(X, Z, t)$, and $\gamma(X, Z, t)$ are known functions and $i$ is the unit vector. The boundary condition is called a Dirichlet boundary condition if the value of $\psi$ is specified ($\beta(X, Z, t) = 0$), a Neumann boundary condition if the normal derivative of $\psi$ is specified ($\alpha(X, Z, t) = 0$), or a Robin boundary condition if $\alpha(X, Z, t) \neq 0$ and $\beta(X, Z, t) \neq 0$. Since the research conducted here is interested in infiltration hereafter the boundary flux is the main concern. The Neumann boundary condition was derived here. Assuming that flux at the top, bottom, right, and left boundaries are $q_{top}$, $q_{bot}$, $q_{right}$, and $q_{left}$, respectively. The boundary elements of the system of equation 3.9 are revised.

Left boundary:

$$q_{left} = -k_X\frac{\partial(\psi + Z)}{\partial X} = -k_X\left(\frac{\psi_{2,j}^{n+1}-\psi_{1,j}^{n+1}}{\frac{\Delta X}{2}}-\frac{\Lambda}{\sqrt{1+\Lambda}}\right)$$

Rearranging,

$$\frac{\Delta X}{2}\left(-\frac{q_{left}}{k_X}+\frac{\Lambda}{\sqrt{1+\Lambda}}\right) = \psi_{2,j}^{n+1}-\psi_{1,j}^{n+1},\ j = 1..N_Z \tag{3.11}$$

Right boundary:

$$q_{right} = -k_X \frac{\partial(\psi + Z)}{\partial X} = -k_X \left( \frac{\psi^{n+1}_{N_X,j} - \psi^{n+1}_{N_X-1,j}}{\frac{\Delta X}{2}} - \frac{\Lambda}{\sqrt{1+\Lambda}} \right)$$

Rearranging,

$$\frac{\Delta X}{2} \left( -\frac{q_{right}}{k_X} + \frac{\Lambda}{\sqrt{1+\Lambda}} \right) = \psi^{n+1}_{N_X,j} - \psi^{n+1}_{N_X-1,j},\ j = 1..N_Z \tag{3.12}$$

Top boundary:

$$q_{top} = -k_Z \frac{\partial(\psi + Z)}{\partial z} = -k_Z \left( \frac{\psi^{n+1}_{i,N_Z} - \psi^{n+1}_{i,N_Z-1}}{\frac{\Delta Z}{2}} + \frac{1}{\sqrt{1+\Lambda}} \right)$$

Rearranging,

$$\frac{\Delta Z}{2} \left( -\frac{q_{top}}{k_Z} - \frac{1}{\sqrt{1+\Lambda}} \right) = \psi^{n+1}_{i,N_Z} - \psi^{n+1}_{i,N_Z-1},\ i = 1..N_X \tag{3.13}$$

Bottom boundary:

$$q_{bot} = -k_Z \frac{\partial(\psi + Z)}{\partial z} = -k_Z \left( \frac{\psi^{n+1}_{i,2} - \psi^{n+1}_{i,1}}{\frac{\Delta Z}{2}} + \frac{1}{\sqrt{1+\Lambda}} \right)$$

Rearranging,

$$\frac{\Delta Z}{2} \left( -\frac{q_{bot}}{k_Z} - \frac{1}{\sqrt{1+\Lambda}} \right) = \psi^{n+1}_{i,2} - \psi^{n+1}_{i,1},\ i = 1..N_X \tag{3.14}$$

Note that for the top Neumann boundary condition, equation 3.13 is only for a situation that rainfall $w$ is less than the hydraulic conductivity $k_s$. For the case that $w > k_s$, a dynamic top boundary condition is:

$$q_{top} = -k_Z \frac{\partial(\psi + Z)}{\partial z},\ \psi_u < 0$$

$$\psi_u = 0,\ \psi_u \geq 0$$

where $\psi_u$ is the up boundary pressure.

As mentioned, a Picard iteration was used for solving the nonlinear equation. The method is simple to code and computationally inexpensive. The computer program is written in FORTRAN 90 and can be found in appendix A.

### 3.1.3 Numerical Discretization

Spatial and temporal discretization can significantly affect the efficiency and convergence of the finite difference scheme. The finer the discretization, the less efficient of the scheme whereas the more accurate the solution. Although using a coarser discretization can significantly improve the efficiency of a given model, it may lead to a convergence problem (i.e., the model may become unstable) or merely an accuracy problem (i.e., the model is insufficiently resolved to meet the solution at the correct precision). A trade-off must be determined between the efficiency and the accuracy for each specified problem. In this study, a fine discretization was used since an accurate numerical benchmark is required. Numerical discretization for each experiment base case can be found in an appendix E.

### 3.1.4 Verification of the Numerical Solution

The numerical scheme has been extensively validated against Gottardi and Venutelli's simulation results [58]. It successfully reproduces moisture profiles with the boundary conditions of both constant pressure head and constant flux at the top of soil column, as shown in Figure 3.2 and Figure 3.3.

Infiltration is mainly a vertical percolation process, and the one-dimensional Richards' equation is often sufficient for the infiltration problem [58]. To test the validity of the model developed here, a simulation is performed with Berino soil with depth $D = 150cm$; the corresponding parameters are obtained from [58]. The soil is initially in an equilibrium state, as shown in Figure 3.4 ($t = 0s$). A rainfall rate is then applied with a value of one half $k_s$, lasting for one hour. Initial and boundary conditions may be written as:

$$h(z, t = 0) = z - 150$$

$$w = \begin{cases} \frac{1}{2}k_s & \text{for } t \leq 1h \\ 0.0 & \text{for } t > 1h \end{cases}$$

$$h(z = 150, t) = 0.0$$

Here, the test case is used as both a verification of the numerical code and as an illustration of the infiltration process, useful for understanding later work. Soil profiles at different times during the test case are shown in Figures 3.4, 3.5, 3.6, and 3.7. At the initial condition, the soil layer is in an equilibrium state. Beginning at $t = 0$, rainfall begins

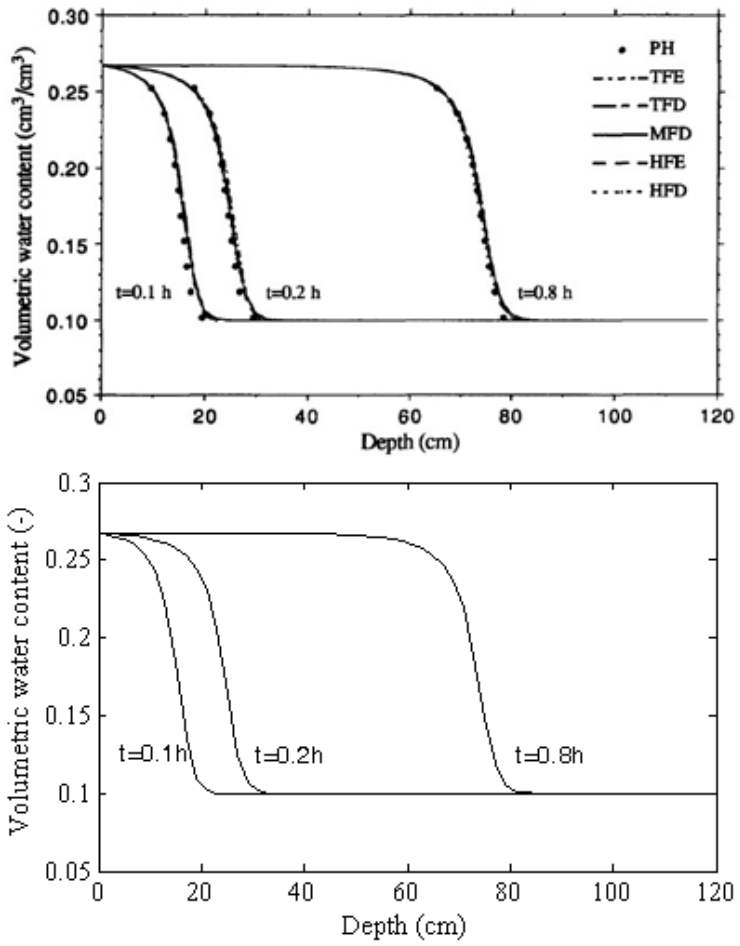


Figure 3.2: Homogenous case with constant pressure at the top of column: Top-Gottardi and Venutelli's (symbols represent different numerical schemes)[58]; bottom-specialized finite difference scheme

arriving at the surface at a specific rate, which is only one half of the saturated hydraulic conductivity, $k_s$. Because the rainfall rate is less than the infiltration capacity, all water will enter into the soil. The first stage, as shown in Figure 3.4, is a purely percolating process. Notice that at the very beginning, the pressure head increases rapidly: at $t = 600s$, the head increased from -150cm to -20cm. The increasing velocity of the pressure head slows down afterward. From time 1200s to time 1800s, the increase in pressure head is less than 5cm; from time 1800s to time 3600s, the increase is less than 2 cm. The water is percolating

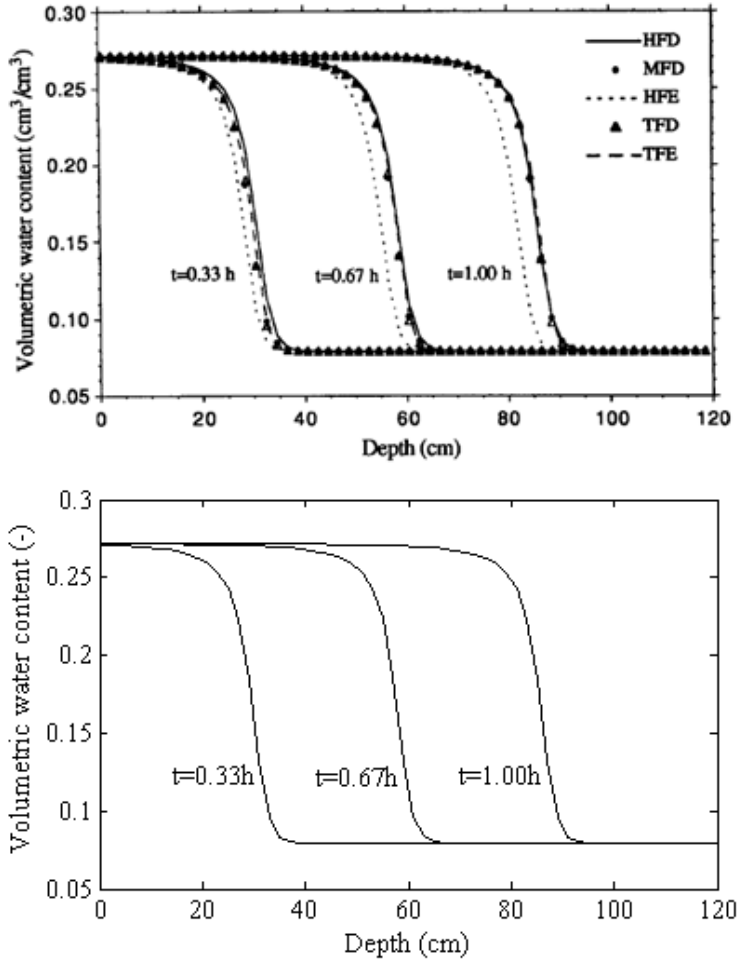


Figure 3.3: Homogenous case with constant flux at the top of column: Top-Gottardi and Venutelli's (symbols represent different numerical schemes)[58]; bottom-specialized finite difference scheme

into the deep soil; meanwhile the pressure head and water content continues to increase, as shown in Figure 3.4.

Rainfall stops at the beginning of the second stage ($t = 3600s$). However, the water that continues to percolate into the deep layer results in a drying process begin from the surface as shown in Figure 3.5. The pressure head and the water content begin to decrease as shown in Figure 3.5. A soil drying process starts at $t = 7200s$ as shown in Figure 3.6.

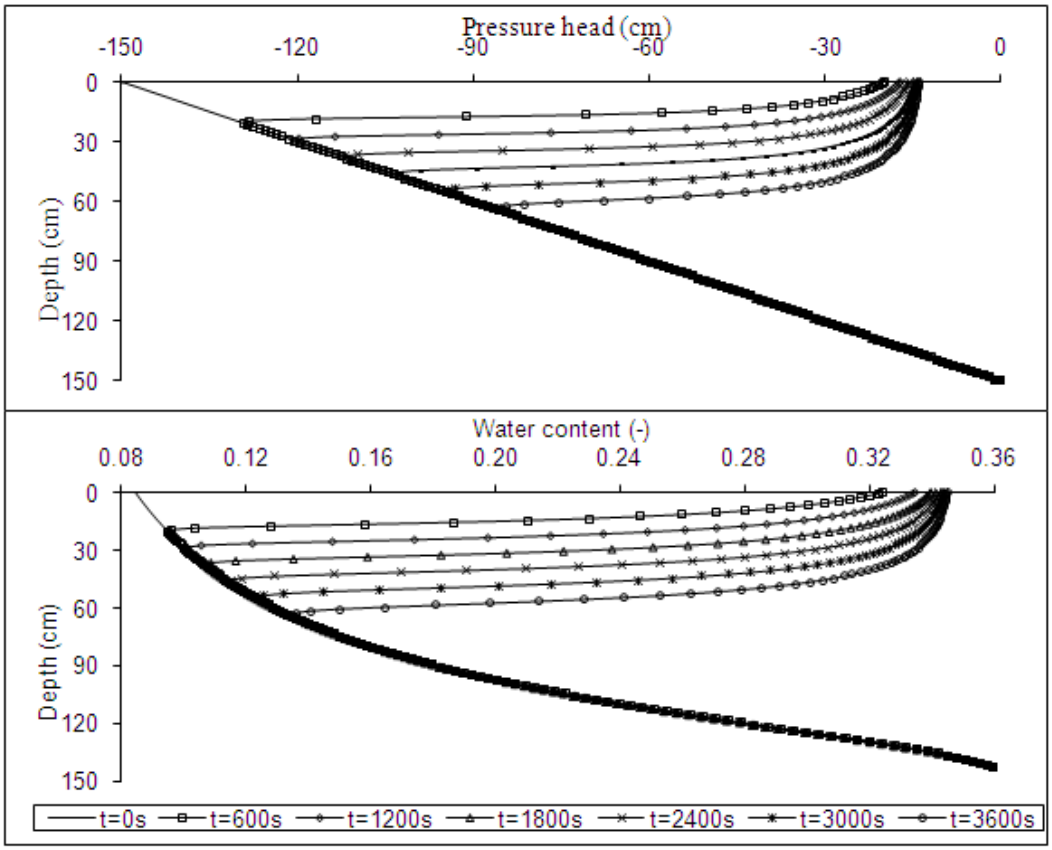


Figure 3.4: Pressure head and water content distribution of the first stage (with flux at the top)

The pressure change in the drying process is similar to that in the percolating process, in which the pressure head changes rapidly at the very beginning and slows down afterward. The pressure head asymptotically approaches an equilibrium state as time approaches semi-infinite ($t = 61200s$) as shown in Figure 3.7.

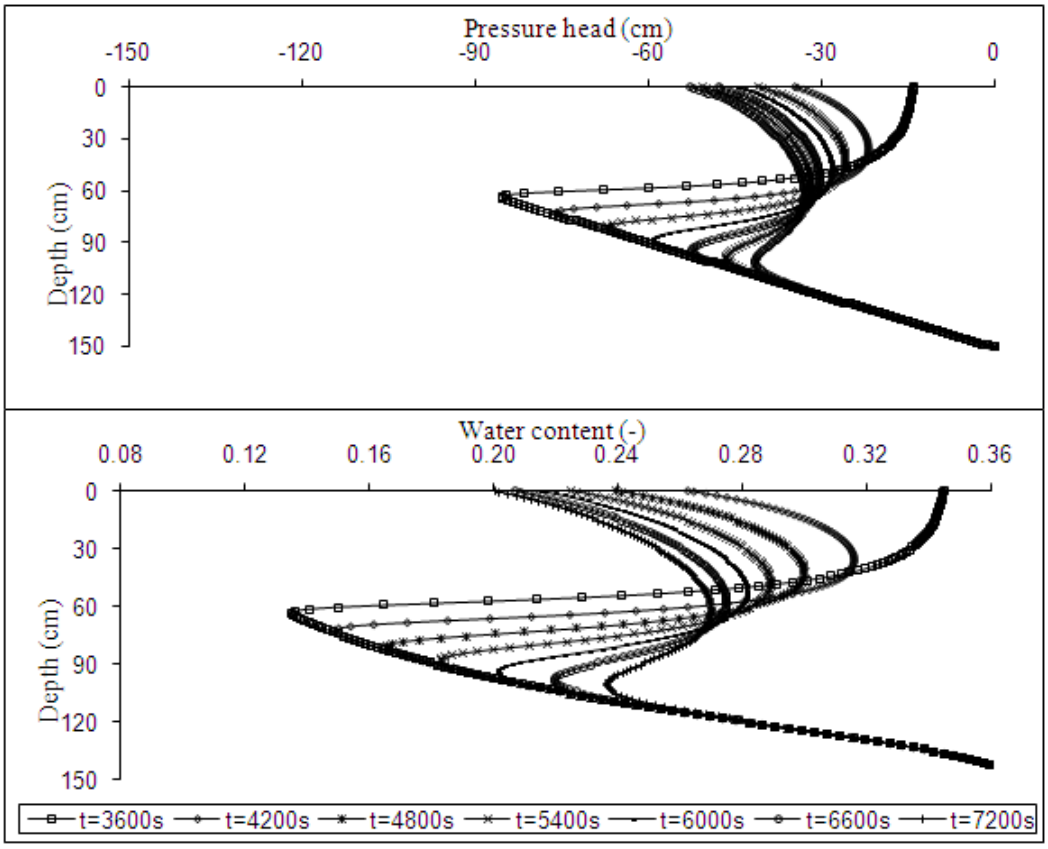


Figure 3.5: Pressure head and water content distribution of the second stage (without flux at the top)

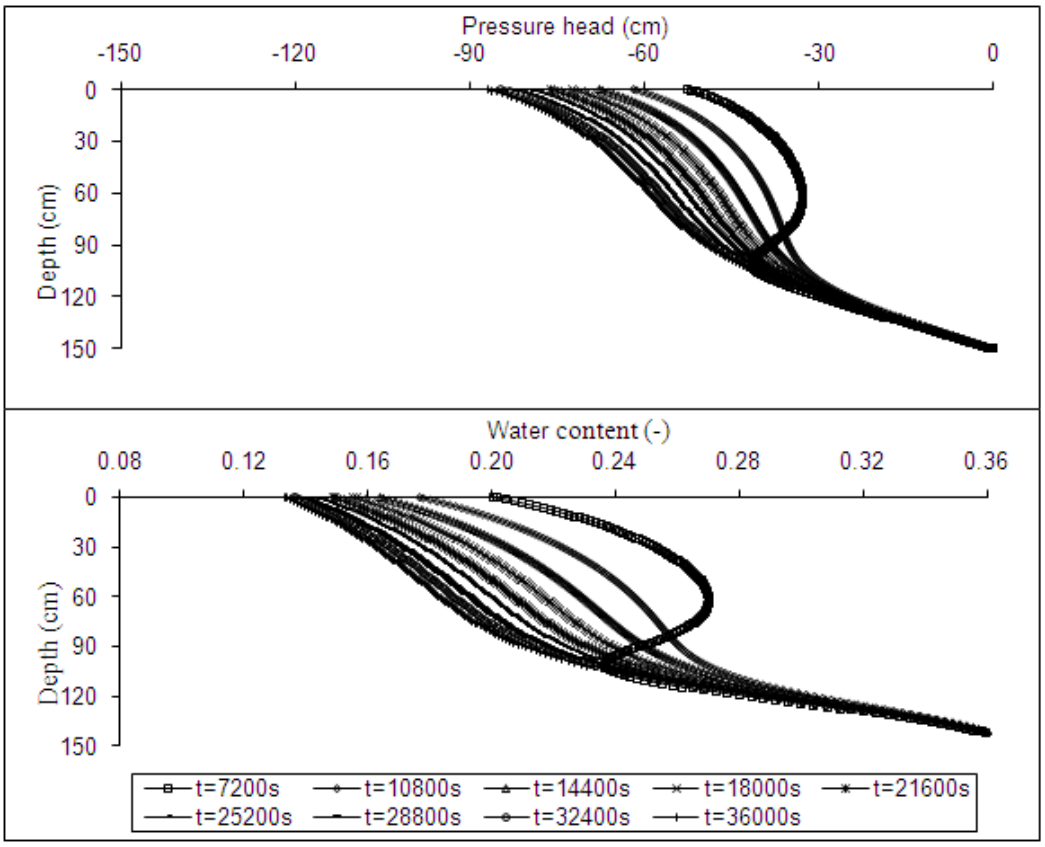


Figure 3.6: Pressure head and water content distribution of the third stage (without flux at the top)

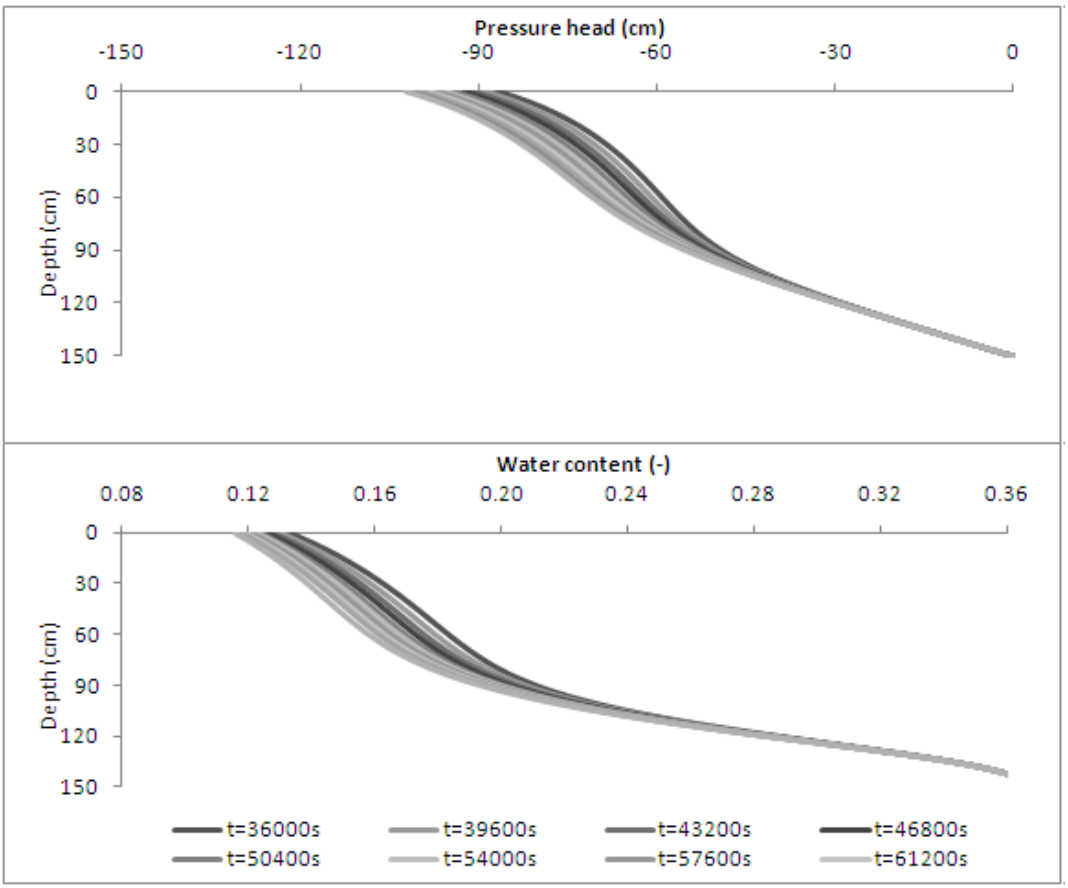


Figure 3.7: Pressure head and water content distribution after the third stage (without flux at the top)

The finite difference scheme provides an appropriate solution to the Richards' equation and performs well in simulating the percolating process, the water redistributing process, and the soil drying process for a rainfall event.

## 3.2 Applicability of the Green-Ampt Model

Note: Much of the material below appears in Liu et al. [81](in review).

The Green-Ampt model is an approximate analytical solution to Richards' equation that is commonly used to simulate infiltration processes in hydrological models and land surface schemes. The Green-Ampt model assumes that neither a water table nor an impermeable layer (e.g., bedrock or a frost table) exist near the soil surface. In regional scale applications, these idealized conditions will often not be met, and it is presently unclear what implications this has for regional water resource models. This section investigates the limiting conditions under which the Green-Ampt model is appropriate and how individual assumptions about lower boundary conditions affect the validity of the model. Guided by the comparison between the Green-Ampt model and numerical solutions to the Richards' equation, various simple revisions to the Green-Ampt model are suggested. Results demonstrate that even when the traditional assumptions are relaxed, the Green-Ampt model often still provides reasonable results for regional-scale analysis and can be amended to account for conditions for which it was not intended.

### 3.2.1 Introduction

Green and Ampt [60] presented the first physically-based equation for describing the infiltration of water into soil. It is based on the fundamental physics of infiltration and provides results that often match well with empirical observations [110]. The Green-Ampt model (GA) (as revised by Mein and Larsen [89] to account for onset of saturation) has been widely used in applied soil physics and hydrology owing to its simplicity, computational expediency, and satisfactory performance for a variety of hydrological applications. It is a key component of many hydrologic models (e.g., CLASS [141], WEPP [103], HSPF [20], and SWAT [99]). While found to be an excellent approximate solution to the Richards' equation (RE) under many parameter combinations ([107], [89],and [6]), the GA model estimates cumulative infiltration by assuming water flow into a vertical homogeneous soil that is infinite in depth. No shallow water table, capillary fringe, or shallow impermeable base is considered. In regional scale applications these idealized conditions will often not be met, and it is presently unclear what implications this has for regional water resource models that use some form of the GA model.

Specifically, the author had not found any studies on the impact of using the GA approximation for flow in a finite soil bounded below by a shallow water table, frost table, or impermeable base. This section investigates under which of these conditions the standard

GA model is appropriate and how individual assumptions affect the applicability of the model.

Here, "true"infiltration behavior is assumed to be represented by the solutions to the one-dimensional RE for vertical unsaturated flow, obtained using the methods described in section 3.1. To test the applicability of the GA model under conditions for which it was not intended, the GA model is here compared to the numerical solutions to the RE. Two special conditions are addressed: the presence of a shallow water table at depth, and the presence of an impermeable surface (representing either a low-permeability soil layer or frost table). Based upon the results of this investigation, a number of simple revisions to the GA model are proposed that lead to improved results under a wider variety of conditions. These revisions are easily implemented in any surface water hydrology model that currently uses the GA infiltration model.

While the implicit form of the GA equation is often solved numerically using a standard Newton-Raphson approach ([56] and [84]), here the iterative analytical solution presented by Barry et al. [5] (equation 29) is used. The results are presented in terms of dimensionless variables, $k_s/w$, and a dimensionless time parameter, $X$, varies from $X = 0$ at $t = 0$ to $X = 1$ at $t = \infty$, and is defined as [38]:

$$X = \left(1 + \frac{\alpha}{wt}\right)^{-1} \tag{3.15}$$

This dimensionless framework provides a new means of examining Green-Ampt infiltration over a wide range of parameter space: all parameter variability is simplified into two dimensionless variables: $k_s/w$ and $X$, rather than the original 4 ($k_s$, $w$, $\alpha$, and $t$), significantly improving our ability to visualize and analyze the problem for the entire range of plausible parameters.

Using this dimensionless formulation, equation 2.21 may be written as:

$$\frac{f(t)}{w} = \begin{cases} 1 & \text{for } X \leq X_p \\ \frac{k_s}{w}\left(1 + \dfrac{1}{-1 - W_{-1}(x)}\right) & \text{for } X > X_p \end{cases} \tag{3.16}$$

where $X_p = \frac{k_s}{w}$ is the dimensionless ponding time, $W_{-1}(x)$ is the lower branch of the Lambert W function, defined as [5]:

$$W_{-1}(x) exp[W_{-1}(x)] = x$$

and $x$ is a function of $X$:

$$x = -\frac{1}{1 - X_p} exp\left[-\frac{1}{1 - X_p} - X_p\left(\frac{X}{1 - x} - \frac{X_p}{1 - X_p}\right)\right]$$

### 3.2.2 Testing Green-Ampt Method Applicability

The presence of a water table, impermeable base, and vertical heterogeneity were individually investigated using the RE numerical model. To confirm the appropriateness of the error quantification used here, simulations were initially conducted on loamy sand, sandy loam, and silt loam (using parameters chosen from Clapp and Hornberger [34]). A constant $\alpha$ was used for all simulations to ensure identical GA simulation results.

With the intent to generalize the performance of the GA model so that the conclusions drawn here are not constrained to any specific soil texture, dimensionless parameters are used to communicate simulation results. To ensure the generality of results, all simulations were run under a wide range of dimensionless time, $X$, and dimensionless hydraulic conductivities, $k_s/w$. For the analytical GA solution, sampling only these two parameters is sufficient to fully characterize all possible infiltration scenarios. However, this is not the case for the RE solution, which is additionally sensitive to the form of the characteristic curves, specific storage, and rainfall rate. Hence, the numerical model was initially perturbed to test for the influence of these parameters beyond that which could be encapsulated in the dimensionless parameters alone. The parameters $X$ and $k_s/w$ were found to encompass most of the variability in the numerical solution behavior and performance. In order to investigate soil property effects on the simulation results, the most important soil property, dimensionless conductivity, $k_s/w$, is set to fall within the range from 0.5 to 1.0. For all tests in the paper, the rainfall intensity is $2k_s$ (3.52e-2 cm/s for sand base case). To test a complete range of times, the simulation duration was set to 60 times the ponding time (e.g., $SD = 60t_p$).

#### Numerical simulation sets

To approximate the infinite depth boundary condition of the GA analytical solution, an appropriate semi-infinite depth for numerical modeling was first identified, requiring that the domain is long enough that the wetting front location is not affected by the bottom boundary before the end of the simulation. This required depth is determined by the rainfall rate, soil properties, and the simulation duration. Here, numerical experiments conducted for the four soils show that the wetting front depth at $120t_p$(i.e., $F(120t_p)/(\theta_s - \theta_0)$) is a reasonable surrogate for a semi-infinite depth, denoted as $D^*$ here. This length is treated here as a characteristic length, used to define a dimensionless distance, $z_D^* = D/D^*$, where $D$ is the physical depth.

The simulation parameters for the initial soil tests, used to determine the semi-infinite depth, are listed in table 3.1. Note that in table 3.1, the dimensionless ponding time,

dimensionless simulation duration, and dimensionless semi-infinite depth are fixed for all soils tested here, and will therefore provide identical dimensionless results for the standard GA model without amendments. Based upon the dimensionless formulation here, these results may be considered representative of results for all soils. Indeed, this was verified via comparisons (not shown) with results for all 4 soil parameterizations in table 3.1.

Table 3.1: Summarization of the simulation parameter sets

| Soil texture | Sand | Loamy sand | Sandy loam | Silt loam |
|---|---|---|---|---|
| $k_s$[cm/s] | 1.76e-2 | 1.56e-2 | 3.47e-3 | 7.20e-4 |
| $\theta_s$[-] | 0.395 | 0.410 | 0.435 | 0.485 |
| $\theta_0$[-] | 0.250 | 0.272 | 0.384 | 0.446 |
| $\psi_{ae}$[cm] | -12.1 | -9.0 | -21.8 | -78.6 |
| $b$[-] | 4.05 | 4.38 | 4.90 | 5.3 |
| $S_s$[1/cm] | 1.0e-6 | 1.0e-6 | 1.0e-6 | 1.0e-6 |
| $\psi_f$[cm] | -13.35 | -14.10 | -22.36 | -50.03 |
| $\alpha$[cm] | 1.94 | 1.94 | 1.94 | 1.94 |
| $t_p$[s] | 54.99 | 62.05 | 278.90 | 1344.17 |
| $SD$[s] | 3299.41 | 3722.73 | 16734.06 | 80650.52 |
| $D^*$[cm] | 854.13 | 896.26 | 1430.56 | 3201.08 |
| $X(t_p)$[-] | 0.499 | 0.499 | 0.499 | 0.499 |
| $X(SD)$[-] | 0.984 | 0.984 | 0.984 | 0.984 |
| $z_D^*$[-] | 1.0 | 1.0 | 1.0 | 1.0 |

Note that two means of calculating the wetting front suction, $\psi_f$,were used for testing. First used is the wetting front suction, as determined by Verseghy [141]:

$$\psi_f = -\frac{b(\psi k - \psi_{ae} k_s)}{k_s/2(b+3)} \tag{3.17}$$

Verseghy's formula is based upon the proposal of Bouwer [23] that the conductivity behind the wetting front can be estimated as $k_s/2$, which is less than $k_s$ due to the air

entrapped during the infiltration process. Equation 3.17 is obtained by substituting the Clapp-Hornberger soil characteristic functions into Neuman's equation [100].

As an alternative approach, Clapp and Hornberger [34] proposed that the wetting front suction can be determined by neglecting the parabolic section of the suction curve when integrating Neuman's equation [100], which results in:

$$\psi_f = -\frac{2b+3}{b+3}\psi_{ae} \tag{3.18}$$

Maximum relative errors between the GA and RE when using equation 3.17 and equation 3.18 are roughly 3 percent. The difference is that GA underestimates infiltration when equation 3.17 is used and overestimates infiltration otherwise. Recognizing that the impact of this choice is relatively minor, equation 3.17 is exclusively used here.

Initial tests were used to directly compare the dimensionless results of the RE and GA under the conditions for which it was intended, i.e., a system with infinite depth. Relative errors for the infiltration rate ($E_f$) and the cumulative infiltration ($E_F$) between the analytical GA solution and the numerical RE solution with semi-infinite depth are depicted in Figure 3.8. It shows that the maximum value for $E_f$ is less than 8 percent and for $E_F$ is less than 3 percent, occurring only after the analytical ponding time ($X = 0.5$) has been reached. Errors first increase, then decrease with time and decrease with increasing $k_s/w$ after the ponding time. The reason for this is discussed in what follows.

Dimensionless infiltration rate as a function of dimensionless time for the GA model and the base case RE model is depicted in Figure 3.9. It shows that the ponding time calculated from the GA model is always less than that of the RE. However, the difference between them, $\delta t_p$, decreases with increasing $k_s/w$ value. Both GA and RE dimensionless infiltration rates converge to the same dimensionless hydraulic conductivity $k_s/w$ at the end of simulation duration. This implies that the simulation duration of $60t_p$ is long enough to characterize the complete GA infiltration process, during which the infiltration rate varies from the rainfall rate to the saturated hydraulic conductivity. Figure 3.9 clearly shows that the maximum difference between the GA and the RE occurs at the RE ponding time. Starting at the GA ponding time, for each individual $k_s/w$ value, the difference increases until the RE ponding time is reached and decreases from then on. These results are consistent with the numerical/analytical comparisons of Mein and Larson [89].

### Shallow Water Table

Water table depth varies due to changes in climate, land cover, or topography, but in many cases is known to be present at a shallow depth. In these cases, it is necessary to

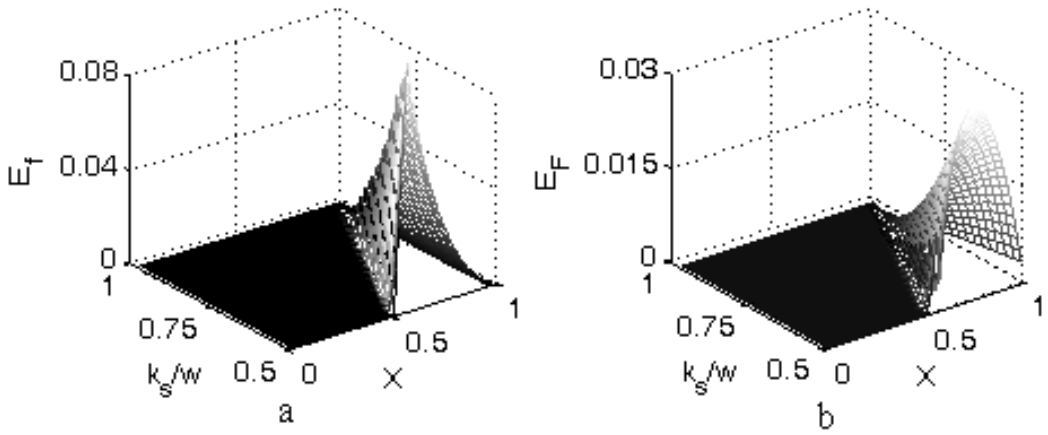


Figure 3.8: Relative error between GA and RE with a semi-infinite depth: (a) dimensionless infiltration rate; (b) dimensionless cumulative infiltration

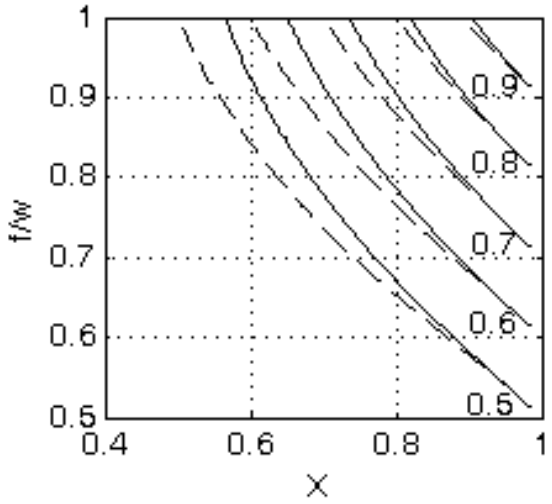


Figure 3.9: Dimensionless infiltration rate, f/w (0.5-0.9), as a function of dimensionless time, X, for variable dimensionless hydraulic conductivity $k_s/w$ : dash-GA; solid-RE

consider the effect of a water table upon the infiltration process. When a water table is present, the wetting front will progress downwards until the entire soil column is saturated,

at which point, the infiltration rate will decelerate to the saturated conductivity of the soil. Since this influence is ignored in the traditional GA model, a corresponding modification is necessary.

The validity of the traditional GA model with the existence of a shallow water table at dimensionless depths of $z_D^*$ =1/40, 1/30, 1/20, 1/10, and 1/5 were investigated, with results depicted in Figure 3.10. Here, the GA model was deemed appropriate if the relative error between the numerically-evaluated infiltration rate with and without the water table is less than 5 percent. If the error exceeds 5%, the GA model was deemed inapplicable, i.e., the water table is too close to the surface to be ignored in infiltration calculations. Figure 3.10 depicts the applicability of the standard GA model for the range of dimensionless water table depths.


Figure 3.10: Applicability of GA model with variable dimensionless water table depth (Left to right: 1/40, 1/30, 1/20, 1/10, and 1/5): Light-applicable; Dark-non-applicable

Figure 3.10 indicates that the general applicability of the GA model is limited by the existence of a water table. Not surprisingly, the applicability of the GA model clearly increases with increasing water table depth. The point at which the traditional GA solution should no longer be used occurs when the wetting front approaches the water table. The larger the dimensionless hydraulic conductivity is, the faster the wetting front progresses downwards. As a consequence, the separation occurs earlier, and sandy soils are more likely to require amendment for water table conditions. Notice that there are small regions at the end of the simulation at which the solution again becomes applicable. This is due to both RE solutions converging to the same dimensionless hydraulic conductivity (i.e., the steady-state solutions are the same with or without a water table). Figure 3.11 depicts the infiltration process for selected conductivities for dimensionless water table depths of $z_D^*$ = 1/40, 1/20 , 1/10, and 1/5, demonstrating precisely what is occurring to the infiltration curve as water table depth varies. In all cases, the transition from GA-type infiltration to infiltration in fully-saturated soil is quite abrupt and relatively insensitive to conductivity.

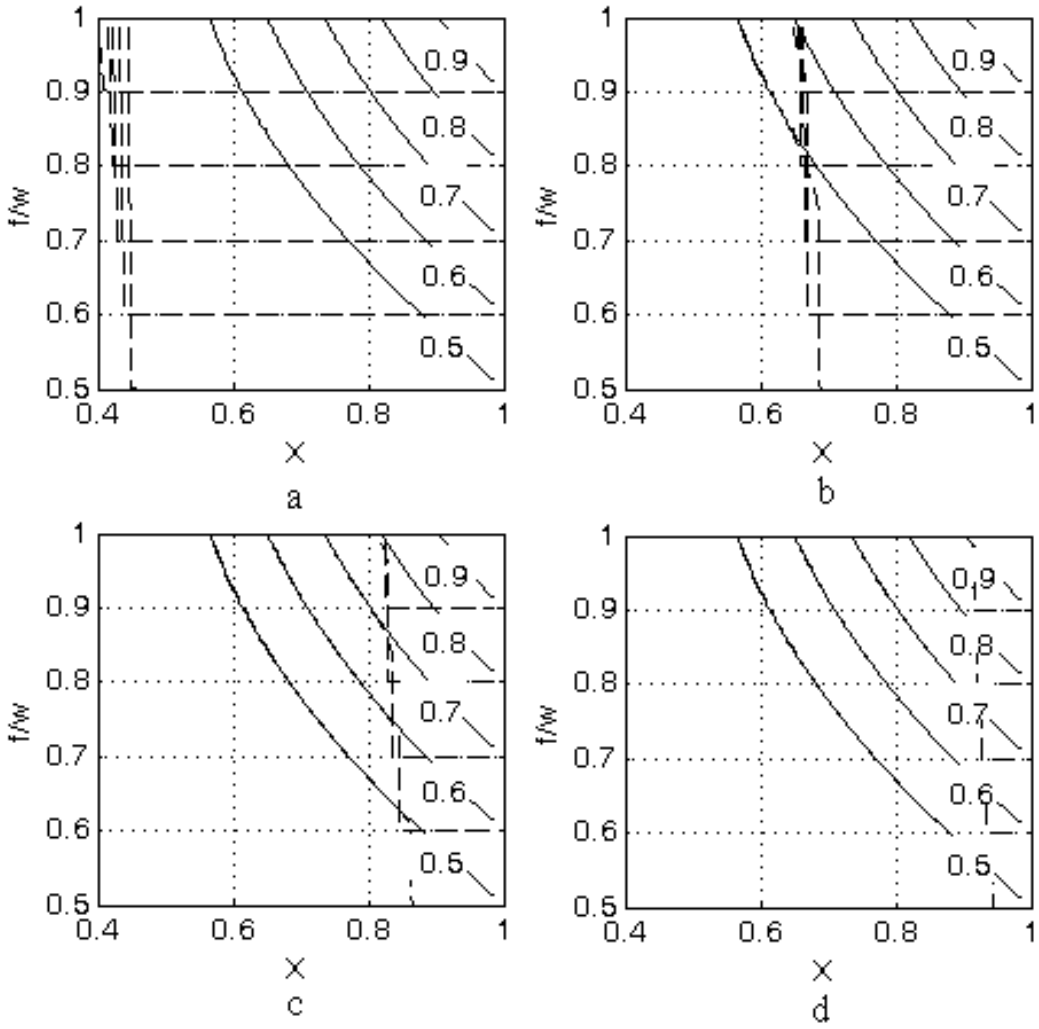


Figure 3.11: Dimensionless infiltration rate, $f/w$, as a function of dimensionless time, $X$, for variable dimensionless conductivity $k_s/w$ (0.5-0.9): solid-RE with dimensionless water table depth at 1.0; dash-RE with dimensionless water table depth at a): 1/40; b): 1/20; c): 1/10; d): 1/5

Once the range of applicability was ascertained, a simple algorithm modification was identified that may be used to account for a water table. This modification is described

and assessed below. Considering that the GA model is not valid from the moment that the wetting front merges with the water table, a modified GA solution which accounts for the existence of the water table was developed as:

$$\frac{f(t)}{w} = \begin{cases} 1 & \text{for } X \leq X_p \\ \frac{k_s}{w}\left(1 + \frac{1}{-1 - W_{-1}(x)}\right) & \text{for } X_p < X < X_C \\ \frac{k_s}{w} & \text{for } X \geq X_C \end{cases} \tag{3.19}$$

$X_c$ is the critical dimensionless time at which the soil column is fully saturated, and is related to the initial water content, soil properties, rainfall rate, and the simulation duration. This revised model is physically consistent with the piston-like flow approximation of the original GA. It is very important to note that $X_c$ is not the same as the dimensionless time, $X_w$, at which the traditional GA wetting front reaches the water table. Instead, the presence of a capillary fringe and vertically non-uniform saturation lead to the piston flow approximation being a poor one as the wetting front will accelerate as water table is approached and consequently cause $X_c$ to be shorter. Therefore it is inadequate to simply use a model whereby the infiltration is set to $k_s$ when the wetting front reaches the water table depth. Rather, to account for this, guided by comparison between the GA model and numerical solutions to the RE, $X_c$ is here empirically determined as:

$$X_C = m\left(\frac{k_s}{w}\right)^2 + n\frac{k_s}{w} + l$$

where $m$, $n$, and $l$ are fitting coefficients related to the dimensionless depth, $z_{D^*}$ , as:

$$m = 73.85z_{D^*}^3 - 46.58z_{D^*}^2 + 7.26z_{D^*} - 0.06$$

$$n = 33.25z_{D^*}^2 - 7.59z_{D^*} - 0.03$$

$$l = 290.09z_{D^*}^3 - 132.39z_{D^*}^2 + 19.39z_{D^*} - 0.13$$

Of course, it is important to discern just what happens if one assumes that the infiltration rate may be set to $k_s$ when the wetting front reaches the water table. Table 3.2 is the comparison between the critical times $X_c$ and $X_w$ for wide range of dimensionless hydraulic conductivity $k_s/w$ and dimensionless time, $X$.

It is clear that $X_c$ occurs much earlier than $X_w$ in all cases, indicating that the simplest approach based upon pure piston flow would lead to overestimates of infiltration. In

Table 3.2: Comparison between the critical times $X_c$, when the wetting front actually intersects the water table and $X_w$, based upon the piston flow assumption of the traditional GA, for a range of dimensionless depths

| $\frac{k_s}{w}$ | $z_D^* = 1/40$ | | $z_D^* = 1/30$ | | $z_D^* = 1/20$ | | $z_D^* = 1/10$ | | $z_D^* = 1/5$ | |
|---|---|---|---|---|---|---|---|---|---|---|
| | $X_c$ | $X_w$ | $X_c$ | $X_w$ | $X_c$ | $X_w$ | $X_c$ | $X_w$ | $X_c$ | $X_w$ |
| 0.5 | 0.457 | 0.941 | 0.547 | 0.957 | 0.687 | 0.972 | 0.872 | - | 0.950 | - |
| 0.6 | 0.448 | 0.931 | 0.537 | 0.949 | 0.676 | 0.967 | 0.857 | - | 0.942 | - |
| 0.7 | 0.440 | 0.922 | 0.530 | 0.942 | 0.669 | 0.962 | 0.847 | 0.982 | 0.936 | - |
| 0.8 | 0.435 | 0.914 | 0.526 | 0.936 | 0.666 | 0.957 | 0.843 | 0.979 | 0.932 | - |
| 0.9 | 0.431 | 0.910 | 0.524 | 0.931 | 0.666 | 0.954 | 0.843 | 0.977 | 0.931 | - |

addition, it can be seen from examining Figure 3.11 that the maximum relative errors in point infiltration occur in this range.

Equation 3.19 indicates that the infiltration rate remains constant when the soil domain is fully saturated, at which point the wetting front merges to the dynamic water table. For very shallow water table cases, $X_c$ can be less than $X_p$, e.g., soil column is saturated before the ponding time. Equation 3.19 is rewritten as:

$$\frac{f(t)}{w} = \begin{cases} 1 & \text{for } X \leq X_C \\ \frac{k_s}{w} & \text{for } X > X_C \end{cases}$$

Relative errors between the modified GA model and the RE for four dimensionless depths for sand with an initial water content of 0.258 (e.g., $\theta_0/\theta_s = 0.65$) are shown in Figure 3.12.

Figure 3.12 indicates that the maximum relative error of the cumulative infiltration ($E_F$) for all tested water table depths is less than 3 percent. These tests were repeated for four additional soils over a range of initial water contents, as summarized in table 3.3. It shows that the revised solution is capable of accommodating the effect of the water table and the maximum relative error is consistent with that of the traditional GA model (i.e. the differences here are on par with the standard GA and numerical solution to RE). Notice that the shallower the water table is, the smaller the error in cumulative flux, $E_F$, is, which indicates that equation 3.19 is suitable for shallow water table boundary conditions.

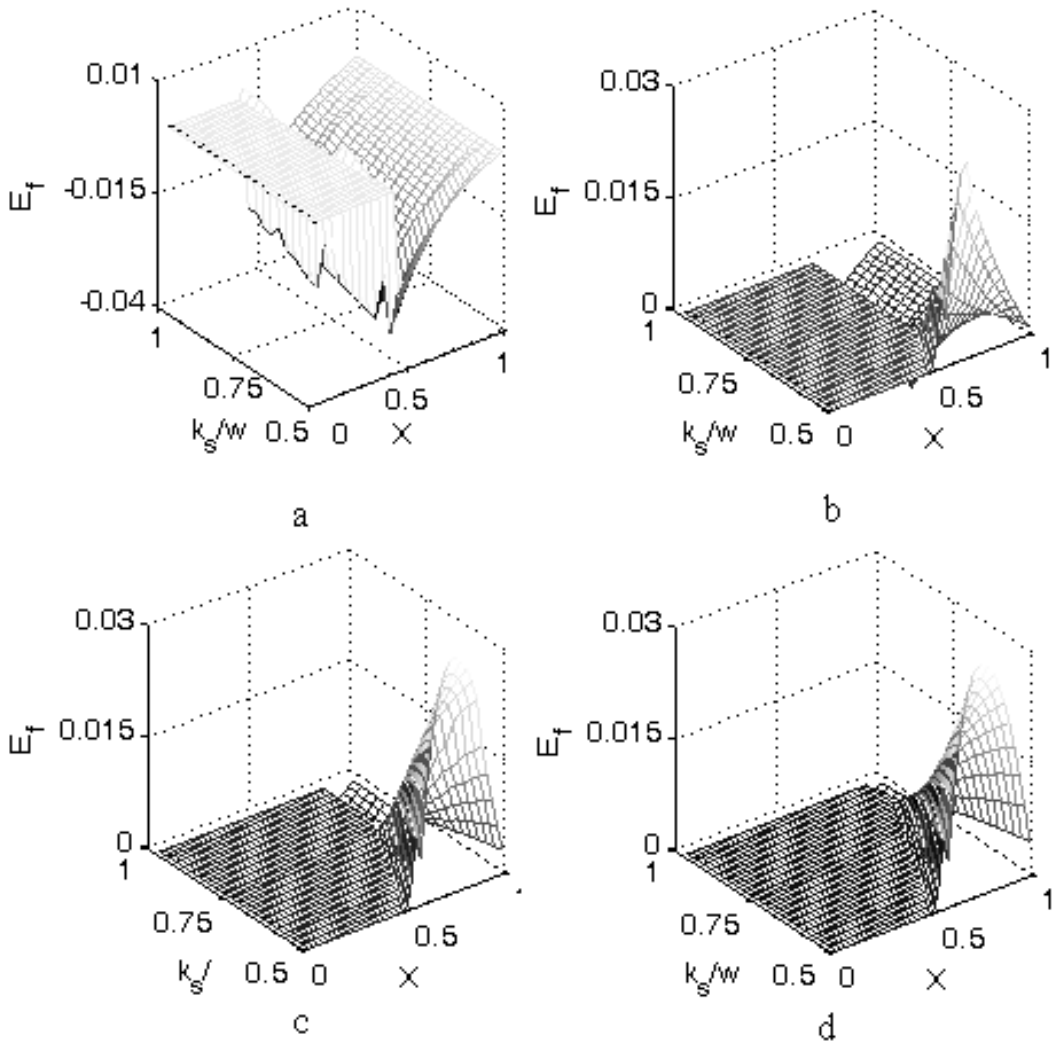


Figure 3.12: Relative error for the modified GA cumulative infiltration for the existence of a water table at dimensionless depth of: a) 1/40; b) 1/20; c) 1/10; d) 1/5

Table 3.3: Maximum relative error ($E_F$) for modified/original GA with shallow water table

| $z_{D^*}$ | $\frac{\theta_0}{\theta_s}$ | Sand | Loamy sand | Sandy loam | Silt loam |
|---|---|---|---|---|---|
| 1/40 | 0.6 | 0.027/0.241 | 0.024/0.241 | 0.020/0.240 | 0.018/0.239 |
| | 0.7 | 0.028/0.244 | 0.029/0.244 | 0.021/0.241 | 0.019/0.241 |
| | 0.8 | 0.059/0.251 | 0.055/0.258 | 0.034/0.243 | 0.027/0.244 |
| | 0.9 | 0.303/0.329 | 0.253/0.361 | 0.256/0.350 | 0.144/0.281 |
| 1/20 | 0.6 | 0.030/0.134 | 0.025/0.130 | 0.019/0.132 | 0.017/0.132 |
| | 0.7 | 0.038/0.132 | 0.033/0.132 | 0.026/0.132 | 0.020/0.129 |
| | 0.8 | 0.061/0.131 | 0.057/0.133 | 0.054/0.127 | 0.036/0.130 |
| | 0.9 | 0.071/0.154 | 0.097/0.159 | 0.055/0.148 | 0.063/0.137 |
| 1/10 | 0.6 | 0.033/0.065 | 0.027/0.065 | 0.020/0.065 | 0.017/0.065 |
| | 0.7 | 0.042/0.062 | 0.035/0.064 | 0.028/0.064 | 0.021/0.063 |
| | 0.8 | 0.078/0.078 | 0.066/0.066 | 0.060/0.061 | 0.040/0.061 |
| | 0.9 | 0.137/0.137 | 0.129/0.129 | 0.116/0.116 | 0.113/0.113 |
| 1/5 | 0.6 | 0.032/0.032 | 0.027/0.030 | 0.020/0.029 | 0.017/0.030 |
| | 0.7 | 0.042/0.042 | 0.036/0.036 | 0.026/0.029 | 0.020/0.029 |
| | 0.8 | 0.075/0.075 | 0.066/0.066 | 0.053/0.053 | 0.040/0.041 |
| | 0.9 | 0.135/0.135 | 0.128/0.128 | 0.117/0.117 | 0.111/0.111 |

### Impermeable Base

Many shallow soils sit upon a relatively impermeable base, such as a frost table, bedrock, or a low permeability soil layer. This depth can vary in both space and time (e.g. due to variations in temperature with the frost table or bedrock topography). When an impermeable base is present, the wetting front progresses downwards until it reaches the bottom of the soil column, at which point, infiltration is forced to cease. This threshold can drastically decrease the percentage of rainfall infiltrating, and is ignored in the traditional GA. There-

fore, neglecting the effect of the impermeable base is detrimental to appropriate runoff separation in hydrological models that use the traditional GA model.

The appropriateness of the standard GA model was assessed for the presence of an impermeable base at dimensionless depths of $z_D^*$ =1/40, 1/30, 1/20, 1/10,and 1/5. Results are shown in Figure 3.13. Here, the applicability of the GA model is defined in the same manner as in the previous section.

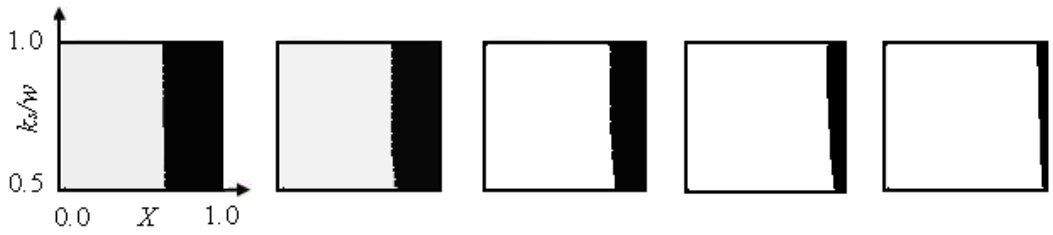


Figure 3.13: Applicability of the GA model with variable dimensionless impermeable base depth (Left to right: 1/40,1/30,1/20, 1/10, and 1/5): Light-applicable; Dark non-applicable

Figure 3.13 indicates that, as with the presence of a water table, the validity of the GA model is limited by the presence of an impermeable base. The separation between the applicable and inapplicable regions is roughly at the moment at which the wetting front location approaches the impermeable base. As expected, the GA validity increases with increasing impermeable base depth. Figure 3.14 depicts the infiltration rate behavior for selected dimensionless conductivities for an impermeable base located at the dimensionless depths of 1/40, 1/20 , 1/10, and 1/5. It is clear that the dimensionless infiltration rate abruptly approaches zero when the wetting front reaches the impermeable base.

Similar to the approach used with the water table case, a modified GA solution which accounts for the existence of the impermeable base is here developed as:

$$\frac{f(t)}{w} = \begin{cases} 1 & \text{for } F < (\theta_s - \theta_0)z \text{ and } X \leq X_p \\ \frac{k_s}{w}\left(1 + \dfrac{1}{-1 - W_{-1}(x)}\right) & \text{for } F < (\theta_s - \theta_0)z \text{ and } X > X_p \\ 0 & \text{for } F \geq (\theta_s - \theta_0)z \text{ and } X > X_p \end{cases} \tag{3.20}$$

Equation 3.20 indicates that infiltration ceases when the wetting front reaches the impermeable base. Note that $z$ denotes the impermeable base depth, and, unlike the case

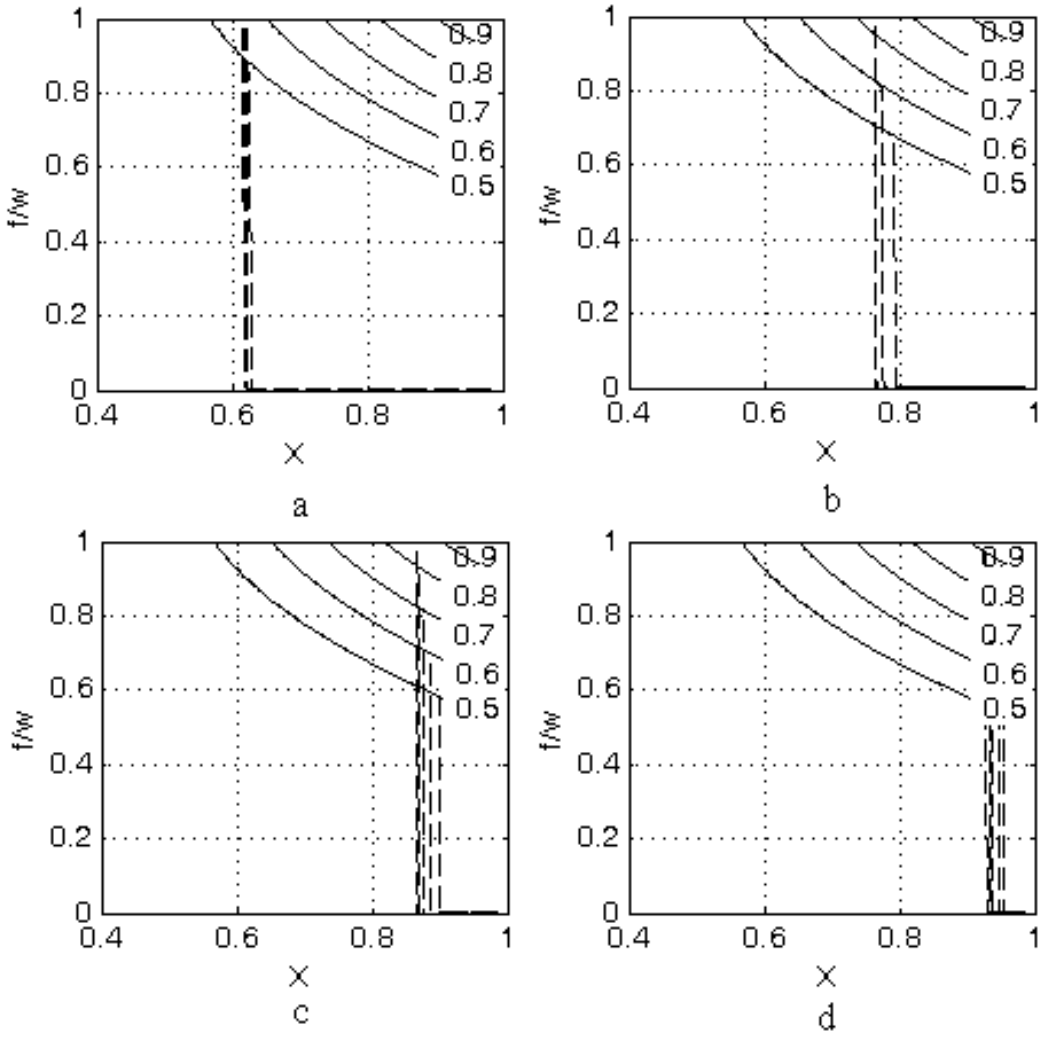


Figure 3.14: Dimensionless infiltration rate, $f/w$, as a function of dimensionless time, $X$, for variable dimensionless conductivity $k_s/w$ (0.5-0.9): solid-RE with dimensionless impermeable base depth at 1.0; dash-RE with dimensionless impermeable base depth at: a): 1/40; b): 1/20; c): 1/10; d): 1/5

of a water table, no corrections are needed to deal with boundary effects that accelerate the wetting front. For a very shallow impermeable base, $F$ can be larger than $(\theta_s - \theta_0)z$ at the ponding time, e.g., the wetting front approaches the impermeable base before the

ponding time is reached. Equation 3.20 is then rewritten as:

$$\frac{f(t)}{w} = \begin{cases} 1 & \text{for } F \geq (\theta_s - \theta_0)z \text{ and } X \leq X_p \\ 0 & \text{for } F \geq (\theta_s - \theta_0)z \text{ and } X > X_p \end{cases}$$

Relative errors of this modified GA model, as compared to the RE model, are shown in Figure 3.15.

Figure 3.15 shows that the revised GA solution is capable of capturing the behavior of the numerical model with an impermeable base and the maximum relative error is consistent with that of the traditional GA model. Maximum relative errors (assessed over the complete spectrum of times and dimensionless rainfall rates) for all four soils with multiple initial water contents are depicted in table 3.4. It is clear that the $E_F$ decreases with a decreasing impermeable base depth, indicating that the approximation actually improves as the shallow impermeable boundary condition approaches the ground surface.

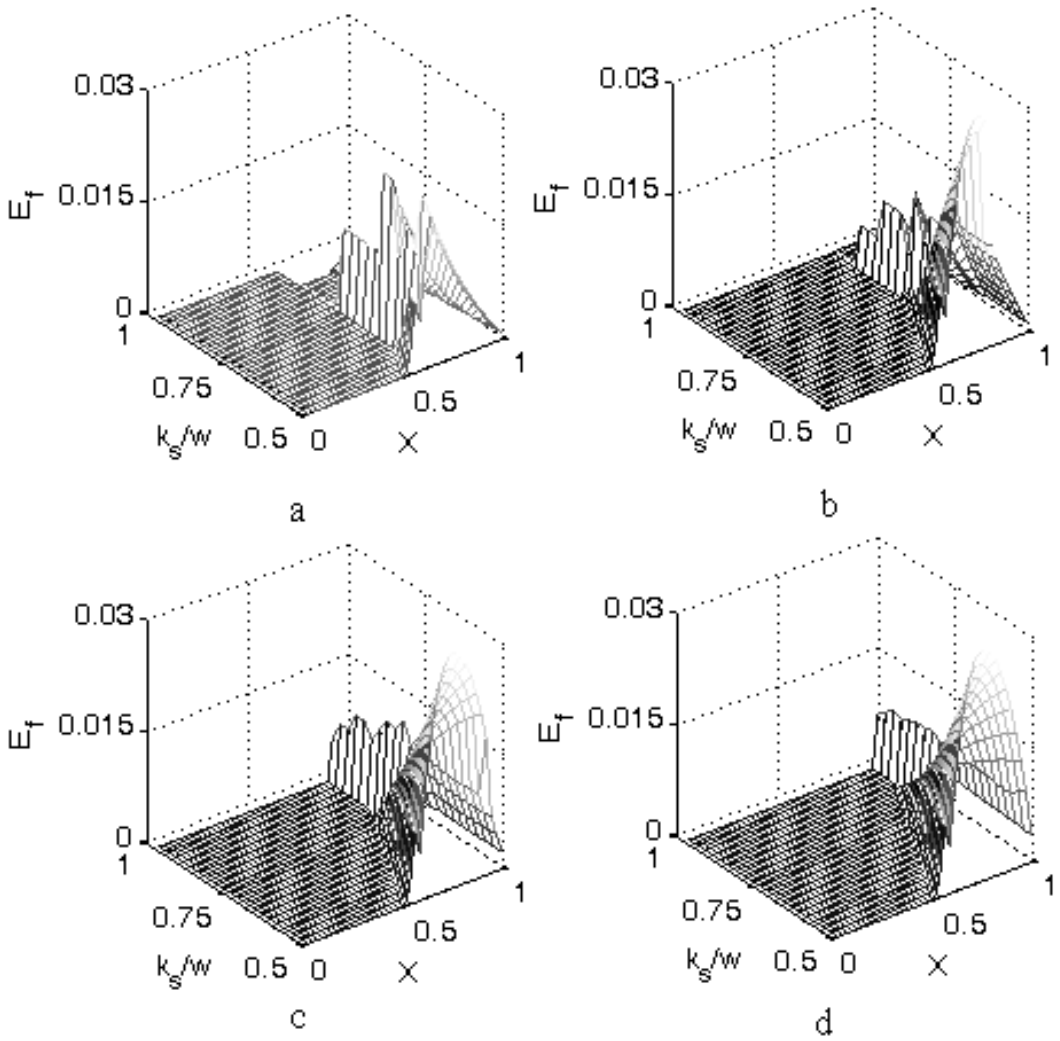


Figure 3.15: Relative error for the modified GA cumulative infiltration for the existence of an impermeable base at dimensionless depth of: a) 1/40; b) 1/20; c) 1/10; d) 1/5

Table 3.4: Maximum relative error ($E_F$) for modified/original GA with impermeable base

| $z_{D^*}$ | $\frac{\theta_0}{\theta_s}$ | Sand | Loamy sand | Sandy loam | Silt loam |
|---|---|---|---|---|---|
| 1/40 | 0.6 | 0.027/0.951 | 0.023/0.972 | 0.018/0.972 | 0.018/0.972 |
| | 0.7 | 0.033/0.961 | 0.027/0.972 | 0.030/0.972 | 0.019/0.972 |
| | 0.8 | 0.046/0.963 | 0.062/0.974 | 0.067/0.973 | 0.044/0.973 |
| | 0.9 | 0.181/0.976 | 0.199/0.979 | 0.199/0.977 | 0.197/0.978 |
| 1/20 | 0.6 | 0.033/0.910 | 0.028/0.945 | 0.020/0.945 | 0.017/0.945 |
| | 0.7 | 0.033/0.919 | 0.035/0.946 | 0.031/0.945 | 0.021/0.945 |
| | 0.8 | 0.067/0.922 | 0.068/0.949 | 0.060/0.947 | 0.048/0.946 |
| | 0.9 | 0.128/0.951 | 0.181/0.955 | 0.199/0.957 | 0.139/0.953 |
| 1/10 | 0.6 | 0.033/0.827 | 0.028/0.891 | 0.020/0.891 | 0.017/0.891 |
| | 0.7 | 0.041/0.836 | 0.035/0.892 | 0.029/0.891 | 0.021/0.891 |
| | 0.8 | 0.067/0.839 | 0.066/0.894 | 0.060/0.893 | 0.047/0.893 |
| | 0.9 | 0.140/0.899 | 0.135/0.908 | 0.116/0.904 | 0.113/0.902 |
| 1/5 | 0.6 | 0.033/0.670 | 0.028/0.783 | 0.020/0.783 | 0.017/0.782 |
| | 0.7 | 0.041/0.785 | 0.034/0.785 | 0.029/0.783 | 0.021/0.783 |
| | 0.8 | 0.066/0.787 | 0.058/0.785 | 0.053/0.784 | 0.041/0.784 |
| | 0.9 | 0.142/0.793 | 0.128/0.803 | 0.117/0.799 | 0.111/0.791 |

**Heterogeneity Variation**

Soil heterogeneity is very important in hydrologic processes, especially in determining surface and subsurface runoff separation. The most important source of heterogeneity for the infiltration process is the saturated hydraulic conductivity, which is often considered well-represented as a random variable with a lognormal distribution ([59]and [151]). Here, the impact of vertical heterogeneity in saturated conductivity was investigated with regard to how it may impact the appropriateness of GA.

A Monte Carlo approach was used to sample the dimensionless hydraulic conductivity for each pair of a given mean, $\bar{k}$, and variance, $\sigma$. The mean is the dimensionless conductivity with a wide range of 0.5 to 1.0. The variance was set to 0.1, 0.2, 0.3, 0.4, and 0.5. For each individual mean/variance pair, 20 realizations of Monte Carlo are used to obtain the average behaviors of the RE solution. Figure 3.16 shows the appropriateness of GA for five different variances. It shows that the GA applicability decreases with increasing vertical heterogeneity, expressed in terms of the standard deviation, $\sigma$, of the vertical averaged saturated conductivity. The separation is worst around the ponding time since the maximum relative error occurs there.

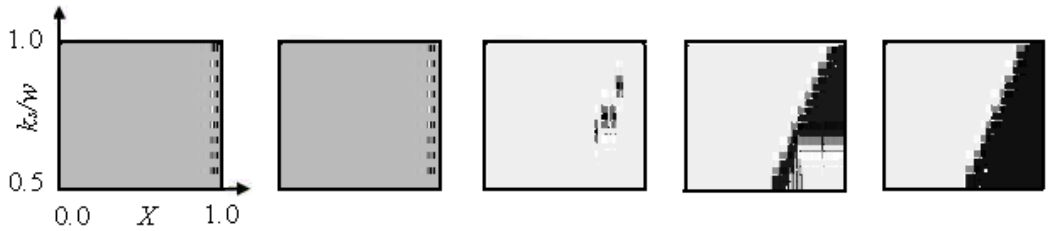


Figure 3.16: Applicability of GA model with variable variance for the vertical heterogeneity in saturated conductivity (Left to right: $\sigma$=0.1, 0.2, 0.3, 0.4, and 0.5): Light-applicable; Dark-non-applicable

Notice that in Figure 3.16, for $\sigma = 0.4$, there are portions applicable after the distinguished separation between the applicable and inapplicable regions. This is due to the difference between the RE with and without heterogeneity decreases with the dimensionless time $X$. It decreases into GA applicable range after the ponding time, which can be seen in Figure 3.17 for a dimensionless hydraulic conductivity of 0.5 with $\sigma = 0.4$. Figure 3.17 is the comparison of dimensionless infiltration rate for different variances. It shows the infiltration curves for the heterogeneous vertical hydraulic conductivity are relatively smooth compared to the existence of a water table and impermeable base, i.e. no obvious turning point occurs.

Figure 3.18 is the relative error between the GA solution and the RE solution with variable variances. An interesting phenomena seen here is that, although the heterogeneity was not considered in the traditional GA model, the model is capable of reproducing the RE with vertical heterogeneous behavior of the RE. The relative error between GA and RE increases with an increasing standard deviation. The maximum $E_f$ is kept to be 8 percent when $\sigma$ is less than 0.5 and is 12 percent with a 0.5 variance. Therefore, modifications to

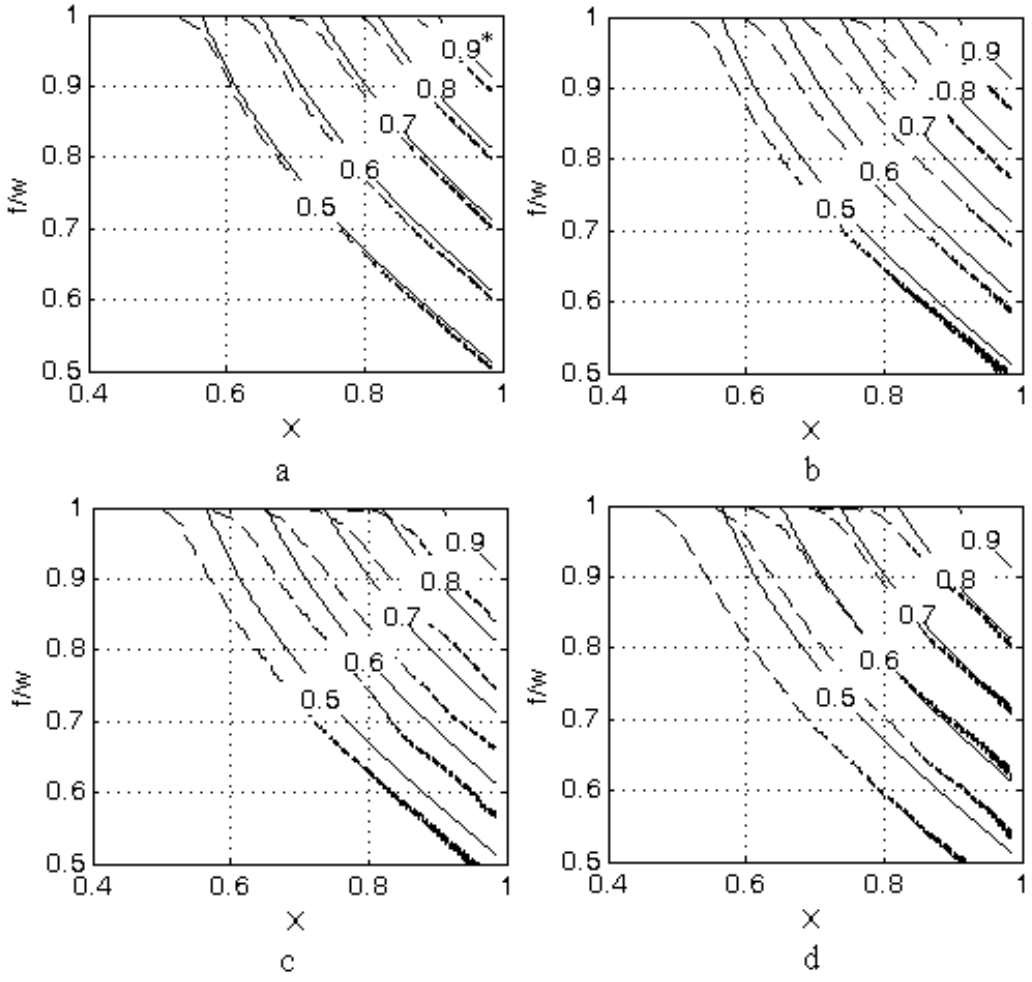


Figure 3.17: Dimensionless infiltration rate, $f/w$, as a function of dimensionless time, $X$, for variable dimensionless conductivity $k_s/w$: solid-RE with homogenous hydraulic conductivity; dash-RE with vertical hydraulic conductivity variance of: a): 0.2; b): 0.3; c): 0.4; d): 0.5

the GA model are deemed unnecessary if the standard deviation of the vertical hydraulic conductivity is less than 0.5.

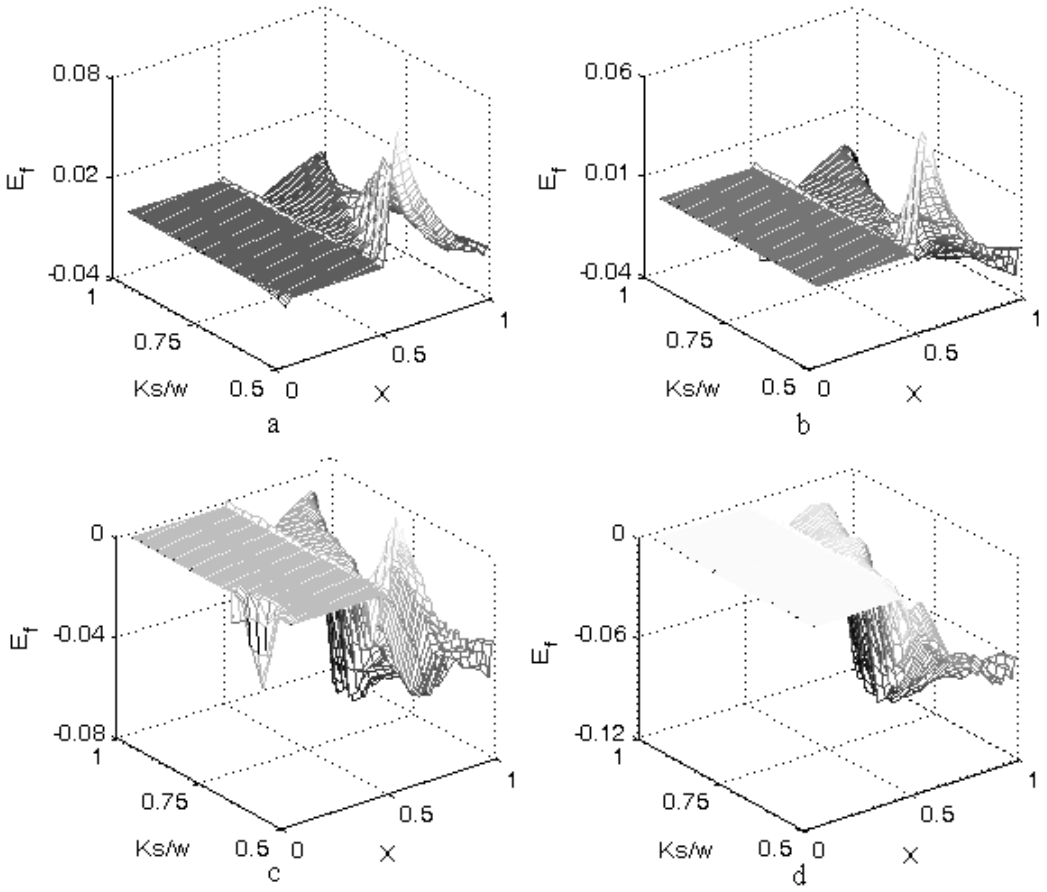


Figure 3.18: Relative error for the infiltration rate between the GA and the RE at: a) $\sigma = 0.2$; b) $\sigma = 0.3$; c) $\sigma = 0.4$; d) $\sigma = 0.5$

### 3.2.3 Discussion

Three assumptions limiting the applicability of the traditional GA model have been addressed and discussed here. Corresponding revisions were proposed. Results show that ignoring shallow boundary conditions in the traditional GA will lead to an overestimation of the amount of infiltrated water. As a result, hydrological models that rely upon the traditional GA infiltration model may improperly estimate runoff. For such hydrological models, modifications to the GA model are necessary in order to obtain an accurate water budget in domains with shallow overburden or a shallow water table. 'Effective' hydraulic

conductivities estimated using manual or automatic calibration may be compensating for this effect, leading to smaller-than-expected hydraulic conductivity estimates. If these conductivities are used elsewhere in the model (e.g., for baseflow or interflow calculation), accurate estimates of other hydrological fluxes may potentially be compromised.

Although the simple modifications recommended here provide satisfactory results for a wide range of soil types and parameters, further verification with experiments and observations is likely needed. For example, the water table depth is dynamic during the infiltration process, and GA initial conditions are not truly consistent with the presence of a capillary fringe. The effect of this phenomenon on infiltration is worthy of further investigation. Only vertical heterogeneity in saturated conductivity is considered here, and the variance is constrained within 0.5. Heterogeneity in initial water content or other soil parameters could also lead to inadequacy of the GA model. All these effects can be investigated in future work.

## 3.3 Runoff-infiltration Partitioning Using an Upscaled Green-Ampt Solution

Note: Much of this section appears in Craig et al. [38].

Of critical importance in hydrological modeling is the determination of infiltration rates into saturated and unsaturated soils. The quantity of infiltration determines the amount of water available for runoff, evaporation, root uptake, and recharge to the groundwater beneath. In the previous section, it was seen that vertical heterogeneity is important but horizontal is too. In detailed physically-based models (e.g., SHE [1]), heterogeneous infiltration processes may be simulated to a high degree of precision by numerically solving Richards equation. For regional-scale lumped models and land surface schemes, however, computational expediency and lack of detailed soil data demands that researchers use a more approximate parameterization of the runoff-infiltration partitioning relationship. Many existing models (e.g., CLASS [141], WEPP [103], HSPF [20], or SWAT [99]) use the Green-Ampt equation [60] for these purposes. Because the Green-Ampt (GA) infiltration equation is an analytical solution to Richards equation, the physical meaning of model parameters ostensibly correspond to soil properties that are measurable in the field. A critical drawback of the approach is that it does not explicitly account for the inevitable heterogeneity at the subbasin (or computational) scale, which has been shown to have a significant impact upon the response of a watershed soils to a rainfall event ([117]; [42]).

Recognizing that heterogeneity of saturated hydraulic conductivity is a significant driver of net basin infiltration, researchers have attempted to develop general upscaled expressions for infiltration based upon direct upscaling of point-scale governing equations [29] or of point-scale infiltration solutions ([87]; [40]; [119]; [120]; [59]). These expressions were of varying complexity, with later extensions addressing complex lateral relationships such as run-on [37], spatial correlation [59], and rainfall variation [93]. While all are theoretically sound within the bounds of their assumptions, these solutions individually suffer from an inability to closely match computational (i.e., Monte Carlo) solutions for the complete range of soil textures, as demonstrated by Corradini et al. [37]. This, in part, is due to lower-order approximations used for the Green-Ampt equation at the point scale (e.g., that of [107]) or empirical approximations that have not been tested under the full range of parameters ([120]; [59]). Most of the approaches additionally require some form of series expansion, Monte Carlo simulation, numerical integration, or Latin Hypercube sampling in order to generate the expected value of infiltration rates ([40]; [59]; [37]), and may perhaps be considered too complex to include in many land surface schemes.

Here, an alternative direct method for upscaling the Green-Ampt solution for laterally

heterogeneous soils is presented, one based upon a new and accurate approximation of the explicit GA solution. The author has developed expressions for variable $\alpha$, which can be used to represent variation in initial saturation, porosity, and/or wetting front matric potential. This supplements similar algorithms developed by Dr. Craig (personal communication). Results are compared to Monte Carlo simulations of spatially random infiltration without run-on.

### 3.3.1 Upscaling Green-Ampt Infiltration Model

Craig et al. [38] developed a new set of formulae for calculating regional-averaged infiltration rates into heterogeneous soils with heterogeneous initial conditions. The solutions are based upon an upscaled approximation of the explicit Green-Ampt infiltration solution, and requires specification of the saturated hydraulic conductivity distribution and/or initial soil water deficit distribution in the subbasin. The portion of this paper developed by the author addressed the variability of initial conditions. The resultant closed-form averaged infiltration equations are easily integrated into existing distributed surface water schemes, and can also be used to calculate saturated soil surface area.

While most discussions of the Green-Ampt solution focus on the evolution of infiltration rates over time, it is revealing to plot infiltration rates as a function of conductivity, as shown in Figure 3.19. Here, the dimensionless time parameter [38], $X$, is used as independent variable.

The curves in this Figure are snapshots in time: for a given conductivity, the infiltration rate decreases with increasing $X$ from $f(0) = w$ to $f(1) = k_s$. The objectives of this section are to first identify appropriate (integrable) approximations for these curves, then to use these approximates in order to develop closed-form explicit expressions for mean infiltration rate subject to a known distribution of saturated conductivity and/or a known distribution of $\alpha$.

Once a reasonable approximation for the infiltration rate as a function of conductivity is found (i.e., a simple approximation of the curves in Figure 3.19 is obtained), the mean infiltration rate for heterogeneous media and/or heterogeneous initial conditions may be obtained by application of simple statistical laws. For example, in the case of heterogeneous conductivity only, the mean infiltration rate, $\bar{f}$, may be calculated as:

$$\bar{f}(t) = \int_0^\infty f(t, k_s) \cdot f_k(k_s) dk_s \tag{3.21}$$

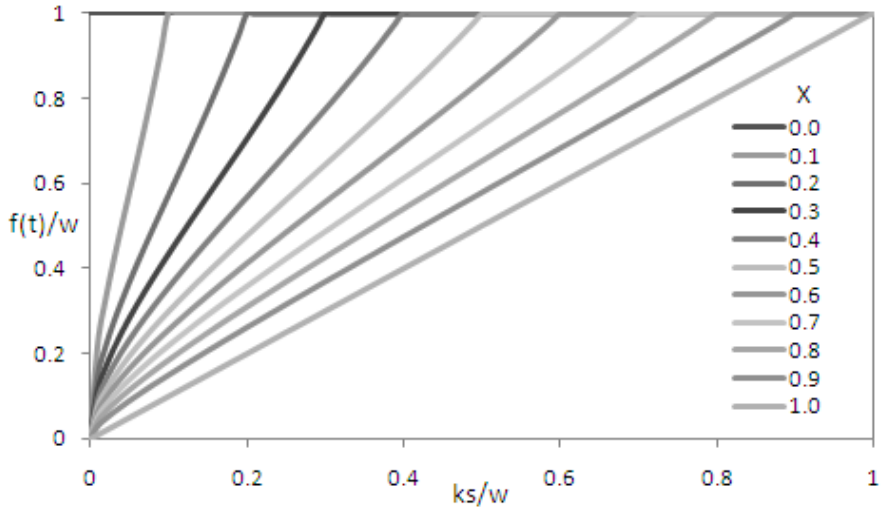


Figure 3.19: Dimensionless Green-Ampt infiltration rate as a function of dimensionless conductivity. Individual curves correspond to snapshots of dimensionless time, $X$, which progresses from $X = 0$ at $t = 0$ to $X = 1$ at $t = \infty$. These curves are independent of the $\alpha$ parameter, which is wholly encapsulated in the dimensionless time parameter, $X$.

where $f_k$ is the frequency distribution of saturated hydraulic conductivity within the modeled domain, represented here using a standard lognormal distribution:

$$f_k(k_s) = \frac{1}{k_s \sigma_Y \sqrt{2\pi}} \exp\left(-\frac{(\ln(k_s) - \mu_Y)^2}{2\sigma_Y^2}\right) \tag{3.22}$$

where $\mu_Y$ and $\sigma_Y$ are the mean and standard deviation of log hydraulic conductivity. A more general expression is available for the case of general variability in both conductivity, initial moisture deficit, and/or wetting front matric potential:

$$\bar{f}(t) = \int_0^\infty \int_0^\infty f(X(t,\alpha), k_s) \cdot f_{k\alpha}(k_s, \alpha) d\alpha dk_s \tag{3.23}$$

where $f_{k\alpha}$ is the joint probability distribution of saturated conductivity and $\alpha$. It is assumed here that there is no lateral relationship between vertical soil columns, either statistically (in the form of spatial correlation) or physically (in the form of run-on processes). The implications of these assumptions are addressed elsewhere ([37]; [93]).

### 3.3.2 Approximations to the $f$-$k_s$ Curves

While usually expressed in implicit form, the Green-Ampt solution may be expressed explicitly in terms of the Lambert $W_{-1}(x)$ function, as described in chapter 2, section 3.

Barry et al. [5](amongst others) have used this in order to develop a family of robust numerical approximants to the explicit Green-Ampt solution. While the approximations developed by Barry et al. are highly accurate and simple to implement (and therefore recommended for use in standard Green-Ampt modeling schemes), they cannot be used to calculate mean infiltration rates in the fashion presented here. The primary issue is the complexity of these approximations with respect to $k_s$ or $\alpha$, which precludes the availability of closed-form expressions for mean infiltration rates using equation 3.21 and 3.23.

Here, the author in conjunction with her supervisor Dr. Craig, has identified an alternative approximation to equation 2.21 that are more amenable to closed-form integration with respect to both $k_s$ and $\alpha$. It is clear from Figure 3.19 that a first-order approximation of infiltration rate may be given by the linear approximation:

$$f(t) = \min\left(w, \frac{k_s}{X}\right) + \epsilon(k_s, X) \tag{3.24}$$

where $\epsilon(k_s, X)$ is the deviation of the exact solution from the linear approximation, plotted in Figure 3.20. The linear approximation of equation 3.24, which corresponds to $W_{-1}(x) \approx -\frac{w}{t} - 1$, is exact at the endpoints ($k_s = 0$ and $k_s \geq X$), and diminishes in quality for reduced ratios of conductivity to rainfall rate. As apparent in Figure 3.20, an error of up to $\approx 13.5\%$ is possible for small conductivities at early times. Equation 3.24 will be used as the starting point for the approximation used here, and an attempt is made to identify viable (and integrable) approximations to $\epsilon(X, k_s)$.

Upon substitution of equations 3.22 and 3.24 into equation 3.21, the first-order contribution to the mean infiltration rate may be directly evaluated using basic calculus, leading to the following first approximation for average infiltration (Craig, personal communication):

$$\begin{aligned} \bar{f}(t) &= \frac{w}{2}\operatorname{erfc}\left(\frac{\ln(wX) - \mu_Y}{\sigma_Y\sqrt{2}}\right) \\ &+ \frac{1}{2X}\exp\left(\mu_Y + \frac{\sigma_Y^2}{2}\right)\operatorname{erfc}\left(\frac{\sigma_Y}{\sqrt{2}} - \frac{\ln(wX) - \mu_Y}{\sigma_Y\sqrt{2}}\right) \\ &+ w\int_0^{X(t)} \epsilon(X(t), k_s) \cdot f_k(k_s) dk_s \end{aligned} \tag{3.25}$$

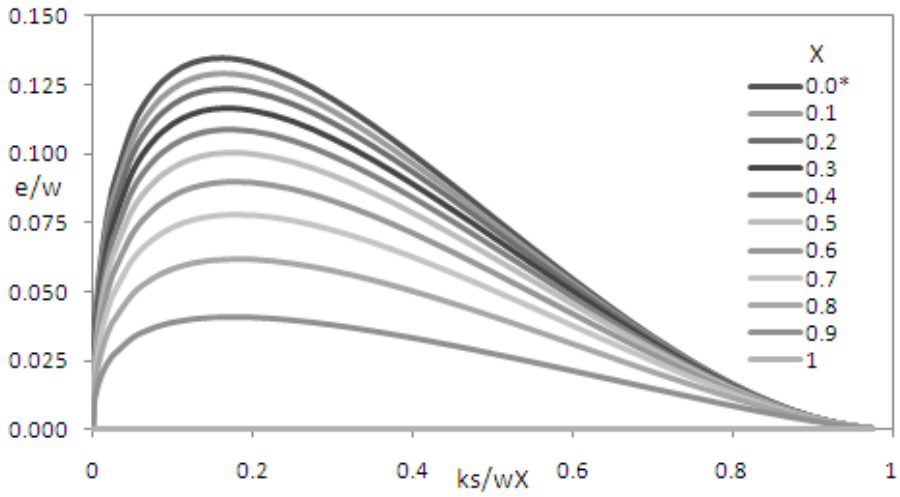


Figure 3.20: Dimensionless epsilon (linear approximation error) as a function of dimensionless conductivity, stretched over the dimensionless ponding time, $X$. The error is at a maximum at early times, diminishing to zero. The curve labeled $0.0^*$ is the limit of $\epsilon$ as $X$ approaches zero.

where $\text{erfc}(x)$ is the complementary error function, expressed in terms of the error function $\text{erf}(x)$ as:

$$\text{erfc}(x) = 1 - \text{erf}(x) = \frac{2}{\sqrt{\pi}} \int_x^\infty e^{t^2} dt$$

and the remaining epsilon term still must be evaluated numerically. The $\epsilon$ function was here approximated using curve fitting techniques. The "true"surface used for fitting was generated using the iterative approximation of [5]. The best approximation found was given by:

$$\epsilon \approx 0.3632 \cdot (1 - X)^{0.484} \left(1 - \frac{k_s}{wX}\right)^{1.74} \left(\frac{k_s}{wX}\right)^{0.38} \tag{3.26}$$

resulting in a maximum error of $0.006w$ (0.6% error), acceptable for nearly all modeling applications, especially considering the errors from ignoring heterogeneity are significantly larger. With this approximation, the remaining integral in equation 3.25 can be evaluated quite effectively with simple single-interval 2-point Gauss quadrature.

Figure 3.21 depicts the difference in behavior between the standard GA model and the upscaled version used here for a number of different mean dimensionless conductivities

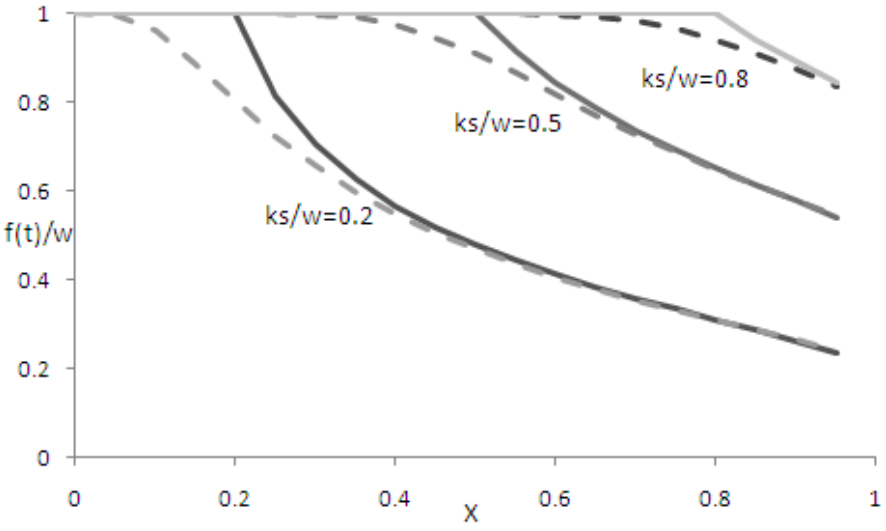


Figure 3.21: Evolution of dimensionless infiltration rate over time for standard (solid) and upscaled (dashed) Green-Ampt solutions. Three different ratios (0.2,0.5,0.8) of average conductivity to rainfall are depicted. The coefficient of variation ($\bar{k}_s/\sigma_k$) for all three upscaled models was kept fixed at 0.5.

with the same coefficient of variation. Notably, the upscaling process smooths out the threshold behavior of the basin, as the ponding time is no longer a fixed point in time. Rather, different locations in space reach saturation at different points in time. Regardless of the degree of heterogeneity, the cumulative infiltration (which is linked with the total volume under the curve) is less than that predicted with the point scale solution. A detailed discussion for the spatial variability in hydraulic conductivity and its effect on the hydrological models can be found in [38]. The primary contribution of the author to the investigation of the heterogeneity was developed using upscaled expressions for variability in soil moisture/wetting front suction, as discussed in what follows.

### 3.3.3 Variable Initial Soil Moisture /Wetting Front Suction

Unlike conductivity, which is known to be well-represented using a log-normal distribution, spatial variation of the aggregate parameter $\alpha = \psi_f|\theta_s - \theta_0|$ is not well-characterized in the literature. The wetting front matric potential, $\psi_f$, is a function of soil texture and

the form of the characteristic soil curves [100], and is therefore correlated to conductivity. It varies roughly linearly with log conductivity, ranging from about 10cm for sands up to 100cm for clays, and can be reasonably well characterized with a normal distribution. Presumably, the initial saturation deficit, $S_d = |\theta_s - \theta_0|$ can also be represented using a normal distribution [106], but due to the presence of fixed upper and lower bounds is likely better represented using a Beta or uniform distribution ([62]; [139]). Multiple field studies of soil moisture distributions have discovered wildly varying distributional characteristics, depending upon characteristics as varied as soil texture, storm duration, vegetation, soil organic content and season ([117]; [90]; [92]; [49]; [77]). Due to the large variation in infiltration behavior from site to site, and the significant number of unknown correlations between variables, it is likely impossible in this case to choose one correct distribution of $\alpha$. Instead, we will assume here for the purpose of mathematical simplicity that $\alpha$ is appropriately represented with a normal distribution characterized by a mean $\mu_\alpha$ and standard deviation $\sigma_\alpha$. To avoid non-negativity, it is recognized that the negative portion of the distribution corresponds to a finite probability of $\alpha$ being equal to zero (i.e., the area under the negative portion of the normal distribution corresponds to the percentage of soil is initially saturated). It is assumed that these distribution parameters may be either calibrated or estimated from known or approximated distributions of $\psi_f$, $\theta_i$, and $\theta_s$. Under these conditions, the function $1/X$ also satisfies a normal distribution, and we are able to once again obtain a simple formula for $f(t)$ subject to a distribution of soil properties, in this case variability in initial moisture content and/or wetting front potential subject to a fixed hydraulic conductivity:

$$\begin{aligned}
\bar{f}(t) &= \frac{w}{2} + \frac{w}{2}\operatorname{erfc}(A) + k_s\left(1 - \operatorname{erf}(B)\right) \\
&+ k_s\left(1 + \frac{\mu_\alpha}{wt}\right)\frac{1}{2}\left[\operatorname{erf}(B) - \operatorname{erf}(A)\right] \\
&+ \frac{k_s}{wt}\frac{\sigma_\alpha}{\sqrt{2\pi}}\left[\exp(-B^2) - \exp(-A^2)\right] \\
&+ w\int_0^{(\frac{w}{k_s}-1)wt} \epsilon(X(\alpha,t),k_s) f_\alpha(\alpha) d\alpha
\end{aligned} \tag{3.27}$$

where $A = (\mu_\alpha - (w/k_s - 1)wt)/(\sqrt{2}\sigma_\alpha)$ and $B = \mu_\alpha/(\sqrt{2}\sigma_\alpha)$. The limit of this expression as $\sigma_\alpha \to 0$ is the original expression from equation 3.24.

Both solutions (equations 3.25 and 3.27) are unique when compared to previous solutions proffered in the literature. First, they are valid over the entire range of parameters and times. They correctly converge upon the standard GA solution in the limit as $\sigma_Y$ and $\sigma_\alpha$ go to zero, a feat unattainable by the empirical approximations of Smith and

Goodrich[120] or Govindaraju et al.[59]. Lastly, because the solutions are cast in terms of the chosen dimensionless quantities, numerical integration of the $\epsilon$ integral is not sensitive to the particular set of parameters; any scheme that works appropriately in dimensionless space is appropriate for all possible model configurations. This, along with the relative simplicity of the solution, encourages inclusion in existing hydrological models.

### 3.3.4 Testing

To test the validity of the above derivations and demonstrate some of the interesting byproducts of the approach, the solution has been directly compared to the results of a Monte Carlo model. For the first test case, spatial heterogeneity in saturated hydraulic conductivity, results are shown in Figure 3.22 and discussion can be found in [38]. Here, the testing for spatial variability in initial soil moisture/wetting front suction, contributed by the author, are described only.

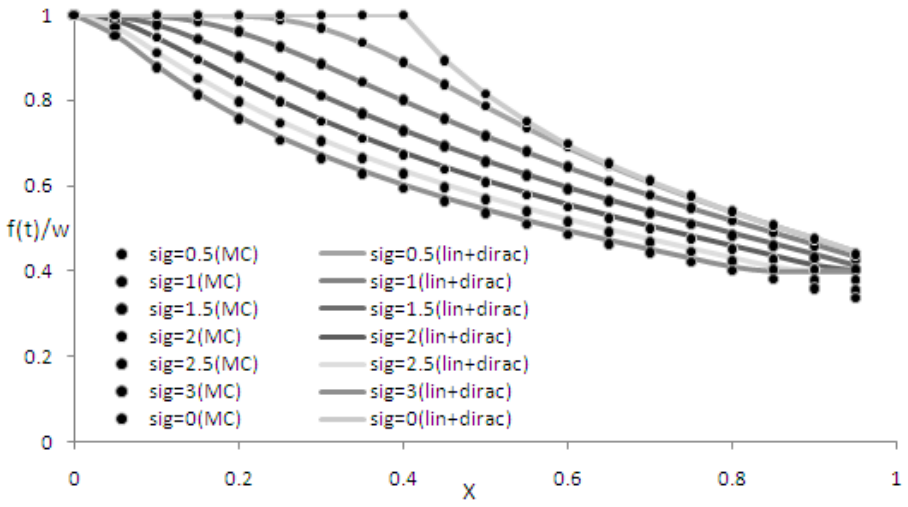


Figure 3.22: Analytical (solid line) and Monte Carlo (circles) dimensionless infiltration curves for a heterogeneous domain with an average conductivity of $\bar{k_s} = 1.6cm/hr$. Variability in conductivity is quantified using the normalized standard deviation of log-conductivity, $\sigma_Y$, which is here varied from 0 (homogeneous) to 3 (highly heterogeneous).

A heterogeneous domain was generated using 25000 parcels with aggregate parameter $\alpha$ that satisfy the normal frequency distribution with standard deviations of $\sigma_Y =$

$0.5, 1.0, 1.5, 2.0, 2.5$, and 3.0, and mean of $\bar{\alpha} = 3.0cm$. Since only vertical processes are considered here, spatial correlation is ignored. For the Monte Carlo simulation, the dimensionless saturated hydraulic conductivity was specified as 0.4. A dimensionless rainfall of was applied to the domain, and the average and cumulative infiltration to the heterogeneous soil were calculated using both the Monte Carlo approach and equation 3.27. Results are depicted in Figure 3.23. It is clear that the analytical upscaling is a very good approximation to the Monte Carlo simulations: maximum errors were on the order of 3%, and are entirely due to the approximation of the $\epsilon$ term, which was integrated using a single interval modified 2-point Gauss-Legendre quadrature. For all practical purposes, the analytical and Monte Carlo solutions may be considered identical in output.

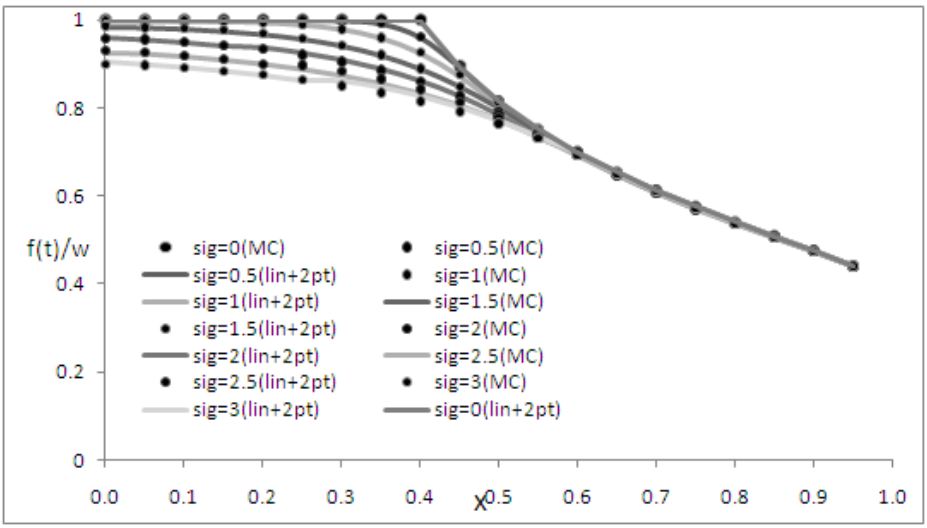


Figure 3.23: Analytical (solid line) and Monte Carlo (circle) dimensionless infiltration curves for a homogeneous domain with spatially variable initial conditions.

Here, the 2-point Gauss quadrature integration had to be modified in order to accurately calculate the integral in equation 3.27 to a sufficient degree of accuracy. The most computationally efficient and reasonably accurate means of calculating the integral in equation 3.27 was found to be a combination of two-point Gauss quadrature (for earlier times, where the impacts of scaling are dominant) and the non-upscaled Lambert approximation [5] (for later times, where upscaling has little or no effect but two-point quadrature can lead to numerical instabilities). Defining $X_c$ as the critical $X$ for the combination, the

modified two-point Gauss quadratic integration is defined as:

$$f(t) = \begin{cases} f_{2p} & \text{for } X \leq X_c \\ f_{Lambert} & \text{for } X > X_c \end{cases} \tag{3.28}$$

where $f_{2p}$ is the solution for single-interval two-point Gauss quadrature, $f_{Lambert}$ is the solution of the Lambert approximation, and $X_c$ is defined as:

$$X_c = \begin{cases} 0.45 & \text{for } \sigma \leq \frac{1}{3}\mu_\alpha \\ f_{Lambert} & \text{for } \sigma > \frac{1}{3}\mu_\alpha \end{cases} \tag{3.29}$$

An interesting byproduct of the upscaling formulation derived is that the evolution of saturated area, $A_s$, during a storm event may be determined as the total area of the basin, $A$, multiplied by the percentage of saturated ground at any point in time [38]:

$$A(t) = A \int_0^{(\frac{w}{k_s}-1)wt} \int_0^{wX} f_{k\alpha}(\alpha, K) dk_s d\alpha \tag{3.30}$$

Which, for a normal $\alpha$ distribution and fixed $ks/w$ leads to:

$$A(t) = \frac{A}{2}\left[\text{erf}\left(\frac{\mu_Y}{\sqrt{2}\sigma_\alpha}\right) - \text{erf}\left(\frac{\mu_\alpha - \left(\frac{w}{k_s} - 1\right)wt}{\sqrt{2}\sigma_\alpha}\right)\right] \tag{3.31}$$

The impact of $\alpha$ heterogeneity upon the saturation progress is depicted in Figure 3.24, for $k_s = 0.4w$ and $\bar{\alpha} = 3$. It illustrates the differences in the transient evolution of surface saturation for varying degrees of heterogeneity in $\alpha$. Instead of the abrupt switch from unsaturated to saturated surface predicted by the classic GA model, the upscaled version appropriately depicts a gradual transition, with some of the soil surface saturating well before the mean ponding time, and some (the soil with high lower soil moisture) staying perpetually dry. The evolution of this process spreads out as heterogeneity increases. Increased heterogeneity results in a more gradual saturation response. However, here the maximum saturation is reached after a finite time period, and the majority of saturation progress occurs after the average ponding time.

While the solution is only shown here for uniform steady rainfall, the approach of Chu [33] may still be used to extend both formulae to unsteady rainfall, as the upscaling approaches have been applied to the infiltration (rather than cumulative infiltration)

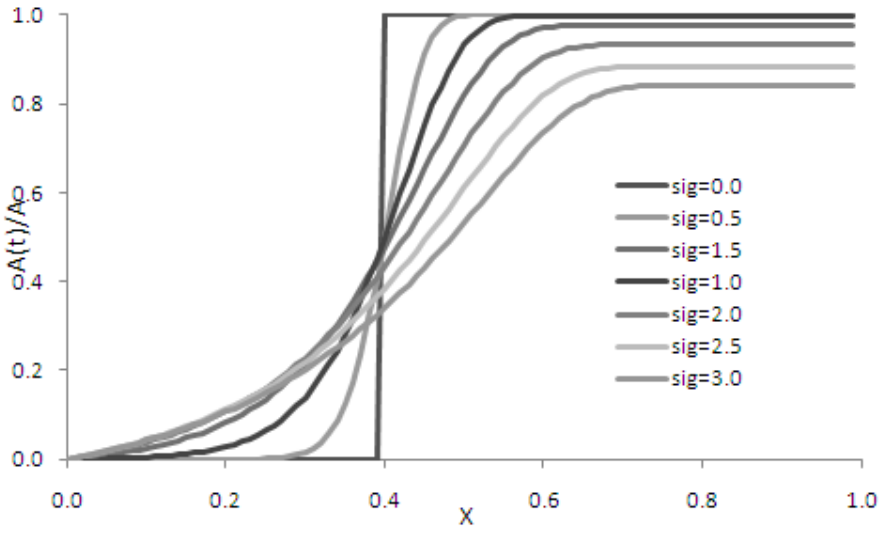


Figure 3.24: Evolution of basin surface saturation for various degrees of heterogeneity in $\alpha$

function. A notable corollary is that, for the variably saturated case, the spatially heterogeneous moisture deficit is a state-variable and changes with time (as would its variance). The change in this variance over time is neglected. Because of this, temporal discrimination has an impact upon the validity of the upscaling approximation. Of course, the homogeneous Green-Ampt model suffers from the same drawbacks, that while an analytical formula is available for infiltration, temporal discretization and time variability in soil moisture will lead to results that do not directly conform to the original analytical formula.

### 3.3.5 Discussion

As is apparent from results of Figures 3.22 and 3.23, the impact of spatial variability on Green-Ampt infiltration is both analytically calculable and significantly influential upon rainfall-runoff calculations. The implications of this heterogeneity have been addressed, in part, by previous authors. This discussion addressed the implications upon the calibration of existing homogeneous models.

As can be seen from comparing Figures 3.22 and 3.23, heterogeneity in $k_s$ has an effect upon the asymptotic solution as time approaches infinity, while variation in $\alpha$ is short-lived, only directly influencing the solution prior to and shortly after the effective (mean)

ponding time. This is an indicator that (1) heterogeneity in soil type is of much greater import than heterogeneity in initial conditions and (2) variation in initial conditions will be of greater importance for short duration storms or during dry antecedent conditions.

## 3.4 Chapter Summary

Multiple improvements to the modeling of infiltration processes have been investigated in this chapter, including accounting for shallow boundary conditions and both vertical and lateral heterogeneity in soil properties and initial conditions/wetting front suction. The improved algorithms have been tested using a specialized unsaturated finite difference code to the Richards' equation for sloping soils and Monte Carlo simulation. Results show that the improved algorithms are capable of addressing the effects they are intended to accommodate.

Applicability of the standard Green-Ampt infiltration model under the non-ideal conditions where a shallow water table or impermeable base is present was investigated using a novel dimensionless formulation. Results show, as one would expect, that the applicability of the GA model increases with increasing depth of the soil layer overlying a water table or impermeable base. Ignoring these shallow boundary conditions leads to inaccurate distribution of runoff. Modifications to the traditional GA model were presented and tested via rigorous comparison with the numerical solution to the RE for a wide range of soil textures and model parameters. The impacts of initial moisture deficit are wholly encapsulated within a special dimensionless parameter $X$, testing the full range of $X$ means that the full range of both times and moisture deficit/initial saturation have been tested. Results demonstrate that even when the assumptions are relaxed, the GA model often still provides reasonable results and can be easily amended to account for a variety of conditions. These amendments can be easily incorporated into existing distributed hydrological models. Once water table or impermeable base corrections are included, the maximum relative errors in cumulative infiltration are consistent with those between the original GA model and numerical (Richards' equation) solutions, and are reasonable for most practical applications.

In section 3.3, explicit approximations of the upscaled Green and Ampt infiltration equation have been derived, which consider lateral heterogeneity in wetting front matric potential, porosity, and/or initial soil moisture (equation 3.27). The approximations have been evaluated against Monte Carlo simulations and shown to produce results accurate to 3% of the computationally-intensive exact cases, at a computational cost similar to the original Green-Ampt formula without upscaling. The integrals obtained from the upscaling

process may be evaluated analytically or with single-interval low-order quadrature, and are therefore quite suitable for inclusion in land surface schemes and other surface water models where computational speed is a significant issue. A critical result here is that the upscaled form of the Green-Ampt equation is behaviorally different than the point-scale solution with upscaled parameters, indicating that calibration alone is insufficient to correctly replicate the infiltration process in heterogeneous media.

# Chapter 4

# Improved Interflow and Infiltration Algorithms for Hydrological Modelling

As discussed in chapter 2, most land surface schemes adopt a flat earth approximation, which does not allow near-surface lateral flow to occur. With this approximation, after a heavy rain, the land surface remains wet for a longer time than in reality. Thus the evaporation can be overestimated, whereas the infiltration can be underestimated. In reality, the earth is scarcely flat. Incorporating topographic characteristics into near surface flow modeling is very important for understanding the near surface hydrological processes. Although lateral flow has been considered in the hillslope hydrology literature, research has been primarily focused on lateral flow in the saturated zone and vertical flow in the unsaturated zone. However, for soils with macro pores and/or high anisotropy, lateral flow in unsaturated zone can play a significant role in near surface runoff processes. The interflow algorithm developed in this chapter is designed to account for lateral flow in both the saturated and unsaturated zones and to provide an improved recharge algorithm for hydrology-land surface schemes. It is physically-based and incorporates both soil hydraulic properties and topographic parameters. The improved interflow algorithm is used to calculate a dynamic saturated area that may then be used for calculation of more accurate partitioning between overland flow and infiltration. The algorithm was incorporated into the Environment Canada hydrology-land-surface model MESH and shown to successfully model a more realistic soil moisture simulation process.

## 4.1 Improvement to the Interflow Algorithm

The interflow algorithm used here as a basis for saturated area calculation was derived from a semi-analytical solution to the Richards' equation. The original semi-analytical solution, the one used as basis for the WATDRAIN1 algorithm, was developed by ignoring the suction gradient term in the Richards' equation. The flow generated is therefore gravity-dominated. Such a gravity-dominated solution works well for regions with wet soils but not suitable for regions that are dry for long periods. To compensate for this drawback, an updated interflow algorithm, WATDRAIN2, has been developed, which is a combination of the gravity dominated solution and the suction dominated steady state solution. Both interflow algorithms have been tested against numerical solutions to the Richards' equation, described in section 3.1. Results show an excellent match between analytical and numerical solutions under the conditions for which they are intended. The algorithm has therefore been deemed suitable for incorporation into hydrological models and land surface schemes.

### 4.1.1 WATDRAIN1 Development

The analytical interflow algorithm currently used in MESH focuses on laterally variable flow in shallow sloping soils. The sloping soil horizon is assumed to be homogeneous and subject only to lateral drainage through a downhill seepage face, as depicted in Figure 4.1.

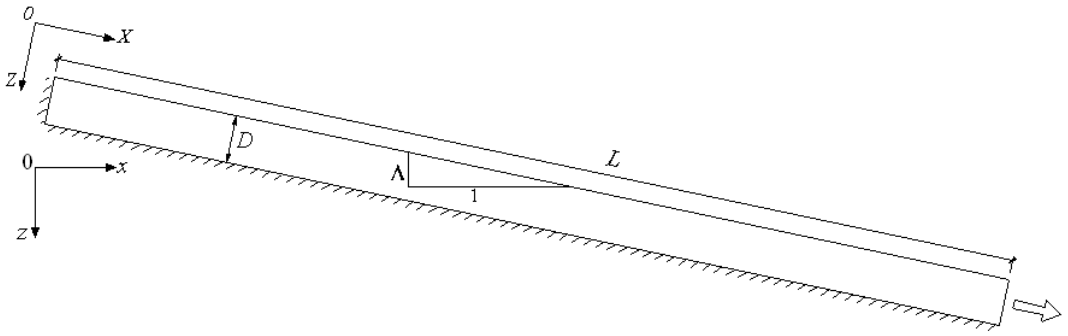


Figure 4.1: The conceptual model of a sloping soil horizon: initially at saturation and allowed to drain to field capacity [124]

The algorithm is based on several assumptions: The initial soil suction is equal to the

air entry pressure for a shallow sloping aquifer; Vertical variation in hydraulic conductivity can be described by an exponential function (following TOPMODEL [18]); Lastly, the suction gradient is assumed to be negligible, which results in an revised one-dimensional Richards' equation as:

$$\theta_s \frac{\partial s}{\partial t} = \frac{\Lambda}{\sqrt{1+\Lambda^2}} \frac{\partial k}{\partial X} \tag{4.1}$$

where $\Lambda$ denotes the slope of the aquifer and $s$ is saturation. Substituting the Clapp and Hornberger functions [34] gives:

$$\frac{\partial s}{\partial t} = -\frac{k_s \Lambda}{\theta_s \sqrt{1+\Lambda^2}} c s^{c-1} \frac{\partial s}{\partial X} \tag{4.2}$$

Equation 4.2 can be solved by using separation of variables approach, as shown in an appendix C, giving:

$$s = \min \left[ 1, \left( \frac{\theta_s \sqrt{1+\Lambda^2}}{c k_s \Lambda} \frac{X}{t} \right)^{\frac{1}{c-1}} \right] \tag{4.3}$$

Defining $k_s = k_{s0} e^{-\lambda z}$, where $k_{s0}$ is the saturated hydraulic conductivity at the surface and $\lambda$ is a decay coefficient for hydraulic conductivity given by:

$$\lambda = \frac{-\ln k_{ref}/k_{s0}}{z_{ref}}$$

where $k_{ref}$ is the horizontal hydraulic conductivity at the depth $z_{ref}$ and $z_{ref}$ is a reference depth.

Applying this solution to the amended Richards' equation, the soil drainage process can be divided into three stages dependent on the saturation at the outflow level: a highly saturated stage ($0 \leq t \leq t_c$); an intermediate stage ($t_c < t < t_b$); and a dry stage ($t \geq t_b$). Note that $t_c$ and $t_b$ are critical times used to distinguish the saturation stages and will be discussed in what follows.

The time $t_c$ is defined as the instant at which the seepage face ceases to be fully saturated as shown in Figure 4.2a. Time $t_c$, may be found by applying equation 4.3 with $s = 1$ at the top right corner, $X = L$ and $Z = H$, and solving:

$$t_c = \frac{\theta_s L \sqrt{1+\Lambda^2}}{c k_{s0} \Lambda}$$

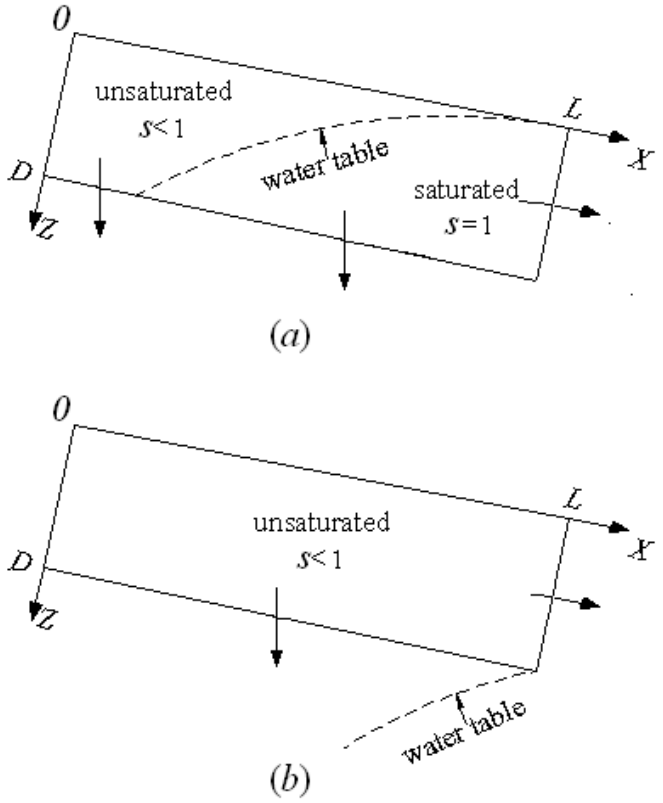


Figure 4.2: Definition of the critical time: (a) $t_c$; (b) $t_b$

The other critical time $t_b$ is the moment after which fully unsaturated conditions occur along the entire seepage face, as shown in Figure 4.2b.

A substituting saturation of 1 at the lower right corner $X = L$ and $Z = H$ into equation 4.3 and solving for $t_b$:

$$t_b = \frac{\theta_s L\sqrt{1+\Lambda^2}}{ck_{s0}\Lambda}e^{\lambda H}$$

For any time, the aquifer bulk saturation (the average volume saturation), $\bar{s}$, can be determined as:

$$\bar{s} = \frac{1}{HL}\iint s(X,Z)dX\,dZ \tag{4.4}$$

where $s(X,Z)$ is given by equation 4.3.

By analytically evaluating this integral, bulk saturation for three stages may be calculated as:

$$\bar{s} = \begin{cases} 1 - \frac{c-1}{\lambda c H}\frac{t}{t_c}\left(1 - e^{-\lambda H}\right) & \text{for } 0 \le t \le t_c \\ \frac{(c-1)^2}{\lambda c H}\left[1 - \left(\frac{t_c}{t}\right)^{\frac{1}{c-1}}\right] + 1 - \frac{1}{\lambda H}\ln\frac{t}{t_c} - \frac{1}{\lambda c H}\left(1 - \frac{t}{t_c}e^{-\lambda H}\right) & \text{for } t_c < t < t_b \\ \frac{(c-1)^2}{\lambda c H}\left(\frac{t_c}{t}\right)^{\frac{1}{c-1}}\left(e^{\frac{\lambda H}{c-1}} - 1\right) & \text{for } t \ge t_b \end{cases} \tag{4.5}$$

Equation 4.5 is only valid for $\lambda > 0$. If there is no decay in the hydraulic conductivity, e.g., soil is vertically homogenous, then $\lambda = 0$. In this case, the water table will be perpendicular to the hillslope bottom as it approaches the downslope seepage face. Soil experiences two stages under such a condition ($\lambda = 0$) instead of three since time $t_c$ and time $t_b$ are equal. The intermediate stage disappears for homogenous soils. The limit of equation 4.5 as $\lambda$ approaches 0 is:

$$\bar{s} = \begin{cases} 1 - \frac{c-1}{c}\frac{t}{t_c} & \text{for } 0 \le t \le t_c \\ \frac{c-1}{c}\left(\frac{t_c}{t}\right)^{\frac{1}{c-1}} & \text{for } t \ge t_c \end{cases} \tag{4.6}$$

Note that equations 4.5 and 4.6 are developed for a soil that is initially fully saturated. However, this expression is needed to evaluate the change in bulk saturation over a single time step, where conditions at the beginning of the time step are $s < 1$. Therefore, for soils that are not initially saturated, the time $t$ in equations 4.5 and 4.6 is rather a surrogate time instead of the time since the element was fully saturated. Given the initial bulk saturation at a real time $t$, the surrogate time $t^*$ is firstly calculated by the inverse form of equation 4.5 or equation 4.6, e.g., $t^* = F(\bar{s})$. Substituting the surrogate time for the next time step into equation 4.5 or equation 4.6, the bulk saturation for time step $t^* + \Delta t$ can be obtained. The storage change, $\Delta u$, in the time interval, $\Delta t$, is then calculated as:

$$\Delta u = \theta_s[\bar{s}(t^* + \Delta t) - \bar{s}(t^*)]HL$$

### 4.1.2 WATDRAIN1 Testing

As discussed in section 3.1, Richards' equation is the governing equation for variably saturated subsurface flow. Here, the WATDRAIN1 algorithm, described in section 4.1.1, has been tested against the numerical solution to Richards' equation (equation 4.1). The WATDRAIN1 interflow algorithm is derived from a simplified form of Richards' equation, which is the limiting case of the full 1D Richards' equation of equation 4.7 with $\varepsilon = 0$.

$$\theta_s\frac{\partial s}{\partial t} = \frac{\partial}{\partial X}\left[k\left(\varepsilon\frac{\partial \psi}{\partial X} - \frac{\Lambda}{\sqrt{1+\Lambda^2}}\right)\right] \tag{4.7}$$

where $\varepsilon$ is an suction gradient index. Equation 4.7 is the full Richards' equation with $\varepsilon = 1$ whereas it is called the adjusted Richards' equation with $\varepsilon < 1$ in this study. Note that in the numerical methods used here, $\varepsilon$ can not be equal to zero, because finite difference methods cannot solve fully hyperbolic problems. Therefore, a very small value $1.0e-6$ is used instead.

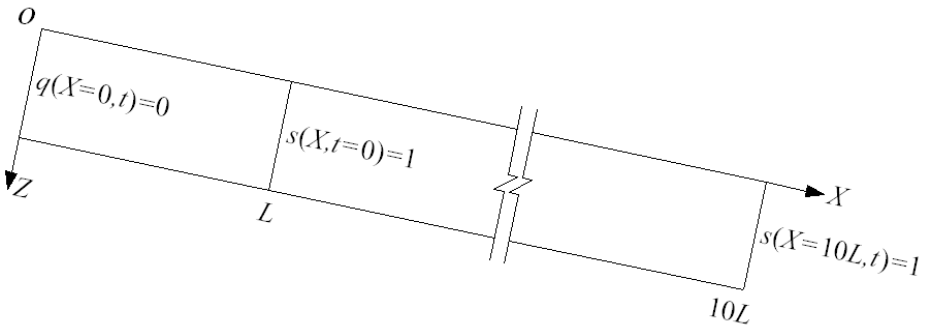


Figure 4.3: Initial and boundary conditions used for the numerical method: The aquifer is initially saturated. There is no flow at $X = 0$ and free flow at $X = L$.

Equation 4.7 was solved numerically by applying the one-dimensional finite difference numerical scheme, in which a no flow boundary condition and a free flow boundary condition are used. The free flow boundary condition is implemented by using a saturated boundary condition at a sufficient distance such that the downstream boundary condition has negligible effect at $L$, thus to approximate a boundary condition at infinity length. Figure 4.3 shows both initial and boundary conditions. Tests have been conducted on three homogeneous sloping aquifers ($\Lambda = 0.01$) with lengths of 15 meters, 150 meters, and 1500 meters, respectively. Soil parameters are consistent with Dingman's sand[45].

Multiple simulations were run and compared against equation 4.3, with $\lambda = 0$. Figure 4.4 demonstrates bulk saturation against time with hillslope length of $15m$, $150m$, and $150m$. It shows that the WATDRAIN1 analytical solutions are able to match the numerical solutions of the adjusted Richards' equation ($\varepsilon \approx 0$) for all three aquifers, i.e. both the numerical and analytical solutions are correct and consistent. However, it is apparent that the WATDRAIN1 analytical solution is a poor match to the full Richards' equation when the hillslope length is short ($L = 15m$). The analytical solution performs well for aquifers with a length of the magnitude of hundred meters and thousand meters.

Figure 4.5 shows the drainage characteristic curves for three hillslope lengths. Not

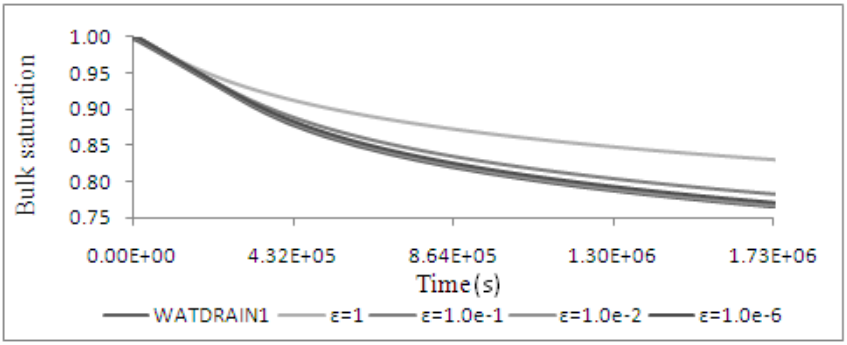


(a)

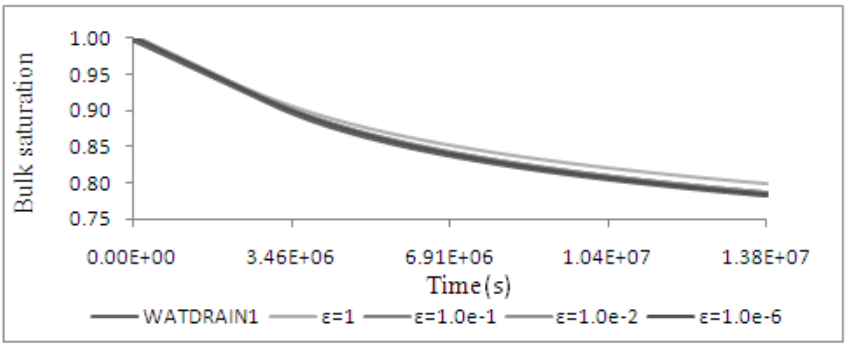


(b)

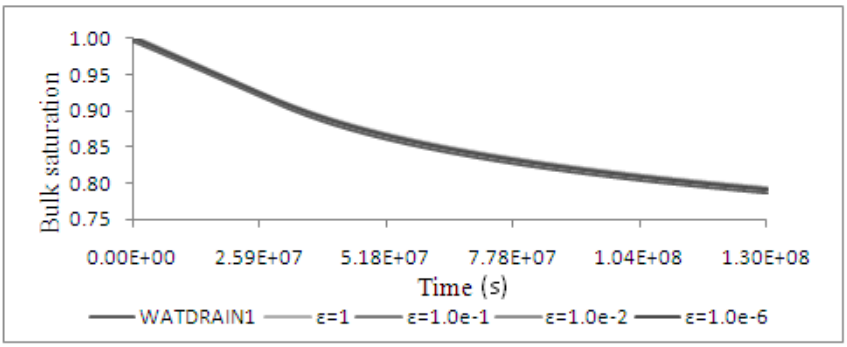


(c)

Figure 4.4: Bulk saturation curves: (a)$L = 15m$; (b) $L = 150m$; (c) $L = 1500m$

surprisingly, the flux calculated from the analytical scheme is always greater than that of the exact numerical scheme due to the absence of a suction gradient in the analyt-

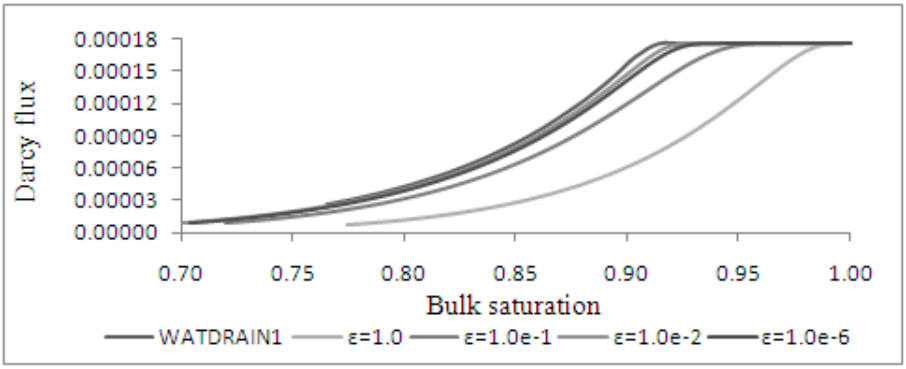


(a)

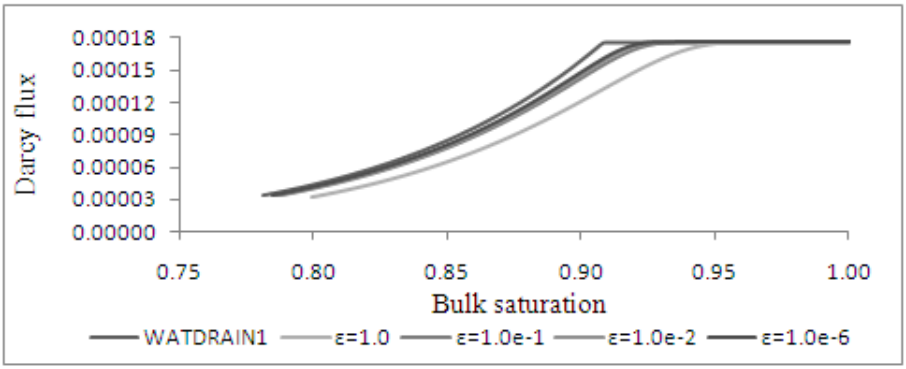


(b)

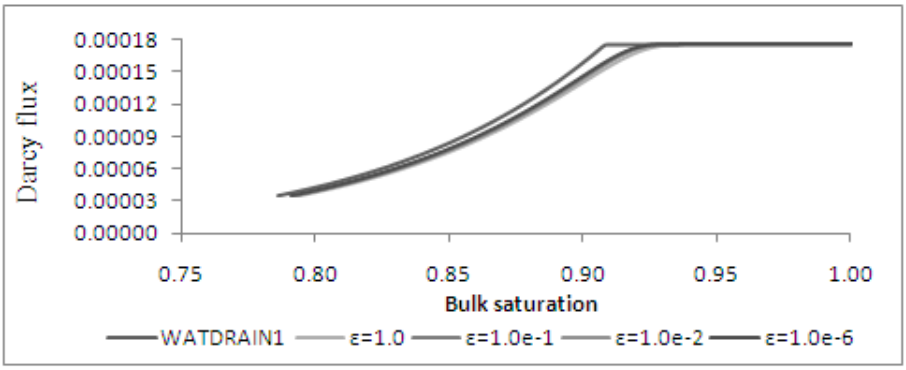


(c)

Figure 4.5: Drainage characteristic curves: (a)$L = 15m$; (b) $L = 150m$; (c) $L = 1500m$

ical scheme. Therefore, the WATDRAIN1 interflow algorithm will result in inaccurate partitioning between surface and subsurface runoff, by increasing surface runoff while consequently decreasing subsurface runoff.

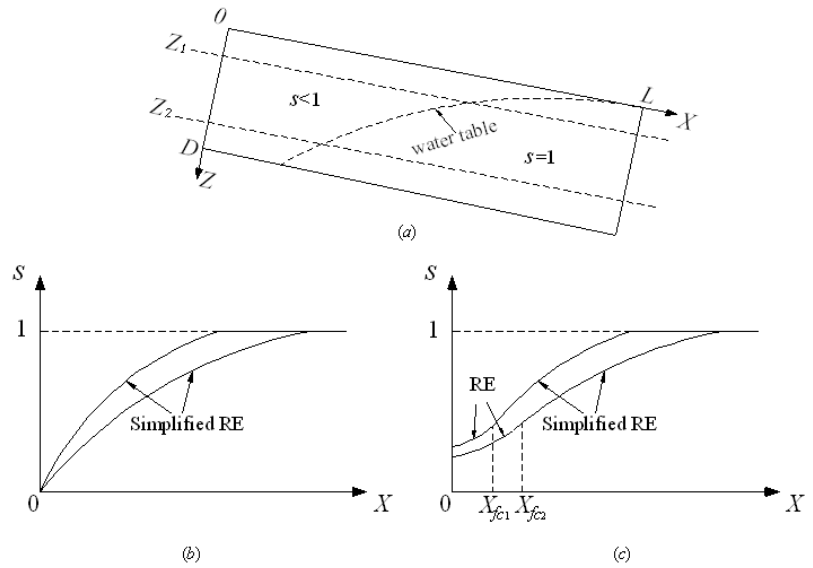


Figure 4.6: Correction of the soil saturation curve at transects $Z_1$ and $Z_2$:a) a computational unit; b) WATDRAIN1 saturation curves at $Z_1$ and $Z_2$; c) realistic saturation curves at $Z_1$ and $Z_2$

It is clear that, while useful, the WATDRAIN1 solution is not perfect. For example, in the current WATDRAIN1 application, for any depth (Figure 4.6a shows two arbitrary positions $Z_1$ and $Z_2$), the soil saturation is equal to zero at $X = 0$ as shown in Figure 4.6b. In natural conditions the soil saturation never can be equal to zero. One of the assumptions is that the suction effect is so small that the suction gradient can be ignored. However, as seen from Richards' equation simulations, the suction gradient increases during the drying process. When this process is considered, the soil saturation curve is rather like the curve as shown in Figure 4.6c. Note that $X_{fc}$ is the position behind which flow is essentially zero. To avoid issues caused by the no suction assumption in WATDRAIN1, a new interflow algorithm, WATDRAIN2, has been developed and is discussed in following sections.

### 4.1.3 WATDRAIN2 Development

To compensate for WATDRAIN1 defects discussed in section 4.1.2, a revised solution, one which can better approximate Richards' equation, is desirable. Here a new algorithm (WATDRAIN2) has been obtained by intelligently merging a gravity-dominated solution similar to that of WATDRAIN1 with the other extreme endpoint, the steady state solution. The derivation of this solution was initially proposed by Dr. E. D. Soulis. The refined representation here was a collaborative effort. In particular, all formal testing and analysis here are conducted by the author.

Here, it is assumed that the soil horizon experiences three states: an initial state, in which the aquifer is fully saturated; a transition state, in which the hillslope is partially saturated; and a steady state, in which the hillslope average water content equals its field capacity. The concept is depicted in Figure 4.7. Note that the boundary condition at $X = L$ is $s = 1$, e.g., the seepage face is constantly saturated.

Here, the initial condition and the uphill boundary condition are consistent with WATDRAIN1. The seepage face boundary condition is assumed to be saturated constantly. Unlike in WATDRAIN1, hydraulic properties (saturation and suction) in WATDRAIN2 depend only on the location along hillslope length and are not vertically variable. The suction head is assumed to be a weighted average of a flowing portion, given by a gravity-dominated solution ($\psi_g$), and the non-flowing portion, given by the steady state suction-dominated solution($\psi_f$).

By analogy with equation 4.3, the gravity-dominated solution is assumed to be in the form of a power expression similar to that of equation 4.3, except an additional term, $\tau(t)$, is used :

$$s_g = \left( \frac{X + \tau(t)}{X_s + \tau(t)} \right)^{\alpha} \tag{4.8}$$

where $X_s$ represents the location of the interface between the saturated and unsaturated soil surface, and $\alpha$ is defined as:

$$\alpha = \left( \frac{1}{c-1} \right) \left( 1 - \frac{X}{X_s} \right)^2$$

Note that the first term $\frac{1}{c-1}$ is identical to the WATDRAIN1 solution. The second term here, determined empirically, is used to adjust the difference between the analytical solution and the numerical solution.

According to the Clapp-Hornberger soil hydraulic characteristic functions [34], the suction may be determined from:

$$\psi_g = \psi_{ae} s_g^{-b} \tag{4.9}$$

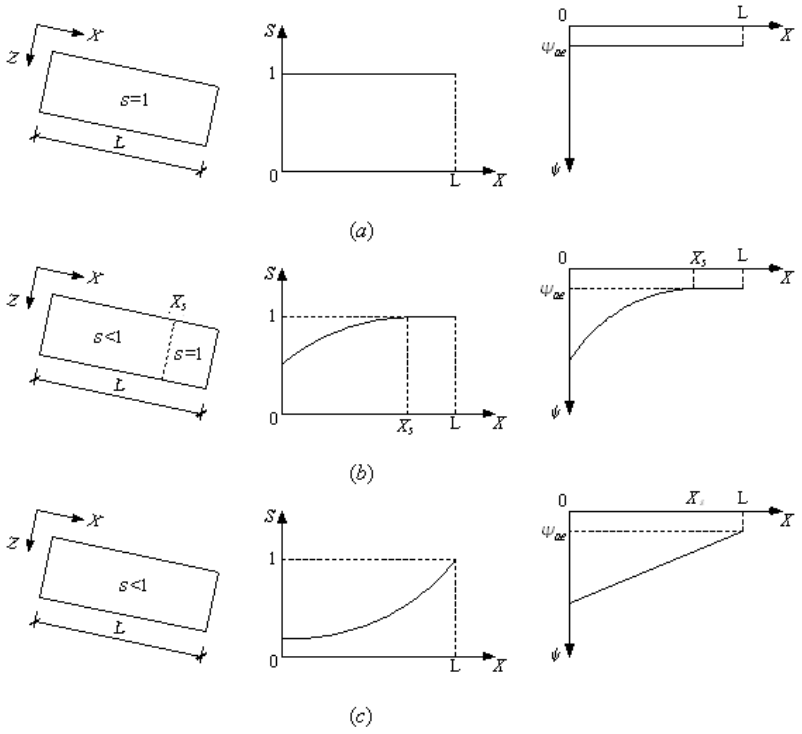


Figure 4.7: WATDRAIN2 conceptual model ($X_s$ represents the location of the interface between the saturated and unsaturated soil surface): (a) Initial state ($X_s = 0$); (b) Transition state ($X_s < L$); ; (c) Steady state ($X_s = L$)

where $\psi_{ae}$ is the air entry pressure.

Flow from the hillslope is initially at a constant rate, $k_s$, until a critical time $t_c^*$, at which time capillary forces begin to have an effect. When this occurs, $X_s$ equals the length of the aquifer, $L$. Before the time $t_c^*$, the total water lost from the hillslope is $\theta_s \int_0^L (1 - s_g)\, dX$. Water lost through the seepage face is $k_s \Lambda t_c^*$. Applying mass balance to the hillslope, $t_c^*$ is therefore calculated as:

$$t_c^* = \frac{\theta_s}{k_s \Lambda} \int_0^L (1 - s_g)\, dX$$

Applying the no flow boundary condition at time $t_c^*$, the unknown $\tau$ at time $t_c^*$, denoted

as $\tau_c$, can be obtained by:

$$\left.\frac{\partial \psi_g}{\partial X}\right|_{X=0} = \Lambda \tag{4.10}$$

Now, with a known critical time $t_c^*$, the aquifer drainage process is divided into three stages: a purely gravity-dominated stage ($0 < t < t_c^*$); a transition stage ($t_c^* < t < t_{max}$); and a purely suction-dominated stage ($t > t_{max}$). Note that $t_{max}$ is a semi-infinite time defined by users. These three states are going to be discussed respectively in what follows.

Guided by the exact solution to Richards' equation at steady state, the suction, $\psi_f$, and the saturation, $s_f$, can be expressed as:

$$\psi_f = \psi_{ae} - \Lambda(L - X) \tag{4.11}$$

$$s_f = \left(\frac{\psi_f}{\psi_{ae}}\right)^{-\frac{1}{b}} \tag{4.12}$$

i.e., at steady state ($t \to \infty$), the matric potential is linear. This is used as one of the endpoint solutions.

During the transition state, the flow is a weighted average of a gravity-dominated flow and a suction-dominated flow. For the purely gravity-dominated case ($t < t_c^*$), the seepage face is totally saturated. The corresponding hydraulic variables, suction $\psi_g$ and saturation $s_g$, are determined by equations 4.8 and 4.9. The only unknown in these two equations is the term $\tau(t)$, which can be calculated by applying the no-flow boundary condition at $X = 0.0$ as expressed in equation 4.10.

When $t_c^* < t < t_{max}$, the flow is assumed to be a weighted combination of a gravity-dominated and a suction- dominated flow solution. The suction during this state has been developed by using the conservation of energy analogy as:

$$\frac{1}{\psi^2} = \frac{w}{\psi_g^2} + \frac{(1-w)}{\psi_f^2} \tag{4.13}$$

where the weighting factor, $w(X,t)$, is found to have the following form:

$$w = s_a(t) + (1 - s_a(t))\theta_s \left(\frac{X}{L}\right)^3 \left(\frac{t_c}{t}\right)^{\left(1-\frac{t_c}{t}\right)^4} \tag{4.14}$$

where $s_a(t)$ represents the saturation at $X = 0$.

After substituting equations 4.9, 4.11, and 4.14 into equation 4.13, there are two unknowns, $\tau(t)$ and $s_a(t)$, in the resulting equation. Both of these unknown functions are highly nonlinear with respect to time and can not be solved analytically. Rigorous numerical solutions have been obtained by using a software library for solving nonlinear systems of equations (http://www.netlib.org/). A detailed description about how to solve for $s_a(t)$ and $\tau(t)$ is found in appendix D. The discussion that follows depicts steps that determine both relationships between $s_a(t)$ and $\tau$, and $\tau(t)$ and $t$.

Taking the derivative of equation 4.13 with respect to $X$ gives:

$$\frac{1}{\psi^3}\frac{\partial\psi}{\partial X} = \frac{w}{\psi_g^3}\frac{\partial\psi_g}{\partial X} + \frac{1-w}{\psi_f^3}\frac{\partial\psi_f}{\partial X} - \left(\frac{1}{2\psi_g^2} + \frac{1}{2\psi_f^2}\right)\frac{\partial w}{\partial X} \tag{4.15}$$

Rearranging both equations 4.13 and 4.15:

$$\left(\frac{\psi_f}{\psi}\right)^2 = w\left(\frac{\psi_f}{\psi_g}\right)^2 + (1-w) \tag{4.16}$$

$$\left(\frac{\psi_f}{\psi}\right)^3\frac{\partial\psi}{\partial X} = w\left(\frac{\psi_f}{\psi_g}\right)^3\frac{\partial\psi_g}{\partial X} + (1-w)\frac{\partial\psi_f}{\partial X} - \frac{\psi_f}{2}\left[\left(\frac{\psi_f}{\psi_g}\right)^2 - 1\right]\frac{\partial w}{\partial X} \tag{4.17}$$

At the no flow boundary ($X = 0$), equations 4.16 and 4.17 become:

$$\left(\frac{\psi_{f0}}{\psi_0}\right)^2 = w\left(\frac{\psi_{f0}}{\psi_{g0}}\right)^2 + (1-w) \tag{4.18}$$

$$\left(\frac{\psi_{f0}}{\psi_0}\right)^3 = \frac{w}{\Lambda}\left(\frac{\psi_{f0}}{\psi_{g0}}\right)^3\left.\frac{\partial\psi_g}{\partial X}\right|_{X=0} + (1-w) \tag{4.19}$$

where subscript 0 represents values at the no flow boundary ($X = 0$). Raising equation 4.18 to the power of 3 and equation 4.19 to the power of 2, the left hand sides are identical to result in:

$$\left[w\left(\frac{\psi_{f0}}{\psi_{g0}}\right)^2 + (1-w)\right]^3 = \left[\frac{w}{\Lambda}\left(\frac{\psi_{f0}}{\psi_{g0}}\right)^3\left.\frac{\partial\psi_g}{\partial X}\right|_{X=0} + (1-w)\right]^2 \tag{4.20}$$

By substituting equation 4.14 into equation 4.20, an implicit relationship between $s_a$ and $\tau(t)$ is determined. Since $\tau(t)$ is only a function of $t$, the relationship between them may be written as:

$$t = \int_{\tau_c}^{\tau_{max}} \frac{\partial t}{\partial\tau(t)}\,d\tau \tag{4.21}$$

where $\tau_{max}$ is the value of $\tau(t)$ at the steady state. Once $\partial t/\partial\tau$ is known, the relationship between $\tau$ and $t$ can be determined. Richards' equation at the no-flow boundary may be written in a simplified form:

$$\theta_s \frac{\partial s}{\partial \tau(t)} \frac{\partial \tau(t)}{\partial t} = k \left. \frac{\partial^2 \psi}{\partial X^2} \right|_{X=0}$$

Therefore, the $\partial t/\partial\tau(t)$ is expressed as:

$$\frac{\partial t}{\partial \tau(t)} = \frac{\theta_s \frac{\partial s}{\partial \tau(t)}}{k \frac{\partial^2 \psi}{\partial X^2}}|_{X=0} \tag{4.22}$$

Substituting equation 4.22 into equation 4.21, an implicit relationship between $t$ and $\tau(t)$ can be obtained through numerically integration. Further to determine the implicit relationship between $s_a(t)$ and $\tau(t)$, use equation 4.20.

With known functions for $\tau(t)$ and $s_a(t)$, the WATDRAIN2 analytical solution is finally assembled as:

$$\psi = \begin{cases} \psi_{ae} \left( \frac{X+\tau(t)}{X_s+\tau(t)} \right)^{-\left(\frac{b}{2b+2}\right)\left(1-\frac{X}{X_s}\right)^2} & \text{for } 0 \le t \le t_c \\ \left( \frac{w}{\psi_g^2} + \frac{1-w}{\psi_f^2} \right)^{-\frac{1}{2}} & \text{for } t_c < t < t_{max} \\ \psi_{ae} - \Lambda(L-X) & \text{for } t \ge t_{max} \end{cases} \tag{4.23}$$

where $\psi_g$ and $\psi_f$ are given by equations 4.9 and 4.11.

### 4.1.4 WATDRAIN2 Testing

Richards' equation (equation 2.2)is here used as numerical "truth" with which the interflow algorithm is compared. The analytical algorithm was first tested on a 400 meter long hillslope with a slope of 0.01, which is here called the base parameter set. The hillslope is initially saturated with a uphill no flow boundary condition and a downhill saturated boundary condition. Figures 4.8 and 4.9 depict the saturation and suction distribution for sand and silt loam soil textures, with parameters derived from [45].

It can be seen from the Figures 4.8 and 4.9 that the analytical solution matches the numerical solution well for both the gravity-dominated and transition stages for sand and silt loam. It is clear from these comparisons that the approximate analytical solution to the Richards' equation is in a reasonable range and accurate enough for most practical

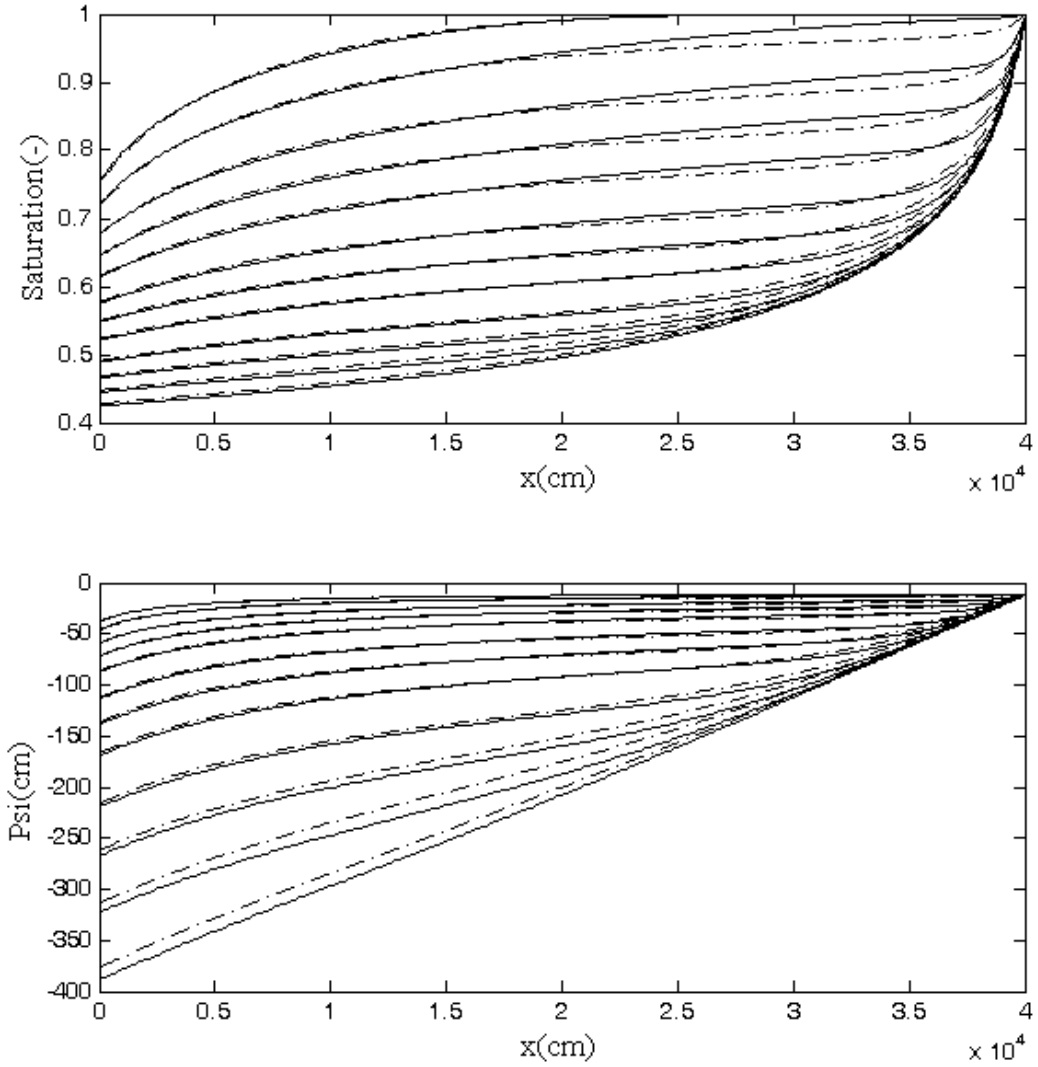


Figure 4.8: Sand saturation and suction curves at mutiple time (From top: $t = 4 \times 10^n d$, $8 \times 10^n d$, and $20 \times 10^n d$ $(n = 1..4)$) with $L = 400m$ and $\Lambda = 0.01$: solid-numerical solution; dashed-WATDRAIN2 analytical solution

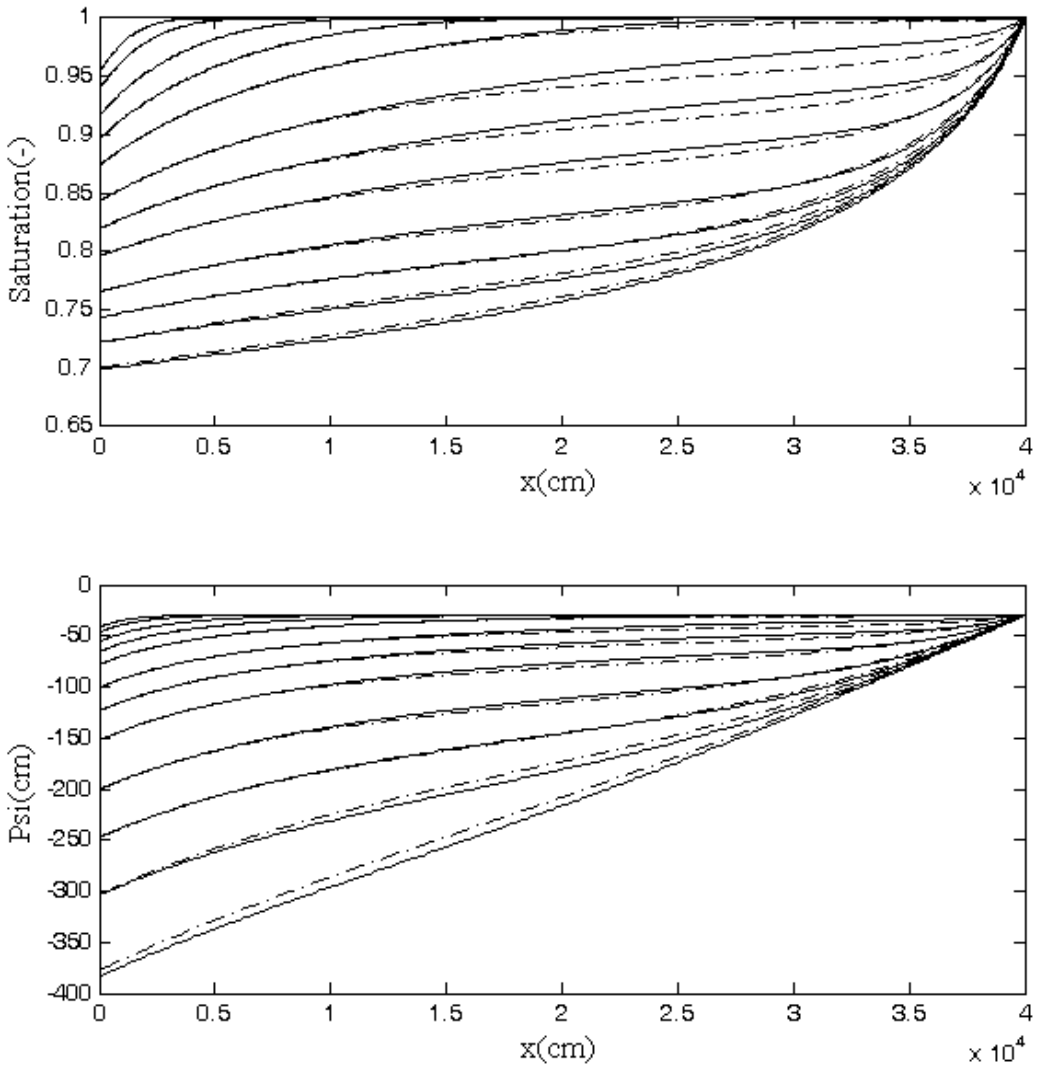


Figure 4.9: Silt loam saturation and suction curves at mutiple time (From top: $t = 4\times10^n d$, $8\times10^n d$, and $20\times10^n d$ $(n = 1..4)$) with $L = 400m$ and $\Lambda = 0.01$: solid-numerical solution; dashed-WATDRAIN2 analytical solution

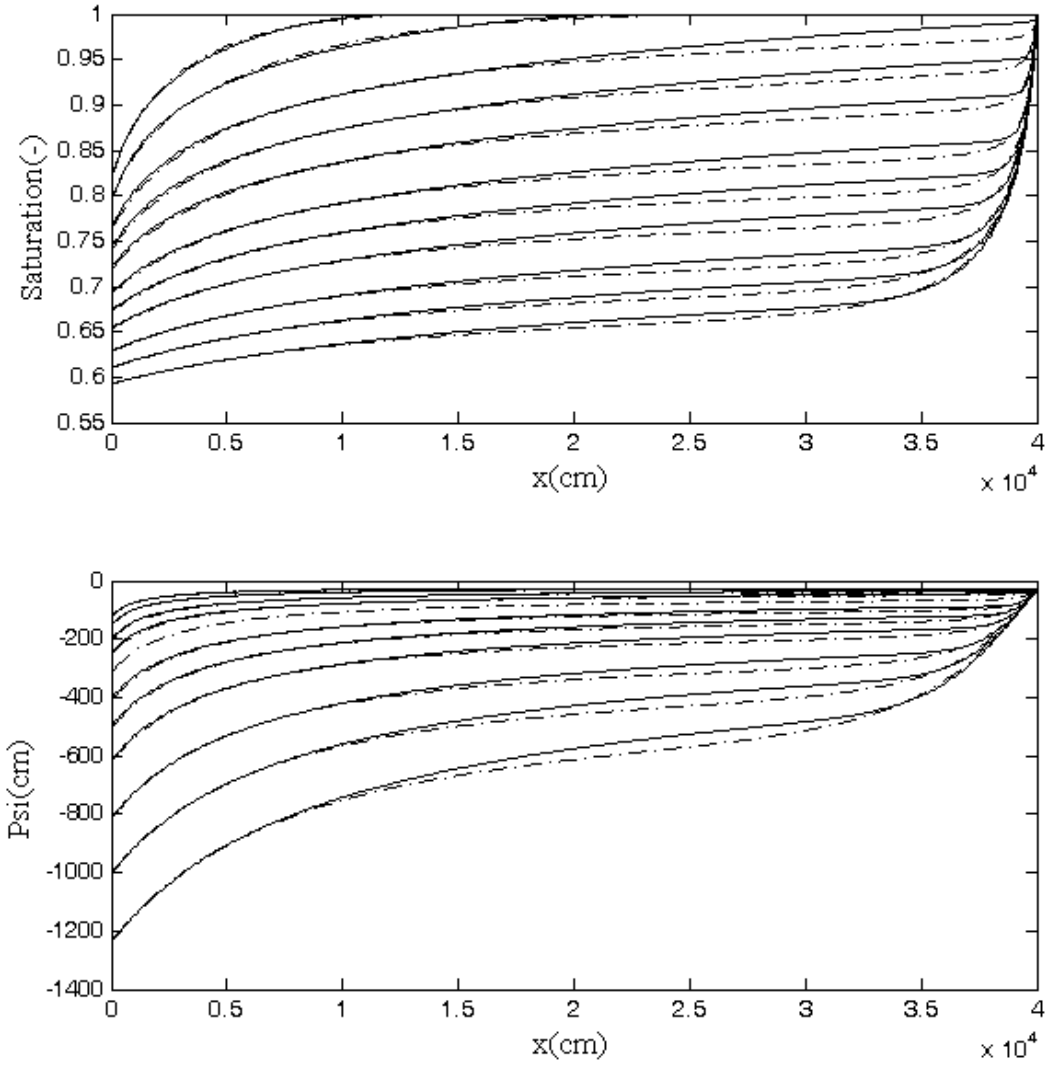


Figure 4.10: Silt loam saturation and suction curves at mutiple time (From top: $t = 2 \times 10^n d$, $4 \times 10^n d$, and $10 \times 10^n d$ $(n = 1..4)$) with $L = 400m$ and $\Lambda = 0.1$: solid-numerical solution; dashed-WATDRAIN2 analytical solution

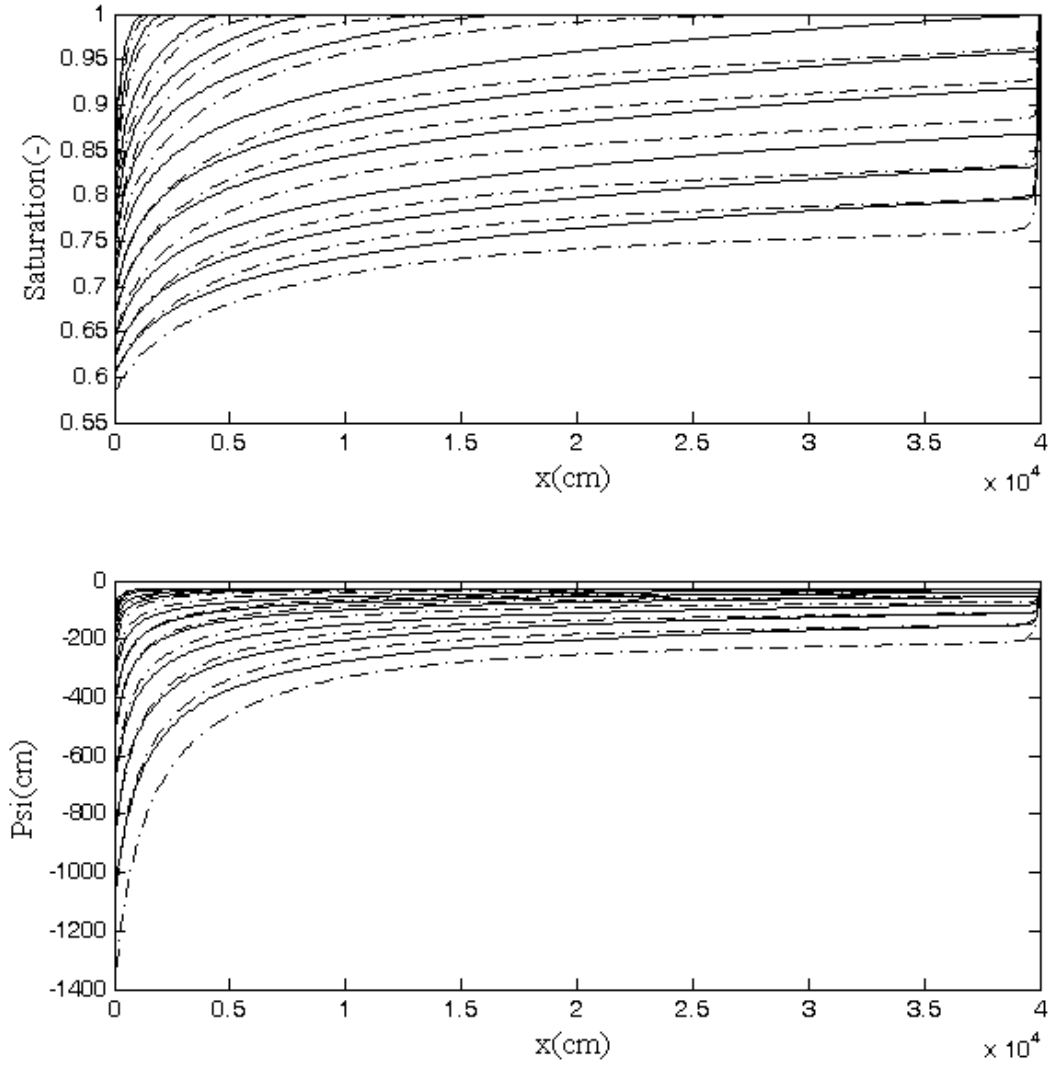


Figure 4.11: Silt loam saturation and suction curves at mutiple time (From top: $t = 0.05 \times 10^n d$, $0.1 \times 10^n d$, and $0.25 \times 10^n d$ $(n = 1..4)$) with $L = 400m$ and $\Lambda = 1.0$: solid-numerical solution; dashed-WATDRAIN2 analytical solution

applications. To verify the robustness of the WATDRAIN2 analytical solution, more tests were conducted on silt loam with different hillslope lengths and a wide range of slopes.

Figure 4.10 shows the saturation and suction curves for a slope of 0.1 and Figure 4.11 shows the saturation and suction curves for a slope of 1.0, other parameters are consistent with the silt loam base testing case. It is clear that WATDRAIN2 analytical solution matches the numerical solution well for the slope of 0.1 and decreases in accuracy for the slope of 1.0. However, for the latter case, the maximum error increases with increasing time and for a large time of $200000d$, the maximum error is less than 5%. The accuracy is still reasonable for practical applications.

Figures 4.12 and 4.13 are the saturation and suction curves for lengths of $40m$ and $4000m$. The WATDRAIN2 analytical solutions match with the numerical solutions well for all lengths. However, the accuracy of the WATDRAIN2 analytical solution increases with increasing hillslope length. It also can be seen that the shorter the hillslope, the faster the hillslope approaches the steady state.

All testing results in this section show that the WATDRAIN2 analytical solution matches the numerical solution perfectly for the gravity-dominated stage ($t < t_c$) and relatively less accurately for the transition stage but the difference between the analytical and numerical solutions is in a reasonable range. Both the analytical solution and the numerical solution will approach the same steady state at a very large time. However, this 'large time' is different dependent on hillslope length and slope.

The weighting function approach has been shown to successfully reproduce the transient soil moisture for dry sandy and silt loam soil textures, as compared to numerical solutions to Richards' equation. However, the choice of weighting function used here is non-unique and therefore not the only way to predict soil moisture profiles: more efforts are needed to identify a robust interpolate between the extreme states of gravity-dominated and suction-dominated flow for all soil textures.

### 4.1.5 Bulk Saturation Curves

The Clapp-Hornberger saturation, as derived from equation 4.13 is:

$$s^{2b} = ws_g^{2b} + (1-w)s_f^{2b} \tag{4.24}$$

As discussed in section 4.1.3, WATDRAIN2 hydraulic properties depend only on the location along hillslope. Therefore, hillslope bulk saturation can be determined as:

$$\bar{s} = \frac{1}{L}\int s dX \tag{4.25}$$

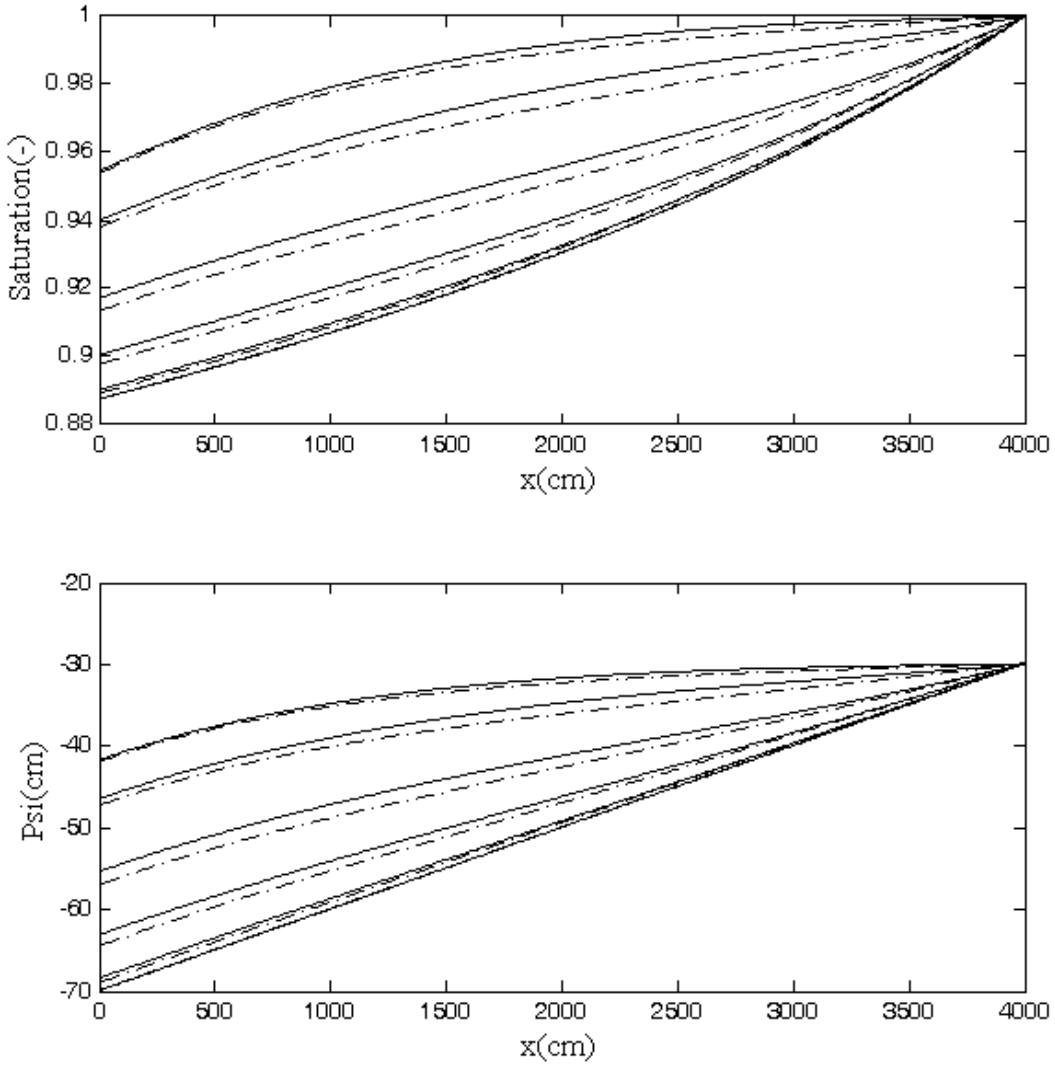


Figure 4.12: Silt loam saturation and suction curves at mutiple time (From top: $t = 4 \times 10^n d$, $8 \times 10^n d$, and $20 \times 10^n d$ $(n = 1..4)$) with $L = 40m$ and $\Lambda = 0.01$: solid-numerical solution; dashed-WATDRAIN2 analytical solution

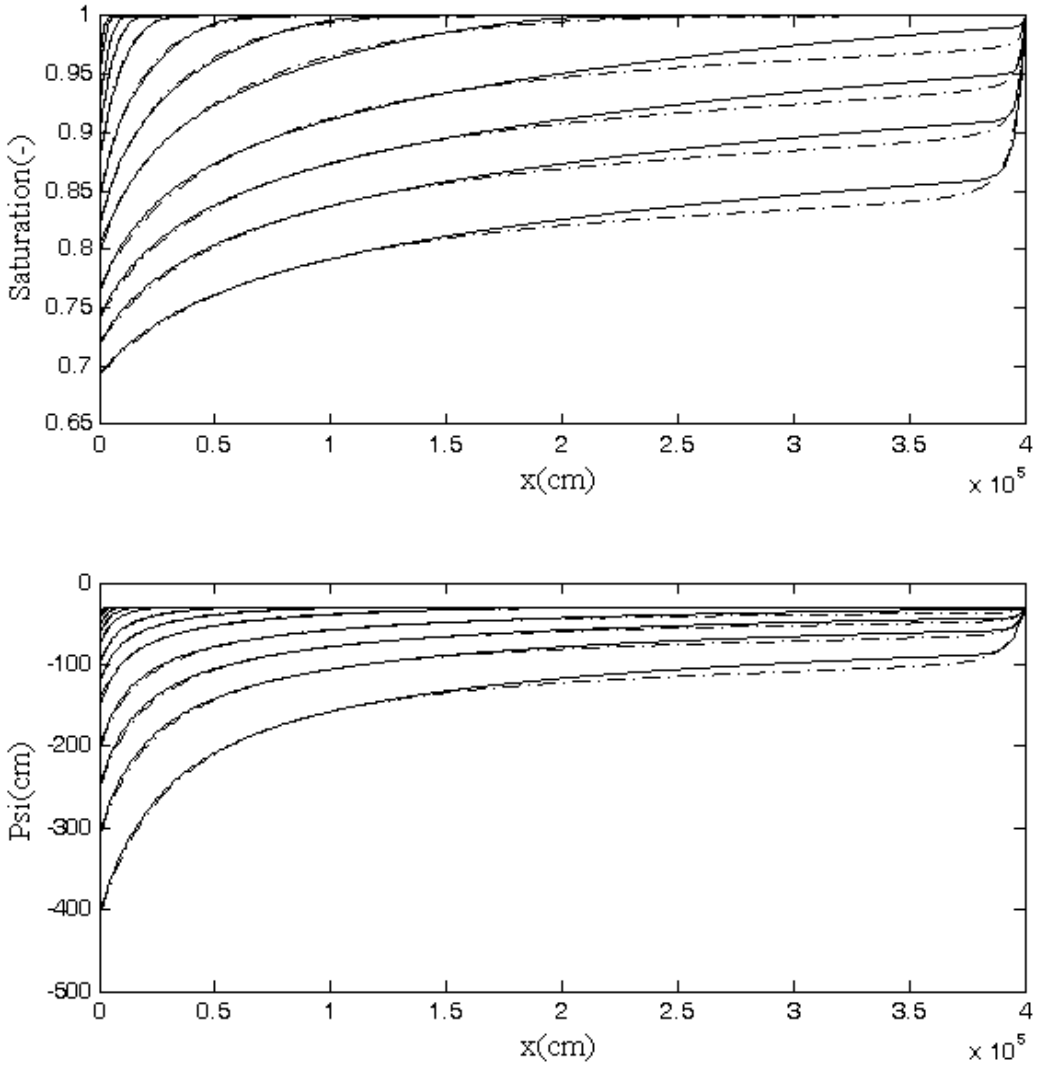


Figure 4.13: Silt loam saturation and suction curves at mutiple time (From top: $t = 4 \times 10^n d$, $8 \times 10^n d$, and $20 \times 10^n d$ $(n = 1..4)$) with $L = 4000m$ and $\Lambda = 0.01$: solid-numerical solution; dashed-WATDRAIN2 analytical solution

Ideally, if an explicit function of $\bar{s} = f(t)$ and its inverse $t = f^{-1}(\bar{s})$ can be derived, the boundary flux, $q$, can be calculated as:

$$q = \frac{\Delta \bar{s} L}{\Delta t}$$

Unlike the WATDRAIN1 analytical solution (equation 4.3), in which an explicit function for bulk saturation ($\bar{s}$) is available (equations 4.5 and 4.6), it is difficult to obtain an explicit bulk saturation function for the WATDRAIN2 analytical solution. The WATDRAIN2 saturation function (equation 4.24) is a highly nonlinear function with respect to time and it is computationally expensive to perform the direct integration required by equation 4.25. In order to reduce the computational cost, a lookup table approach is taken, where the saturation curve is precalculated. Figure 4.14 is an example bulk saturation curve obtained from the interflow algorithm for a silt loam texture [45]. The lookup process is described below.

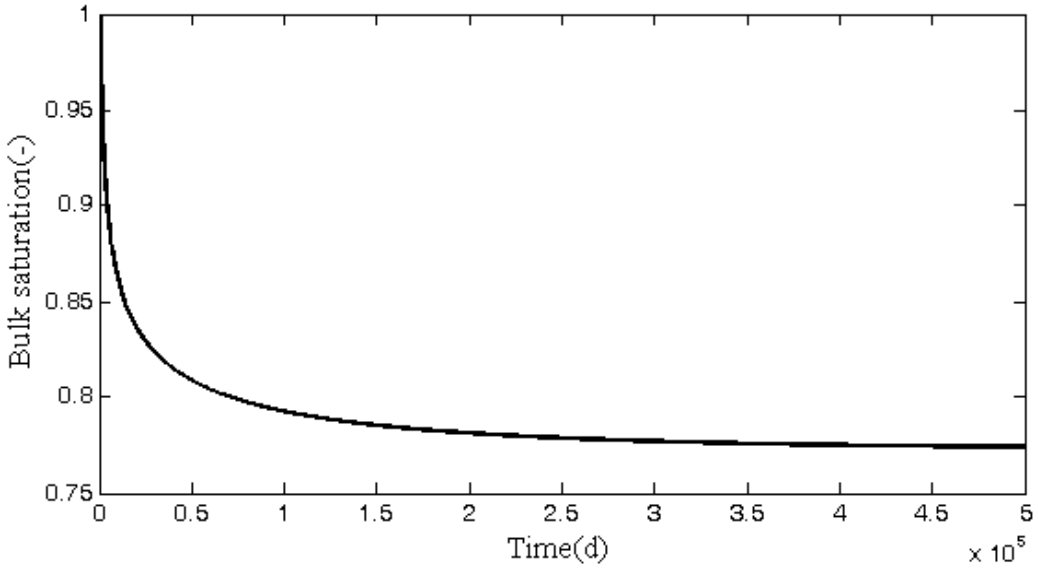


Figure 4.14: Silt loam bulk saturation profile

For a shallow sloping aquifer, if the initial bulk saturation is known, the corresponding time, $t$, can be numerically determined from equation 4.25. For the next time step, the bulk saturation $\bar{s}(t + \Delta t)$ is numerically calculated from the $t + \Delta t$.

To obtain $\bar{s}_1$ from $\bar{s}_0$, the process is:

- Step1: Calculate $t_0$ from the given $\bar{s}_0$ using the inverse form of bulk saturation equation 4.25.
- Step2: Determine next time step $t_1 = t_0 + \Delta t$.
- Step3: Compute $\bar{s}_1$ at the given $t_1$ using the bulk saturation equation 4.25.

The bulk saturation curves consist of a discrete set of known data points, therefore interpolation has to be used. Here, a simple linear interpolation method was used since the saturation change in one time step is not large and can be approximated by a straight line.

## 4.2 Improved Coupling of Infiltration and Interflow Processes

The improved interflow algorithm described in section 4.1 provides a robust and efficient explicit relation between the boundary flux and the soil internal variables. It also produces useful information for dynamically calculating a runoff contribution area, and is here used to inform the calculation of infiltration and overland runoff. The improved infiltration-interflow algorithm is suitable to incorporate into any hydrological model or land surface scheme.

In this study, the improved infiltration-interflow algorithm has been incorporated into a hydrology-land-surface scheme MESH, which is an integrated system that combines the distributed hydrological model WATFLOOD [76] and the land surface scheme CLASS [141] [142]. This integrated system is designed to be linked with atmospheric models. CLASS is typical of many Land Surface Schemes (LSSs) that exist today. CLASS is primarily designed to calculate the vertical water and energy budget and has an appropriate interface for atmospheric models. It focuses on soil moisture and thermal energy estimation but relies upon the standard "flat earth" methods for interflow and infiltration.

The original MESH soil model simulates both energy and water flux. It is difficult to show how much contribution the improved interflow from section 4.1 has on the soil moisture simulation process due to interactions between many hydrological processes near the surface. Here, a stand-alone CLASS-based soil model was used instead, which is a simple single soil model excluding the effects from other hydrological processes. The improved infiltration-interflow algorithm was implemented in this single soil model and compared against results from the standard uncoupled model algorithms, because it is easier to interpret the various features of this simple model's hydrograph and understand the cause-and-effect relationships in the model output.

A stand alone CLASS-based soil model is first discussed in this section and then, guided by the comparison with the numerical solution to the Richards' equation, modifications to the CLASS-based soil model are suggested. Results show that by coupling the infiltration and interflow processes, a more realistic manner of hydrograph can be obtained. Results also show that the behavior of the interflow algorithm can be significantly affected by topography and soil properties.

### 4.2.1 A Stand Alone CLASS-based Soil Model

Here, to simplify the model development and analysis process, a stand alone soil model has been built by modifying the CLASS source code. This model excludes all energy flux, temperature, and evaporation processes, available in the full version of CLASS. Three soil layers are used to discretize the soil column. Infiltration is simulated by a traditional implicit Green-Ampt model. Flow between soil layers is calculated by a finite difference form of Richards' equation. Hydraulic head gradient at the soil bottom is assumed to be 1. Therefore, baseflow is calculated based on the hydraulic conductivity of the third layer.

The stand alone soil model is composed of the main simulation driver (from the CLASS source code file CLASSW.f90) and 10 subroutines. The function of each subroutine is described here. All files names and function are consistent with Verseghy's [140]:

- CLASSW (CLASSW.f90): Calls subroutines to perform surface water budget calculations.
- grinfl (grinfl.f90): Quantifies movement of liquid water between soil layers under conditions of infiltration.
- wfill (wfill.f90): Evaluates infiltration of water into soil under unsaturated conditions.
- wflow (wflow.f90): Evaluates infiltration of water into soil under saturated conditions using the Green-Ampt model.
- wend (wend.f90): Recalculates liquid water content of soil layers after infiltration, and calculates baseflow.
- grdran (grdran.f90): Quantifies movement of liquid water between soil layers under non-infiltrating conditions, in response to gravity and tension forces using a finite difference approximation for the Richards' equation.
- watrof (watrof.f90): Calculates overland flow and interflow components of the surface runoff.
- watdrain (watdrain.f90): Calculates interflow by using storage change.
- tmcalc (tmcalc.f90): Calculates overland flow using Manning's formula and pond water depth. Adjust water stores accordingly.
- chkwat (chkwat.f90): Checks for closure of the surface water budget, and for unphysical values of certain variables.

- xit (xit.f90): Prints the name of the subroutine and an error code when an error condition is encountered.

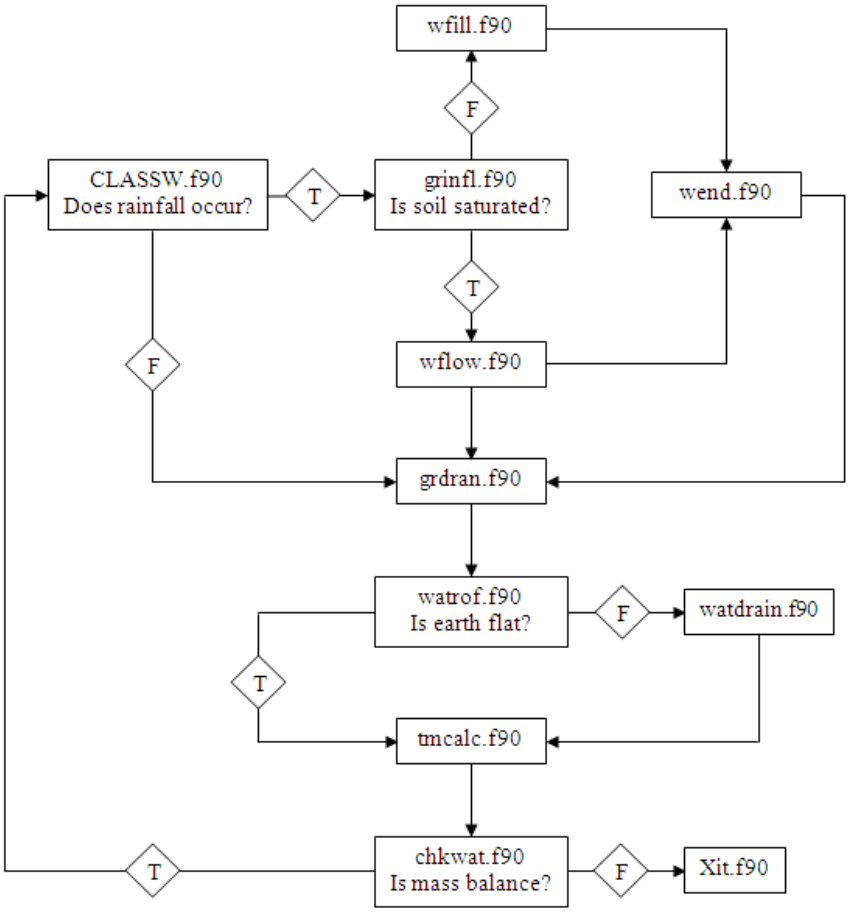


Figure 4.15: CLASS-based soil model flow chart: T=true; F=false

Figure 4.15 shows the flow chart for the stand alone soil model. At the start of a rainfall event, it is assumed that the soil is unsaturated. Unsaturated infiltration occurs first and then the unsaturated assumption is checked for validity for each layer. If there is ponded water on the surface or the first layer wetting front hydraulic conductivity is nearly zero, saturated infiltration occurs immediately. If the wetting front depth at the ponding time is deeper than the first soil layer, depth of the wetting front will be calculated for successive layers until the wetting front is located. If the soil layer properties vary, the actual wetting

front depth will be adjusted according to the depth calculated by the property of using individual soil layers. Flow between soil layers is calculated by using the average water content from the previous time step and then the water content is updated. After that the overflow is calculated at the end of current time step. Since the lateral and vertical processes have been treated separately, these two processes are individually discussed and then will be coupled using the new infiltration-interflow algorithm, which is discussed in section 4.2.3.

### 4.2.2 Uncoupled Soil Model

Vertical flow and lateral flow are calculated separately and independently in the MESH soil model, as done in many other hydrological models. For each time step, the average water content calculated from the vertical process is used as the initial water content for the lateral process. After deducting the amount of water lost due to interflow, the updated water content is used as the initial water content for the vertical process in the next time step. There are no other physical connections between these two processes, which may result in wrong simulation of the hydrological process and provide unrealistic hydrographs.

#### Problems with the Current MESH Baseflow Simulation Algorithm

The CLASS-based soil model has been tested by using hypothetical rainfall distributions in all experiments. Since the main objective of this work is to investigate more physically-based infiltration and interflow processes, the test mainly focuses on the case where the rainfall rate is larger than the saturated hydraulic conductivity, during which the infiltration rate is controlled by the infiltration capacity. Soil parameters here are consistent with silt loam [45]. The simulation duration is set to 10 days, and each rainfall event lasts at least for one day. Figure 4.16 shows the the uncoupled soil model hydrograph and the rainfall hyetograph.

There are several odd artefacts that can be observed in the hydrograph of Figure 4.16. These occur either at the moment that the wetting front approaches the bottom of the third layer (points A,B and C) or during the rainfall event in which the rainfall intensity is less than the saturated hydraulic conductivity $k_s$ (between D and E). The former issue exists due to a model strategy MESH uses: baseflow in MESH is calculated in different ways depending on the bottom layer saturation level. If the bottom layer is fully saturated, the baseflow will be supplied by the incoming water otherwise the baseflow will be supplied by the bottom layer. The bottom layer can be fully saturated when the wetting front

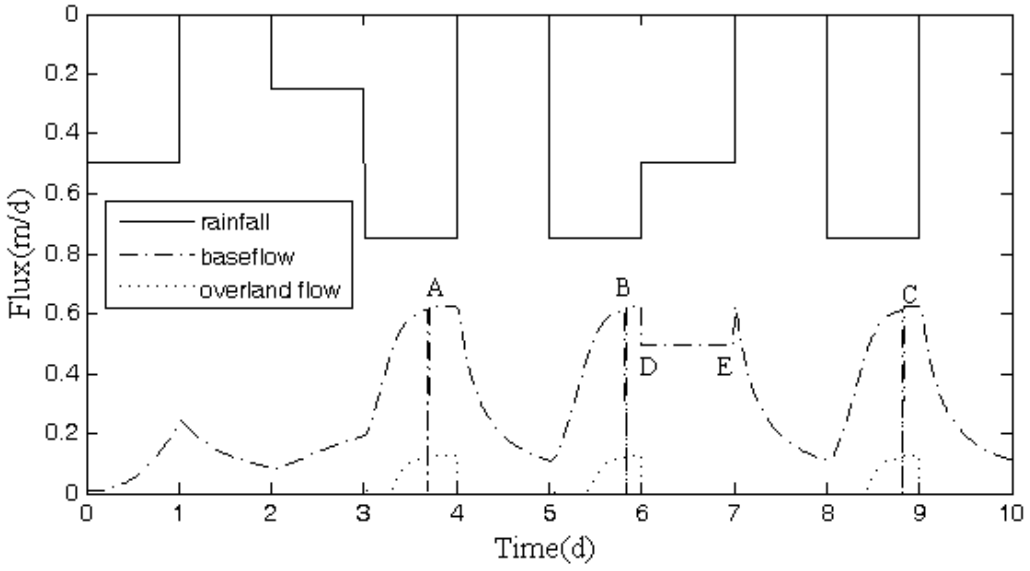


Figure 4.16: Problems in CLASS-based soil model hydrograph: no baseflow at A, B and C; baseflow equals rainfall intensity between D and E

across the bottom of the third layer. MESH will recalculate the wetting front depth if the wetting front depth calculated in the current time step is below the bottom of the current soil layer for considering the soil heterogeneity between two successive layers. The amount of time required for the wetting front to reach the bottom of the current soil layer is then recalculated. At the end of this specific amount of time, all incoming water has been used for satisfying the fully saturated condition of the current layer and no water is left for drainage/baseflow. Therefore, baseflow from the bottom layer at the these moments (A, B, and C) abruptly (and unphysically) drop to zero.

The latter case, between D and E, is relatively complex. As mentioned earlier, baseflow in MESH is simulated in different ways according to the third soil layer saturation level. If the wetting front approaches the bottom of the third layer, which indicates the soil is fully saturated, baseflow is controlled by the incoming water. Such a scheme works well if the incoming water is greater than the bottom Darcy's flux ($w > k_s$) while it does not work for situations if the incoming water is less than the Darcy's flux ($w \leq k_s$), e.g., when the amount of incoming water is less than the amount of water out of the bottom layer. Soil in this case should gradually become unsaturated under such conditions instead of staying saturated as MESH indicates in Figure 4.17.

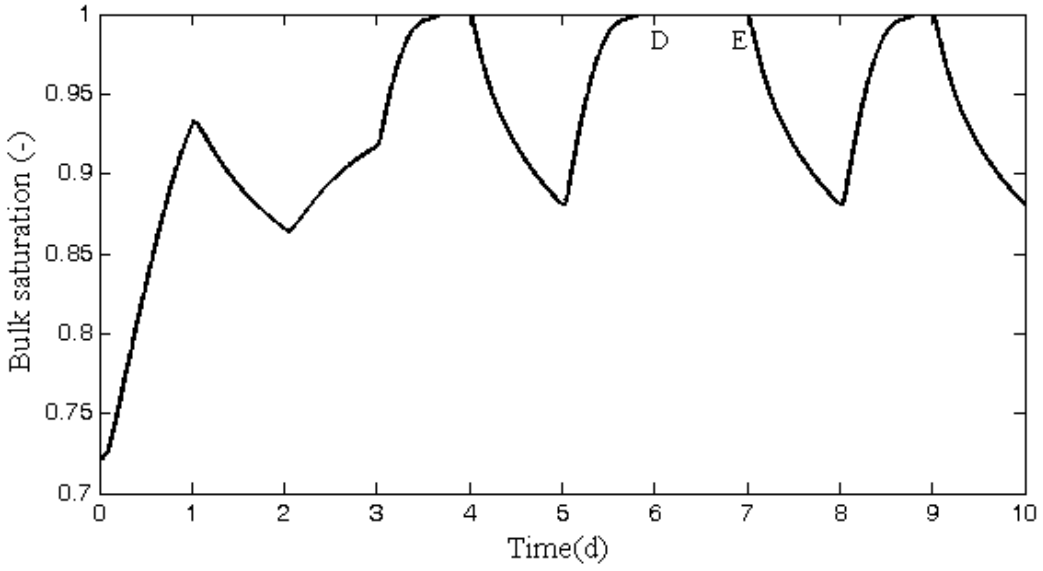


Figure 4.17: Soil bulk saturation for the hydrograph of Figure 4.16: Baseflow equals rainfall intensity start at D, causing MESH to underestimate the baseflow rate and overestimate saturation start at D

Since the suction gradient at the third layer bottom is always assumed to be zero in MESH [141], the baseflow should be equal to the saturated hydraulic conductivity at time D. However, Figure 4.16 shows that the modeled base flow is forced to equal the rainfall rate, which is less than hydraulic conductivity. In reality, the base flow should be governed by the bottom layer saturation level, which means that the base flow for such a situation ($w < k_s$) should be greater than the rainfall intensity. In order to confirm the intuitive conclusion drawn here, numerical solutions to the 2D Richards' equation with the same parameter sets, rainfall events, and initial and boundary conditions are shown in Figures 4.18 and 4.19.

Figure 4.18 shows a gradually decreasing baseflow in the period between D and E instead of an abrupt drop from $k_s$ to $w$ as shown in Figure 4.16. Figure 4.19 shows that the bulk saturation is decreasing at time D instead of staying saturated as shown in Figure 4.17. All these conflicts indicate that a modification to the MESH soil model for the conditions of $w < k_s$ is necessary.

Problems occurred either at the moment that the wetting front approached the bottom

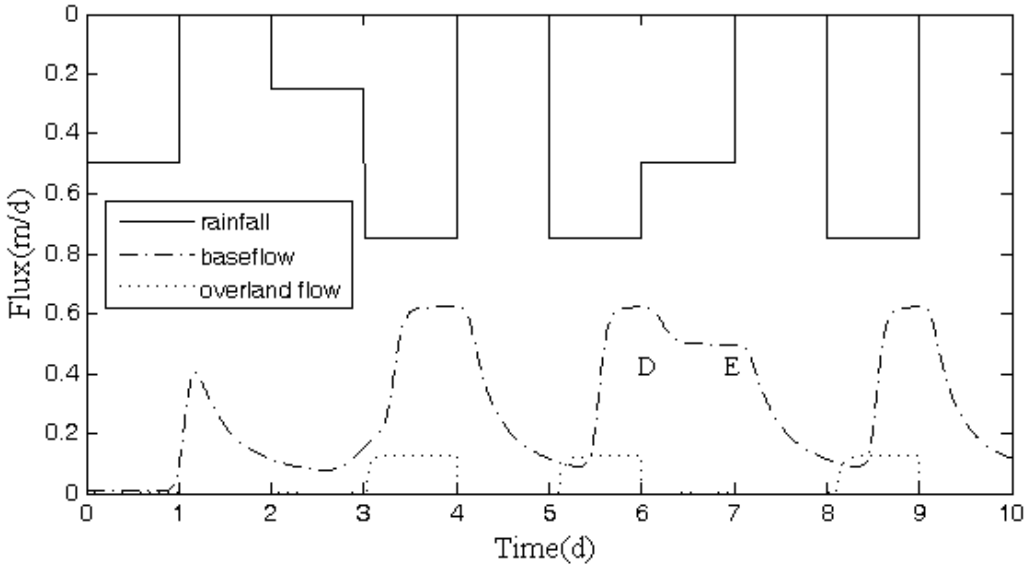


Figure 4.18: Richards' equation hydrograph

of the third layer (cases A,B and C) or during a rainfall event where the rainfall intensity was less than the saturated hydraulic conductivity (between D and E). Two simple modifications are suggested under such conditions. The baseflow under the first situation should be obtained by comparing the incoming water and the Darcy's flux. Whichever is bigger should be used for determining the baseflow rate. The water under such situations is supplied by the water in the bottom layer. For the second situation, the baseflow should be controlled by the Darcy's flux instead of the incoming water. Revisions to the wend.f90 source code have been made to compensate for these defects, in which the base flow occurs due to gravity and water is supplied by the bottom layer. Figures 4.20 and 4.21 demonstrate the hydrograph and soil profiles for the modified soil model.

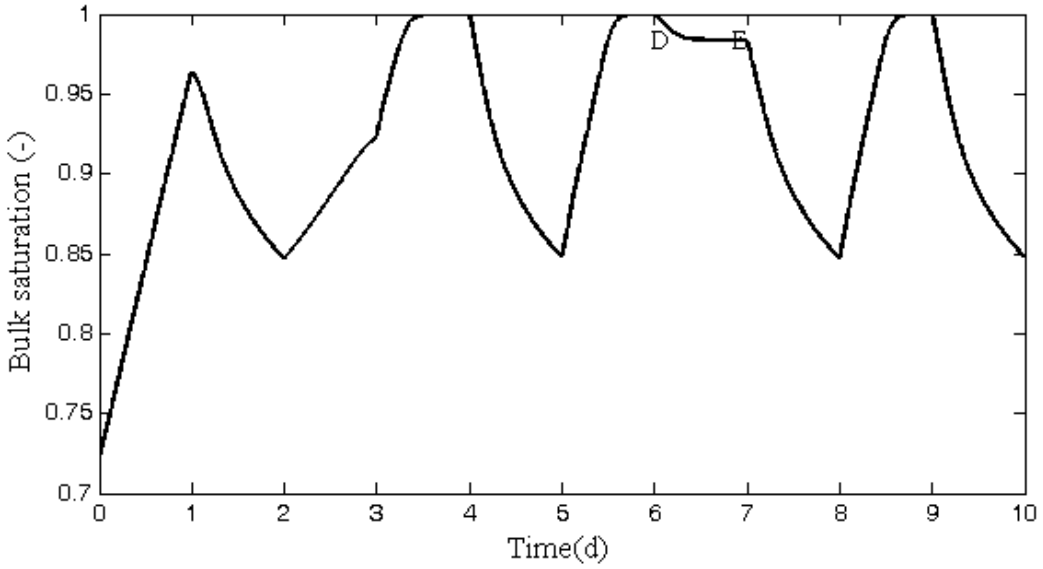


Figure 4.19: Richards' equation soil bulk saturation

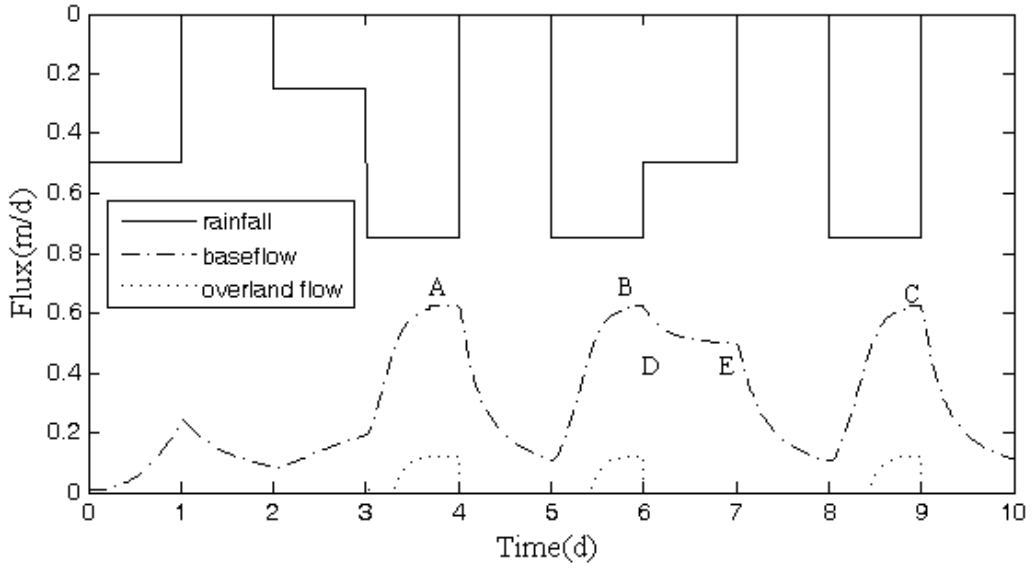


Figure 4.20: MESH soil model hydrograph, after repairs

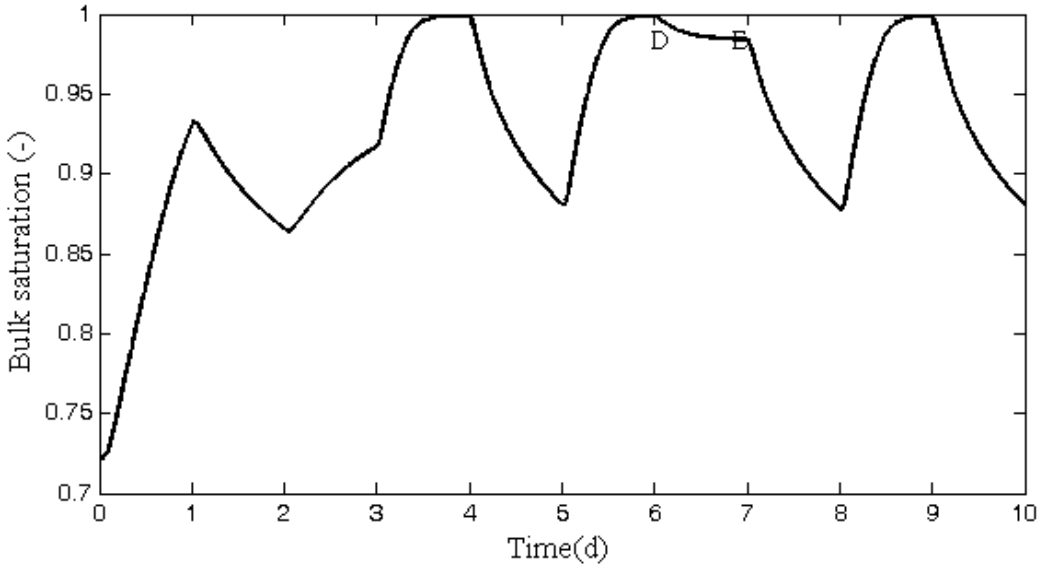


Figure 4.21: MESH soil model bulk saturation, after repairs

In comparing the modified soil model results (4.20 and 4.21) with the Richards' equation results (4.18 and 4.19), it is clear that the modified soil model is capable of replicating the Richards' equation hydrograph except for a lower response to the first rainfall event and underestimation of the overland flow. The lateral process has not been coupled and it is believed that the improved interflow algorithm is able to compensate the drawback by using a coupling soil moisture simulation process as follows.

### 4.2.3 Saturated Hillslope Coupling Method

As discussed in section 4.2.2, the uncoupled model underestimates overland flow when compared to the Richards' equation. This may be partly because MESH soil model tracks only the bulk saturation. The infiltration rate, $i$, is calculated based on this bulk saturation and typically controlled by the infiltration capacity for intense rainfall events. Such an approach is not unreasonable for infiltration on flat ground. However, on a hillslope, the downhill area often is observed to be saturated. In this area, overland flow can be generated during rainfall events, even if the average hillslope bulk saturation is less than 1. The infiltration into this saturated downslope area is constrained by the saturated hydraulic conductivity, e.g., $f = k_s$. This physical process has been observed in the field but has not

been addressed by the MESH soil model and is still imperfectly represented in many other hydrologic algorithms (e.g., TOPMODEL). In this lateral interflow study, a new algorithm is proposed to link vertical processes through physical connections on this saturated area to provide a more accurate physically-based soil moisture simulation process. Figure 4.22 shows the distinction between the uncoupled and coupled infiltration-interflow algorithms and the infiltration and interflow coupling process.

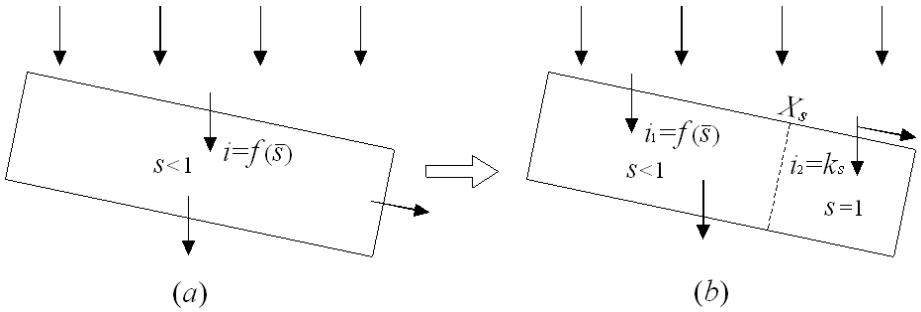


Figure 4.22: Evolution of the coupling process: (a) uncoupled: infiltration is a function of bulk saturation ($f = f(\bar{s})$); (b)coupled: infiltration is a function of bulk saturation for $X < X_s$ ($f_1 = f(\bar{s})$) and is equal to saturated hydraulic conductivity for $X > X_s$ ($f_2 = k_s$)(dashed line represents a water table)

As discussed in section 4.1, $X_s$ in Figure 4.22 represents the location of the interface between the saturated and unsaturated soil surface. This location is determined using the interflow solution of section 4.1. For the area uphill of $X_s$, infiltration is calculated using the standard Green-Ampt model while for the area downhill (located at $X > X_s$), the infiltration rate is limited by the saturated hydraulic conductivity. The mean infiltration rate can be determined by:

$$f = f_2 + (f_1 - f_2)\frac{X_s}{L} \tag{4.26}$$

Since more overland flow will be generated on the saturated area, the use of this approach will always result in less water infiltrating into the soil.

Various experiments are used here to investigate the effect of the coupled model on the soil moisture simulation process. Since the coupling process is aimed at the case where a dynamic saturated area exists, higher intensive rainfall events ($w > k_s$) have been used for all tests. For the case of $w < K_s$, all water from rainfall will infiltrate into the soil and no coupling process is required. In addition, the impact of soil anisotropy and

topography effects have also been assessed during the experiments. The base experiment was conducted on a sloping isotropic aquifer with a length of 400 meters and a slope of 0.01. Soil parameters for the base case are consistent with silt loam (using parameters from [45]) and the soil is initially dry with a saturation of 0.5.

Figure 4.23 compares the net contribution of each flow process to surface water for the uncoupled soil model and the coupled soil model. It demonstrates that for an isotropic soil, the interflow effect is very small. The coupled model replicates the amount of total runoff but causes a redistribution between the contributing processes. The overland flow increases and the baseflow consequently decreases, which implies that the use of the uncoupled model will result in an overestimated hydraulic conductivity when calibrated to the field measured data.

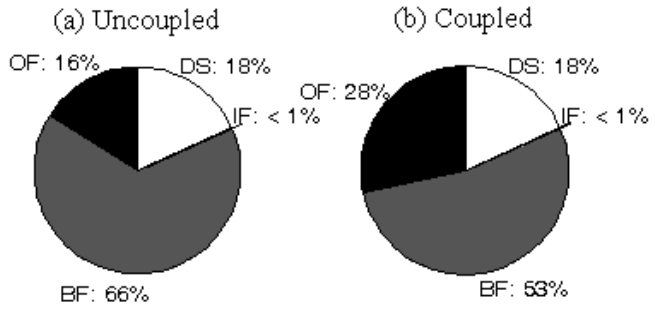


Figure 4.23: Flow components comparison for an isotropic soil: OF-Overland flow; BF-Baseflow; IF-Interflow; DS- Change in storage

Figure 4.24 depicts the hydrographs for both soil models. It demonstrates that the coupled soil model is capable of replicating the runoff peak except for the first rainfall event. Notice that the sloping aquifer is initially dry (with a saturation of 0.5). In such cases, the coupled soil model generates overland flow before the soil is fully saturated. The coupled model shows a delayed runoff peak as compared to the uncoupled soil model.

Figure 4.25 shows the bulk saturation for both soil models. Notice that at the end of the first rainfall event, the uncoupled model shows the soil is fully saturated. More water is entering into the soil and the bulk saturation for the coupled soil is unsaturated since most of rain becomes the overland flow. This also can be seen from rainfall events 2,3 and 4, in which the soil modeled by the coupled model becomes saturated later than that of the uncoupled model since less water being infiltrated during each rainfall event.

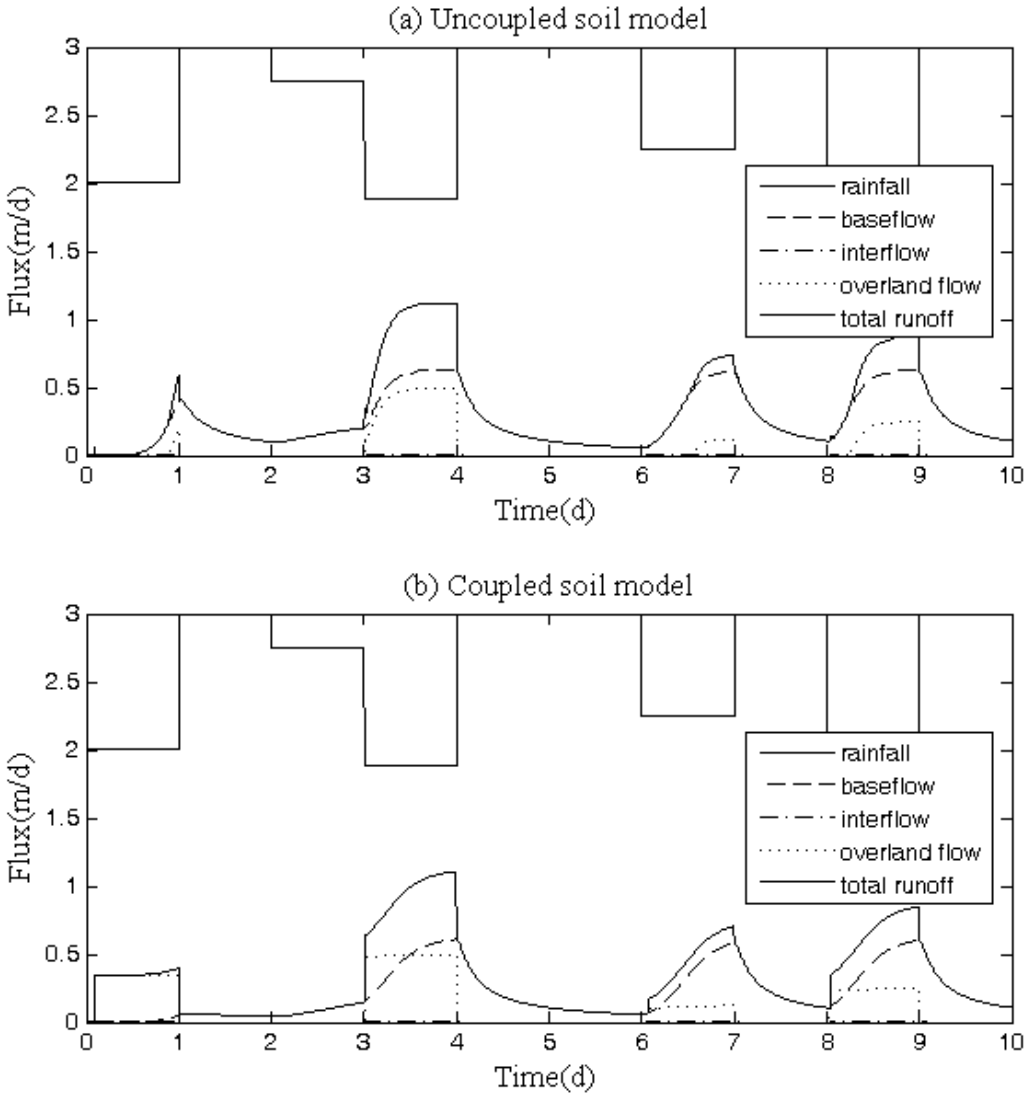


Figure 4.24: MESH soil model hydrograph

Figure 4.23 indicates that the amount of interflow is very small. To investigate what conditions are suitable for the improved interflow algorithm and how these conditions

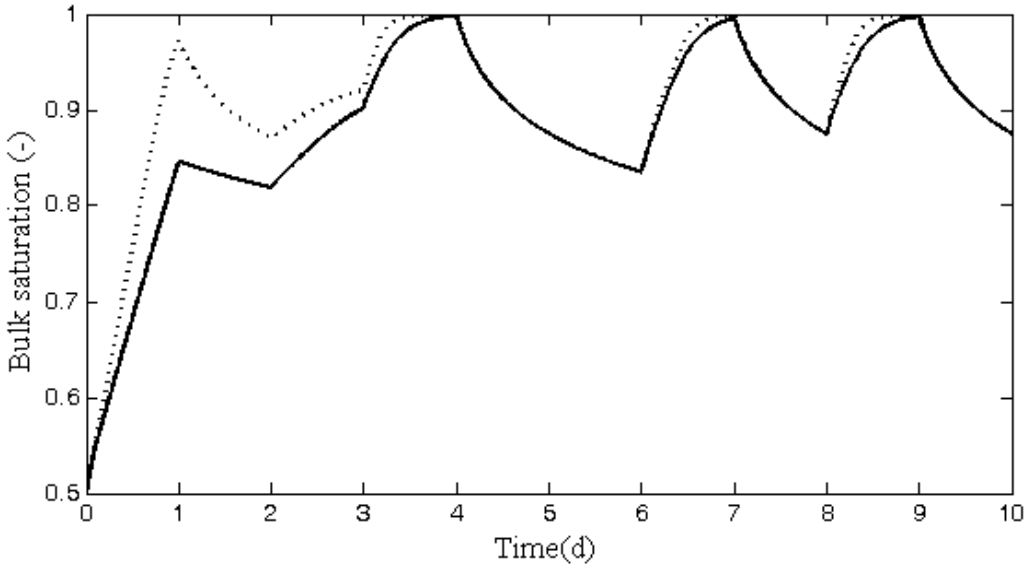


Figure 4.25: MESH soil model bulk saturation: Dot-uncoupled soil model; Solid line-coupled soil model

affect the algorithm behavior, experiments have been designed for anisotropic soils. Freeze and Cherry [52] addressed that in the field, the regional anisotropy values ($k_x$ : $k_y$) are commonly on the order of 100:1 or even larger. Here, the values of 100:1, 1000:1, and an extreme case 10000:1 are investigated. Figure 4.26 depicts the effect of anisotropy on the contributing processes. Not surprisingly, the interflow increases with increasing anisotropy and becomes extremely significant for high anisotropic soils, which indicates that for high anisotropic soils, the interflow is a crucial flow component and must be accounted for.

A topographic parameter, surface slope $\Lambda$, is being accounted for in the improved interflow algorithm. Tests were conducted on an anisotropic soil ($k_x$ : $k_y$=100:1) with various slopes from 0.01 to 0.5 to investigate the topographic effect on the soil moisture simulation process and implications for engineering practice. The results are shown in Figure 4.27. It can be seen that increasing slope increases interflow and decreases baseflow. Variation topographic parameters causes redistribution among the interflow, baseflow and overland flow.

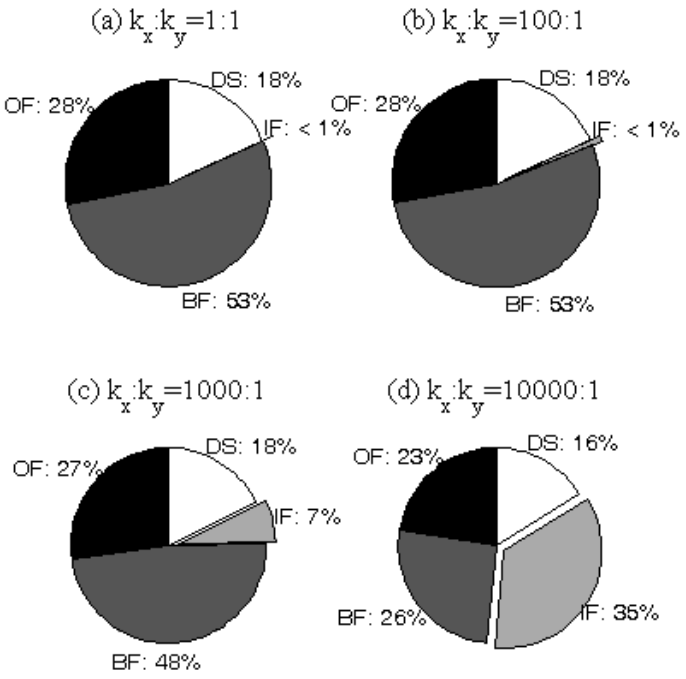


Figure 4.26: Anisotropy effect on flow components: OF-Overland flow; BS- Baseflow; IF-Interflow; DS- Change in storage

### 4.2.4 Impact of Soil Model Choice on Calibration

Most hydrologic models are a simplified representation of physical processes in the real world [145]. When the model conceptualization and the process of the real world are similar, the model parameters may be obtained by direct measurement of the real system [61]. However, at the current stage our knowledge of the land surface physics is unable to describe the real system perfectly. Hence, the concordance between the conceptual model and the real world is rarely acquired [61]. Moreover, the parameters in our models, such as that of soil hydraulic conductivity, do not necessarily correspond to physical parameters because of the heterogeneity of process response and unknown scale-dependence of parameters [15]. Consequently, some model parameters must be determined through calibration process to minimize the uncertainty [143]. Using different models will therefore lead to different parameter estimates.

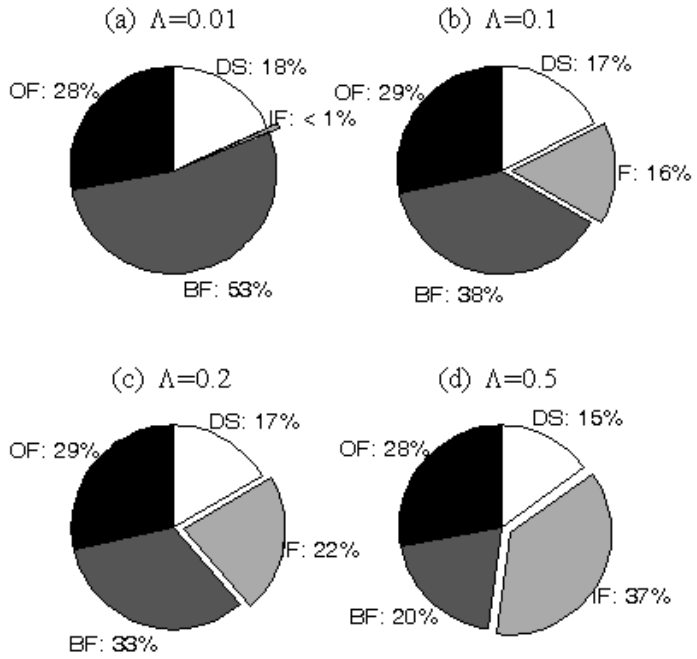


Figure 4.27: Topography effect on flow components for a anisotropic soil: OF-Overland flow; BF- Baseflow; IF-Interflow; DS- Change in storage

In this study, calibrating the stand alone soil model using the measured data is difficult since there is no data available. Here, the data from the coupled soil model was used as a benchmark to test the parameter accuracy of the uncoupled soil model. A heuristic optimization algorithm, Dynamically Dimensioned Search (DDS) algorithm [136], is used for calibrating the uncoupled soil model parameters to the output of the coupled soil model. The DDS algorithm "is a novel and simple stochastic single-solution based heuristic global search algorithm that was developed for the purpose of finding good global solutions (as opposed to globally optimal solutions) within a specified maximum objective function (or model) evaluation limit" [137].

The DDS algorithm automatically samples the parameters' values within the parameter boundaries. A subroutine code is written to read these values and puts them into the soil model input files. The DDS has been revised and can link all of these elements together and prompt the simulation process. The process is shown in Figure 4.28.

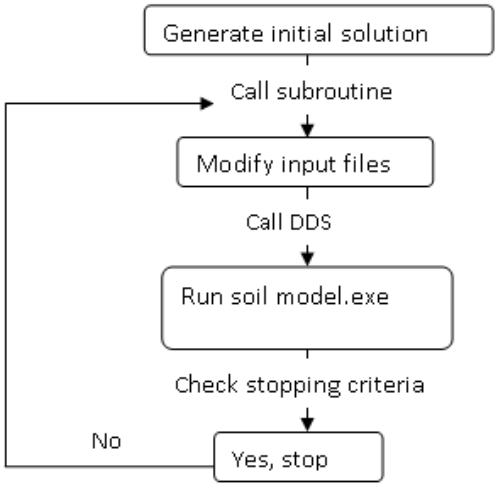


Figure 4.28: Representation of the calibration process

The objective function used here is the NASH-Sutcliffe coefficient, $R^2_{NS}$ [45]:

$$R^2_{NS} = 1 - \frac{\sum_{i=1}^{N} \left(Q_i - \hat{Q}_i\right)^2}{\sum_{i=1}^{N} \left(Q_i - m_Q\right)^2}$$

where $i$ is the $ith$ time series, $Q_i$ is measured values (coupled soil model overland flow here), $\hat{Q}_i$ is simulated values (uncoupled soil model overland flow here), and $m_Q$ is the average value of $Q$ for the period being simulated.

Saturated hydraulic conductivity, $k_s$, is selected as the optimization algorithm decision variable. The decision variable range was set to be $[1/4k_s, 2k_s]$. Figure 4.29 shows the flow components comparison for uncoupled/coupled soil model and calibrated uncoupled soil model. The calibrated hydraulic conductivity is $0.85k_s$, e.g., presuming the coupled soil model is more physically accurate, the uncoupled soil model overestimates the hydraulic conductivity. The overland flow percentage increases and the baseflow decreases after calibration, which is closer to the physically-based coupled soil model results.

Figure 4.30 is the hydrograph for uncoupled/coupled soil model and calibrated uncoupled soil model. Note that calibrated uncoupled soil model hydrograph is still off the coupled soil model hydrography, especially for the first rainfall event.

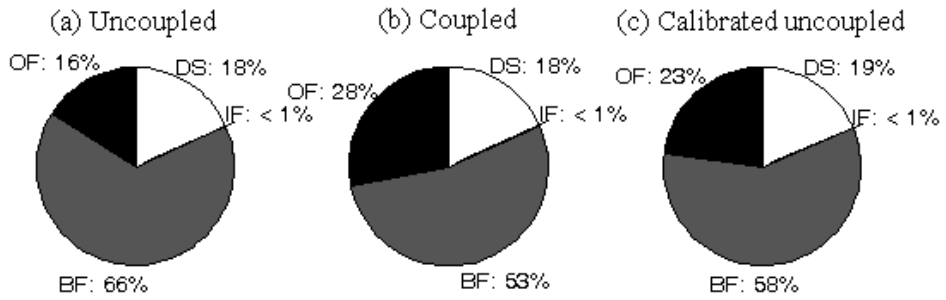


Figure 4.29: Flow components comparison for uncoupled/coupled soil model and one parameter calibrated uncoupled soil model: OF-Overland flow; BF- Baseflow; IF-Interflow; DS- Change in storage

A second calibration was conducted, varying three parameters: hydraulic conductivity, $k_s$, porosity, $\theta_s$, and air entry pressure, $\psi_0$. Figures 4.31 and 4.32 are the flow components comparisons and hydrgraphs. They show that with three parameters being calibrated, the uncoupled model is capable of replicating the coupled soil model results only by decreasing the hydraulic conductivity ($0.88k_s$), increasing the porosity ($1.05\theta_s$), and decreasing air entry pressure ($0.26\psi_0$).

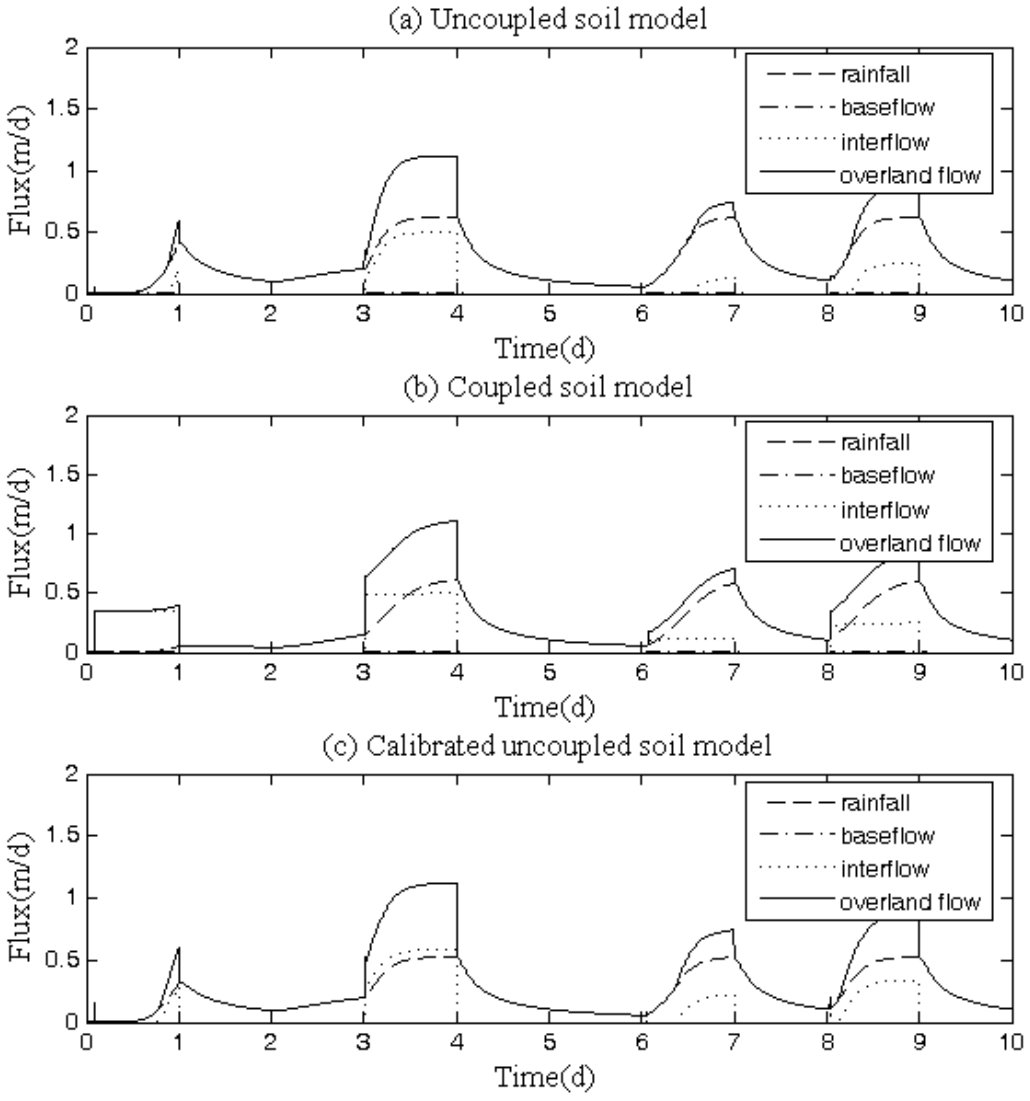


Figure 4.30: Hydrograph comparison, with only $k_s$ being calibrated

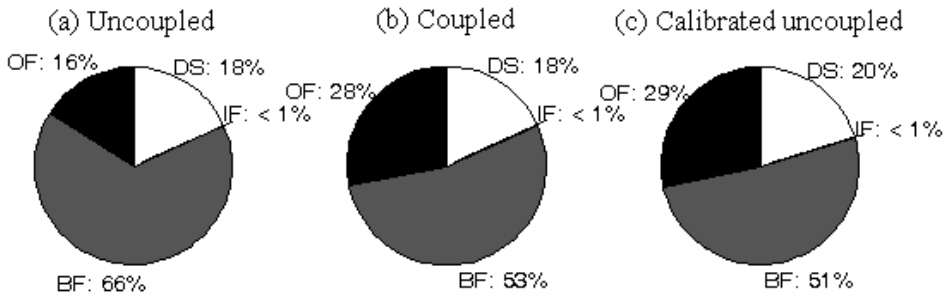


Figure 4.31: Flow components comparison for uncoupled/coupled soil model and three parameters calibrated uncoupled soil model: OF-Overland flow; BF- Baseflow; IF-Interflow; DS- Change in storage

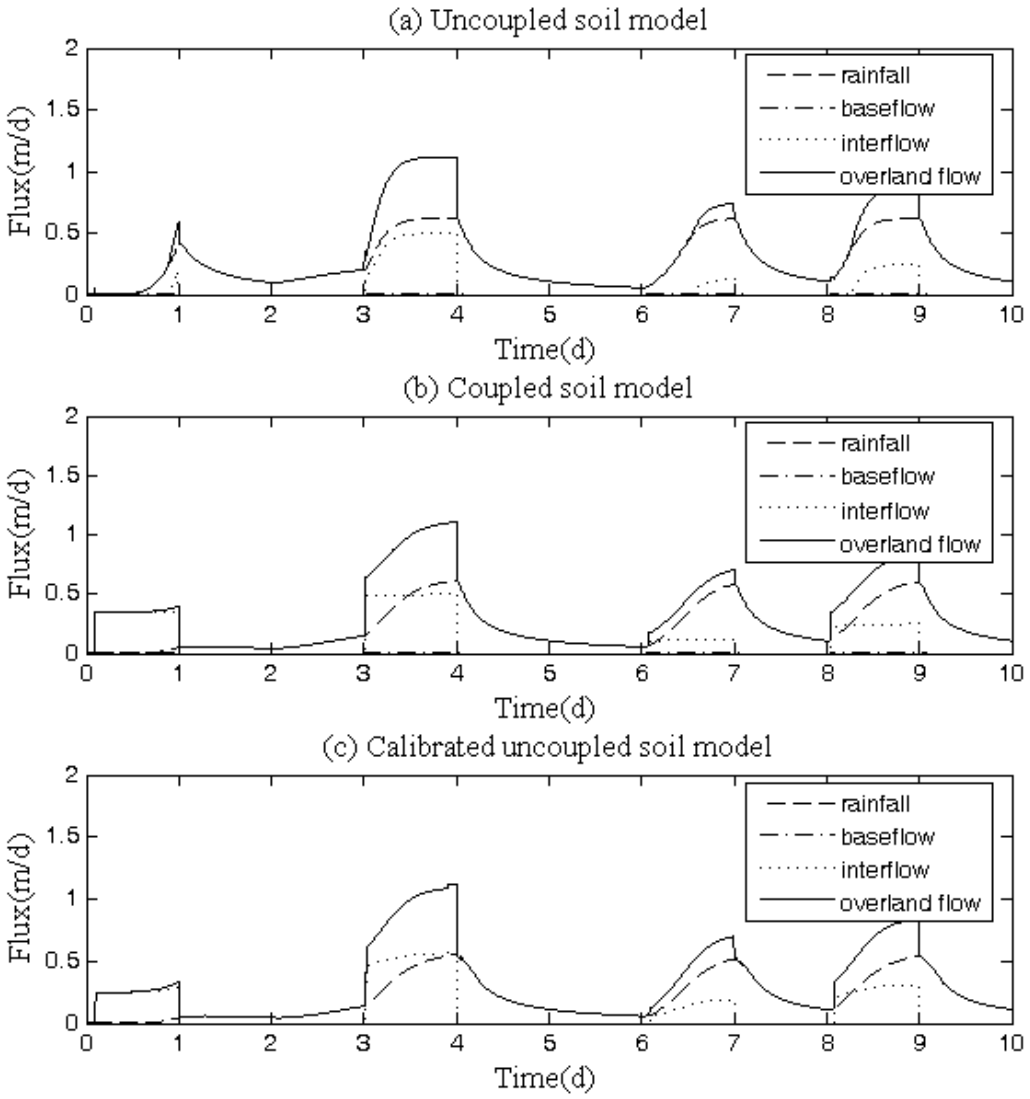


Figure 4.32: Hydrograph comparison, with three parameters, $k_s$, $\theta_s$, and $\psi_0$, being calibrated

## 4.3 Chapter Summary

An improved interflow algorithm and coupled infiltration-interflow algorithm were derived and tested in this chapter. The interflow algorithm was based upon an existing semi-analytical solution to the Richards' equation for wet soils and has been extended to dry soils using the conservation of energy analog to merge a semi-analytical gravity solution and a steady state solution. Both versions of the algorithms were evaluated against the numerical solution of Richards' equation and have been shown capable of reproducing the saturation and suction distributions under a wide range of conditions.

The updated interflow algorithm can be used to determine a dynamic saturated area at the surface (i.e., the contributing area for overland flow), allowing infiltration and interflow to be coupled, providing a more physically-based soil moisture simulation process. The algorithm has been incorporated into a stand alone hydrology-land surface scheme MESH soil model. The coupled model replicated the total amount of runoff of the uncoupled soil model, but caused redistribution among the contributing processes. As expected, the overland flow increased and the base flow decreased due to more overland flow generated on the saturated area. The results indicate that the MESH effective hydraulic conductivity will be always smaller than the field measurements in order to compensate for an underestimated overland flow. This was verified through a number of calibration tests in section 4.2.4.

The improved interflow algorithm was developed and tested against rigorous numerical solutions and is capable of representing the boundary flux as a function of soil internal states. It couples the infiltration and interflow processes to provide a more realistic manner of hydrograph and is suitable for incorporation into distributed hydrological models and land surface schemes.

# Chapter 5

# Conclusions

The primary contribution of this thesis is a set of efficient physically-based algorithms for near surface flow simulation. Multiple approaches were taken to provide improved relationships for infiltration and lateral drainage, fluxes and storage. These algorithms were tested against a specialized Richards' equation for sloping soils and Monte Carlo simulations and demonstrated both reasonable accuracy and improved physical representation of hydrological processes observed in the field.

## 5.1 A Summary of Major Findings

### 5.1.1 Applicability of the Green-Ampt (GA) Infiltration Model

Applicability of the GA infiltration models is limited when shallow boundary conditions are present. Neglecting shallow boundary conditions in the traditional GA leads to an overestimation in the amount of infiltrated water. As a result, hydrological models that rely upon the traditional GA infiltration model may improperly estimate runoff. For such hydrological models, modifications to the GA model are necessary in order to obtain an accurate water budget in domains with shallow overburden or a shallow water table. 'Effective' hydraulic conductivities estimated using manual or automatic calibration may be compensating for this effect, leading to smaller-than-expected hydraulic conductivity estimates. If these conductivities are used elsewhere in the model (e.g., for baseflow or interflow calculation), accurate estimates of other hydrological fluxes may potentially be compromised. The impact of vertical heterogeneity in saturated conductivity was also investigated

with regard to how it may impact the appropriateness of the GA infiltration model. It was found that the GA applicability decreases with increasing vertical heterogeneity. An interesting phenomena found in this study is that, although the heterogeneity was not considered in the traditional GA model, the model is capable of reproducing the RE with vertical heterogeneous behavior of the RE within a reasonable deviation ($\sigma \leq 0.5$).

Guided by the comparison between the GA infiltration model and numerical solutions to the Richards' equation, various simple revisions to the GA infiltration model with shallow boundary conditions were suggested. Results demonstrated that even when the traditional assumptions were relaxed, the GA model often still provides reasonable results for regional-scale analysis and could be amended to account for conditions for which it was not intended.

### 5.1.2 Regional Heterogeneity in Infiltration

Regional heterogeneity is very important in hydrologic processes, especially in determining surface and subsurface runoff separation. What is found in this study is that when estimated from automatic or manual calibration to appropriate field data, the calculated hydraulic conductivity will not correspond to the average conductivity in the domain, but rather underestimates the conductivity by a factor proportional to the degree of spatial variability, i.e., with a high degree of heterogeneity, the upscaled solution generates more surface runoff and less infiltration than the "equivalent" point scale solution.

A new set of formulae for calculating regionally-averaged infiltration rates into heterogeneous soils with heterogeneous initial conditions was presented. The solutions were based upon an upscaled approximation of the explicit Green-Ampt infiltration solution, and required specification of the spatial distribution of saturated hydraulic conductivity and/or initial soil water deficit in the subbasin. The approximations have been evaluated against Monte Carlo simulations and shown to produce results accurate to 3% of the computationally-intensive exact cases, at a computational cost similar to the original Green-Ampt formula without upscaling. A critical result here is that the upscaled form of the Green-Ampt equation is behaviorally different than the point-scale solution with upscaled parameters, indicating that calibration alone is insufficient to correctly replicate the infiltration process in heterogeneous media.

### 5.1.3 Coupling interflow and infiltration processes

Soil lateral flow has been recognized to be an important subsurface runoff component but the most appropriate means of calculating lateral unsaturated flow form hillslopes has yet

to be identified. An analytical interflow algorithm for variably saturated hillslopes was developed, rigorously tested against numerical solutions, and updated in this study. The updated interflow algorithm can be used to determine a dynamic saturated area at the surface (i.e., the contributing area for overland flow), allowing infiltration and interflow to be coupled, providing a more physically-based soil moisture simulation process. The algorithm has been incorporated into a stand alone hydrology-land surface scheme MESH soil model. The coupled model replicated the total amount of runoff of the uncoupled soil model, but causes redistribution among the contributing processes. As expected, the overland flow increased and the base flow decreased due to more overland flow generated on the saturated area. The results indicate that the MESH effective hydraulic conductivity will be always smaller than the field measurements in order to compensate for an underestimated overland flow. This was verified through a number of calibration tests.

It was also found that isotropy and topography have significant effects on the soil moisture simulation process. High anisotropy will result in an increasing subsurface runoff while decreasing surface runoff. The amount of interflow increases with increasing slope. The improved algorithm couples the infiltration and interflow processes on the dynamic saturated area to provide a better understanding of hydrograph components and is suitable for incorporation into distributed hydrological models and land surface schemes.

# APPENDICES

# Appendix A

# FORTRAN Code for Numerical Solution to Richards' Equation

```
do kkk=1,maxit                  ! Begin of the Picard iteration
   piccrit=0.0
   phip=phi
   do kk=1,itmax                  ! Begin of the SOR
      crit=0.0
      do i=1,ncols-1
         cleft=1.0
         cright=1.0
         if (i==2) then
            cleft=8.0/3.0
            cright=4.0/3.0
         end if
         if (i==ncols-1) then
            cleft=4.0/3.0
            cright=8.0/3.0
         end if
 !
         do j=1,nrows
            cup=1.0
            cdown=1.0
            if (j==2) then
               cup=4.0/3.0
```

```
            cdown=8.0/3.0
          end if
          if (j==nrows-1) then
              cup=8.0/3.0
              cdown=4.0/3.0
          end if
 icr=ip(i)+j
 phiold=phi(icr)
 if (i==1) then    ! left boundary
     b(icr)=(2.0*leftflux/(k(icr)+k(icr+nrows))-v)*delx/2.0
     phi(icr)=(1.0-w)*phi(icr)+w*(b(icr)-(-1.0*phi(icr+nrows)))/1.0
 elseif (i==ncols) then  ! right boundary
     b(icr)=(2.0*rightflux/(k(icr)+k(icr-nrows))-v)*delx/2.0
     phi(icr)=(1.0-w)*phi(icr)+w*(b(icr)-1.0*phi(icr-nrows))/(-1.0)
 elseif (j==1) then    ! bottom boundary
     b(icr)=(2.0*botflux/(k(icr)+k(icr+1))+1.0)*dely/2.0
     phi(icr)=(1.0-w)*phi(icr)+w*(b(icr)-(-1.0*phi(icr+1)))/1.0
 elseif (j==nrows) then  ! top boundary
     b(icr)=(2.0*topflux/(k(icr)+k(icr-1))+1.0)*dely/2.0
     phi(icr)=(1.0-w)*phi(icr)+w*(b(icr)-1.0*phi(icr-1))/(-1.0)
 else
 !******************** RHL' (A) and LHS (b) ************************
if (kind==1) then  ! Arithematic mean
   kinileft=(kini(icr)+kini(icr-nrows))/2.0
   kiniup=(kini(icr)+kini(icr+1))/2.0
   kinidown=(kini(icr)+kini(icr-1))/2.0
   kiniright=(kini(icr)+kini(icr+nrows))/2.0
   !
   kleft=(k(icr)+k(icr-nrows))/2.0
   kup=(k(icr)+k(icr+1))/2.0
   kdown=(k(icr)+k(icr-1))/2.0
   kright=(k(icr)+k(icr+nrows))/2.0
elseif (kind==2) then  ! Harmonic mean
   kinileft=2.0*kini(icr)*kini(icr-nrows)/(kini(icr)+kini(icr-nrows))
   kiniup=2.0*kini(icr)*kini(icr+1)/(kini(icr)+kini(icr+1))
   kinidown=2.0*kini(icr)*kini(icr-1)/(kini(icr)+kini(icr-1))
   kiniright=2.0*kini(icr)*kini(icr+nrows)/(kini(icr)+kini(icr+nrows))
   !
```

```
              kleft=2.0*k(icr)*k(icr-nrows)/(k(icr)+k(icr-nrows))
   kup=2.0*k(icr)*k(icr+1)/(k(icr)+k(icr+1))
   kdown=2.0*k(icr)*k(icr-1)/(k(icr)+k(icr-1))
   kright=2.0*k(icr)*k(icr+nrows)/(k(icr)+k(icr+nrows))
elseif (kind==3) then  ! Geometric mean
   kinileft=(kini(icr)*kini(icr-nrows))**0.5
   kiniup=(kini(icr)*kini(icr+1))**0.5
   kinidown=(kini(icr)*kini(icr-1))**0.5
   kiniright=(kini(icr)*kini(icr+nrows))**0.5
   !
              kleft=(k(icr)*k(icr-nrows))**0.5
   kup=(k(icr)*k(icr+1))**0.5
   kdown=(k(icr)*k(icr-1))**0.5
   kright=(k(icr)*k(icr+nrows))**0.5
     endif
 A=(1.0-lambda)*(cright*kiniright/delx**2.0*phiini(icr+nrows)+ &
  &                cleft*kinileft/delx**2.0*phiini(icr-nrows)+ &
  &                    cup*kiniup/dely**2.0*phiini(icr+1)+     &
  &                cdown*kinidown/dely**2.0*phiini(icr-1)-     &
  &             (cright*kiniright/delx**2.0+                   &
  &                cleft*kinileft/delx**2.0+                   &
  &                    cup*kiniup/dely**2.0+                   &
  &                cdown*kinidown/dely**2.0)*phiini(icr)-      &
  &              v*(kiniright-kinileft)/delx+                  &
  &             (kiniup-kinidown)/dely)
            b(icr)=-(lambda*(Ss*theta(icr)/thetas+c(icr))+
  & (1.0-lambda)*(Ss*thetaini(icr)/thetas+cini(icr)))*phiini(icr)/delt- &
  &       lambda*(-v*(kright-kleft)/delx+(kup-kdown)/dely)-A
 if (i==2 .or. i==ncols-1) then
     A=(1.0-lambda)*(cright*kiniright/delx**2.0*phiini(icr+nrows)+&
      &                cleft*kinileft/delx**2.0*phiini(icr-nrows)+ &
      &                    cup*kiniup/dely**2.0*phiini(icr+1)+     &
      &                cdown*kinidown/dely**2.0*phiini(icr-1)-     &
      &             (cright*kiniright/delx**2.0+                   &
      &                cleft*kinileft/delx**2.0+                   &
      &           cup*kiniup/dely**2.0+                     &
      &                cdown*kinidown/dely**2.0)*phiini(icr)-      &
      &   4.0/3.0*v*(kiniright-kinileft)/delx+                     &
```

```
     &             (kiniup-kinidown)/dely)
         b(icr)=-(lambda*(Ss*theta(icr)/thetas+c(icr))+                &
          & (1.0-lambda)*(Ss*thetaini(icr)/thetas+cini(icr)))*phiini(icr)/delt-&
          &       lambda*(-4.0/3.0*v*(kright-kleft)/delx+(kup-kdown)/dely)-A
       endif
       if (j==2 .or. j==nrows-1) then
         A=(1.0-lambda)*(cright*kiniright/delx**2.0*phiini(icr+nrows)+ &
          &                cleft*kinileft/delx**2.0*phiini(icr-nrows)+ &
          &                    cup*kiniup/dely**2.0*phiini(icr+1)+     &
          &                cdown*kinidown/dely**2.0*phiini(icr-1)-     &
          &             (cright*kiniright/delx**2.0+                   &
          &                cleft*kinileft/delx**2.0+                   &
          &                    cup*kiniup/dely**2.0+                   &
          &                cdown*kinidown/dely**2.0)*phiini(icr)-      &
          &            v*(kiniright-kinileft)/delx+                    &
          &      4.0/3.0*(kiniup-kinidown)/dely)
         b(icr)=-(lambda*(Ss*theta(icr)/thetas+c(icr))+                &
        & (1.0-lambda)*(Ss*thetaini(icr)/thetas+cini(icr)))*phiini(icr)/delt- &
        &       lambda*(-v*(kright-kleft)/delx+4.0/3.0*(kup-kdown)/dely)-A
       endif
         !******************** End of RHL' and LHS*********************
          ! SOR
          phi(icr)=(1.0-w)*phi(icr)+                                   &
         & w*(b(icr)-                                                  &
         &           lambda*(cleft*kleft/delx**2.0*phi(icr-nrows)+  &
         &                   cdown*kdown/dely**2.0*phi(icr-1)+      &
         &                       cup*kup/dely**2.0*phi(icr+1)+      &
         &                   cright*kright/delx**2.0*phi(icr+nrows)))/&
         &         (-lambda*(cleft*kleft/delx**2.0+                  &
         &                   cdown*kdown/dely**2.0+                  &
         &                       cup*kup/dely**2.0+                  &
         &                   cright*kright/delx**2.0)-               &
         &     (1.0-lambda)*(Ss*thetaini(icr)/thetas+cini(icr))/delt)
             endif
!  if (phi(icr)>=phiini(icr)) phi(icr)=phiini(icr)
             diff=dabs(phi(icr)-phiold)
             if (diff>crit) crit=diff
          enddo
```

```
      enddo
      if (crit<tol) exit
   enddo                              ! End of SOR
   ! update the material properties for next Picard iteration
   do i=1,ncols
      do j=1,nrows
         icr=ip(i)+j
         call soil(icr,phi,theta,c,k,scind,stind,thetas,ks,s,cc)
         if (j==2 .and. i>=2 .and. i<=ncols-1) th_accu=th_accu+theta(icr)*delx
  enddo
   enddo
   piccrit=maxval(dabs(phip(1:nrows*ncols)-phi(1:nrows*ncols)))
   if (piccrit<tol) exit
enddo    ! end of the Picard iteration
```

# Appendix B

# Upscaled Green-Ampt Model for Spatial Variability in Initial Condition

## B.1 Upscaled Solution Derivation

Recall the linear approximation for the GA infiltration rate

$$f(t) = \min\left(w, \frac{k_s}{X}\right) + \epsilon(k_s, X)$$

and the upscaled GA solution for homogenous conductivity and heterogenous initial condition:

$$\bar{f}(t) = \int_0^\infty f(X(t,\alpha)) \cdot f_\alpha(\alpha) d\alpha$$

Soil initial condition is here assumed to be a random variable represented by using a standard normal distribution:

$$f_\alpha(\alpha) = \frac{1}{\sigma_\alpha\sqrt{2\pi}} e^{-\frac{(\alpha-\mu_\alpha)^2}{2\sigma_\alpha^2}}$$

Therefore,

$$\begin{aligned} \bar{f}(t) &= \int_0^\infty f(X(t,\alpha)) \cdot f_\alpha(\alpha) d\alpha \\ &= \int_0^{\alpha_0} k_s\left(1 + \frac{\alpha}{wt}\right) \frac{1}{\sigma_\alpha\sqrt{2\pi}} e^{-\frac{(\alpha-\mu_\alpha)^2}{2\sigma_\alpha^2}} d\alpha + \int_{\alpha_0}^\infty w \frac{1}{\sigma_\alpha\sqrt{2\pi}} e^{-\frac{(\alpha-\mu_\alpha)^2}{2\sigma_\alpha^2}} d\alpha \end{aligned} \quad \text{(B.1)}$$

where $\alpha_0$ is determined by:

$$w = k_s\left(1+\frac{\alpha_0}{wt}\right) \Longrightarrow \alpha_0 = \left(\frac{w}{k_s}-1\right)wt$$

Now, equation B.1 can be written as:

$$\begin{aligned}
\bar{f}(t) &= \int_0^{\left(\frac{w}{k_s}-1\right)wt} k_s\left(1+\frac{\alpha}{wt}\right)\frac{1}{\sigma_\alpha\sqrt{2\pi}}e^{-\frac{(\alpha-\mu_\alpha)^2}{2\sigma_\alpha^2}}d\alpha + \int_{\left(\frac{w}{k_s}-1\right)wt}^{\infty} w\frac{1}{\sigma_\alpha\sqrt{2\pi}}e^{-\frac{(\alpha-\mu_\alpha)^2}{2\sigma_\alpha^2}}d\alpha \\
&= -\frac{k_s}{2\sqrt{2\pi}wt}\left[2\sigma_\alpha e^{-\frac{(\mu_\alpha-\alpha)^2}{2\sigma^2}} + \sqrt{2\pi}(\mu_\alpha+wt)erf\left(\frac{\mu_\alpha-\alpha}{\sqrt{2}\sigma}\right)\right]\Bigg|_0^{\left(\frac{w}{k_s}-1\right)wt} \\
&\quad -\frac{w}{2}\,erf\left(\frac{\mu_\alpha-\alpha}{\sqrt{2}\sigma}\right)\Bigg|_{\left(\frac{w}{k_s}-1\right)wt}^{\infty} \\
&= \frac{k_s}{2\sqrt{2\pi}wt}\left\{2\sigma_\alpha e^{-\frac{\mu_\alpha^2}{2\sigma^2}} + \sqrt{2\pi}(\mu_\alpha+wt)erf\left(\frac{\mu_\alpha}{\sqrt{2}\sigma}\right) - 2\sigma_\alpha e^{-\frac{\left[\mu_\alpha-\left(\frac{w}{k_s}-1\right)wt\right]^2}{2\sigma_\alpha^2}} - \right. \\
&\quad \left.\sqrt{2\pi}(\mu_\alpha+wt)erf\left[\frac{u-\left(\frac{w}{k_s}-1\right)wt}{\sqrt{2}\sigma_\alpha}\right]\right\} - \frac{w}{2}\left\{-1-erf\left[\frac{\mu_\alpha-\left(\frac{w}{k_s}-1\right)wt}{\sqrt{2}\sigma_\alpha}\right]\right\} \\
&= \frac{k_s\sigma_\alpha e^{-\frac{\mu_\alpha^2}{2\sigma_\alpha^2}}}{\sqrt{2\pi}wt} + \frac{k_s(\mu_\alpha+wt)erf\left(\frac{\mu_\alpha}{\sqrt{2}\sigma_\alpha}\right)}{2wt} - \frac{k_s\sigma_\alpha e^{-\frac{\left[\mu_\alpha-\left(\frac{w}{k_s}-1\right)wt\right]^2}{2\sigma_\alpha^2}}}{\sqrt{2\pi}wt} - \\
&\quad \frac{k_s(\mu_\alpha+wt)erf\left[\frac{u-\left(\frac{w}{k_s}-1\right)wt}{\sqrt{2}\sigma_\alpha}\right]}{2wt} + \frac{w}{2} + \frac{w}{2}erf\left[\frac{\mu_\alpha-\left(\frac{w}{k_s}-1\right)wt}{\sqrt{2}\sigma_\alpha}\right] \\
&= \frac{w}{2} + \frac{w}{2}erf(A) + \frac{k_s\sigma_\alpha}{\sqrt{2\pi}wt}\left(e^{-B^2}-e^{-A^2}\right) + \frac{k_s(\mu_\alpha+wt)}{2wt}\left[erf(B)-erf(A)\right] \quad \text{(B.2)}
\end{aligned}$$

where

$$A = \frac{\mu_\alpha-\left(\frac{w}{k_s}-1\right)wt}{\sqrt{2}\sigma_\alpha}$$

$$B = \frac{\mu_\alpha}{\sqrt{2}\sigma_\alpha}$$

Note that the limitation of equation B.2 as $\sigma_\alpha$ approaches 0 is,

$$\bar{f}(t) = \begin{cases} w & \mu_\alpha \leq \left(\frac{w}{k_s} - 1\right) \\ k_s\left(\frac{\mu_\alpha}{wt} + 1\right) & \mu_\alpha > \left(\frac{w}{k_s} - 1\right) \end{cases} \tag{B.3}$$

which is the linear approximation to the GA infiltration rate.

The evaluation of the saturated area, $A_s$, is:

$$\begin{aligned} A_s(t) &= A\int_0^{\frac{w}{k_s}-1} f_\alpha(\alpha)d\alpha \\ &= A\int_0^{\frac{w}{k_s}-1} \frac{1}{\sigma_\alpha\sqrt{2\pi}} e^{-\frac{(\alpha-\mu_\alpha)^2}{2\sigma_\alpha^2}} d\alpha \\ &= -\frac{A}{2}\, erf\left(\frac{\mu_\alpha - \alpha}{\sqrt{2}\sigma_\alpha}\right)\Bigg|_0^{\frac{w}{k_s}-1} \\ &= -\frac{A}{2} erf\left(\frac{\mu_\alpha - \left(\frac{w}{k_s} - 1\right)}{\sqrt{2}\sigma_\alpha}\right) + \frac{A}{2} erf\left(\frac{\mu_\alpha}{\sqrt{2}\sigma}\right) \end{aligned} \tag{B.4}$$

## B.2 C++ Code for Upscaled Green-Ampt Model

```
#include <math.h>
#include <iostream>
#include <iomanip>
#include <fstream>
#include <string>
using namespace std;

const double PI=3.141592653589793238;
inline void        lowerswap(double &u,const double v){if (v<u){u=v;}}
inline void        upperswap(double &u,const double v){if (v>u){u=v;}}
double CalcPondingTime(const double &alpha, const double &Ks,const double &w);

/*-------------------------------------------------------------
 Calculate X
-------------------------------------------------------------
```

```
returns dimensionless time, X from dimensionless time t* =w*t/alpha
-------------------------------------------------------------*/
double CalcX(const double &tstar)
{
  if (tstar==0.0){return 0.0;}
return 1.0/(1.0/tstar+1.0);
}
/*-------------------------------------------------------------
 Calculate t*
-------------------------------------------------------------
returns dimensionless time, t* =w*t/alpha from dimensionless time X
-------------------------------------------------------------*/
double CalcTstar(const double &X)
{
  if (X==0.0){return 0.0;}
  if (X==1.0){return 1e10;}
return 1.0/(1.0/X-1.0);
}
/*-------------------------------------------------------------
 erfc(x)
-------------------------------------------------------------
complementary error function
-------------------------------------------------------------*/
double erfc(const double &x)
{
//From Charbeneau, Groundwater Hydraulics and Pollutant Transport, 2000
double tmp(fabs(x)); //take abs so that we are always in positive quadrant.
static double fun;
static double f1;
static double tmp2;
static double tmp3;

if(tmp > 3.0){
f1  = (1.0 - 1.0/(2.0 * tmp * tmp)
       + 3.0/(4.0 * pow(tmp,4))
       - 5.0/(6.0 * pow(tmp,6)));
fun = f1 * exp(-tmp * tmp) / (tmp * sqrt(PI));
}
```

```
else{
tmp2 = 1.0 / (1.0 + (0.3275911 * tmp));
tmp3 =   0.254829592  * tmp2       //5th order polynomial interpolation
   - (0.284496736 * tmp2 * tmp2)
   + (1.421413741 * pow(tmp2,3))
   - (1.453152027 * pow(tmp2,4))
   + (1.061405429 * pow(tmp2,5));
fun = tmp3 * exp(-tmp * tmp);
}
if (tmp == x) {return fun;}
else{return (2-fun);}
}
/*------------------------------------------------------------
 erf(x)
------------------------------------------------------------
 error function
------------------------------------------------------------*/
double erf(const double &x)
{
return 1-erfc(x);
}
/*------------------------------------------------------------
 falpha(k;mu,sig)
------------------------------------------------------------
normal probability distribution of alpha given mean and std dev
(mu_Y and sig_Y) of distribution
------------------------------------------------------------*/
double falpha(const double &alpha, const double &mu_Y, const double &sig_Y)
{
return 1.0/sig_Y/sqrt(2.0*PI)*exp(-(pow(alpha-mu_Y,2)/sig_Y/sig_Y/2.0));
}
/*------------------------------------------------------------
 Smooth GA
------------------------------------------------------------
analytical / semi-analytical upscaling of GA infiltration with
spatially variable alpha
if eps_in=0, then only linear approximation (eqn 10 from Craig et al)
         =1, then use dirac approx of epsilon integral
```

```
 =2, then use 2pt gauss integration of epsilon integral
 =3, then numerically integrate epsilon integral
 =4, then numerically integrate everything
-------------------------------------------------------------*/
double Smooth_GA_alpha( const double &t,
const double &Ks,
const double &mu_Y,
const double &sig_Y,
const double &w,
int eps_in)
{
//eqn 10 from text
double sum =0.0;
    //upper limit (wX) in normalized Y space
double A   =(mu_Y-(w/Ks-1.0)*w*t)/sig_Y/sqrt(2.0);
double B   =mu_Y/sig_Y/sqrt(2.0);
if (sig_Y==0 && mu_Y>=(w/Ks-1.0)*w*t){A=1e99;}
if (sig_Y==0 && mu_Y<(w/Ks-1.0)*w*t){A=-1e99;}
if (sig_Y==0) {B=1e99;}
    if (eps_in==0)
{
sum+=0.5*(erf(B)-erf(A));
}
else if (eps_in==1)
{
//numerically integrated (working):
double maxalp=(mu_Y-(w/Ks-1)*w*t)/sig_Y/sqrt(2.0);
double minalp=mu_Y-4*sig_Y;
double dalp=(maxalp-minalp)/25000;//needs really high resolution!
double integ(0.0),alpi;
for (double alp=minalp;alp<maxalp;alp+=dalp)
{
alpi=(alp+0.5*dalp);
integ+=falpha(alpi,mu_Y,sig_Y)*dalp;
}
sum=integ;//overwrites linear approximation

}
```

```
return sum;
}
void main()
{
//double kow;
double X;
double t;
double w=4.0;
double Ks=0.4*w;
ofstream OUT;
OUT.open("GASmoothing.csv");

//plot results of MC versus smoothing
//Header
double alphabar=3.0;// 3.12
double mu_Y;
int num_real=25000;
OUT<<"Ks="<<Ks<<endl;
OUT<<"alphabar="<<alphabar<<endl;
OUT<<"w="<<w<<endl;
OUT<<"t,X,";
for (double sig=0.0;sig<=3.0+0.0001;sig+=0.5)
{
OUT<<"sigma="<<sig<<",";
//OUT<<"sig="<<sig<<"(NUM),";
}
OUT<<endl;
//data:
for (X=0.00001;X<=1.0001;X+=0.01)
{
t=CalcTstar(X)*alphabar/w;
        OUT<<t<<","<<X<<",";
for (double sig=0.0;sig<=3.0+0.0001;sig+=0.5)
{
mu_Y=alphabar;
OUT<<Smooth_GA_alpha(t,Ks,mu_Y,sig,w,0)<<",";
//OUT<<Smooth_GA_alpha(t,Ks,mu_Y,sig,w,1)<<",";
}
```

```
OUT<<endl;
}
cout<<"Completed"<<endl;
}
```

# Appendix C

# WATDRAIN1 Interflow Algorithm

## C.1 A Semi-analytical Solution to the Amended Richards' Equation

One dimensional Richards' equation for a slopping aquifer can be expressed as:

$$\theta_s \frac{\partial s}{\partial t} = \frac{\partial}{\partial X}\left(k\frac{\partial \psi}{\partial X} + k\frac{\Lambda}{\sqrt{1+\Lambda^2}}\right) \tag{C.1}$$

The suction gradient, $\frac{\partial \psi}{\partial X}$, can be neglected to result in:

$$\theta_s \frac{\partial s}{\partial t} = \frac{\Lambda}{\sqrt{1+\Lambda^2}}\frac{\partial k}{\partial X} \tag{C.2}$$

Substituting Clapp-Hornberger functions into equation C.2:

$$\theta_s \frac{\partial s}{\partial t} = \frac{k_s \Lambda c s^{c-1}}{\sqrt{1+\Lambda^2}}\frac{\partial s}{\partial X} \tag{C.3}$$

Solving equation C.3 by separation of variables. Assuming $s = AX^B t^D$:

$$\frac{\partial s}{\partial X} = ABx^{B-1}t^D = \frac{B}{x}s$$

$$\frac{\partial s}{\partial t} = ADx^B t^{D-1} = \frac{D}{t}s$$

Back substitute above equations into equation C.3:

$$\theta_s \frac{D}{t} s = \frac{k_s \Lambda c s^{c-1}}{\sqrt{1+\Lambda^2}} \frac{B}{X} s$$

$$\theta_s \frac{D}{t} = \frac{k_s \Lambda c}{\sqrt{1+\Lambda^2}} A^{c-1} B X^{B(c-1)-1} t^{D(c-1)}$$

One can get:

$$\begin{cases} B(c-1) - 1 = 0 \\ D(c-1) = -1 \\ \frac{k_s \Lambda c}{\sqrt{1+\Lambda^2}} = \theta_s D \end{cases} \tag{C.4}$$

Therefore,

$$\begin{cases} B = \frac{1}{c-1} \\ D = -\frac{1}{c-1} \\ A = \left( \frac{\theta_s \sqrt{1+\Lambda^2}}{k_s \Lambda c} \right)^{\frac{1}{c-1}} \end{cases} \tag{C.5}$$

Final solution can be written as:

$$s = \left( \frac{\theta_s \sqrt{1+\Lambda^2}}{k_s \Lambda} \cdot \frac{x}{t} \right)^{\frac{1}{c-1}}$$

## C.2 Bulk Saturation Derivation

As discussed in Chapter 4, section 4.1, soil drainage process can be divided into three stages dependent on the saturation at the outflow level: a high saturated stage ($0 \leq t \leq t_c$); an intermediate stage ($t_c < t < t_b$); and a dry stage ($t \geq t_b$). Bulk saturation for each stage is going to discussed in what follows.

$$s = \left( \frac{t_c}{t e^{-\lambda h}} \cdot \frac{X}{L} \right)^{\frac{1}{c-1}}$$

For $0 \leq t \leq t_c$, the soil domain was divided into two parts and do the integral separately.

$$\bar{s} = \frac{1}{HL} (\bar{s}_1 + \bar{s}_2)$$

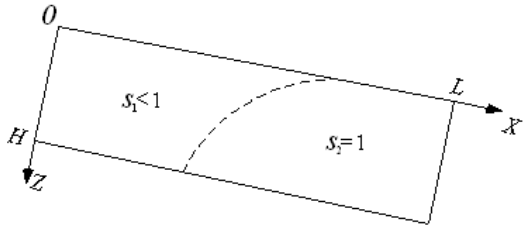


Figure C.1: High saturated stage ($0 \le t \le t_c$)

$$
\begin{aligned}
\bar{s} &= \frac{1}{HL}\left[\int_0^H \int_0^{\frac{te^{-\lambda h}}{t_c}L} \left(\frac{t_c}{te^{-\lambda h}}\cdot\frac{X}{L}\right)^{\frac{1}{c-1}} dXdZ + \int_0^H \int_{\frac{te^{-\lambda h}}{t_c}L}^{L} dXdZ\right] \\
&= \frac{1}{HL}\left[\left(\frac{t_c}{tL}\right)^{\frac{1}{c-1}} \int_0^H e^{\frac{\lambda h}{c-1}} \int_0^{\frac{te^{-\lambda h}}{t_c}L} X^{\frac{1}{c-1}} dXdZ + \int_0^H \left(L - \frac{te^{-\lambda h}}{t_c}L\right) dZ\right] \\
&= \frac{1}{HL}\left[\left(\frac{t_c}{tL}\right)^{\frac{1}{c-1}} \int_0^H e^{\frac{\lambda h}{c-1}}\cdot\frac{c-1}{c} X^{\frac{c}{c-1}}\Big|_0^{\frac{te^{-\lambda h}}{t_c}L} dZ + HL - \frac{tL}{t_c}\int_0^H e^{-\lambda h} dZ\right] \\
&= \frac{1}{HL}\left[\frac{c-1}{c}\frac{tL}{t_c}\int_0^H e^{-\lambda h} dZ + HL + \frac{tL}{\lambda t_c}\left(e^{-\lambda H}-1\right)\right] \\
&= \frac{1}{HL}\left[\frac{c-1}{c}\frac{tL}{t_c}\left(-\frac{1}{\lambda}\right) e^{-\lambda h}\Big|_0^H + HL + \frac{tL}{\lambda t_c}\left(e^{-\lambda H}-1\right)\right] \\
&= \frac{1}{HL}\left[\frac{c-1}{c}\frac{tL}{t_c}\left(-\frac{1}{\lambda}\right)\left(e^{-\lambda H}-1\right) + HL + \frac{tL}{\lambda t_c}\left(e^{-\lambda H}-1\right)\right] \\
&= \frac{1}{HL}\left[HL - \frac{c-1}{c}\frac{tL}{\lambda t_c}\left(e^{-\lambda H}-1\right) + \frac{tL}{\lambda t_c}\left(e^{-\lambda H}-1\right)\right] \\
&= \frac{1}{HL}\left[HL - \frac{(c-1)tL}{\lambda c t_c}\left(1-e^{-\lambda H}\right)\right] \\
&= 1 - \frac{(c-1)t}{\lambda c H t_c}\left(1-e^{-\lambda H}\right) \qquad \text{(C.6)}
\end{aligned}
$$

For $t_c < t < t_b$, the soil domain was divided into three parts and do the integral separately.

$$\bar{s} = \frac{1}{HL}(\bar{s}_1 + \bar{s}_2 + \bar{s}_3)$$

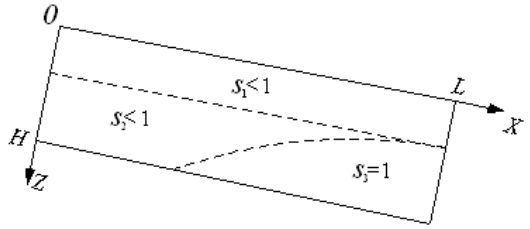


Figure C.2: Intermediate stage ($t_c < t < t_b$)

$$
\begin{aligned}
\bar{s}_1 &= \int_0^{\frac{1}{\lambda}\ln\frac{t}{t_c}} \int_0^L \left(\frac{t_c}{te^{-\lambda h}} \cdot \frac{X}{L}\right)^{\frac{1}{c-1}} dX dZ \\
&= \left(\frac{t_c}{tL}\right)^{\frac{1}{c-1}} \int_0^{\frac{1}{\lambda}\ln\frac{t}{t_c}} e^{\frac{\lambda h}{c-1}} \int_0^L X^{\frac{1}{c-1}} dX dZ \\
&= \left(\frac{t_c}{tL}\right)^{\frac{1}{c-1}} \int_0^{\frac{1}{\lambda}\ln\frac{t}{t_c}} e^{\frac{\lambda h}{c-1}} \cdot \frac{c-1}{c} L^{\frac{c}{c-1}} dZ \\
&= \frac{c-1}{c}\left(\frac{t_c}{t}\right)^{\frac{1}{c-1}} L\frac{c-1}{\lambda}\, e^{\frac{\lambda h}{c-1}}\Big|_0^{\frac{1}{\lambda}\ln\frac{t}{t_c}} \\
&= \frac{(c-1)^2 L}{\lambda c}\left(\frac{t_c}{t}\right)^{\frac{1}{c-1}} \left[\left(\frac{t}{t_c}\right)^{\frac{1}{c-1}} - 1\right] \\
&= \frac{(c-1)^2 L}{\lambda c}\left[1 - \left(\frac{t_c}{t}\right)^{\frac{1}{c-1}}\right]
\end{aligned}
$$

$$
\begin{aligned}
\bar{s}_2 &= \int_{\frac{1}{\lambda}\ln\frac{t}{t_c}}^{H} \int_0^{\frac{te^{-\lambda h}}{t_c}L} \left(\frac{t_c}{te^{-\lambda h}} \cdot \frac{X}{L}\right)^{\frac{1}{c-1}} dX dZ \\
&= \left(\frac{t_c}{tL}\right)^{\frac{1}{c-1}} \int_{\frac{1}{\lambda}\ln\frac{t}{t_c}}^{H} e^{\frac{\lambda h}{c-1}} \int_0^{\frac{te^{-\lambda h}}{t_c}L} X^{\frac{1}{c-1}} dX dZ \\
&= \left(\frac{t_c}{tL}\right)^{\frac{1}{c-1}} \int_{\frac{1}{\lambda}\ln\frac{t}{t_c}}^{H} e^{\frac{\lambda h}{c-1}} \frac{c-1}{c} \left(\frac{te^{-\lambda h}}{t_c} L\right)^{\frac{1}{c-1}} dZ \\
&= \frac{tL}{t_c}\frac{c-1}{c} \int_{\frac{1}{\lambda}\ln\frac{t}{t_c}}^{H} e^{-\lambda h} dZ \\
&= \frac{tL}{t_c}\frac{c-1}{c} \left(-\frac{1}{\lambda}\right) e^{-\lambda h}\Big|_{\frac{1}{\lambda}\ln\frac{t}{t_c}}^{H} \\
&= \frac{tL}{t_c}\frac{c-1}{c} \left(\frac{1}{\lambda}\right) \left(\frac{t_c}{t} - e^{-\lambda H}\right) \\
&= \frac{(c-1)L}{\lambda c} \left(1 - \frac{t}{t_c} e^{-\lambda H}\right)
\end{aligned}
$$

$$
\begin{aligned}
\bar{s}_3 &= \int_{\frac{1}{\lambda}\ln\frac{t}{t_c}}^{H} \int_{\frac{te^{-\lambda h}}{t_c}L}^{L} dX dZ \\
&= \int_{\frac{1}{\lambda}\ln\frac{t}{t_c}}^{H} \left(1 - \frac{te^{-\lambda h}}{t_c}\right) L dZ \\
&= L\left[h + \frac{t}{t_c}\frac{1}{\lambda} e^{-\lambda h}\right]\Bigg|_{\frac{1}{\lambda}\ln\frac{t}{t_c}}^{H} \\
&= L\left[H + \frac{t}{t_c}\frac{1}{\lambda} e^{-\lambda H} - \frac{1}{\lambda}\ln\frac{t}{t_c}\frac{1}{\lambda}\right] \\
&= HL - \frac{L}{\lambda}\ln\frac{t}{t_c} + \frac{L}{\lambda}\left(\frac{t}{t_c} e^{-\lambda H} - 1\right)
\end{aligned}
$$

Therefore, the overall bulk saturation is:

$$\begin{aligned}
\bar{s} &= \frac{1}{HL}\left[\frac{(c-1)^2 L}{\lambda c}\left[1-\left(\frac{t_c}{t}\right)^{\frac{1}{c-1}}\right]+\frac{(c-1)L}{\lambda c}\left(1-\frac{t}{t_c}e^{-\lambda H}\right)+HL-\frac{L}{\lambda}\ln\frac{t}{t_c}+\frac{L}{\lambda}\left(\frac{t}{t_c}e^{-\lambda H}-1\right)\right] \\
&= \frac{(c-1)^2}{\lambda c H}\left[1-\left(\frac{t_c}{t}\right)^{\frac{1}{c-1}}\right]+\frac{c-1}{\lambda c H}\left(1-\frac{t}{t_c}e^{\lambda H}\right)+1-\frac{1}{\lambda H}\ln\frac{t}{t_c}+\frac{1}{\lambda H}\left(\frac{t}{t_c}e^{-\lambda H}-1\right) \\
&= \frac{(c-1)^2}{\lambda c H}\left[1-\left(\frac{t_c}{t}\right)^{\frac{1}{c-1}}\right]+1-\frac{1}{\lambda H}\ln\frac{t}{t_c}-\frac{1}{\lambda c H}\left(1-\frac{t}{t_c}e^{-\lambda H}\right) \qquad \text{(C.7)}
\end{aligned}$$

For $t > t_b$,

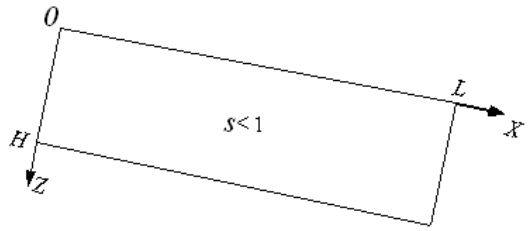


Figure C.3: Dry stage ($t \geq t_b$)

$$\begin{aligned}
\bar{s} &= \frac{1}{HL}\int_0^H\int_0^L\left(\frac{t_c}{te^{-\lambda h}}\cdot\frac{X}{L}\right)^{\frac{1}{c-1}}dXdZ \\
&= \frac{1}{HL}\left(\frac{t_c}{tL}\right)^{\frac{1}{c-1}}\int_0^H e^{\frac{\lambda h}{c-1}}\int_0^L X^{\frac{1}{c-1}}dXdZ \\
&= \frac{1}{HL}\left(\frac{t_c}{tL}\right)^{\frac{1}{c-1}}\int_0^H e^{\frac{\lambda h}{c-1}}\frac{c-1}{c}\,X^{\frac{c-1}{c}}\Big|_0^L dZ \\
&= \frac{1}{HL}\left(\frac{t_c}{tL}\right)^{\frac{1}{c-1}}\frac{c-1}{c}L^{\frac{c-1}{c}}\int_0^H e^{\frac{\lambda h}{c-1}}dZ \\
&= \frac{c-1}{c}\left(\frac{t_c}{t}\right)^{\frac{1}{c-1}}\frac{c-1}{\lambda H}\left(e^{\frac{\lambda H}{c-1}}-1\right) \\
&= \frac{(c-1)^2}{\lambda c H}\left(\frac{t_c}{t}\right)^{\frac{1}{c-1}}\left(e^{\frac{\lambda H}{c-1}}-1\right) \qquad \text{(C.8)}
\end{aligned}$$

# Appendix D

# WATDRAIN2 Interflow Algorithm

## D.1 Parameter Calculation

Function SolNonLinear(xx,vcase) is a function that solves the SYSTEMS of nonlinear equation, by ARGONNE NATIONAL LABORATORY. MINPACK PROJECT. MARCH 1980. BURTON S. GARBOW, KENNETH E. HILLSTROM, JORGE J. MORE. The author keep the essential algorithm and made changes to it for solving the specific WATDRAIN2 interflow algorithm.

- vcase=1 - solving for $X_c$ (Function 2)
- vcase=2 - solving for $X_s$ and $\tau$ for $t < t_c$ (Function 1)
- vcase=3 - solving for $X_s$ and $\tau$ for $t > t_c$ (Function 3)
- vcase=4 - solving for $\tau_{max}$ (Function 4)

Function 1: Solving for $X_s$ and $\tau$ for $t < t_c$

$$\begin{cases} \frac{\partial \psi_g}{\partial X}|_{X=0} = \Lambda \\ k_s \Lambda t = \int_0^{X_s} \theta_s (1 - s_g)\, dX \end{cases} \tag{D.1}$$

Recalling the gravity-dominated solution (equation 4.9) and taking derivative:

$$\psi_g = \psi_{ae}\left(\frac{X+\tau}{X_s+\tau}\right)^{-\frac{b}{2b+2}\left(1-\frac{X}{X_s}\right)^2} \tag{D.2}$$

$$\frac{\partial \psi_g}{\partial X} = \psi_g \frac{b}{2b+2}\left(1-\frac{X}{X_s}\right)\left[\frac{2}{X_s}\ln\frac{X+\tau}{X_s+\tau} - \left(1-\frac{X}{X_s}\right)\frac{1}{X+\tau}\right] \tag{D.3}$$

Therefore, systems of equations D.1 becomes:

$$\begin{cases} \psi_{ae}\left(\frac{\tau}{X_s+\tau}\right)^{-\frac{b}{2b+2}} \frac{b}{2b+2}\left(\frac{2}{X_s}\ln\frac{\tau}{X_s+\tau} - \frac{1}{\tau}\right) = \Lambda \\ k_s \Lambda t = \int_0^{X_s} \theta_s(1-s_g)\, dX \end{cases} \tag{D.4}$$

Function 2: Solving for $X_{bt_c}$ ($\tau$ at time $t_c$):

Since $X_s = L$ at time $t_c$, there is only one unknown variable in systems of equations D.1. The first one can be used for deterging $X_{bt_c}$.

$$\psi_{ae}\left(\frac{\tau}{L+\tau}\right)^{-\frac{b}{2b+2}} \frac{b}{2b+2}\left(\frac{2}{L}\ln\frac{\tau}{L+\tau} - \frac{1}{\tau}\right) = \Lambda \tag{D.5}$$

Function 3: Solving for $s_a$ and $\tau$ for $t > t_c$

Instead of setting up systems of equations for solving $s_a$ and $\tau$, here $\tau$ was numerically calculated and then to determine the value of $s_a$ by a quadratic equation in one variable related to $\tau$ later. $\tau$ is a function of time $t$ as expressed in equation 4.21. $\frac{\partial t}{\partial x_b}$ is calculated based on the continuity equation at $X = 0$. No flow boundary condition at $X = 0$ results in a continuity equation as:

$$\theta_s \frac{\partial s}{\partial \tau}\frac{\partial \tau}{\partial t} = k\frac{\partial^2 \psi}{\partial X^2}$$

therefore,

$$\frac{\partial t}{\partial \tau} = \frac{\theta_s \frac{\partial s}{\partial \tau}}{k\frac{\partial^2 \psi}{\partial X^2}}$$

where

$$\frac{\partial s}{\partial \tau} = \frac{1}{2b}\frac{s_g^{2b}}{s^{2b-1}}\frac{\partial w}{\partial \tau} + w\left(\frac{s_g}{s}\right)^{2b-1}\frac{\partial s_g}{\partial \tau} - \frac{1}{2b}\frac{s_f^{2b}}{s^{2b-1}}\frac{\partial w}{\partial \tau}$$

and

$$\begin{aligned}\frac{\partial^2\psi}{\partial X^2} &= \frac{\partial w}{\partial X}\left[\left(\frac{\psi}{\psi_g}\right)^3\frac{\partial\psi_g}{\partial X}-\left(\frac{\psi}{\psi_f}\right)^3\frac{\partial\psi_f}{\partial X}\right]+\left[3w\left(\frac{\psi}{\psi_g}\right)^2\frac{\partial\psi_g}{\partial X}-\frac{\psi^2}{\psi_g}\frac{\partial w}{\partial X}\right]\frac{\psi_g\frac{\partial\psi}{\partial X}-\psi\frac{\partial\psi_g}{\partial X}}{\psi_g^2}+w\left(\frac{\psi}{\psi_g}\right)^3\frac{\partial^2\psi_g}{\partial X^2}\\ &+ \frac{1}{2}\frac{\partial w}{\partial X}\frac{\partial\psi}{\partial X}\left[-\left(\frac{\psi}{\psi_g}\right)^2+\left(\frac{\psi}{\psi_f}\right)^2\right]+\left[3(1-w)\left(\frac{\psi}{\psi_f}\right)^2\frac{\partial\psi_f}{\partial X}+\frac{\psi^2}{\psi_f}\frac{\partial w}{\partial X}\right]\frac{\psi_f\frac{\partial\psi}{\partial X}-\psi\frac{\partial\psi_f}{\partial X}}{\psi_f^2}\end{aligned} \tag{D.6}$$

Starting with equation 4.20 at $x=0$, the left hand side ($lhs$) and the right hand side ($rhs$) are divided by $s_a$:

$$\begin{aligned}\frac{lhs}{s_a} &= \left[\left(\frac{\psi_{f0}}{\psi_{g0}}\right)^6+\left(\frac{\psi_{f0}}{\psi_{g0}}\right)^2-\left(\frac{\psi_{f0}}{\psi_{g0}}\right)^4-1\right]s_a^2\\ &+ \left[\left(\frac{\psi_{f0}}{\psi_{g0}}\right)^4-4\left(\frac{\psi_{f0}}{\psi_{g0}}\right)^2+3\right]s_a+3\left(\frac{\psi_{f0}}{\psi_{g0}}\right)^2+\frac{1}{s_a}-3\\ \frac{rhs}{s_a} &= \left[\left(\frac{\psi_{f0}}{\psi_{g0}}\right)^6\left(\frac{\partial\psi_g}{\partial X}\right)^2\frac{1}{\Lambda^2}-2\left(\frac{\psi_{f0}}{\psi_{g0}}\right)^2\frac{\partial\psi_g}{\partial X}\frac{1}{\Lambda}+1\right]s_a\\ &+ \frac{1}{s_a}+2+2\left(\frac{\psi_{f0}}{\psi_{g0}}\right)^2\frac{\partial\psi_g}{\partial X}\frac{1}{\Lambda}\end{aligned}$$

It is clear that $\frac{lhs}{s_a}-\frac{rhs}{s_a}=0$ leads to:

$$\begin{aligned}&\left[m^6-1+3m^2-3m^4\right]\Lambda^2s_a^2\\ &+\left[-6m^2\Lambda^2+3m^4\Lambda^2-m^6n^2+2\Lambda^2+2m^3n\Lambda\right]s_a\\ &+\left[-\Lambda^2+3m^2\Lambda^2-2m^3n\Lambda\right]=0\end{aligned} \tag{D.7}$$

where $m=\frac{\psi_{f0}}{\psi_{g0}}$ and $n=\frac{\partial\psi_g}{\partial X}|_{X=0}$. Equation D.7 is a quadratic equation in one variable respect to $s_a$.

$$s_a=\frac{-B+\sqrt{B^2-4AC}}{2A}$$

where

$$\begin{aligned}A &= m^6-1+3m^2-3m^4\\ B &= -6m^2\Lambda^2+3m^4\Lambda^2-m^6n^2+2\Lambda^2+2m^3n\Lambda\\ C &= -\Lambda^2+3m^2\Lambda^2-2m^3n\Lambda\end{aligned}$$

Function 4: Solving for $\tau_{max}$.

$\tau_{max}$ is defined as the $\tau$ at the infinite time, e.g., at the steady state. Flow is purely suction dominated at the steady state and $s_a = 0$. As can be seen in equation D.7,

$$-\Lambda^2 + 3m^2\Lambda^2 - 2m^3n\Lambda = 0$$

## D.2 Useful Derivatives

$$
\begin{aligned}
\frac{\partial \psi_f}{\partial X} &= \Lambda \\
\frac{\partial^2 \psi_f}{\partial X^2} &= 0 \\
\frac{\partial \psi_g}{\partial X} &= \frac{b\psi_g}{2b+2}\left(1-\frac{X}{X_s}\right)\left[\frac{2}{X_s}\ln\frac{X+\tau}{X_s+\tau}-\left(1-\frac{X}{X_s}\right)\frac{1}{X+\tau}\right] \\
\frac{\partial^2 \psi_g}{\partial X^2} &= \frac{1}{\psi_g}\left(\frac{\partial \psi_g}{\partial X}\right)^2-\frac{1}{X_s-X}\frac{\partial \psi_g}{\partial X}+\frac{b\psi_g}{2b+2}\left(1-\frac{X}{X_s}\right)\left[\frac{3}{X_s(X+\tau)}+\left(1-\frac{X}{X_s}\frac{1}{(X+\tau)^2}\right)\right] \\
\frac{\partial w}{\partial X} &= 3(1-s_a)\frac{\theta_s}{X_s}\left(\frac{X}{X_s}\right)^2\left(\frac{t_c}{t}\right)^{\left(1-\frac{t_c}{t}\right)^4} \\
\frac{\partial \psi}{\partial X} &= w\left(\frac{\psi}{\psi_g}\right)^3\frac{\partial \psi_g}{\partial X}-\frac{\psi}{2}\left(\frac{\psi}{\psi_g}\right)^2\frac{\partial w}{\partial X}+(1-w)\left(\frac{\psi}{\psi_f}\right)^3\frac{\partial \psi_f}{\partial X}+\frac{\psi}{2}\left(\frac{\psi}{\psi_f}\right)^2\frac{\partial w}{\partial X} \\
\frac{\partial^2 \psi}{\partial X^2} &= \frac{\partial w}{\partial X}\left[\left(\frac{\psi}{\psi_g}\right)^3\frac{\partial \psi_g}{\partial X}-\left(\frac{\psi}{\psi_f}\right)^3\frac{\partial \psi_f}{\partial X}\right]+\left[3w\left(\frac{\psi}{\psi_g}\right)^2\frac{\partial \psi_g}{\partial X}-\frac{\psi^2}{\psi_g}\frac{\partial w}{\partial X}\right]\frac{\psi_g\frac{\partial \psi}{\partial X}-\psi\frac{\partial \psi_g}{\partial X}}{\psi_g^2} \\
&+ w\left(\frac{\psi}{\psi_g}\right)^3\frac{\partial^2 \psi_g}{\partial X^2}+\frac{1}{2}\frac{\partial w}{\partial X}\frac{\partial \psi}{\partial X}\left[-\left(\frac{\psi}{\psi_g}\right)^2+\left(\frac{\psi}{\psi_f}\right)^2\right] \\
&+ \left[3(1-w)\left(\frac{\psi}{\psi_f}\right)^2\frac{\partial \psi_f}{\partial X}+\frac{\psi^2}{\psi_f}\frac{\partial w}{\partial X}\right]\frac{\psi_f\frac{\partial \psi}{\partial X}-\psi\frac{\partial \psi_f}{\partial X}}{\psi_f^2} \\
\frac{\partial m}{\partial \tau} &= -\frac{\psi_f}{\psi_g^2}\frac{\psi_g}{\partial \tau} \\
\frac{\partial A}{\partial \tau} &= 6m\Lambda^2\left(m^4-2m^2+1\right)\frac{\partial m}{\partial \tau} \\
\frac{\partial B}{\partial \tau} &= 6m\left[-2\Lambda^2+2m^2\Lambda^2-m^4\left(\frac{\partial \psi_g}{\partial X}\right)^2+m\Lambda\frac{\partial \psi_g}{\partial X}\right]\frac{\partial m}{\partial \tau}+2m^3\left(-m^3\frac{\partial \psi_g}{\partial X}+\Lambda\right)\frac{\partial}{\partial \tau}\left(\frac{\partial \psi_g}{\partial X}\right) \\
\frac{\partial C}{\partial \tau} &= 6m\Lambda\left(\Lambda-m\frac{\partial \psi_g}{\partial X}\right)\frac{\partial m}{\partial \tau}-2m^3\Lambda\frac{\partial}{\partial \tau}\left(\frac{\partial \psi_g}{\partial X}\right) \\
\frac{\partial s_a}{\partial \tau} &= \frac{\left[\frac{1}{2}(B^2-4AC)^{-\frac{1}{2}}\left(2B\frac{\partial B}{\partial \tau}-4C\frac{\partial A}{\partial \tau}-4A\frac{\partial C}{\partial \tau}\right)-\frac{\partial B}{\partial \tau}\right]2A-2\left(\sqrt{B^2-4AC}-B\right)\frac{\partial A}{\partial \tau}}{4A^2}
\end{aligned}
$$

$$
\begin{aligned}
\frac{\partial}{\partial\tau}\left(\frac{\partial\psi_g}{\partial X}\right) &= \frac{1}{\psi_g}\frac{\partial\psi_g}{\partial X}\frac{\partial\psi_g}{\partial\tau} + \frac{b\psi_g}{2b+2}\left(1-\frac{X}{X_s}\right)\left[\frac{2(X_s-X)}{(X_s+\tau)(X+\tau)} + \left(1-\frac{X}{X_s}\right)\frac{1}{(X+\tau)^2}\right] \\
\frac{\psi_g}{\partial\tau} &= -\frac{b\psi_g}{2b+2}\left(1-\frac{X}{X_s}\right)^2\frac{X_s-X}{(X+\tau)(X_s+\tau)} \\
\frac{\partial w}{\partial\tau} &= \left[1-\frac{\theta_s X}{X_s}\left(\frac{t_c}{t}\right)^{\left(1-\frac{t_c}{t}\right)^4}\right]\frac{\partial s_a}{\partial\tau} \\
\frac{\partial s_g}{\partial\tau} &= \frac{s_g}{2b+2}\left(1-\frac{X}{X_s}\right)^2\frac{X_s-X}{(X+\tau)(X_s+\tau)} \\
\frac{\partial s}{\partial\tau} &= \frac{1}{2b}\frac{s_g^{2b}}{s^{2b-1}}\frac{\partial w}{\partial\tau} + w\left(\frac{s_g}{s}\right)^{2b-1}\frac{\partial s_g}{\partial\tau} - \frac{1}{2b}\frac{s_f^{2b}}{s^{2b-1}}\frac{\partial w}{\partial\tau}
\end{aligned}
$$

## D.3 FORTRAN Code for Determining WATDRAIN2 Parameters

Note there are many temporary variables in this FORTRAN file. They are corresponding to:

temp1=$\frac{\psi_{f0}}{\psi_{g0}}$

temp2=$A$

temp3=$B$

temp4=$C$

temp5=$\frac{\psi_{f0}}{\psi_{g0}}\frac{\partial\psi_g}{\partial\tau}$

temp6=$\frac{\partial^2\psi}{\partial X^2}$

temp7=$\frac{\partial A}{\partial\tau}$

temp8=$\frac{\partial B}{\partial\tau}$

temp9=$\frac{\partial C}{\partial\tau}$

temp10=$\frac{\partial s_a}{\partial\tau}$

The code is in what follows:

```
!     **********
!     Modified by Lucy Liu on Feb. 2010, 4 functions (FCN):
!     Function 1: solving for xst and xbb for t<tc
!     Function 2: solving for xbbtc
!     Function 3: solving for xaa and xbb for t>tc
!     Function 4: solving for xbbmax
C     **********
C
C     THIS PROGRAM TESTS CODES FOR THE SOLUTION OF N NONLINEAR
C     EQUATIONS IN N VARIABLES. IT CONSISTS OF A DRIVER AND AN
C     INTERFACE SUBROUTINE FCN. THE DRIVER READS IN DATA, CALLS THE
C     NONLINEAR EQUATION SOLVER, AND FINALLY PRINTS OUT INFORMATION
C     ON THE PERFORMANCE OF THE SOLVER. THIS IS ONLY A SAMPLE DRIVER,
C     MANY OTHER DRIVERS ARE POSSIBLE. THE INTERFACE SUBROUTINE FCN
C     IS NECESSARY TO TAKE INTO ACCOUNT THE FORMS OF CALLING
C     SEQUENCES USED BY THE FUNCTION SUBROUTINES IN THE VARIOUS
C     NONLINEAR EQUATION SOLVERS.
C
C     SUBPROGRAMS CALLED
C
C       USER-SUPPLIED ...... FCN
C
C       MINPACK-SUPPLIED ... DPMPAR,ENORM,HYBRD1,INITPT,VECFCN
C
C       FORTRAN-SUPPLIED ... DSQRT
C
C     ARGONNE NATIONAL LABORATORY. MINPACK PROJECT. MARCH 1980.
C     BURTON S. GARBOW, KENNETH E. HILLSTROM, JORGE J. MORE
C
C     **********
      subroutine SolNonLinear(x,vcase)
      implicit none
      INTEGER I,IC,INFO,K,LWA,N,NFEV,NPROB,NREAD,NTRIES,NWRITE,vcase
      INTEGER NA(60),NF(60),NP(60),NX(60)
      DOUBLE PRECISION FACTOR,FNORM1,FNORM2,ONE,TEN,TOL
      DOUBLE PRECISION FNM(60),FVEC(40),WA(2660),X(40)
      DOUBLE PRECISION DPMPAR,ENORM
      EXTERNAL FCN
```

```
      DOUBLE PRECISION t,tc
      DOUBLE PRECISION ks,phi,psi0,b
DOUBLE PRECISION L,slope
      COMMON /REFNUM/ NPROB,NFEV
common /time/ t,tc
common /soil/ ks,phi,psi0,b
common /length/ L,slope
C
C     LOGICAL INPUT UNIT IS ASSUMED TO BE NUMBER 5.
C     LOGICAL OUTPUT UNIT IS ASSUMED TO BE NUMBER 6.
C
      DATA NREAD,NWRITE /5,6/
C
      DATA ONE,TEN /1.0D0,1.0D1/
      TOL = DSQRT(DPMPAR(1))
      LWA = 2660
      IC = 0
! Modified by Lucy on Feb, 2010
if (vcase==1) then
   NPROB=2
   N=1
   NTRIES=1
elseif (vcase==2) then
   NPROB=1
   N=2
   NTRIES=1
elseif (vcase==3) then
   NPROB=3
   N=1
   NTRIES=1
elseif (vcase==4) then
   NPROB=4
   N=1
   NTRIES=1
endif
 !  10 CONTINUE
!         READ (NREAD,50) NPROB,N,NTRIES
!    write(*,*) NPROB,N,NTRIES
```

```
!         data NPROB,N,NTRIES /    1,    2,    1/
          IF (NPROB .LE. 0) GO TO 30
          FACTOR = ONE
          DO 20 K = 1, NTRIES
             IC = IC + 1
             CALL INITPT(N,X,NPROB,FACTOR)
             CALL VECFCN(N,X,FVEC,NPROB)
             FNORM1 = ENORM(N,FVEC)
!             WRITE (NWRITE,60) NPROB,N
             NFEV = 0
             CALL HYBRD1(FCN,N,X,FVEC,TOL,INFO,WA,LWA)
             FNORM2 = ENORM(N,FVEC)
             NP(IC) = NPROB
             NA(IC) = N
             NF(IC) = NFEV
             NX(IC) = INFO
             FNM(IC) = FNORM2
!             WRITE (NWRITE,70) FNORM1,FNORM2,NFEV,INFO,(X(I), I = 1, N)
!       write (NWRITE,*) IC
!   write (NWRITE,*) "Lucy x(i)",(X(I), I = 1, N)
!   write (NWRITE,*) "Lucy f(i)",(FVEC(i),i=1,N)
             FACTOR = TEN*FACTOR
   20        CONTINUE
!         GO TO 10
   30 CONTINUE
!      WRITE (NWRITE,80) IC
!      WRITE (NWRITE,90)
!      DO 40 I = 1, IC
!         WRITE (NWRITE,100) NP(I),NA(I),NF(I),NX(I),FNM(I)
!   40    CONTINUE
!      STOP
   50 FORMAT (3I5)
   60 FORMAT ( //// 5X, 8H PROBLEM, I5, 5X, 10H DIMENSION, I5, 5X //)
   70 FORMAT (5X, 33H INITIAL L2 NORM OF THE RESIDUALS, D15.7 // 5X,
     *        33H FINAL L2 NORM OF THE RESIDUALS  , D15.7 // 5X,
     *        33H NUMBER OF FUNCTION EVALUATIONS  , I10 // 5X,
     *        15H EXIT PARAMETER, 18X, I10 // 5X,
     *        27H FINAL APPROXIMATE SOLUTION // (5X, 5D15.7))
```

```
   80 FORMAT (12H1SUMMARY OF , I3, 16H CALLS TO HYBRD1 /)
   90 FORMAT (39H NPROB   N    NFEV  INFO  FINAL L2 NORM /)
  100 FORMAT (I4, I6, I7, I6, 1X, D15.7)
C
C     LAST CARD OF DRIVER.
      return
C
      END
      SUBROUTINE FCN(N,X,FVEC,IFLAG)
      INTEGER N,IFLAG
      DOUBLE PRECISION X(N),FVEC(N)
DOUBLE PRECISION t,tc
C     **********
C
C     THE CALLING SEQUENCE OF FCN SHOULD BE IDENTICAL TO THE
C     CALLING SEQUENCE OF THE FUNCTION SUBROUTINE IN THE NONLINEAR
C     EQUATION SOLVER. FCN SHOULD ONLY CALL THE TESTING FUNCTION
C     SUBROUTINE VECFCN WITH THE APPROPRIATE VALUE OF PROBLEM
C     NUMBER (NPROB).
C
C     SUBPROGRAMS CALLED
C
C       MINPACK-SUPPLIED ... VECFCN
C
C     ARGONNE NATIONAL LABORATORY. MINPACK PROJECT. MARCH 1980.
C     BURTON S. GARBOW, KENNETH E. HILLSTROM, JORGE J. MORE
C
C     **********
      INTEGER NPROB,NFEV
      COMMON /REFNUM/ NPROB,NFEV
common /time/ t,tc
      CALL VECFCN(N,X,FVEC,NPROB)
      NFEV = NFEV + 1
      RETURN
C
C     LAST CARD OF INTERFACE SUBROUTINE FCN.
C
      END
```

```
      SUBROUTINE VECFCN(N,X,FVEC,NPROB)
      INTEGER N,NPROB
      DOUBLE PRECISION X(N),FVEC(N)
      DOUBLE PRECISION pftemp,pgtemp,dpgdxtemp,xaatemp0,ddpgdxdxbbtemp
      DOUBLE PRECISION, external :: quasol
DOUBLE PRECISION, external :: sg,pg,dpgdx,pf,sf,w,p,s
      DOUBLE PRECISION, external :: d2pgdx2,dwdx,dpdx,d2pdx2
DOUBLE PRECISION, external :: dpgdxbb,ddpgdxdxbb,dsgdxbb,dsdxbb
C     **********
C
C     SUBROUTINE VECFCN
C
C     THIS SUBROUTINE DEFINES FOURTEEN TEST FUNCTIONS. THE FIRST
C     FIVE TEST FUNCTIONS ARE OF DIMENSIONS 2,4,2,4,3, RESPECTIVELY,
C     WHILE THE REMAINING TEST FUNCTIONS ARE OF VARIABLE DIMENSION
C     N FOR ANY N GREATER THAN OR EQUAL TO 1 (PROBLEM 6 IS AN
C     EXCEPTION TO THIS, SINCE IT DOES NOT ALLOW N = 1).
C
C     THE SUBROUTINE STATEMENT IS
C
C       SUBROUTINE VECFCN(N,X,FVEC,NPROB)
C
C     WHERE
C
C       N IS A POSITIVE INTEGER INPUT VARIABLE.
C
C       X IS AN INPUT ARRAY OF LENGTH N.
C
C       FVEC IS AN OUTPUT ARRAY OF LENGTH N WHICH CONTAINS THE NPROB
C         FUNCTION VECTOR EVALUATED AT X.
C
C       NPROB IS A POSITIVE INTEGER INPUT VARIABLE WHICH DEFINES THE
C         NUMBER OF THE PROBLEM. NPROB MUST NOT EXCEED 14.
C
C     SUBPROGRAMS CALLED
C
C       FORTRAN-SUPPLIED ... DATAN,DCOS,DEXP,DSIGN,DSIN,DSQRT,
```

```
C                              MAX0,MIN0
C
C     ARGONNE NATIONAL LABORATORY. MINPACK PROJECT. MARCH 1980.
C     BURTON S. GARBOW, KENNETH E. HILLSTROM, JORGE J. MORE
C
C     **********
      integer ii
DOUBLE PRECISION hh,xx1,xx2,xx3,intf
      INTEGER I,IEV,IVAR,J,K,K1,K2,KP1,ML,MU
      DOUBLE PRECISION C1,C2,C3,C4,C5,C6,C7,C8,C9,EIGHT,FIVE,H,ONE,
     *                 PROD,SUM,SUM1,SUM2,TEMP,TEMP1,TEMP2,TEN,THREE,
     *                 TI,TJ,TK,TPI,TWO,ZERO,
     *                 temp3,temp4,temp5,temp6,temp7,temp8,fxx,xbbtemp0,
     *                 temp9,temp10,delxbb
 !     DOUBLE PRECISION DFLOAT
DOUBLE PRECISION t,tc
DOUBLE PRECISION ks,phi,psi0,b
DOUBLE PRECISION L,slope
DOUBLE PRECISION xbbtc,xbbmax
common /time/ t,tc
common /soil/ ks,phi,psi0,b
common /length/ L,slope
common /xbb/ xbbtc,xbbmax
common /temp/ xbbtemp0
c
c
      DATA ZERO,ONE,TWO,THREE,FIVE,EIGHT,TEN
     *     /0.0D0,1.0D0,2.0D0,3.0D0,5.0D0,8.0D0,1.0D1/
      DATA C1,C2,C3,C4,C5,C6,C7,C8,C9
     *     /1.0D4,1.0001D0,2.0D2,2.02D1,1.98D1,1.8D2,2.5D-1,5.0D-1,
     *      2.9D1/

!      DFLOAT(IVAR) = IVAR
C
C     PROBLEM SELECTOR.
C
      GO TO (10,20,30,40), NPROB
C
```

```
C     FUNCTION 1, solving for xst and xbb for t<tc.
C
   10 CONTINUE
c ***********************************************************
      if (x(1)<0.0) x(1)=1.0D0
if (x(1)>xbbmax) x(1)=xbbmax
if (x(2)<0.0) x(2)=1.0D0
      if (x(2)>L) x(2)=L
      fvec(1)=psi0*(x(1)/(x(1)+x(2)))**(-b/(2.0D0*b+2.0D0))*
     +        b/(2.0D0*b+2.0D0)*(2.0D0/x(2)*
     +        (log(x(1))-log(x(2)+x(1)))-1.0D0/x(1))-slope
      intf=0.0D0
hh=x(2)/5000.0D0
do ii=1,5000
   xx1=ii*hh-hh/2.0D0-hh/2.0D0/dsqrt(3.0D0)
   xx2=ii*hh-hh/2.0D0+hh/2.0D0/dsqrt(3.0D0)
   intf=intf+hh/2.0D0*phi*(1.0D0-sg(xx1,x(1),x(2)))
     +            +hh/2.0D0*phi*(1.0D0-sg(xx2,x(1),x(2)))
enddo
fvec(2)=intf-ks*slope*t
c ***********************************************************
      GO TO 380
C
C     FUNCTION 2, solving for xbbtc.
C
   20 CONTINUE
c ***********************************************************
      if (x(1)<0.0) x(1)=1.0D0
      fvec(1)=psi0*(x(1)/(x(1)+L))**(-b/(2.0D0*b+2.0D0))*
     +        b/(2.0D0*b+2.0D0)*(2.0D0/L*
     +        (log(x(1))-log(L+x(1)))-1.0/x(1))-slope
c ***********************************************************
      GO TO 380
C
C     FUNCTION 3, ssolving for xaa and xbb for t>tc.
C
   30 CONTINUE
c ***********************************************************
```

```
      if (x(1)>1.0) x(1)=1.0D0
if (x(1)<0.0) x(1)=0.0D0
delxbb=10.0D0
      xbbtemp0=xbbtc-delxbb/2.0D0
sum=tc
! do ii=1,5000
!   if (xbbtemp0>xbbmax .or. sum>t) exit
do while (xbbtemp0<xbbmax .and. sum<t)
            xbbtemp0=xbbtemp0+delxbb
      pftemp=pf(0.0D0)
      pgtemp=pg(0.0D0,xbbtemp0,L)
            dpgdxtemp=dpgdx(0.0D0,xbbtemp0,L)
      ddpgdxdxbbtemp=ddpgdxdxbb(0.0D0,xbbtemp0,L)
      ! m
  temp1=pftemp/pgtemp
      ! temp2=A
      temp2=(temp1**6.0D0-1.0D0+3.0D0*temp1**2.0D0-
     +      3.0D0*temp1**4.0D0)*slope**2.0
      ! temp3=B
      temp3=-6.0D0*temp1**2.0D0*slope**2.0+
     +       3.0D0*temp1**4.0D0*slope**2.0-
     +       temp1**6.0D0*dpgdxtemp**2.0D0+
     +       2.0D0*slope**2.0D0+
     +       2.0D0*temp1**3.0D0*dpgdxtemp*slope
      ! temp4=C
      temp4=-slope**2.0D0+3.0D0*temp1**2.0D0*slope**2.0D0-
     +       2.0D0*temp1**3.0D0*dpgdxtemp*slope
      xaatemp0=quasol(temp2,temp3,temp4)
      temp5=-pftemp/pgtemp**2.0*dpgdxbb(0.0D0,xbbtemp0,L)
  ! d2pdx2
      temp6=d2pdx2(0.0D0,xbbtemp0,L,xaatemp0)  ! x,xbb,xs,xaa
      !
      ! temp7=dAdxbb
      temp7=6.0D0*temp1*temp5*(temp1**4.0D0+
     +             1.0D0-2.0D0*temp1**2.0D0)*slope**2.0D0
      ! temp8=dBdxbb
      temp8=6.0D0*temp1*temp5*
     +             (-2.0D0*slope**2.0D0+2.0D0*temp1**2.0D0*
```

```
     +            slope**2.0D0-temp1**4.0D0*dpgdxtemp**2.0+
     +             temp1*dpgdxtemp*slope)+
     +             2.0D0*temp1**3.0D0*ddpgdxdxbbtemp*
     +             (-temp1**3.0D0*dpgdxtemp+slope)
      ! temp9=dCdxbb
      temp9=6.0D0*temp1*slope*temp5*
     +             (slope-temp1*dpgdxtemp)-
     +             2.0D0*temp1**3.0D0*slope*ddpgdxdxbbtemp
      ! temp10=dxaadxbb
      temp10=((0.5D0*(temp3**2.0D0-4.0D0*temp2*temp4)**(-0.5D0)*
     +      (2.0D0*temp3*temp8-4.0D0*temp7*temp4-4.0D0*temp2*
     +             temp9)-temp8)*2.0D0*temp2-2.0D0*temp7*
     +             (DSQRT(temp3**2.0D0-4.0D0*temp2*temp4)-temp3))/
     +             (4.0D0*temp2**2.0)
      ! test
      if (temp6/=0.0D0) then
         fxx=phi*dsdxbb(0.0D0,xbbtemp0,L,xaatemp0,temp10) /temp6/
     +             (ks*s(0.0D0,xbbtemp0,L,xaatemp0)**(2.0D0*b+3.0D0))
         if (fxx>0.0) sum=sum+fxx*delxbb
      endif
enddo
if (xbbtemp0<xbbmax) xbbtemp0=xbbtemp0+delxbb/2.0D0
dpgdxtemp=dpgdx(0.0D0,xbbtemp0,L)
!m
temp1=pftemp/pgtemp
!A
temp2=(temp1**6.0D0-1.0D0+3.0D0*temp1**2.0D0-
     +      3.0D0*temp1**4.0D0)*slope**2.0
!B
temp3=-6.0D0*temp1**2.0D0*slope**2.0+
     +       3.0D0*temp1**4.0D0*slope**2.0-
     +       temp1**6.0D0*dpgdxtemp**2.0D0+
     +       2.0D0*slope**2.0D0+
     +       2.0D0*temp1**3.0D0*dpgdxtemp*slope
!C
temp4=-slope**2.0D0+3.0D0*temp1**2.0D0*slope**2.0D0-
     +       2.0D0*temp1**3.0D0*dpgdxtemp*slope
fvec(1)=temp2*x(1)**2.0D0+temp3*x(1)+temp4
```

```
c ********************************************************
      GO TO 380
C
C     FUNCTION 4, solving for xbbmax.
C
   40 CONTINUE
c ********************************************************
      if (x(1)<xbbtc) x(1)=xbbtc
if (x(1)>1000.0*L) x(1)=1000.0*L
pftemp=pf(0.0D0)
pgtemp=pg(0.0D0,x(1),L)
      fvec(1)=3.0*pftemp**2.0*pgtemp**4.0*slope**2.0-
     +        2.0*pftemp**3.0*pgtemp**3.0*slope*
     +        dpgdx(0.0D0,x(1),L)-pgtemp**6.0*slope**2.0
c ********************************************************
      GO TO 380
C

  380 CONTINUE
      RETURN
C
C     LAST CARD OF SUBROUTINE VECFCN.
C
      END
      SUBROUTINE INITPT(N,X,NPROB,FACTOR)
      INTEGER N,NPROB
      DOUBLE PRECISION FACTOR
      DOUBLE PRECISION X(N)
C     **********
C
C     SUBROUTINE INITPT
C
C     THIS SUBROUTINE SPECIFIES THE STANDARD STARTING POINTS FOR
C     THE FUNCTIONS DEFINED BY SUBROUTINE VECFCN. THE SUBROUTINE
C     RETURNS IN X A MULTIPLE (FACTOR) OF THE STANDARD STARTING
C     POINT. FOR THE SIXTH FUNCTION THE STANDARD STARTING POINT IS
C     ZERO, SO IN THIS CASE, IF FACTOR IS NOT UNITY, THEN THE
C     SUBROUTINE RETURNS THE VECTOR  X(J) = FACTOR, J=1,...,N.
```

```
C
C     THE SUBROUTINE STATEMENT IS
C
C       SUBROUTINE INITPT(N,X,NPROB,FACTOR)
C
C     WHERE
C
C       N IS A POSITIVE INTEGER INPUT VARIABLE.
C
C       X IS AN OUTPUT ARRAY OF LENGTH N WHICH CONTAINS THE STANDARD
C         STARTING POINT FOR PROBLEM NPROB MULTIPLIED BY FACTOR.
C
C       NPROB IS A POSITIVE INTEGER INPUT VARIABLE WHICH DEFINES THE
C         NUMBER OF THE PROBLEM. NPROB MUST NOT EXCEED 14.
C
C       FACTOR IS AN INPUT VARIABLE WHICH SPECIFIES THE MULTIPLE OF
C         THE STANDARD STARTING POINT. IF FACTOR IS UNITY, NO
C         MULTIPLICATION IS PERFORMED.
C
C     ARGONNE NATIONAL LABORATORY. MINPACK PROJECT. MARCH 1980.
C     BURTON S. GARBOW, KENNETH E. HILLSTROM, JORGE J. MORE
C
C     **********
      INTEGER IVAR,J
      DOUBLE PRECISION C1,H,HALF,ONE,THREE,TJ,ZERO
!      DOUBLE PRECISION DFLOAT
      DATA ZERO,HALF,ONE,THREE,C1 /0.0D0,5.0D-1,1.0D0,3.0D0,1.2D0/
!      DFLOAT(IVAR) = IVAR
C
C     SELECTION OF INITIAL POINT.
C
      GO TO (10,20,30,40), NPROB
C
C     FUNCTION 1, solving for xst and xbb for t<tc.
C
   10 CONTINUE
      x(1)=20.0D0
      X(2) = 2000.0D0
```

```
      GO TO 200
C
C     FUNCTION 1, solving for xbbtc.
C
   20 CONTINUE
      x(1)=100.0D0
      GO TO 200
C
C     FUNCTION 3, solving for xaa and xbb for t>tc.
C
   30 CONTINUE
      X(1) = 0.8D0
      GO TO 200
C
C     FUNCTION 4, solving for xbbmax.
C
   40 CONTINUE
      x(1)=30000.0D0
      GO TO 200
C

  200 CONTINUE
C
C     COMPUTE MULTIPLE OF INITIAL POINT.
C
      IF (FACTOR .EQ. ONE) GO TO 250
      IF (NPROB .EQ. 6) GO TO 220
         DO 210 J = 1, N
            X(J) = FACTOR*X(J)
  210       CONTINUE
         GO TO 240
  220 CONTINUE
         DO 230 J = 1, N
            X(J) = FACTOR
  230       CONTINUE
  240 CONTINUE
  250 CONTINUE
      RETURN
```

```
C
C     LAST CARD OF SUBROUTINE INITPT.
C
      END
! *************quadratic equation of one variable*********
function quasol(x,x1,x2)
real (kind=8) :: x,x1,x2
           quasol=(dsqrt(x1**2.0D0-4.0D0*x*x2)-x1)/(2.0D0*x)
return
end
!
! *************d2pgdx2************
function d2pgdx2(x,x1,x2)
real (kind=8) :: x,x1,x2,pgtemp
      real (kind=8) :: ks,phi,psi0,b
      common /soil/ ks,phi,psi0,b
   pgtemp=pg(x,x1,x2)
   d2pgdx2=b/(2.0D0*b+2.0D0)*
     +           ((1.0D0-x/x2)*dpgdx(x,x1,x2)-pgtemp/x2)*
     +           (2.0D0/x2*log((x+x1)/(x2+x1))-(1.0D0-x/x2)/(x+x1))+
     +           b/(2.0D0*b+2.0D0)*(1.0D0-x/x2)*pgtemp/(x+x1)*
     +           (3.0D0/x2+(1.0D0-x/x2)/(x+x1))
return
end

!
! *************dwdx************
function dwdx(x)  ! xaa
real (kind=8) :: x
real (kind=8) :: L,slope
real (kind=8) :: ks,phi,psi0,b
real (kind=8) :: t,tc
common /soil/ ks,phi,psi0,b
common /length/ L,slope
common /time/ t,tc
   dwdx=(1.0D0-x)*phi/L*(tc/t)**((1.0D0-tc/t)**(b/4.0D0))
return
end
```

```
!
! *************dpdx************
function dpdx(x,x1,x2,x3)  ! x,xbb,xs,xaa
real (kind=8) :: x,x1,x2,x3
real (kind=8) :: pgtemp,ptemp,pftemp
      real (kind=8) :: ks,phi,psi0,b
      real (kind=8) :: L,slope
common /soil/ ks,phi,psi0,b
common /length/ L,slope
          pgtemp=pg(x,x1,x2)
    ptemp=p(x,x1,x2,x3)
    pftemp=pf(x)
    dpdx=w(x,x3)*(ptemp/pgtemp)**3.0D0*
     +         dpgdx(x,x1,x2)-ptemp/2.0D0*
     +         (ptemp/pgtemp)**2.0D0*dwdx(x3)+
     +         (1.0D0-w(x,x3))*(ptemp/pftemp)**3.0D0*
     +         (slope)+ptemp/2.0D0*
     +         (ptemp/pftemp)**2.0D0*dwdx(x3)
return
end
!
! *************d2pdx2************
function d2pdx2(x,x1,x2,x3)  ! x,xbb,xs,xaa
real (kind=8) :: x,x1,x2,x3
real (kind=8) :: ptemp,pgtemp,pftemp,dpdxtemp
real (kind=8) :: dpgdxtemp,wtemp,dwdxtemp
      real (kind=8) :: ks,phi,psi0,b
      real (kind=8) :: L,slope
common /soil/ ks,phi,psi0,b
common /length/ L,slope
    ptemp=p(x,x1,x2,x3)
    pgtemp=pg(x,x1,x2)
    pftemp=pf(x)
    dpdxtemp=dpdx(x,x1,x2,x3)
    dpgdxtemp=dpgdx(x,x1,x2)
    wtemp=w(x,x3)
    dwdxtemp=dwdx(x3)
    d2pdx2=dwdxtemp*((ptemp/pgtemp)**3.0D0*
```

```
     +        dpgdxtemp-(ptemp/pftemp)**3.0D0*(slope))+
     +           (3.0D0*wtemp*(ptemp/pgtemp)**2.0D0*
     +           dpgdxtemp-ptemp**2.0D0/pgtemp*
     +           dwdxtemp)*(pgtemp*dpdxtemp-
     +           ptemp*dpgdxtemp)/pgtemp**2.0D0+
     +           wtemp*(ptemp/pgtemp)**3.0D0*
     +         d2pgdx2(x,x1,x2)+1.0D0/2.0D0*dwdxtemp*dpdxtemp*
     +           (-(ptemp/pgtemp)**2.0D0+
     +           (ptemp/pftemp)**2.0D0)+
     +           (3.0D0*(1.0D0-wtemp)*(ptemp/pftemp)**2.0D0*
     +           (slope)+ptemp**2.0D0/pftemp*dwdxtemp)*
     +           (pftemp*dpdxtemp-ptemp*(slope))/
     +           pftemp**2.0D0
return
end
!
! *************dpgdxbb**************
function dpgdxbb(x,x1,x2)  ! x,xbb,xs
real (kind=8) :: x,x1,x2
      real (kind=8) :: ks,phi,psi0,b
      real (kind=8) :: L,slope
common /soil/ ks,phi,psi0,b
common /length/ L,slope
dpgdxbb=-b/(2.0D0*b+2.0D0)*(1.0D0-x/x2)**2.0D0*
     +        (x2-x)/((x+x1)*(x2+x1))*pg(x,x1,x2)
return
end
!
! *************ddpgdxdxbb**************
function ddpgdxdxbb(x,x1,x2)  ! x,xbb,xs
real (kind=8) :: x,x1,x2
      real (kind=8) :: pgtemp
      real (kind=8) :: ks,phi,psi0,b
      real (kind=8) :: L,slope
common /soil/ ks,phi,psi0,b
common /length/ L,slope
    pgtemp=pg(x,x1,x2)
          ddpgdxdxbb=1.0D0/pgtemp*dpgdx(x,x1,x2)*
```

```
     +               dpgdxbb(x,x1,x2)+pgtemp*b/(2.0D0*b+2.0D0)*
     +               (1.0D0-x/x2)*(2.0D0/x2*(x2-x)/((x+x1)*(x2+x1))+
     +               (1.0D0-x/x2)/(x+x1)**2.0D0)
return
end
!
! ************dsgdxbb*****************
function dsgdxbb(x,x1,x2)  ! x,xbb,xs
real (kind=8) :: x,x1,x2
      real (kind=8) :: ks,phi,psi0,b
      real (kind=8) :: L,slope
common /soil/ ks,phi,psi0,b
common /length/ L,slope
          dsgdxbb=1.0D0/(2.0D0*b+2.0D0)*(1.0D0-x/x2)**2.0D0*
     +            sg(x,x1,x2)*(x2-x)/((x+x1)*(x2+x1))
return
end
!
! *************dsdxbb*****************
function dsdxbb(x,x1,x2,x3,x4)  ! x,xbb,xs,xaa,dwdxbb
real (kind=8) :: x,x1,x2,x3,x4
      real (kind=8) :: sgtemp,stemp
      real (kind=8) :: ks,phi,psi0,b
      real (kind=8) :: L,slope
common /soil/ ks,phi,psi0,b
common /length/ L,slope
    sgtemp=sg(x,x1,x2)
          stemp=s(x,x1,x2,x3)
          dsdxbb=sgtemp**(2.0D0*b)/
     +           stemp**(2.0D0*b-1.0D0)/(2.0D0*b)*x4+
     +           w(x,x3)*(sgtemp/stemp)**
     +           (2.0D0*b-1.0D0)*dsgdxbb(x,x1,x2)-
     +           sf(x)**(2.0D0*b)/stemp**
     +           (2.0D0*b-1.0D0)/(2.0D0*b)*x4
return
end
```

## D.4 FORTRAN Code for Linear Interpolation

```
 subroutine WAT_DRAIN2(klat,thpor,psi0,b,slope,dd,IL2,IG,i,j,asat_t0,asat_t1)
 implicit none
 integer i,j,IL2,IG,k,ifound
 integer WATcount(IL2,IG)
 real DELT,TFREZ
 real klat,thpor,psi0,b,slope,dd
 real var,asat_t0,asat_t1
 real xs,t0,t1
 real IntAlgit(IL2,IG,10000),IntAlgt(IL2,IG,10000)
 real IntAlgdelt(IL2,IG,10000)
     real IntAlgxst(IL2,IG,10000),IntAlgs(IL2,IG,10000)
     COMMON /CLASS1/ DELT,TFREZ
 ifound=0
     WATcount(i,j)=WATcount(i,j)+1
     if (WATcount(i,j)==1) then
        write (*,*) 'Obtaining bulk saturation curve for layer',j
! Bulk saturation
         call BulkSat(klat,thpor,psi0,b,slope,dd)
       open(88,file='BulkSat.txt')
        do k=1,10000
           read (88,"(i10,4e15.5)",iostat=var)  IntAlgit(i,j,k),   &
                  &            IntAlgt(i,j,k),IntAlgdelt(i,j,k),   &
                  &             IntAlgxst(i,j,k),IntAlgs(i,j,k)
       if (var<0) exit
        enddo
    close(88)
 endif
 do k=1,10000
if (IntAlgs(i,j,k)<1.0e-6) exit
    if (asat_t0>=IntAlgs(i,j,k)) then
   ifound=1
   if (k>1) then
      t0=IntAlgt(i,j,k)-(IntAlgs(i,j,k)-asat_t0)/(IntAlgs(i,j,k)-          &
       & IntAlgs(i,j,k-1))*(IntAlgt(i,j,k)-IntAlgt(i,j,k-1))
      t1=t0+DELT
```

```
      if (t1<IntAlgt(i,j,k)) then
         asat_t1=IntAlgs(i,j,k)-(IntAlgt(i,j,k)-t1)/(IntAlgt(i,j,k)-t0)*   &
               & (IntAlgs(i,j,k)-asat_t0)
         if (asat_t1>asat_t0) asat_t1=asat_t0
         if (asat_t1<IntAlgs(i,j,k)) asat_t1=IntAlgs(i,j,k)
         !xs=IntAlgxst(i,j,k-1)+(t1-IntAlgt(i,j,k-1))/(IntAlgt(i,j,k)-     &
           & IntAlgt(i,j,k-1))*(IntAlgxst(i,j,k)-IntAlgxst(i,j,k-1))
      else
         asat_t1=IntAlgs(i,j,k+1)-(IntAlgt(i,j,k+1)-t1)/(IntAlgt(i,j,k+1)- &
               & IntAlgt(i,j,k))*(IntAlgs(i,j,k+1)-IntAlgs(i,j,k))
         if (asat_t1>IntAlgs(i,j,k)) asat_t1=IntAlgs(i,j,k)
         if (asat_t1<IntAlgs(i,j,k+1)) asat_t1=IntAlgs(i,j,k+1)
         !xs=IntAlgxst(i,j,k)+(t1-IntAlgt(i,j,k))/(IntAlgt(i,j,k+1)-       &
           & IntAlgt(i,j,k))*(IntAlgxst(i,j,k+1)-IntAlgxst(i,j,k))
      endif
   else
      t0=IntAlgt(i,j,k)-(IntAlgs(i,j,k)-asat_t0)/(IntAlgs(i,j,k)-1.0)*      &
               & IntAlgt(i,j,k)
      t1=t0+delt
      if (t1<IntAlgt(i,j,k)) then
         asat_t1=IntAlgs(i,j,k)-(IntAlgt(i,j,k)-t1)/(IntAlgt(i,j,k)-t0)*    &
                     & (IntAlgs(i,j,k)-asat_t0)
         !xs=t1/IntAlgt(i,j,k)*IntAlgxst(i,j,k)
      else
         asat_t1=IntAlgs(i,j,k+1)-(IntAlgt(i,j,k+1)-t1)/(IntAlgt(i,j,k+1)- &
               & IntAlgt(i,j,k))*(IntAlgs(i,j,k+1)-IntAlgs(i,j,k))
         !xs=IntAlgxst(i,j,k)+(t1-IntAlgt(i,j,k))/(IntAlgt(i,j,k+1)- &
           & IntAlgt(i,j,k))*(IntAlgxst(i,j,k+1)-IntAlgxst(i,j,k))
      endif
   endif
endif
if (ifound==1) exit
 enddo
     if (ifound==0) asat_t1=asat_t0
return
end
```

# Appendix E

# Numerical Discretization

Table E.1: Numerical Discretization for each experiment base case

| – | Sand | Loamy sand | Sandy loam | Silt loam | Remarks |
|---|---|---|---|---|---|
| $\Delta z$ (cm) | 0.4 | 0.5 | 0.8 | 3.0 | Green-Ampt model applicability |
| $\Delta t$ (s) | 1.0 | 3.0 | 30 | 300.0 | |
| $\Delta z$ (cm) | 1.0 | - | - | 1.0 | Improved interflow/infiltration |
| $\Delta t$ (s) | 3.0 | - | - | 300.0 | |

# Bibliography


[1] M. B. Abbott, J. C. Bathurst, J. A. Cunge, P.E. OConnell, and J. Rasmussen. An introduction to the european system: Systeme hydrologique europeen (she). *Journal of hydrology*, 87:61–77, 1986. 3, 12, 70

[2] B. Ambroise, J. Freer, and K. J. Beven. Application of a generalized topmodel to the small ringelbach catchment, voages, france. *Water Resources Research*, 32(7):2147–2159, 1996. 15

[3] B. Ambroise, K. J., and J. Freer. Towards a generation of the topmodel concepts: topographic indices of hydrological similarity. *Water Resources Research*, 32(7):2135–2145, 1996. 16

[4] P. M. Barrios and K. Beven. Evaluation of topmodel. *Southern Cooperative Series Bulletin*, 1998.

[5] D. A. Barry, J. Y. Paralange, L. Li, D. S. Jeng, and M. Crapper. Green-ampt approximations. *Advances in Water Resources*, 28(10):1003–1009, 2005. 28, 50, 73, 74, 78

[6] D. A. Barry, J.-Y. Parlange, G. C. Sander, and M. Sivaplan. A class of exact solution for richards equation. *Journal of Hydrology*, 142:29–46, 1992. 26, 28, 49

[7] K. Beven. Kinematic subsurface stormflow. *Water Resources Resaerch*, 17:14191424., 1981.

[8] K. Beven. Infiltration into a class of vertically nonuniform soils. *Hydrological Sciences*, 29(4):425–434, 1984. 28, 29

[9] K. Beven. Hillslope runoff processes and flood frequency characteristics. *A. D. Abrahams (ed.) Hillslope Processes*, pages 187–202, 1986. 15

[10] K. Beven. Linking parameters across scales: sub-grid parameterizations and scale dependent hydrological models. *Hydrological Process*, 9:507–525, 1995. 3

[11] K. Beven. Topmodel. *Computer Models and Watershed Hydrology*, pages 627–668, 1995. 32

[12] K. Beven. Topmodel: a critique. *Hydrological Process*, 11(9):1069–1086, 1997. 3

[13] K. Beven. Searching for the holy grail of scientific hydrology: Qt=h(s,r,delt t) a as closure. *Hydrology and earth system sciences*, 10(5):609 –618, 2006. 5

[14] K. Beven and E. Wood. Cathment geomorphology and the dynamics of runoff contributing areas. *J. Hydrol.*, 65:139–158, 1983.

[15] K. J. Beven. Changing ideas in hydrology the case of physically-based models. *Journal of Hydrology*, 105:157–172, 1989. 119

[16] K. J Beven. *Rainfall-runoff modeling: the primer*. Wiley, 2000. 10

[17] K. J. Beven. *Rainfall Runoff Modelling: The Primer*. John Wiley and Sons, 2002. 12, 14

[18] K. J. Beven and M. J. Kirkby. A physically based variable contributing area model of basin hydrology. *Hydrol. Sci. Bull.*, 24(1):43–69, 1979. 85

[19] W. H. Beyer. *CRC Standard Mathematical Tables, 28th ed.* FL: CRC Press, 1987.

[20] B.R. Bicknell, J.C. Imhoff, J.L. Kittle J., T.H. Jobes, and A.S. Donigian. Hydrological simulation program-fortran. user's manual for release 12. Technical report, U.S. EPA, Ecosystem Research Division, Athens, Georgia/U.S. Geological Survey, Office of Surface Water, Reston, Virginia, USA, 2001. 49, 70

[21] J. Boussinesq. Thorie des ondes et des remous qui se propagent le long d'un canal rectangulaire horizontal, en communiquant au liquide contenu dans ce canal des vitesses sensiblement pareilles de la surface au fond. *Journal de Mathmatique Pures et Appliques*, 17:55108, 1872. 14

[22] J. Boussinesq. Boussinesq, recherches thoriques sur lcoulement des nappes deau infiltres dans le sol et sur le dbit des sources. *J. Math. Pure. Appl. 5me. Ser.*, 10:578, 1904. 14

[23] H. Bouwer. Rapid field measurement of air entry value and hydraulic conductivity of soil as significant parameters in flow system analysis. *Water Resources Research*, 2(4):729–738, 1966. 52

[24] R. H. Brooks and A.T. Corey. Hydraulic properties of porous media. Technical report, Colorado State University, Fort Collins, CO, 1964. 10, 11

[25] W. Brutsaert. The permeability of a porous medium determined from certain probability laws for pore size distribution. *Water Resources Research*, 4(2):425–434, 1968.

[26] W. Brutsaert. Vertical infiltration in dry soil. *Water Resources Research*, 13:363–368, 1977. 26

[27] W. Brutsaert. The unit response of groundwater outflow from a hillslope. *Water Resource Research*, 30(10):2759–2763, 1994. 13

[28] L. Chen and M. H. Young. Green-ampt infiltration model for sloping surfaces. *Water Resources Research*, 42(7):1–9, 2005. 29

[29] Z.-Q. Chen, , R. S. Govindaraju, and M. L. Kavvas. Spatial averaging of unsaturated flow equations under infiltration conditions over areally heterogeneous fields, 1. Development of models. *Water Resour. Res.*, 30:523533, 1994. 70

[30] C. W. Childs. 14th conference, international association for great lakes research, toronto, canada, april 19-21,1971. 1971.

[31] E. C. Childs and M. Bybordi. The vertical movement of water in stratified porous material. 1. infiltration. *Water Resources Research*, 5(2):446–459, 1969. 28

[32] E.C. Childs. The water-table, equipotentials and streamlines in drained land. *III. Soil Sci.*, 59:405415, 1945. 25

[33] S. T. Chu. Infiltration during an unsteady rain. *Water Resources Research*, 14(3):461–466, 1978. 29, 79

[34] R. B. Clapp and G. M. Hornberger. Empirical equations for some soil hydraulic properties. *Water Resources Research*, 14:601–604., 1978. 10, 11, 37, 51, 53, 85, 92

[35] T. P. Clement, W. R. Wise, and J. Molz F. A physical based, two-dimensional, finite-difference algorithm for modeling variably saturated flow. *Journal of Hydrology*, 161:71–90, 1994.

[36] N. Collis-George. Infiltration equations for simple soil systems. *Water Resources Research.*, 13:395–403, 1977. 26

[37] C. Corradini, R. S. Govindaraju, and R. Morbidelli. Simplified modelling of areal average infiltration at the hillslope scale. *Hydrological Processes*, 16(9):1757–1770, 2002. 70, 72

[38] J. R. Craig, G. Liu, and E. D. Soulis. Runoff-infiltration partitioning using an upscaled green-ampt solution. *Hydrol. Process*, 24:1–7, 2010. 50, 70, 71, 75, 77, 79

[39] J. Crank and P. Nicolson. A practical method for numerical evaluation of solutions of partial differential equations of the heat conduction type. *Proc. Camb. Phil. Soc.*, 43:5067, 1947.

[40] G. Dagan and E. Bresler. Unsaturated flow in spatially variable fields, 1. Derivation of models of infiltration and redistribution. *Water Resour. Res.*, 19:413–420, 1983. 70

[41] H. Darcy. Dtermination des lois d'coulement de l'eau  travers le sable. *Les Fontaines Publiques de la Ville de Dijon*, page 590594, 1856. 8

[42] A. P. J. DeRoo, Hazelhoff L., and G. M. B. Heuvelink. Estimating the effects of spatial variability of infiltration on the output of a distributed runoff and soil erosion model using monte carlo methods. *Hydrol. Process*, 6:127–143, 1992. 70

[43] R.E. Dickinson, A. Henderson-Sellers, and P. J. Kennedy. Biosphere-atmosphere transfer scheme (bats) version le as coupled to the ncar community climate model. Technical report, NCAR, 1992. 18, 21

[44] S. L. Dingman. *Physical Hydrology.* Macmillan Publishing Company: New York, 1994.

[45] S.L Dingman. *Physical Hydrology.* Prentice-Hall, Inc., Upper Saddle River, New Jersey 07458, 2002. 32, 88, 96, 104, 109, 116, 121

[46] J. Duan and N. Miller. A generalized power function for the subsurface transmissivity profile in topmodel. *Water Resources Research*, 33(11):2559–252, 1997. 16

[47] J. Dupuit. *Estudes Thoriques et Pratiques sur le mouvement des Eaux dans les canaux dcouverts et  travers les terrains permables (Second Edition ed.).* Paris: Dunod., 1863.

[48] R. Essery, M. Best, and P. Cox. Moses 2.2 technical documentation. hadley centre technical note 30. Technical report, Met Office, 2001. 18, 21

[49] J. S. Famiglietti, D. Ryu, M. Rodell A. A. Berg, and T. J. Jackson. Field observations of soil moisture variability across scales. *Water Resources Research*, 44, 2008. 76

[50] P. Forchheimer. Ueber die ergiebigkeit von brunnen- anlagen und sickerschlitzen. *Z Architkt Ing Verlag*, 32:539563, 1886.

[51] M. Franchini, J. Wendling, C. Obled, and E. Todini. Phydical interpretation and sensitivity analysis of the topmodel. *Jounal of Hydrology*, 175:293–338, 1996. xi, 15

[52] R. A. Freeze and Cherry J. A. *Groundwater*. Prentice Hall, Englewood Cliffs, NJ 07632, 1979. 118

[53] W. Gardner. Some steady-state solutions of the unsaturated moisture flow equation with application to evaporation from a water table. *Soil Sci.*, 85:228–232, 1958. 10, 11

[54] K. Gavin and J. Xue. A sloped method to analyze infiltration into unsaturated soil slopes. *Computers and Geotechnics*, 35:223–230, 2008. 29

[55] T. A. Ghezzehei, T.J. Kneafsey, and G. W. Su. Correspondence of the gardner and van genuchten/mualem relative permeability function parameters. *water resources research*, 43:1–7, 2007. 10

[56] B. P. Ginger, J. J. Stone, D. P. Guertin, and L. J. Lane. a strip model approach to parameterize a coupled green-ampt kinematic wave model. *Journal of the american water resources association*, 38(5):1363–1377, 2002. 50

[57] G. Gottardi and A. Venutelli. Control-colume finite-element model for two-dimensional overland flow. *Advanced Water resources*, 16(3):277–284, 1993.

[58] G. Gottardi and A. Venutelli. Richards: Computer program for the numerical simulation of one-dimensional infiltration into unsaturated soil. *Computer & Geosciences*, 19(9):1239–1266, 1993. xii, 42, 43, 44

[59] R. S. Govindaraju, R. Morbidelli, and C. Corradini. Areal infiltration modeling over soils with spatially correlated hydraulic conductivities. *Journal of Hydrologic Engineering*, 6(2):150–158, 2001. 65, 70, 77

[60] W. H. Green and G. A. Ampt. Studies on soil physics, 1: The flow of air and water through soils. *Journal of Agricultural Science*, 4(1):1–24, 1911. 26, 49, 70

[61] H. V. Gupta, L. A. Bastidas, S. Sorooshian, W. J. Shuttleworth, and Z. L. Yang. Parameter estimation of a land surface scheme using multicriteria methods. *Journal of Geophysical Research*, 104(D16):491–503, 1999. 119

[62] J. D. Haskett, Y. A. Pachepsky, and B. Acocka. Use of the beta distribution for parameterizing variability of soil properties at the regional level for crop yield estimation. *Agricdhual Systems*, 48:73–86, 1995. 76

[63] J. D. Hewlwtt and A. R. Hibbert. Moisture and energy conditions within a sloping mass during drainage. *J. of Geophys. Res.*, 68:1081–1087, 1963.

[64] D. Hillel. *Fundamentals of Soil Physics*. Academic Press. New York, NK, 1980. 23

[65] H. N. Holtan, C. B. England, G. P. Lawless, and G. A. Schumaker. Moisture-tension data for selected soils on experimental watersheds. *Agr. Res. Serv.*, pages 41–144, 1968. 24

[66] R. E. Horton. An approach towards a physical interpretation of infiltration capacity. *Soil Science Society of America Proceedings*, 5:399–417, 1940. 24

[67] F. Hossain. Non-linearity of storage-discharge relationship: implications for radar rainfall-based stream flow prediction uncertainty. Submitted to Journal of Hydrologic Engineering,2005. 17, 19

[68] S. M. Hsu, C. Ni, and P. Hung. Assessment of three infiltration formulas based on model fitting on richards equation. *Journal of Hydrologic Enginnering*, 7(5):373–379, 2002.

[69] I. Iorgulescu and A. Musy. Generalization of topmodel for a power law transmissivity profile. *Hydrological Process*, 11:1353–1355, 1997. 16

[70] Y. Jia and N. Tamai. Modeling infiltration into a multi-layered soil during a unsateady rain. *Annual Journal of Hydraulic Engineering*, 41:31–36, 1997. 29

[71] M. Kirkby. Hillslope runoff processes and models. *Jounal of Hydrology*, 100:315–339, 1988. 3

[72] J. H. Knight. *Solution of the non-linear diffusion equation: existence, uniqueness, and estimation*. PhD thesis, Australian National University, Canberra., 1973. 26

[73] A. N. Kostiakov. On the dynamics of the coefficient of water percolation in soils and on the necessity of studying it from a dynamic point of view for the purposes of amelioration. *Trans. Com. Int. Soc. Soil Sci.*, pages 17–21, 1932. 24

[74] N. Kouwen. Watflood/watrote hydrological model routing and flow forecasting system. Technical report, University of Waterloo, 2006. 31, 32

[75] N. Kouwen, E. D. Soulis, A. Pietroniro, J. Donald, and R. A. Harrington. Grouped response units for distributed hydrologic modeling. *J. of Water Resources Planning and Management*, 119(3):289–305, 1991. 30

[76] N. Kouwen, R. Soulis, F. Seglenieks, A. Bingeman, and B. Davison. An introduction to watflood and watclass. In *MAGS: Model Cross-Training Course*, 2002. 106

[77] T. Lakhankar, H. Ghedira, M. Temimi, A. E. Azar, and R. Khanbilvardi. Effect of land cover heterogeneity on soil moisture retrieval using active microwave remote sensing data. *Remote Sens.*, 1:80–91, 2009. 76

[78] G.H. Leavesley, R.W. Lichty, B.M. Troutman, and L.G. Saindon. Precipitation-runoff modeling system: Users manual. Technical report, U.S. Geological Survey Water Investigation Report. 83-4238., 1983. 30

[79] X. Liang and D. P. Lettenmaier. A simple hydrologically based model of land surface water and energy fluxes for general circulation models. *J. of Geophysical Research*, 99(D7):14415–14428, 1994. 12, 16, 18, 22

[80] X. Liang, E. F. Wood, and D. P. Lettenmaier. Surface soil moisture parameterization of the vic-2l model: evaluation and modification. *Global and Planetary Change*, 13:195–206, 1996. 16, 17

[81] G Liu, J. R. Craig, and E. D. Soulis. Applicability of the green-ampt infiltration model with shallow boundary conditions. Accepted for publication by Hydrologic Engineering, 2010. 49

[82] G. Liu, E. D. Soulis, and J. R. Craig. An analytical interflow scheme for distributed hydrological models: numerical tests in a homogenous soil. In *Calibration and Reliability in Groundwater Modeling Managing Groundwater and the Environment*, 2009.

[83] G. Liu, E. D. Soulis, and J. R. Craig. Evaluation of an explicit solution to the green-ampt infiltration equation. In *The 7th International Conference on Calibration and Reliability in Groundwater Modeling "Managing Groundwater and the Environment"*, 2009. 28

[84] J. Liu, J. Zhang, and J. Feng. Green-ampt model for layered soils with nonuniform initial water content under unsteady infiltration. *Soil Science Society of America*, 72:1041–1047, 2008. 29, 50

[85] I. Lorgulescu and A. Musy. Generalization of topmodel for a power law transmissivity profile. *Hydrol. Ptocess.*, 11:1353–1355, 1997.

[86] D. R. Mailapalli, W. W. Wallender, R. Singh, and N.S. Raghuwanshi. Application of a nonstandard explicit integration to solve green and ampt infiltration equation. *Journal of Hydrologic Engineering*, 13(2):203–206, 2009.

[87] R. A. Maller and M. L. Sharma. An analysis of areal infiltration considering spatial variability. *Jounal of Hydrology*, 52:2537, 1981. 70

[88] S. Manabe. Climate and ocean circulation: The atmospheric circulation and the hydrology of the earths surface. *Monthly Weather Review*, 97(11):739–805, 1969. 3, 12, 17, 19

[89] R. G. Mein and C. L. Larson. Modeling infiltration during a steady rain. *Water Resources Research*, 9 (2):384394, 1973. 49, 53

[90] M. Merzougui and G. F. Gifford. Spatial variability of infiltration rates on a semiarid seeded rangeland. *Hydrol. Sci. Journal*, 32 (3):243250, 1987. 76

[91] V. J. Mezencev. Theory of formation of the surface runoff (in russian). *Meteorolgia I gidrologia*, 3:3346, 1948. 24

[92] G. R. Miller, D. D. Baldocchi, B. E. Law, and T. Meyersd. An analysis of soil moisture dynamics using multi-year data from a network of micrometeorological observation sites. *Advances in Water Resources*, 30(5):1065–1081, 2007. 76

[93] R. Morbidelli, C. Corradini, and R. S. Govindaraju. A field-scale infiltration model accounting for spatial heterogeneity of rainfall and soil saturated hydraulic conductivity. *Hydrological Processes*, 20(7):1465–1481, 2006. 70, 72

[94] R. Morbidelli, C. Corradini, and R. S. Govindaraju. A simplified model for estimating field-scale surface runoff hydrographs. *Hydrological Processes*, 21(13):1772–1779, 2007.

[95] S. Mouelhi, C. Michel, C. Perrin, and V. Andreassian. Linking stream flow to rainfall at the annual time step: The manabe bucket model revisited. *Journal of Hydrology*, 328:283 296, 2006.

[96] A. Musy. Ecole polytechnique fdrale, lausanne, suisse. *e-drologie*, 2001. xi, 23

[97] I. D. Nathale, L. Katia L., and P. Alain. Sechiba, a new set of parameterization of the hydrologic exchanges at the land-atmosphere interface within the lmd atmospheric general circulation model. *J. Clim*, 6:248–273, 1993. 21

[98] M. A. Nearing, B. Y. Liu, L. M. Risse, and X. Zhang. Curve numbers and green-ampt effective hydraulic conductivities,. *Water Resources Bulletin*, 32 (1):125136, 1996.

[99] S. L. Neitsch, J. G. Arnold, J. R. Kiniry, and J. R. Williams. Assessment tool theoretical documentation. Technical report, Grassland, Soil and Water Research Laboratory, Agricultural Research Service, Temple, Texas, 2002. 49, 70

[100] S. P. Neuman. Wetting front pressure head in the infiltration model of green and ampt. *Water Resources Research*, 12(3):564–566, 1976. 53, 76

[101] G. Niu, Z. L. Yang, R. E. Dickinson, L. E. Gulden, and H. Su. Development of a simple groundwater model for use in climate models and evaluation with gravity recovery and climate experiment data. *J. of Geophysical Research*, 112, 2007. 16

[102] J. Noihlan and S. Planton. A simple parameterization of land surface processes for meterological models. *Mon. Weahter Rev.*, 117:536–549, 1989. 18, 20

[103] NSERL. Usda-water erosion prediction project, hillslope profile and watershed model documentation. Technical report, National Soil Erosion Research Laboratory, 1995. 3, 12, 49, 70

[104] J. Y. Parlange. A note on the green and ampt equation. *Soil Science*, 119(6):466–467, 1975. 26

[105] J. Y. Parlange and R. Haverkamp. *Infiltration and ponding time. In unsaturated flow in hydrologic modeling, Theory and Practice*. Kluwer Academic Publishers. Boston, MA, 1989.

[106] D. K. Patgiri and T. C. Baruah. Spatial variability of total porosity, air entry potential and saturation water content in a cultivated inceptisol. I. Semivariance analysis. *Agricultural Water Management*, 27(1):1–9, 1995. 76

[107] J. R. Philip. The theory of infiltration: 4 sorptivity and algebraic infiltration equations. *Soil Science*, 84:257–264, 1957. 24, 26, 49, 70

[108] J. R. Philip. Extend techniques of calculation of soil-water movement with some physical consequences. *Tran. Int. Congr. soil Sci.*, 1:1–9, 1968.

[109] A. J Pitman. The evolution of, and revolution in, land surface schemes designed for climate models. *International Journal of Climatology*, 23:479510, 2003. 1

[110] V. Ravi and J. R. Williams. Estimation of infiltration rate in the vadose zone: Compilation of simple mathematical models. Technical report, US EPA, ORD, EPA/600/R-97/128a, 1998. 28, 49

[111] A. L. Richards. Capillary conduction of liquid throgh porous media. *Physics*, 1:316–333, 1931. 9

[112] M. A. Nearing Risse, L. M. and M. R. Savabi. Determining the green-ampt effective hydraulic conductivity from rainfall-runoff data for the wepp model. *Transactions of the ASAE*, 37 (2):411418, 1994.

[113] G. D. Salvucci and D. Entekhabi. Explicit expressions for green-ampt (delta function diffusivity) infiltration rate and cumulative storage. *Water Resources Research*, 30(9):2661–2663, 1994. 28

[114] SCS. *Hydrology, national engineering handbook,supplement a, section 4, chapter 10,*. Washington, DC., 1956, 1964, 1971, 1993.

[115] S. E. Serrano. Explicit solution to green and ampt infiltration equation. *Journal of Hydrology Engineering*, 6(4):336–340, 2001. 28

[116] S. E. Serrano. Improved decomposition solution to green and ampt equation. *Journal of Hydrology Engineering*, 8(3):158–160, 2003. 28

[117] M. L. Sharma, G. A. Gander, and C.G. Hunt. Spatial variability of infiltration in a watershed. *Jounal of Hydrology*, 45(1-2):101–122, 1980. 70, 76

[118] J. Simunek, M. Th. van Genuchten, and M. Sejna. The hydrus software package for simulating the two- and three-dimensional movement of water, heat, and multiple solutes in variably-saturated media. Technical report, 1University of California Riverside, Riverside, CA, 2006. 3, 12

[119] M. Sivapalan and E. F. Wood. Spatial heterogneity and scale in the infiltration response of catchments. *Scale Problems in Hydrology, Water Science and Technology Library, D. Reidel, Dordrecht.*, page 81106, 1986. 70

[120] R. E. Smith and D. C. Goodrich. Model for rainfall excess patterns on randomly heterogeneous area. *Journal of Hydrological Engineering*, 5:355362, 2000. 70, 77

[121] R. E. Smith, K. R. J. Smettem, P. Broadbridge, and D.A. Woolhiser. *Infiltration Theory for Hydrologic Applications.* American Geophysical Union, Washington, DC, 2002. 10, 25

[122] W. O. Smith. Infiltration in sand and its relation to groundwater recharge. *Water Resources Research*, 6:237–248, 1967.

[123] E. D. Soulis. 2006. Personal consultant. 3

[124] E. D. Soulis, J. R. Craig, V. Fortin, and G. Liu. A simple expression for the bulk field capacity of a sloping soil horizon. Submitted to Hydrological Processes. xiv, 84

[125] E. D. Soulis, G. Liu, and J. R. Craig. Update on ip3 soil water budget: progress towards an analytical solution for sand hallow aquifers. 2008.

[126] E. D. Soulis, G. Liu, and J. R. Craig. Update on ip3 soil water budget: development of an analytical interflow scheme. In *IP3/WC2N Joint Annual Workshop, Lake Louise, AB, Lake Louise Inn, Canada.*, 2009.

[127] E. D. Soulis, G. Liu, J. R. Craig, and Vincent Fortin. Update on ip3 soil water budget: verification of a revised analytical soil moisture parameterization scheme. 2008.

[128] E. D. Soulis, G. Liu, and F. Seglenieks. From the micro- to the meso-scale, the mags ti e approach. In *IUGG XXIV2007 conference poster*, 2007.

[129] E. D. Soulis, K. R. Snelgrove, N. Kouwen, and F. Seglenieks. Towards closing the vertical water balance in canadian atmospheric models: coupling of the land surface scheme class with the distributed hydrological model watflood. *Atmosphere Ocean*, 38(1):251–269, 2000. 5

[130] E.D Soulis and A. Pietroniro. A framework for hydrological modelling in mags. In *Prediction in Ungauged Basins: Approaches for Canadas Cold Regions*, 2004. 4

[131] F. Stagnitti, M.B. Parlange, T.S. Steenhuis, and J.-Y. Parlange. Drainage from a uniform soil layer on a hillslope. *Water Resources Research*, 22(5):631–634, 1986.

[132] J. F. Stamm, E. F. Wood, and D. P. Lettenmaier. Sensitivity of a gcm simulation of global climate to the representation of land-surface hyarology. *J. Cliamte*, 7(8):1218–1239, 1994. 12, 16

[133] D. Swartzendruber. The applicability of darcys law. *Soil Sci. Soc. Ameri. Proc.*, 32:11–18, 1968.

[134] D. Swartzendruber and F. R. Clague. An inclusive infiltration equation for downward water entry into soil. *Water Resources Resaerch*, 25(4):619–626, 1989. 25, 26

[135] N Thomson. Cive 774 advanced numerical methods for environmental applications. Course notes, Fall 2007. 40

[136] B. A. Tolson. Optimization in environmental water resources. course note, Winter 2006. 120

[137] B. A. Tolson and C. A. Shoemaker. Dynamically dimensioned search algorithm for computationally efficient watershed model calibration. *Water Resour. Res.*, 43:W01413,doi:10.1029/2005WR004723., 2007. 120

[138] M. Th. Van Genuchten. A closed-form equation for predicting the hydraulic conductivity of unsaturated soils. *Soil Science Society of America Journal*, 44:892–898, 1980. 10, 11

[139] Det Norske Veritas. Statistical representation of soil data, recommended practice report dnv-rp-c207. Technical report, 1997. 76

[140] D. Verseghy. Class the canadian land surface scheme (version 3.4). Technical report, Climate Research Division, Science and Tecnology Branch, Enviornment Canda, 2009. 107

[141] D.L. Verseghy. Class - a canadian land surface scheme for gcms i. soil model. *International Journal of Climatology*, 11:111–133, 1991. 3, 18, 20, 49, 52, 70, 106, 111

[142] D.L. Verseghy. Class - a canadian land surface scheme for gcms ii. vegetation model and coupled runs. *International Journal of Climatology*, 13:347–370, 1993. 106

[143] J. A. Vrugt, H. V. Gupta, W. Bouten, and S. Sorooshian. A shuffled complex evolution metropolis algorithm for optimization and uncertainty assessment of hydrologic model parameters. *Water Resource Resarch*, 39(8):1201, doi:10.1029/2002WR001642, 2003. 119

[144] Q. Wang, M. Shao, and Horton R. Modified green and ampt models for layered soil infiltration and muddy water infiltration. *Soil Science*, 164(7):445–453, 1998. 29

[145] H. S. Wheater, Jakeman A. J., and K.J. Beven. *Progress and directions in rainfall-runoff modeling, In: Modelling change in environmental systems*, chapter Chapter 5, pages 101–132. Wiley, Chichester, UK, 1993. 119

[146] R. Z. Whipkey and M. J. Kirkby. *Hillslope hydrology.* Wiley, 1978.

[147] E. F. Wood, D. P. Lettenmaier, and V. G. Zartarian. A land-surface hydrology parameterization with subgrid variability for general circulation models. *J. Geophys. Res.*, 97(D3):27172728, 1992.

[148] E. F. Wood, M. Sivapalan, K. Beven, and L. Band. Effects of spatial variability and scale with implications to hydrologic modeling. *J. Hydrol.*, 102:29–47, 1988. 30

[149] Y. k. Xue, F. J. Zeng, and C. A. Schlosser. Ssib and its sensitivity to soil properties-a case study using hapex-mobilhy data. *Global and Planetary Change*, 13:183–194, 1996. 18, 22

[150] E. G. Youngs. Soil physics and hydrology. *Journal of Hydrology*, 100:411–431, 1988. 14, 23

[151] H. Zhai and C. H. Benson. The log-normal distribution for hydraulic conductivity of compacted clays: Two or three parameters? *Geotechnical and Geological Engineering*, 24(5):1149–1162, 2005. 65

[152] H. zhang, S. X. Chen, and S. Y. Chen. Numerical simulation of infiltration in unsaturated soil. *Rock and soil mechanics*, 25(5):715–718, 2003.